

VOLUME XLVII

GEMS & GEMOLOGY

WINTER 2011



Dyed Purple Ethiopian Opal

Garnet Composition from Gem Properties

Symmetry Boundaries for Round Brilliants

Odontolite in Antique Jewelry

Safety of Irradiated Blue Topaz

THE QUARTERLY JOURNAL OF THE GEMOLOGICAL INSTITUTE OF AMERICA



pg. 262




pg. 287

EDITORIAL

- 259 **Great Expectations**
Jan Iverson

FEATURE ARTICLES

- 260 **Dyed Purple Hydrophane Opal**
Nathan Renfro and Shane F. McClure
 Evidence indicates that opal with a vivid purple bodycolor, reportedly from a new deposit in Mexico, is actually dyed hydrophane from Ethiopia.
- 272 **Determining Garnet Composition from Magnetic Susceptibility And Other Properties**
Donald B. Hoover
Garnet compositions derived from measurements of physical properties correspond closely with results obtained using chemical data.
- 286 **GIA's Symmetry Grading Boundaries for Round Brilliant Cut Diamonds**
Ron H. Geurts, Ilene M. Reinitz, Troy Blodgett, and Al M. Gilbertson
GIA's boundary limits for 10 symmetry parameters, measured by optical scanners, will improve consistency in the symmetry grading of round brilliants.

NOTES & NEW TECHNIQUES

- 296 **A Historic Turquoise Jewelry Set Containing Fossilized Dentine (Odontolite) and Glass**
Michael S. Krzemnicki, Franz Herzog, and Wei Zhou
Investigation of six antique brooches identified most of their "turquoise" cabochons as odontolite.

RAPID COMMUNICATIONS

- 302 **The Radioactive Decay Pattern of Blue Topaz Treated by Neutron Irradiation**
Jian Zhang, Taijin Lu, Manjun Wang, and Hua Chen
Some "London Blue" topaz contains radioactive trace impurities that may require several years to reach a safe level.

REGULAR FEATURES

- 308 **Lab Notes**
Fancy Vivid purple diamond • Strongly purple-colored black diamond • HPHT-treated diamond with the fluorescence pattern of an HPHT-grown synthetic • Type IIb diamond with long phosphorescence • Clarity-enhanced opal with artificial matrix • Ethiopian black opal • Coated bead-cultured freshwater pearls • Tenebrescent zircon
- 316 **Gem News International**
Chondrodite from Tanzania • Blue dolomite from Colombia • Fluorite from Namibia • Common opal from Western Australia • A bicolor, bi-pattern hydrophane opal • Chatoyant quartz with cinnabar inclusions • Quartz with acicular emerald inclusions • Quartz with izoklakeite inclusions • Ruby and sapphire mining in Pakistan • Color-change sphene from Pakistan/Afghanistan • Cobalt blue-colored spinel from Vietnam • Trapiche spinel from Mogok, Myanmar • Non-nacreous "cat's-eye pearls" • Large synthetic quartz • Sugar-acid treatment of opal from Wollo, Ethiopia • Conference reports
- 336 **Book Reviews/Gemological Abstracts Online Listing**



pg. 312

EDITORIAL STAFF

Editor-in-Chief
Jan Iverson
jan.iverson@gia.edu

Senior Manager, Communications
Amanda Luke

Editor, Gem News International
Brendan M. Laurs

Circulation Coordinator
Martha Rivera
(760) 603-4000, ext. 7142
martha.rivera@gia.edu

Editor and Technical Specialist
Brendan M. Laurs
blaurs@gia.edu

Editor, Gemological Abstracts
Brendan M. Laurs

Contributing Editor
James E. Shigley

Editor-in-Chief Emeritus
Alice S. Keller

Associate Editor
Stuart D. Overlin
soverlin@gia.edu

Editors, Lab Notes
Thomas M. Moses
Shane F. McClure

Editors, Book Reviews
Susan B. Johnson
Jana E. Miyahira-Smith

PRODUCTION STAFF

Art Director
Nanette Newbry
Studio 2055

Image Specialist
Kevin Schumacher

G&G Online:
gia.metapress.com

EDITORIAL REVIEW BOARD

Ahmadjan Abduriyim
Tokyo, Japan

Shigeru Akamatsu
Tokyo, Japan

Edward W. Boehm
Chattanooga, Tennessee

James E. Butler
Washington, DC

Alan T. Collins
London, UK

John L. Emmett
Brush Prairie, Washington

Emmanuel Fritsch
Nantes, France

Jaroslav Hyřl
Prague, Czech Republic

A. J. A. (Bram) Janse
Perth, Australia

E. Alan Jobbins
Caterham, UK

Mary L. Johnson
San Diego, California

Anthony R. Kampf
Los Angeles, California

Robert E. Kane
Helena, Montana

Lore Kiefert
Lucerne, Switzerland

Michael S. Krzemnicki
Basel, Switzerland

Thomas M. Moses
New York, New York

Mark Newton
Coventry, UK

George R. Rossman
Pasadena, California

Kenneth Scarratt
Bangkok, Thailand

James E. Shigley
Carlsbad, California

Christopher P. Smith
New York, New York

Wuyi Wang
New York, New York

Christopher M. Welbourn
Reading, UK

SUBSCRIPTIONS

Copies of the current issue may be purchased for \$29.95 plus shipping. Online subscriptions are \$74.95 for one year (4 issues). Combination print + online subscriptions are \$139.95 in the U.S. and \$160 elsewhere for one year. Canadian subscribers should add GST. Discounts are available for group subscriptions, renewals, GIA alumni, and current GIA students. For institutional rates, contact the Associate Editor. Subscriptions include *G&G's* monthly gemological e-newsletter, the *G&G eBrief*.

To purchase subscriptions and single issues (print or PDF), visit store.gia.edu or contact the Circulation Coordinator.

PDF versions of individual articles and sections from Spring 1981 forward can be purchased at gia.metapress.com for \$12 each. Visit gia.edu/gandg for free online access to the 1934–2010 subject and author index and all 1934–1980 issues.

Gems & Gemology's five-year impact factor (for 2005–2009) is 1.737, according to the 2010 Thomson Reuters Journal Citation Reports (issued June 2011). *Gems & Gemology* is abstracted in Thomson Reuters products (*Current Contents: Physical, Chemical & Earth Sciences* and Science Citation Index—Expanded, including the Web of Knowledge) and other databases. For a complete list of sources abstracting *G&G*, go to gia.edu/gandg.

Gems & Gemology welcomes the submission of articles on all aspects of the field. Please see the Guidelines for Authors at gia.edu/gandg or contact the Editor. Letters on articles published in *Gems & Gemology* are also welcome.

Abstracting is permitted with credit to the source. Libraries are permitted to photocopy beyond the limits of U.S. copyright law for private use of patrons. Instructors are permitted to photocopy isolated articles for noncommercial classroom use without fee. Copying of the photographs by any means other than traditional photocopying techniques (Xerox, etc.) is prohibited without the express permission of the photographer (where listed) or author of the article in which the photo appears (where no photographer is listed). For other copying, reprint, or republication permission, please contact the Editor.

Gems & Gemology is published quarterly by the Gemological Institute of America, a nonprofit educational organization for the gem and jewelry industry.

Postmaster: Return undeliverable copies of *Gems & Gemology* to GIA, The Robert Mouawad Campus, 5345 Armada Drive, Carlsbad, CA 92008.

Our Canadian goods and service registration number is 126142892RT.

Any opinions expressed in signed articles are understood to be opinions of the authors and not of the publisher.

ABOUT THE COVER



The recent appearance of purple play-of-color opal, reportedly from a new deposit in Mexico, has heightened interest in the origin and nature of this material. In this issue, Nathan Renfro and Shane McClure offer gemological and spectroscopic evidence that this opal is actually dyed hydrophane from Ethiopia's Wollo Province. The fine untreated Wollo opals on the cover consist of a 35.32 ct oval cabochon in the center courtesy of William Larson (Palagems.com, Fallbrook, California) surrounded by two pieces of rough (8.16 and 12.78 g) and four polished stones (6.95–32.55 ct) that are courtesy of David Artinian (Clear Cut Inc., Poway, California). Photos by Robert Weldon.

Color separations for *Gems & Gemology* are by Pacific Plus, Carlsbad, California.
Printing is by Allen Press, Lawrence, Kansas.

GIA World Headquarters The Robert Mouawad Campus 5345 Armada Drive Carlsbad, CA 92008 USA

© 2011 Gemological Institute of America All rights reserved. ISSN 0016-626X

GREAT EXPECTATIONS

We all have great expectations for 2012. I've gone a step further with my New Year's resolutions by creating a "goals" book. Not only do I write down my goals, but I also add details such as how and when I will achieve them, and include pictures to make it more visual.

So, what new things can you expect from *Gems & Gemology* in the year ahead? Our goal is to create an enhanced digital journal, one that offers a more interactive experience for our online audience, in support of what we already do. Digital is changing the way information is consumed, and it provides a unique opportunity to reinvent the way we engage with you, our readers. Digital is beyond relevant: It is the future.

But first we finish 2011. Our final issue of the year includes a report by GIA researchers on a new purple opal that's been hitting the market. Although it was reportedly natural material from Mexico, gemological investigation identified it as dyed opal from Ethiopia. Because this hydrophane opal can be very absorbent, we can expect to see many other treatments applied to it.

Our goal is to create an enhanced digital journal, one that offers a more interactive experience for our online audience, in support of what we already do.

Another piece by GIA researchers examines symmetry parameters in diamond grading. Thanks to improvements in measuring round brilliants with optical scanners, GIA can now evaluate symmetry more consistently. This measurement-based procedure will complement the visual assessment of symmetry, which is one of the components of GIA's diamond cut grade.

We also feature a set of six antique brooches, apparently from the early- to mid-19th century, set with light blue cabochons that were once thought to be turquoise. Analysis revealed that most of the supposed turquoise cabochons are actually fossilized dentine, also known as odontolite.

In this issue, we also highlight neutron-irradiated "London Blue" topaz. Some trace impurities in this topaz become radioactive after neutron irradiation. The authors found that irradiated samples from China contained up to four of these radioactive impurities. Most of the samples were safe to handle 95 days after irradiation, but others will require several years to reach a safe level.

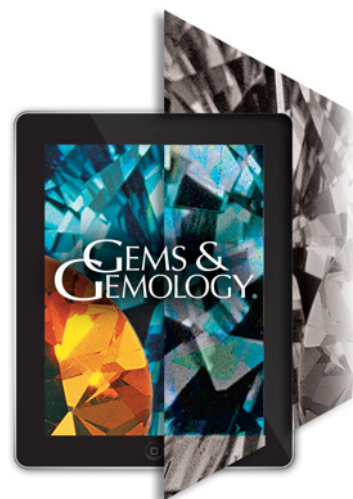


I suspect that many of us, when we were younger, thought we'd be flying around in space pods by now instead of driving cars. Yet when the future arrives, we find that technology never changes as fast as our minds imagined it! As we progress in our digital offerings, we are going to keep it simple by delivering relevant content in innovative ways.

In 2012, I hope you achieve your goals and meet your expectations.

Cheers,

Jan Iverson | Editor-in-Chief | jan.iverson@gia.edu



DYED PURPLE HYDROPHANE OPAL

Nathan Renfro and Shane F. McClure

Opals with an unusual purple bodycolor and strong play-of-color have recently appeared in the market. Reportedly from a new deposit in Mexico, they have a vivid bodycolor unlike that of any natural play-of-color opal seen in the trade so far. This alone was enough to raise suspicion, and gemological and spectroscopic evidence indicates that the purple coloration is artificial. A comparison of this purple opal with numerous samples from Ethiopia's Wollo Province strongly suggests that it is actually dyed hydrophane opal from those deposits. Several previously undocumented characteristics of Wollo opals are described, including zeolite mineral inclusions.

Not often is a significant new deposit discovered of a well-known gem material. The 1994 discovery of play-of-color opal in Ethiopia's Shewa Province sparked the industry's attention. Unfortunately, much of this opal turned out to be unstable, and spontaneous fracturing rendered it largely unusable for jewelry (Johnson et al., 1996). In 2008, another large Ethiopian deposit was found in the province of Wollo. While similar in appearance to some of the Shewa material, this opal appears to be much more stable than its predecessor (Rondeau et al., 2010). The 2011 Tucson show saw an abundant influx of beautiful and relatively inexpensive opal from the Wollo deposit.

The new Ethiopian material displayed a property not often seen in opal. Much of the opal is hydrophane, meaning it is very porous and easily absorbs water (or other liquids), often turning translucent or transparent in the process. The degree to which these stones show this property varies, but some absorb water so readily that the tiny bubbles escaping from their surface give the impression of effervescence. This property, while interesting to watch, also

has an important implication: Any gem material that absorbs liquids so easily has the potential to be treated by methods such as dyeing or impregnation. Recognizing this possibility, we performed several experiments to determine the effect of such treatments on this opal, before they appeared in the market. These experiments—which were surprisingly successful—led us to believe that it would only be a matter of time until we encountered such treated material in the trade.

Indeed, in October 2011, we were presented with several samples of hydrophane opal that had a bright purple bodycolor (not known to occur naturally in play-of-color opal; e.g., figure 1), and our suspicions were immediately raised (Renfro and McClure, 2011). In addition, these opals were said to be from a new source in Mexico, but everything about them except the color reminded us of Ethiopian opal from Wollo.

Purple opal has been reported from several localities, including Mexico. However, all of the material examined to date was opaque (or at best translucent) and did not possess play-of-color. The purple in these common opals has been attributed to inclusions of fluorite (Fritsch et al., 2002).

While the color of the new play-of-color samples was said to be natural, the authenticity of any gem material can only be proven through scientific analysis and observation. Our goal in this study is to

See end of article for About the Authors and Acknowledgments.

GEMS & GEMOLOGY, Vol. 47, No. 4, pp. 260–270,
<http://dx.doi.org/10.5741/GEMS.47.4.260>.

© 2011 Gemological Institute of America

answer two fundamental questions: Is this purple opal naturally colored, and is it actually from a new deposit in Mexico? This article also reports the results of an experiment on the dyeing of hydrophane opal from Wollo Province.

MATERIALS AND METHODS

Nine purple opal cabochons ranging from 4.13 to 15.25 ct, and nine rough opal samples between 0.66 and 1.96 g, were submitted for testing at GIA's Carlsbad laboratory. Seven of the rough opals had a purple bodycolor of varying intensity, but one had a distinct green-blue bodycolor (0.76 g) and another was light blue (0.93 g). Client permission was obtained for potentially destructive testing on these stones, as hydrophane opal will occasionally crack when soaked in liquid (author NR's personal experience). To expand our sample base, we subsequently borrowed 22 rough opals (0.57–3.96 g) from the same source that submitted the purple cabochons. These ranged from light to very dark purple, except for three samples showing no visible purple color. Two of the 22 samples also showed an amber color zone. We also examined approximately 2 kg of rough natural hydrophane opal from Wollo (loaned from two reputable sources who obtained them in Ethiopia) for comparison with the purple opal.

We performed standard gemological characterization of all cut samples (both dyed and natural) with a Duplex II refractometer, a desk-model spectroscope, a long- and short-wave 4 watt UV lamp, and a gemological microscope. Inclusions were identified with a Renishaw InVia Raman microscope using a 514 nm argon-ion laser at a resolution of 1 cm^{-1} .

Visible spectroscopy measurements were made by soaking one purple opal cabochon and the green-blue piece of rough opal in acetone (with the client's permission) for 54 hours, and then placing the acetone in standard 1 cm glass cuvettes for analysis with a Perkin Elmer Lambda 950 spectrometer. We used a data interval and slit width of 1 nm, and baseline correction was accomplished using a 1 cm glass cuvette filled with pure acetone. Spectroscopy was not performed directly on the opals themselves, in order to eliminate interference from light scatter and the intrinsic opal spectrum that would prevent us from making baseline-corrected measurements of any dye present in the samples. Such measurements were necessary for color analysis, as described below.

From the absorption spectrum of the acetone solutions, we calculated color space coordinates to



Figure 1. The purple bodycolor of this new opal, reportedly from Mexico, raised concerns about the origin of the material. Shown here are three rough samples ranging from 1.28 to 3.09 g and five cabochons weighing 5.31–9.32 ct. Photo by Robert Weldon.

visually verify that the spectra collected were indeed responsible for the samples' coloration. Because of the very low absorption values of the solutions, they needed to be concentrated to visually resolve color. Since we could not physically concentrate our solutions and still have enough volume to fill the cuvettes, this was done artificially by multiplying the absorption values by a factor of 15. This method is equivalent to a solute (dye) concentration 15 times greater than that in the original solutions due to the linearity of absorption. The absorption values of the artificially "concentrated" acetone solutions were converted to transmission spectra using GRAMS spectroscopy software by Thermo; CIE L*a*b* color space coordinates were calculated using the GRAMS color analysis application. These coordinates were imported into Adobe Photoshop to produce color samples.

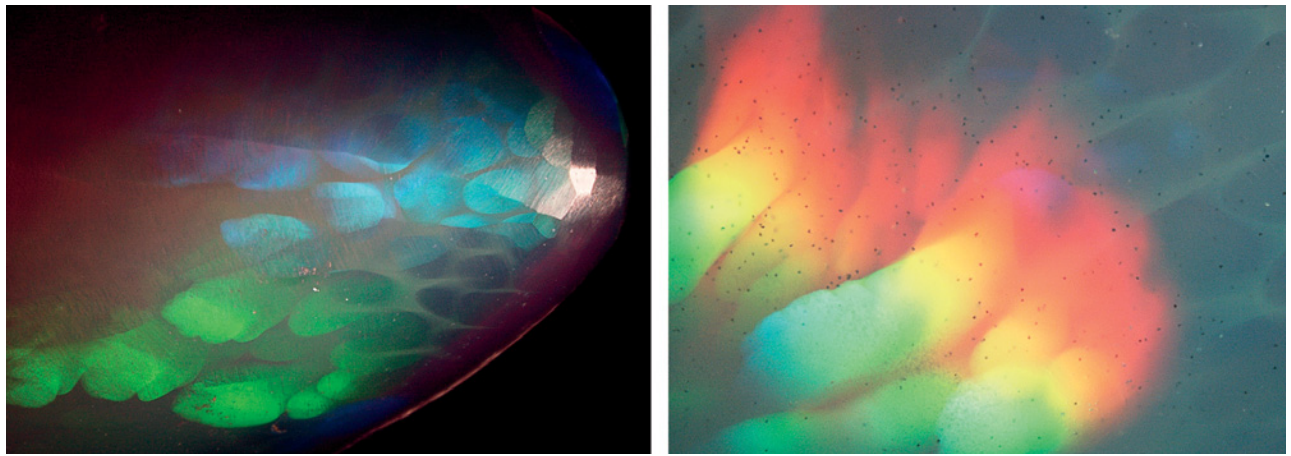


Figure 2. The purple opal (left, image width 7.8 mm) displayed a “digit” pattern of play-of-color and a cellular pattern of potch that had a greenish cast, much like natural Wollo opal (right, image width 4.3 mm). Photomicrographs by S. F. McClure.

Chemical analysis of 15 samples (seven untreated white Wollo opals and eight purple samples) was performed using a Thermo X Series II ICP-MS with a New Wave Research UP-213 laser ablation sampling system and a frequency-quintupled Nd:YAG laser (213 nm wavelength) with a 4 ns pulse width. We used 55- μm -diameter ablation spots, a fluence of around 10 J/cm², and a 7 Hz repetition rate. Qualitative chemical analysis of two rough samples (one treated and one untreated) showing black surface material was also performed with a Thermo ARL Quant-X EDXRF system in a vacuum, utilizing no filter at 4 kV and 1.98 mA, and a cellulose filter at 8 kV and 1.98 mA.

As noted above, given the hydrophane character of Wollo opal, it should be amenable to dyeing. To test this, eight rough (0.17–1.42 g) and three cabochons (1.65–3.55 ct) of hydrophane opal from the personal collection of author NR were immersed in variously colored solutions prepared from Sharpie permanent markers and acetone. The samples were soaked for anywhere from several minutes to several hours, depending on how rapidly the solution was

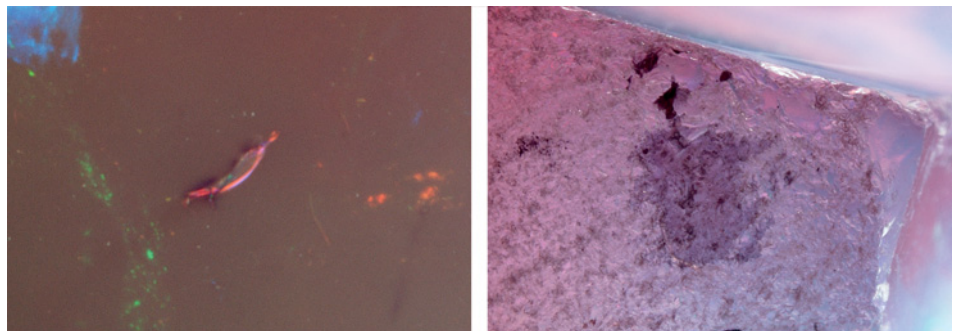
absorbed. After removal from the solution, the samples were dried under a tensor lamp for several hours until the acetone had completely evaporated.

RESULTS AND DISCUSSION

Gemological Properties. All the opals provided by our client were clearly hydrophane, as they tended to feel sticky when handled, a result of the opal trying to draw moisture from the skin. The spot RI measurements of the nine purple opal cabochons ranged from 1.37 to 1.41. The SG was between 1.70 and 1.77, as measured hydrostatically before allowing the stones to completely soak full of water. All samples showed a very weak blue reaction to long- and short-wave UV radiation. A broadband absorption was seen in the desk-model spectroscope from ~550 to 600 nm.

Magnification revealed octahedral to irregularly shaped dark crystals of pyrite, tube-like inclusions that resembled fossilized plant matter, and cellular play-of-color referred to as a “digit pattern” because of its resemblance to fingers (figure 2; Rondeau et al., 2010). The pattern consists of relatively large rounded cells separated by a thin network of potch (common

Figure 3. In many of the purple opals, color concentrations were evident in surface pits (left, image width 2.2 mm), and on unpolished areas (right, image width 2.4 mm). Photomicrographs by S. F. McClure.



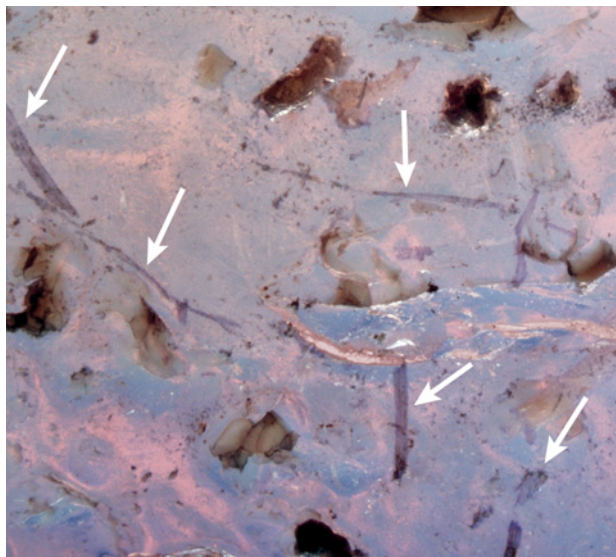
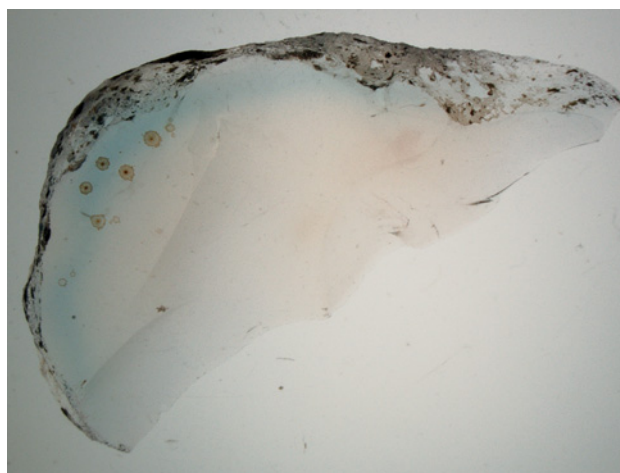


Figure 4. Surface-reaching inclusions in the purple opals sometimes had a purple color. Those shown here probably consist of fossilized plant matter. Photomicrograph by S. F. McClure; image width 3.1 mm.

opal without play-of-color) that has a slightly greenish appearance. Also seen in some samples were subtle purple color concentrations around pits, scratches, surface-reaching fractures, and sometimes on unpolished surfaces (figure 3). Some surface-reaching inclusions were also purple (figure 4). However, not all of the samples showed color concentrations.

Gem materials are often immersed in a liquid of similar refractive index to see subtle internal features such as color zoning. This is particularly help-

Figure 5. Immersion of this light blue rough opal in water showed a surface-conformal color layer, which is indicative of treatment. Photomicrograph by N. Renfro; image width 9.5 mm.



ful with rough material. With opal, water serves as an adequate immersion liquid. One of the rough stones in the initial group had a light blue bodycolor and did not appear to be treated. We were quite surprised when immersion revealed a blue zone along the surface of the stone (figure 5). This type of surface-conformal coloration is indicative of color treatment in many gem materials, including beryllium- and titanium-diffused corundum, smoke-treated opal, and dyed agate.

Spectroscopy of the Dye. No color was observed in the acetone after soaking the purple sample for up

NEED TO KNOW

- In late 2011, purple opal showing strong play-of-color appeared in the market, reportedly from a new deposit in Mexico.
- The presence of a dye was indicated by soaking the opal in acetone for an extended period (54 hours), followed by spectroscopic processing of the solution that yielded a purple color consistent with the opal's bodycolor.
- Physical, chemical, and microscopic properties of the purple opal overlap those of hydrophane opal from Ethiopia's Wollo Province, except for the purple color.
- Dye experiments on Wollo hydrophane opal produced vivid bodycolors.
- Multiple lines of evidence indicate that the purple opal is actually dyed Wollo hydrophane.

to 16 hours. After 54 hours, the acetone solution appeared very light purple. Spectroscopy of this sample revealed a broad asymmetrical feature with an apparent maximum located at about 594 nm and a shoulder close to 557 nm (figure 6, top). This feature was consistent with the broadband absorption observed in the desk-model spectroscope.

The CIE L*a*b* coordinates calculated using GRAMS and Adobe Photoshop software yielded a purple color (figure 6, center), consistent with the bodycolor of the opal. This proved that the coloring agent of the purple opal can be partially removed with acetone, and since we know of no naturally occurring coloring agent showing this behavior, we concluded that the opals are colored by an artificially introduced dye.

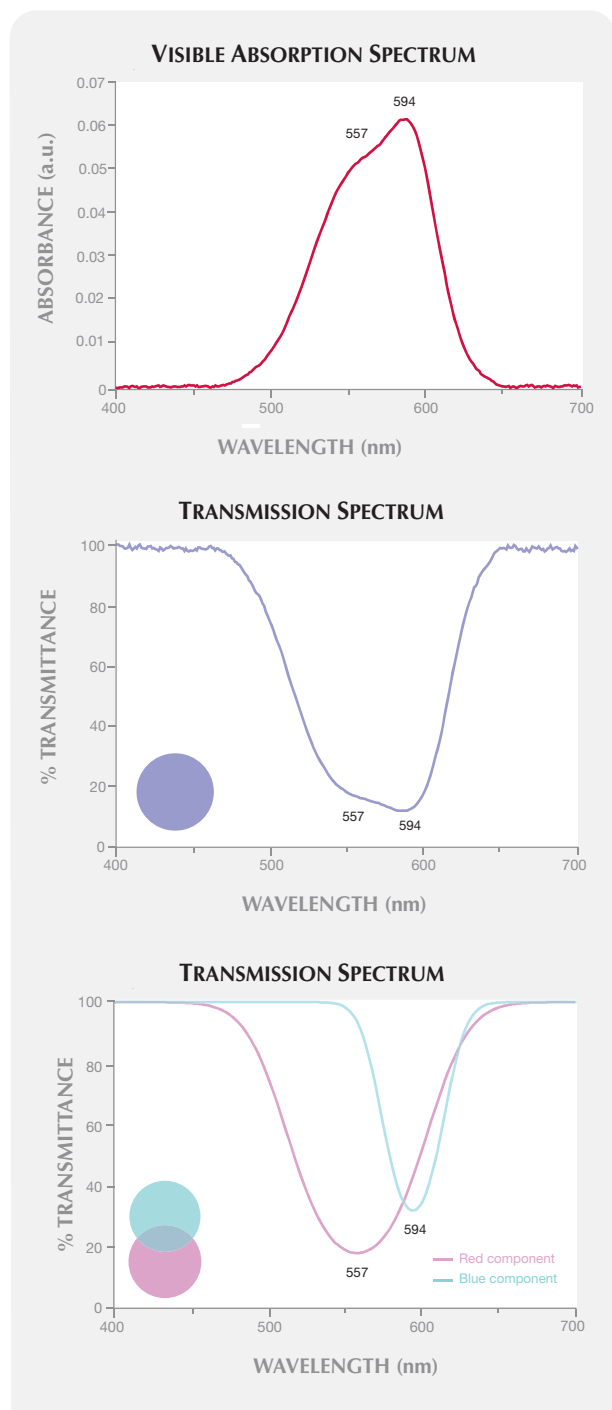


Figure 6. After a purple opal was soaked in acetone, the solution's visible-range spectrum revealed a broad asymmetrical absorption feature (top). The absorption from the artificially "concentrated" dye (center, transmission spectrum) generated a CIE $L^*a^*b^*$ color space coordinate consistent with the opal's purple bodycolor. Two color components of the purple dye were resolved from the transmission spectrum (bottom). The 557 nm feature produced the purplish pink component, and the 594 nm feature contributed the blue one.

To better understand the absorption spectrum of the purple dye, we used the peak fitting application of GRAMS to resolve the individual features from the asymmetric absorption (figure 6, bottom). The full width at half maximum (FWHM) of the 557 nm feature was 72 nm, and the FWHM of the 594 nm feature was 36 nm. Processing of these component spectra showed that the 557 nm feature was responsible for a purplish pink component, while the 594 nm band contributed a blue component. The combination of these purplish pink and blue features is responsible for the purple color.

This dye extraction procedure was also applied to the green-blue piece of rough (figure 7, inset). After the opal had soaked in acetone for several hours, we measured the solution's visible absorption. A broad band was recorded at 627 nm (figure 7); the calculated color was again consistent with the opal's bodycolor.

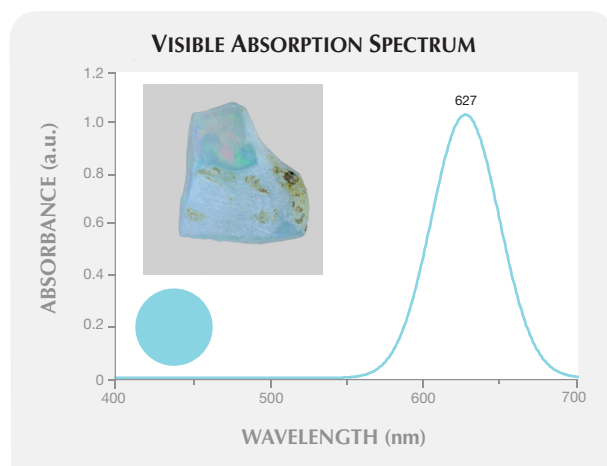


Figure 7. A green-blue opal was also soaked in acetone, and spectroscopy of the solution revealed a broad absorption feature centered at 627 nm. The corresponding color space coordinates yielded a color sample consistent with the bodycolor of the sample. Inset photo by Robison McMurtry.

Comparison of Dyed Purple Opal to Wollo Hydrophane. We compared the physical appearance, gemological properties, and other analytical results for the dyed material with opals from Wollo Province to assess the original source of the treated opal and help investigate claims of Mexican origin.

Gemological Properties. The RI and SG values of the dyed opal were virtually identical to those of Wollo opal. This is notable because both properties are par-

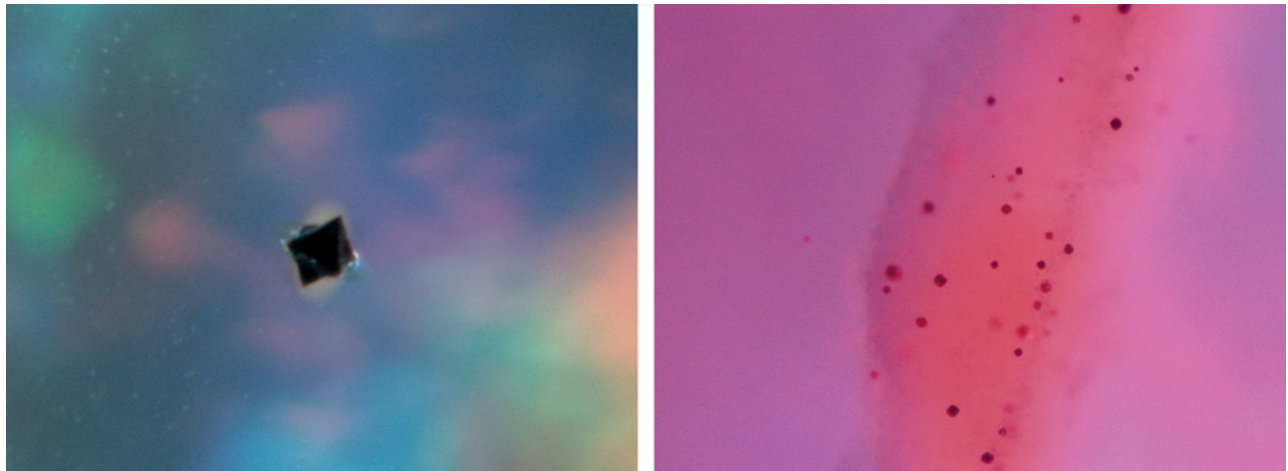


Figure 8. Both the Wollo (left) and dyed purple (right) opals showed irregular to octahedral black-appearing crystals of pyrite. Photomicrographs by N. Renfro (left, image width 0.8 mm) and S. F. McClure (right, image width 1.7 mm).

ticularly low for play-of-color opal (Webster, 1996). Ultraviolet fluorescence was also very similar between the two (see also Rondeau et al., 2010).

Most opal is porous to a minor degree, but it is quite unusual for it to be so porous as to qualify as hydrophane. Both Wollo opal and the purple opal display this property—sometimes it is so prominent that the transparency can be seen to improve as it soaks up water. Mexican hydrophane opal is known, but to our knowledge it is opaque and light pink or brown (with or without play-of-color).

The structure of the play-of-color is also noteworthy. Wollo opal sometimes displays an unusual “digit pattern” to its play-of-color that many consider unique to Ethiopian material (Rondeau et al., 2010). We observed this same pattern in some of the

purple opal. A similar pattern has been reported in some opal from Virgin Valley, Nevada, but it was smaller and had a slightly different appearance (Gübelin and Koivula, 2005).

Inclusions. Microscopic characteristics are essential to any comparison of gem materials. All of the features described in this section were seen in both the untreated Wollo samples and the purple opals. Among those reported previously in Ethiopian opal are small black octahedral crystals that have been suggested to be pyrite (Johnson et al., 1996; Rondeau et al., 2010; figure 8) and irregular tubular inclusions with a cellular structure that are probably fossilized plant matter (Rondeau et al., 2011; figure 9). Though neither can be considered unique to Ethiopia, pyrite

Figure 9. Irregular tube-like inclusions that appear to be fossilized plant matter occurred in both the Wollo opal (left, image width 4.4 mm) and the dyed opal (right, image width 5.0 mm) samples. Photomicrographs by S. F. McClure.



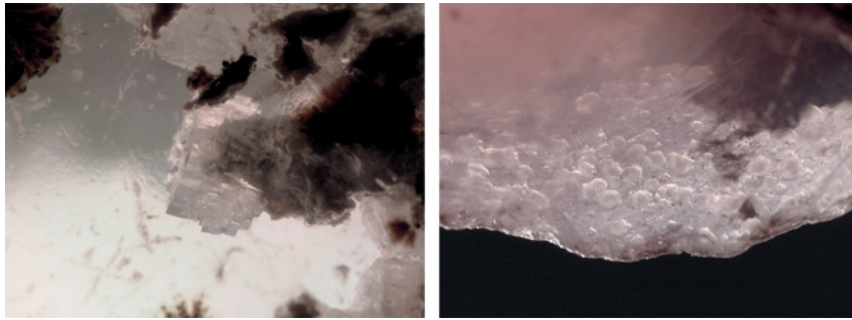


Figure 10. Pseudo-cubic crystals of a zeolite mineral (possibly chabazite) were found in both Wollo opal (left, image width 2.0 mm) and the dyed purple opal (right, image width 4.3 mm). We believe this is the first report of this mineral as an inclusion in opal. Photomicrographs by S. F. McClure.

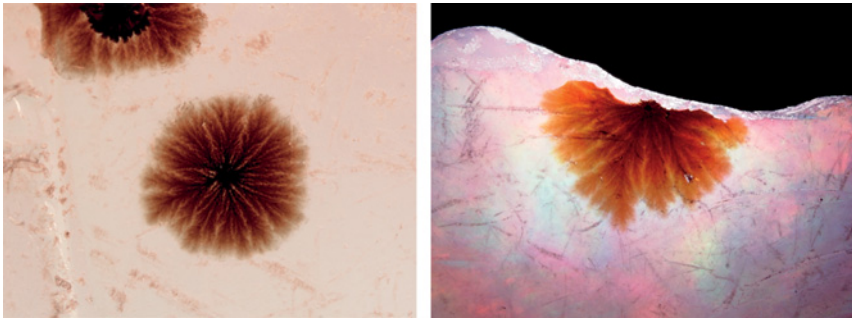


Figure 11. Surface to subsurface circular radiating brown inclusions were occasionally visible in both Wollo opal (left, image width 2.0 mm) and the dyed purple material (right, image width 6.5 mm). Photomicrographs by S. F. McClure.

octahedra are certainly rare in gem opal. Plant matter is found included in opal from a number of other deposits.

We discovered another type of inclusion that to the best of our knowledge has not been reported in opal: a zeolite mineral, possibly chabazite. It formed numerous small, transparent, colorless, euhedral pseudo-cubic crystals (figure 10). They were present only in rough material, at or near the surface, but always included within the opal, whether the natural Wollo or dyed purple material. The crystals appear to have been growing on the matrix before it was engulfed by the opal.

Also found in the rough opal samples, either at or just below the surface, was a flat round brown material with a radial structure (figure 11). These were typically seen along fracture surfaces. We were unable to match their Raman spectra to anything in our database.

Surface Characteristics. Because we examined numerous rough samples of both natural Wollo and dyed purple opal, we noted some surface features that would not be visible on cut stones.

Layers of a dark brown to black opaque material were present on many of the natural Wollo samples. The same material was found on the surface of the rough purple opal we examined—the only difference being that it was distinctly purplish (figure 12). We were unable to obtain a conclusive Raman spectrum from this material, but the spectra did indicate the presence of amorphous carbon. EDXRF analysis detected considerable Mn. Previous studies of Ethiopian opal have identified such material as a manganese oxide (Johnson et al., 1996; Rondeau et al., 2010).

The rough Ethiopian opal we examined sometimes had a brownish pink to pink opaque material on the surface that was very friable and had a matte

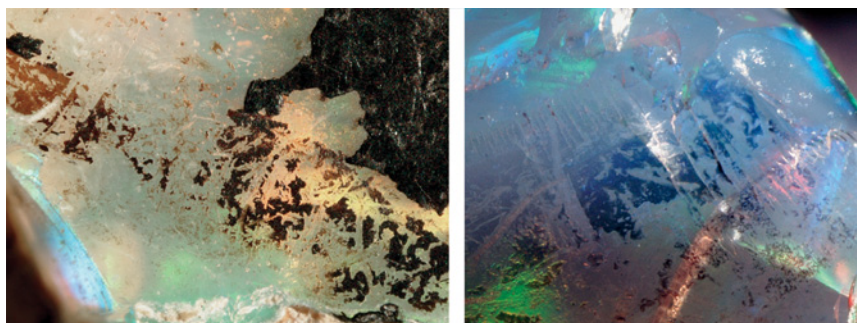


Figure 12. Black to brownish black surface coatings were present on rough pieces of both the Wollo (left) and purple (right) opals, the only difference being the purplish cast of the coating on the dyed material. Photomicrographs by S. F. McClure; image width 6.7 mm.

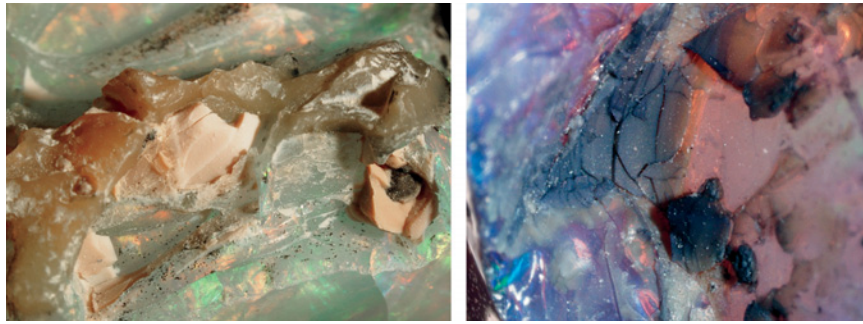


Figure 13. Some Wollo opals displayed opaque material on the surface that may be a type of common opal (left, image width 8.0 mm). Some of the purple samples showed similar material, except that it was purplish gray (right, image width 5.9 mm). Photomicrographs by S. F. McClure.



Figure 14. Well-formed quartz crystals with very short prism faces were visible in the matrix of both Wollo opal (left, image width 2.3 mm) and the dyed purple material (right, image width 1.4 mm). Photomicrographs by S. F. McClure.

or dull fracture luster (figure 13, left). Raman spectroscopy gave a poor unidentifiable signal, and LA-ICP-MS analysis showed it was composed primarily of Si. We suspect it is some kind of highly disordered common opal. This same material was found on the surface of some of the rough purple opal, the only difference being the color: It was mostly dark gray and uneven, with much darker fractures and an often purplish cast (figure 13, right).

Matrix. Many of the rough samples, both natural Wollo and dyed purple, still had matrix attached to them. The matrix was typically beige, though several pieces of the dyed opal had matrix that was very dark purplish gray. In all cases, it was a soft clay-like material that contained numerous mineral grains. These matrix-hosted mineral grains were found in both the Wollo and the purple opal, and consisted of:

(1) transparent light brown hexagonal crystals of quartz with very short prism faces (figure 14), some of which showed dissolution features and contained rounded light green and black inclusions (figure 15); (2) prismatic colorless to light yellow crystals of K-feldspar; and (3) dark green prismatic fractured crystals of aegirine, a pyroxene (figure 16). The quartz and feldspar were common, but we observed only one example of the aegirine in a Wollo opal and one in a purple sample.

One question that arises is how the purple opal can be dyed if the matrix of some pieces is still the natural beige color. Digging into an area of dark purplish gray matrix with a needle probe showed the normal beige color just below the surface (figure 17). This indicates that the dye did not penetrate the matrix very deeply. Therefore, one possible explanation for the natural-colored matrix on the purple

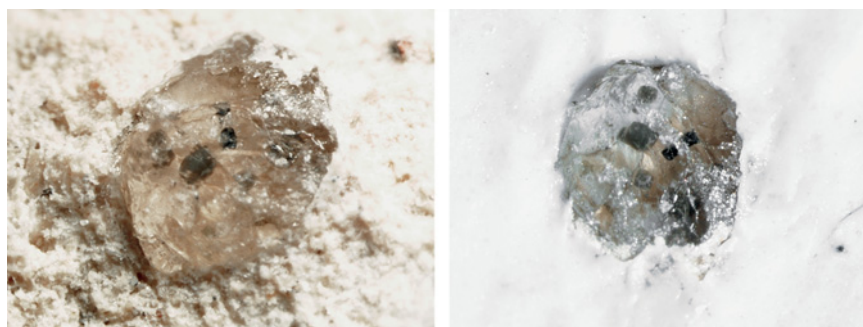


Figure 15. Some of the etched quartz attached to the matrix of both kinds of opals contained identical inclusions of a translucent green material and a black mineral (too small to identify with Raman analysis). Photomicrographs by S. F. McClure; image width 1.4 mm (left, Wollo opal; right, dyed purple opal).

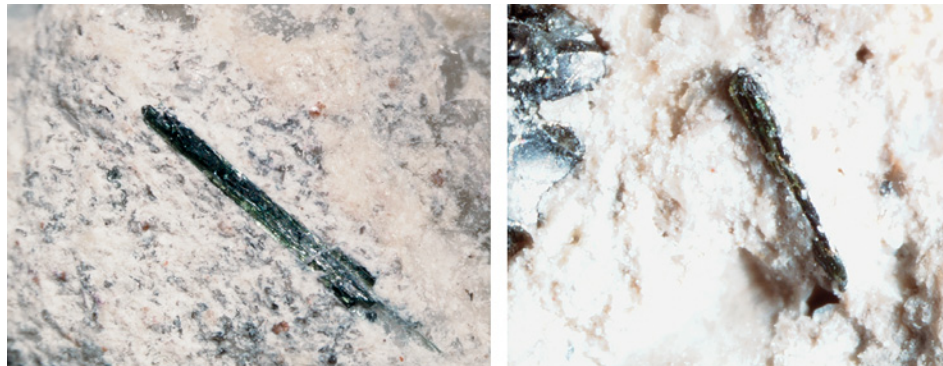
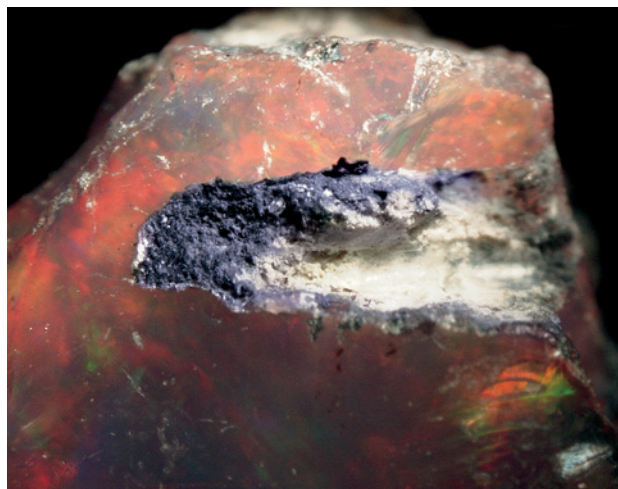


Figure 16. Aegirine crystals were found in the matrix of one Wollo (left, image width 2.2 mm) and one dyed purple opal (right, image width 1.9 mm). Photomicrographs by S. F. McClure.

opal is that the top layer of matrix was removed after the stones were dyed. The softness of the matrix would make this easy to do.

Chemical Composition. We suspected that chemical analysis would provide important clues to the origin of the purple opal. Gaillou et al. (2008) found that opal from the initial Ethiopian deposits at Shewa was easily distinguished by its high Ca content (>1000 ppmw), combined with the presence of Nb. That study found high Ca in orange to brown opals only—white Ethiopian opals were not discussed. Two years later, in a report on Wollo opal, Rondeau et al. (2010) noted a high Ba content (>100 ppmw) in white opals. This was based on a very small sample base, and the article acknowledged that further analyses were necessary.

Figure 17. In some instances, areas of matrix still attached to the rough purple opal had a dark purplish gray color. When scratched with a probe, the matrix under the surface displayed the normal beige color. Photomicrograph by S. F. McClure; image width 5.9 mm.



The small number of samples (15 total) analyzed for this study makes it difficult to detect meaningful chemical trends. Overall, the Ca content of all samples was much higher than the threshold reported by Gaillou et al. (2008): 8,000–10,000 ppmw or higher. Additionally, all the samples contained trace amounts of Nb. The Ba content of the purple opals tended to be lower (80–155 ppmw) but reached 475 ppmw. The Ba content of the untreated Wollo opal was higher overall (175–285 ppmw), but ranged from 65 to 1400 ppmw. There are several possible explanations for this, one of which is that we do not know the starting color of the dyed opal. It could have been yellowish or orangy, in which case it would be expected to have a lower Ba content, as reported by Rondeau et al. (2010). None of the other elements showed any meaningful trends. Clearly, further investigation is necessary to assess the compositional range of these opals.

Dyeing Ethiopian Hydrophane. Vivid bodycolors were produced in our dye experiments (figure 18), and they show how easy it is to artificially color Ethiopian hydrophane opal. We also noted dye concentrations around fine scratches and pits in the surface, implying that the dye transport mechanism is a function of surface area. As scratches represent localized zones of high surface area, it is reasonable to conclude that the transport of a mobile fluid in the opal is driven by capillarity.

To support this hypothesis, we scratched “GIA” on one white Ethiopian opal cabochon and immersed it in our blue dye solution for several seconds. The dye penetrated the stone much deeper in the area immediately surrounding the scratched letters (figure 19, left and center). Very fine scratches on the cabochon were also visibly colored by the blue dye. We then tested the stability of the dyed color by soaking the stone in pure acetone. After several hours, the acetone turned slightly blue and the stone became more uniformly colored and lighter (figure 19, right).

A second dyed blue opal was soaked in water for more than a week with no observable change in the color of the opal or the water. The stability of the dye is therefore largely dependent on the type of solvent to which it is exposed.

Interestingly, the client discovered that soaking the purple opals in hydrogen peroxide would decolorize them. With the client's permission, we demonstrated this on a 0.57 g piece of rough purple opal, soaking it in a 3% solution of hydrogen peroxide for 72 hours. A significant amount of color was lost from the stone, which had a light purplish gray appearance after soaking (figure 20). An absorption spectrum collected on the hydrogen peroxide after soaking the purple opal was featureless. This suggests that the dye was not necessarily removed from the opal or dissolved into the hydrogen peroxide solution; instead, the dye molecules were chemically altered into a compound that does not absorb visible light, or bleached. This technique may be effective in decolorizing some dyed opal, but it would be highly dependent on the type of dye used.

Identification and Origin of Dyed Purple Opal.

Purple color has never been reported for natural play-of-color opals. Microscopic examination strongly suggested the presence of a dyeing agent in the purple sample we examined: color concentrations in fractures and surface pits, patches of purple color on the surface, surface-reaching inclusions that were purple, and certain characteristics on the surface of the rough such as opaque material with dark purplish gray fractures and layers of a dark brown to black material with a purple cast. Proof of dye treatment was that the color could be partially

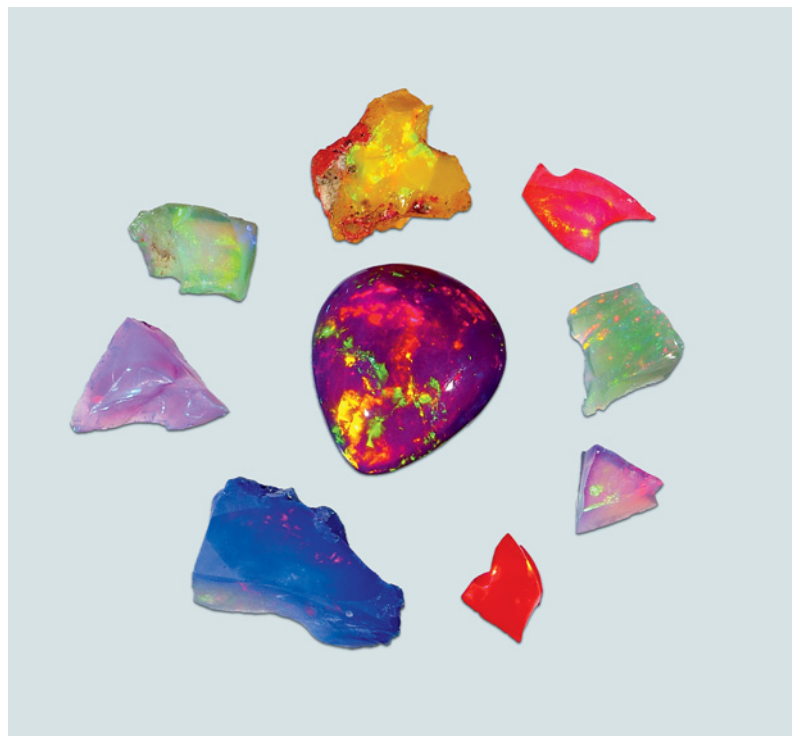
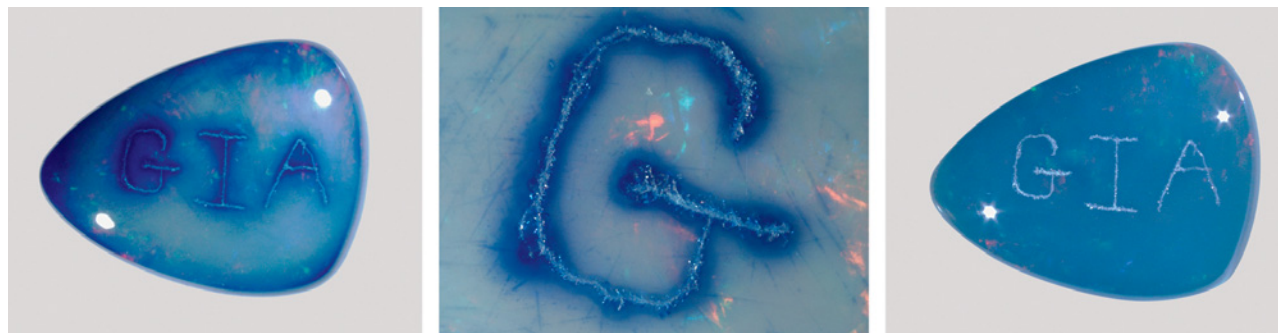


Figure 18. A variety of vivid colors were easily produced by dyeing white Wollo opals with solutions prepared from permanent marker ink and acetone. The cabochon in the center was submitted by a client and weighs 8.77 ct. The rough samples weigh 0.17–1.42 ct; photo by C. D. Mengason.

removed with acetone.

The purported Mexican origin of the purple opal can be dismissed. Instead, the purple material presents all the characteristics of opals from the Wollo deposit in Ethiopia. Both opals are hydrophane, sometimes showing a cellular play-of-color separated by greenish internal patch. Some contain tiny octa-

Figure 19. This 1.75 ct Wollo opal with “GIA” scratched onto the surface shows how dye transport is faster in localized regions with a high surface area, such as pits and scratches (left and center). After the opal was soaked in pure acetone for several hours, the blue dye was homogeneously distributed, eliminating visible dye concentrations (right). Photos by N. Renfro; center image width is 3.8 mm.



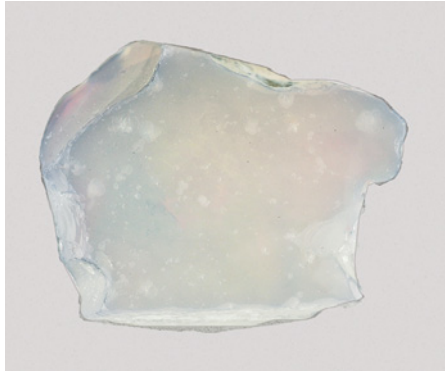


Figure 20. This 0.57 g rough piece of opal is shown before (left) and after (right) its purple color was removed by soaking in hydrogen peroxide for 72 hours. Photos by Robison McMurtry.

hedral inclusions of pyrite and rod- or tube-like inclusions that are probably fossilized plant matter. They have similar RI, SG, and UV fluorescence characteristics, as well as surface layers of manganese oxide. In addition to these properties, we observed some unusual inclusions in both Wollo and dyed purple samples that have not been reported previously, such as transparent pseudo-cubic crystals of a zeolite mineral (probably chabazite) and flat radial brown inclusions.

CONCLUSION

The evidence presented in this study indicates that

the purple samples examined by GIA were dyed opals from Ethiopia. The distinct hydrophane nature of Ethiopian opal makes it susceptible to many kinds of treatment—dyeing is just one. Smoke treatment of this opal to turn it black was recently described (Williams and Williams, 2011), as was sugar treatment (see the Gem News International entry on pp. 333–334 of this issue). Dyeing this material to more believable colors, such as the orange of Mexican fire opal, may pose new identification challenges, and we can expect to see more treatments applied to this hydrophane opal in the future.

ABOUT THE AUTHORS

Mr. Renfro (nathan.renfro@gia.edu) is staff gemologist, and Mr. McClure is director of Identification Services, at GIA's laboratory in Carlsbad.

ACKNOWLEDGMENTS

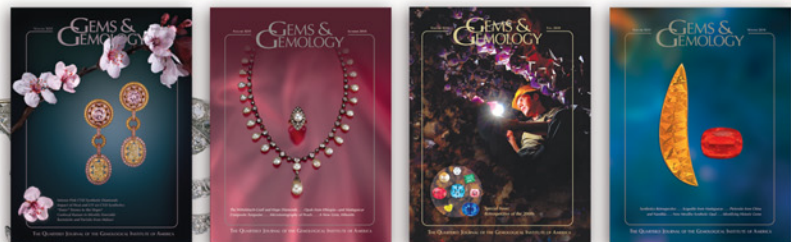
The authors are grateful to David Artinian (Clear Cut Inc.,

Poway, California) for supplying untreated samples of Wollo opal. Hussain Rezayee (Rare Gems & Minerals, Beverly Hills, California) provided additional samples. We thank Evan Caplan for his insights and information, and Dr. James Shigley for his assistance with the manuscript.

REFERENCES

- Fritsch E., Ostrooumov M., Rondeau B., Barreau A., Albertini D., Marie A.-M., Lasnier B., Wery J. (2002) Mexican gem opals—Nano and micro structure, origin of colour, and comparison with other common opals of gemological significance. *Australian Gemmologist*, Vol. 21, No. 6, pp. 230–233.
- Gaillou E., Delaunay A., Rondeau B., Bouhnik-le-Coz M., Fritsch E., Cornen G., Monnier C. (2008) The geochemistry of gem opals as evidence of their origin. *Ore Geology Reviews*, Vol. 34, pp. 113–126, <http://dx.doi.org/10.1016/j.oregeorev.2007.07.004>.
- Gübelin E., Koivula J. (2005) *Photoatlas of Inclusions in Gemstones*, Vol. 2. Opinio Publishers, Basel, Switzerland.
- Johnson M.L., Kammerling R.C., DeGhionno D.G., Koivula J.I. (1996) Opal from Shewa Province, Ethiopia. *G&G*, Vol. 32, No. 2, pp. 112–120, <http://dx.doi.org/10.5741/GEMS.32.2.112>.
- Renfro N., McClure S. (2011) A new dyed purple opal. News from Research, Sept. 26, www.gia.edu/research-resources/news-from-research/Dyed%20Purple%20Opal%201004.pdf.
- Rondeau B., Fritsch E., Mazzero F., Gauthier J., Cenko-Tok B., Bekele E., Gaillou E. (2010) Play-of-color opal from Wegel Tena, Wollo Province, Ethiopia. *G&G*, Vol. 46, No. 2, pp. 90–105, <http://dx.doi.org/10.5741/GEMS.46.2.90>.
- Rondeau B., Fritsch E., Bodeur Y., Mazzero F., Cenko T., Bekele E., Ayalew D., Cenko-Tok B., Gauthier J.-P. (2011) Wollo opals—A powerful source from Ethiopia. *InColor*, No. 17 (Summer), pp. 24–35.
- Webster R. (1996) *Gems: Their Sources, Descriptions and Identification*, 5th ed. Butterworth-Heinemann Ltd., Oxford, UK.
- Williams B., Williams C. (2011) Smoke treatment in Wollo opal. www.stonegroup.com/SmokeTreatmentinWolloOpal.pdf [date accessed: Sept. 22, 2011].

What's *missing* from your collection?



Spring-Winter 2010

Spring 2007

Pink-to-Red Coral: Determining Origin of Color
Serenity Coated Colored Diamonds
Trapiche Tourmaline from Zambia

Summer 2007

Global Rough Diamond Production since 1870
Durability Testing of Filled Diamonds
Chinese Freshwater Pearl Culture
Yellowish Green Diopside and Tremolite from Tanzania
Polymer-Impregnated Turquoise

Fall 2007

The Transformation of the Cultured Pearl Industry
Nail-head Spicule Inclusions in Natural Gemstones
Copper-Bearing Tourmalines from New Deposits in Paraíba State, Brazil
Type Ia Diamond with Green-Yellow Color Due to Ni

Winter 2007

Latest CVD Synthetic Diamonds from Apollo Diamond Inc.
Yellow Mn-Rich Tourmaline from Zambia
Fluorescence Spectra of Colored Diamonds
An Examination of the Napoleon Diamond Necklace

Spring 2008

Copper-Bearing (Paraíba-type) Tourmaline from Mozambique
A History of Diamond Treatments
Natural-Color Purple Diamonds from Siberia

Summer 2008

Emeralds from Byrud (Eidsvoll), Norway
Creating a Model of the Koh-i-Noor Diamond
Coated Tanzanite
Coloring of Topaz by Coating and Diffusion Processes

Fall 2008

Identification of Melee-Size Synthetic Yellow Diamonds
Aquamarine, Maxixe-Type Beryl, and Hydrothermal Synthetic Blue Beryl
A New Type of Synthetic Fire Opal: Mexifire
The Color Durability of "Chocolate Pearls"

Winter 2008

Color Grading "D-to-Z" Diamonds at the GIA Laboratory
Rubies and Sapphires from Winza, Tanzania
The Wittelsbach Blue

Spring 2009

The French Blue and the Hope: New Data from the Discovery of a Historical Lead Salt
Gray-Blue-Violet Hydrogen-Rich Diamonds from the Argyle Mine
Hackmanite/Sodalite from Myanmar and Afghanistan
Pink Color Surrounding Growth Tubes and Cracks in Tourmalines from Mozambique
Identification of the Endangered Pink-to-Red Stylaster Corals by Raman Spectroscopy

Summer 2009

Celebrating 75 Years of *Gems & Gemology*
The "Type" Classification System of Diamonds
Spectral Differentiation Between Copper and Iron Colorants in Gem Tourmalines
Andalusite from Brazil
Peridot from Sardinia, Italy

Fall 2009

Characterization of "Green Amber"
Crystallographic Analysis of the Tavernier Blue
"Fluorescence Cage": Visual Identification of HPHT-Treated Type I Diamonds
Ammolite Update
Polymer-Filled Aquamarine
Yellow-Green Hatiyne from Tanzania
Aquamarine from Masino-Bregaglia Massif, Italy

Winter 2009 (PDF only)

Ruby and Sapphire Production and Distribution: A Quarter Century of Change
Cutting Diffraction Gratings to Improve Dispersion ("Fire") in Diamonds
Chrysoptase and Prase Opal from Haneti, Central Tanzania
Demantoid from Val Malenco, Italy

Spring 2010

Strongly Colored Pink CVD Lab-Grown Diamonds
Color Alterations in CVD Synthetic Diamond with Heat and UV Exposure
Possible "Sister" Stones of the Hope Diamond
Confocal Micro-Raman Spectroscopy
Bastnäsite-(Ce) and Parisite-(Ce) from Malawi

Summer 2010

The Wittelsbach-Graff and Hope Diamonds: Not Cut from the Same Rough
Play-of-Color Opal from Ethiopia
A New Type of Composite Turquoise
Fire Opal from Madagascar
X-ray Computed Microtomography Applied to Pearls
Hibonite: A New Gem Mineral

Fall 2010

An Era of Sweeping Change in Diamond and Colored Stone Production and Markets
Gem Localities of the 2000s
Gemstone Enhancement and Its Detection in the 2000s
Developments in Gemstone Analysis Techniques and Instrumentation During the 2000s

Winter 2010

Synthetic Gem Materials in the 2000s
Yellow Scapolite from Madagascar
Pietersite from Namibia and China
Update on Mexifire Synthetic Fire Opal
Gems in a Ciborium from Einsiedeln Abbey

GEMS & GEMOLOGY®

The Quarterly Journal
That Lasts A Lifetime

Now Available
Online:

All Articles
and Issues 1981–2011

Get PDF Articles at
gia.metapress.com

Electronic (PDF) versions of all articles from Spring 1981 forward are available as part of *Gems & Gemology* Online.

Order Back Issues (Print and PDF)
at store.gia.edu

or Call Toll Free 800-421-7250 ext. 7142
or 760-603-4000 ext. 7142
Fax 760-603-4070

E-mail gandg@gia.edu
or write to

Gems & Gemology
PO Box 9022, Carlsbad, CA
92018-9022, USA

Complete volumes of 1992–2011 print
back issues (except 2009) are available,
as are limited issues from 1985–1991.

10% discount for GIA Alumni and active
GIA students.

Order Your
**BACK
ISSUES**
CHARTS & BOOKS

Today!



For a complete list of articles from 1981 forward, visit gia.edu/gandg.



DETERMINING GARNET COMPOSITION FROM MAGNETIC SUSCEPTIBILITY AND OTHER PROPERTIES

Donald B. Hoover

Quantitative measurements of magnetic susceptibility combined with RI or SG data can provide an easy and inexpensive way of inferring garnet composition. At the time this technique was first applied to faceted garnets (Hoover et al., 2008), a reference set of samples with well-characterized compositions was not available. GIA subsequently provided 28 garnets and their chemical data determined by electron microprobe for a comparison with end-member compositions calculated from magnetic susceptibility measurements and other properties. The results show that end-member compositions based on microprobe data have error margins similar to most of those derived from directly measured properties.

Garnet is a diverse gem material showing an attractive palette of colors (e.g., figure 1) and incorporating a variety of chemical components that are responsible for widely ranging values of physical properties. The several end-member species may occur as nearly pure compositions or, more commonly, complex assemblages. The principal species (table 1) are pyrope, almandine, and spessartine (pyral-spite garnets), and grossular, andradite and minor uvarovite (ugrandite garnets). Other end-member species, including goldmanite (vanadium rich), knorringite (chromium rich), and schorlomite (titanium rich) also may be present in small amounts, and these are mainly important for their effect on garnet coloration.

In the past, gemologists have been limited in their ability to determine garnet composition by only having RI and possibly SG data as quantitative

measures, in combination with color and spectroscopic data, to infer a garnet composition that is most probable. These compositions were limited to one or two end members; for garnets in which three or more end members were important, gemologists had no effective recourse.

In recent years, with the availability of very strong rare-earth magnets, gemologists have started to apply magnetic attraction as a tool for gem identification (see, e.g., <http://gemstonemagnetism.com>). Although all materials respond to an applied magnetic field in some way (box A), it is the transition elements in garnet that give rise to a measureable magnetic attraction (reported here as the volume magnetic susceptibility) if they are present as principal components. Recently, Hoover and Williams (2007) developed a simple, inexpensive apparatus to measure volume susceptibility on cut gems (box B). Hoover et al. (2008) derived garnet composition from plots of RI versus susceptibility, and followed the conventional characterization of Stockton and Manson (1985) in defining garnet varieties (pyrope, pyrope-almandine, almandine, almandine-spessar-

See end of article for About the Author and Acknowledgments.

GEMS & GEMOLOGY, Vol. 47, No. 4, pp. 272–285,
<http://dx.doi.org/10.5741/GEMS.47.4.272>.

© 2011 Gemological Institute of America

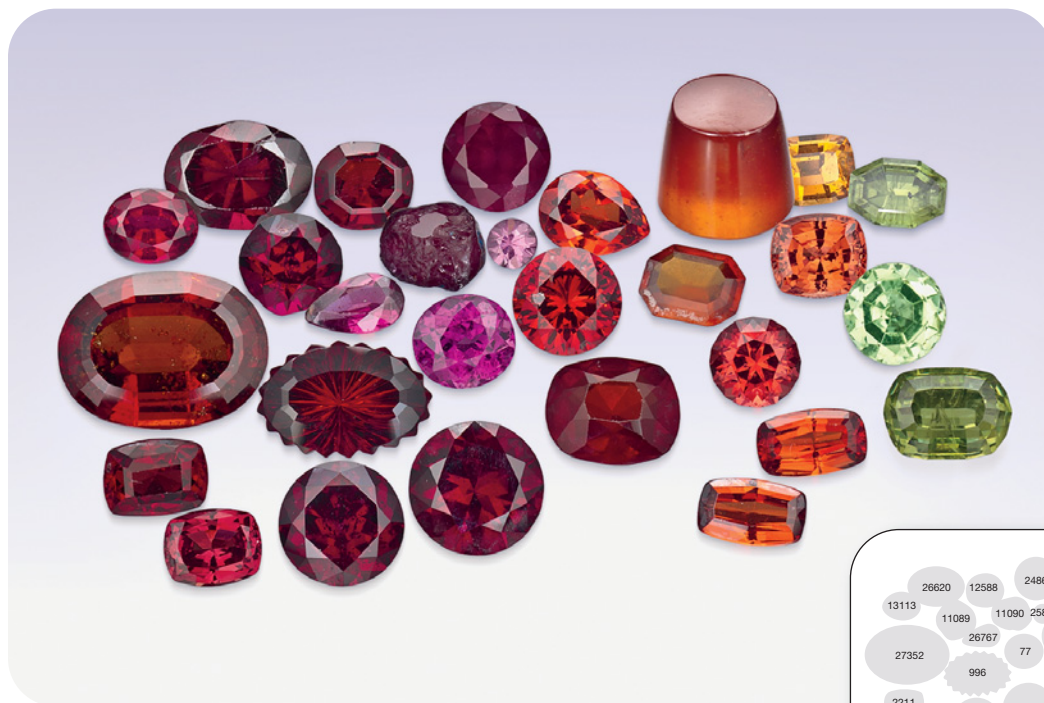
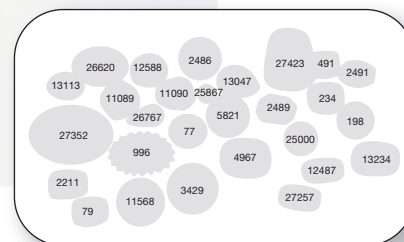


Figure 1. This photo shows the 28 GIA garnet samples used in this study (0.18–9.82 ct). Photo by Robert Weldon.



tine, etc.). Furthermore, the magnetic susceptibility technique permitted a quantitative measure of garnet composition consisting of three end members, not two, when RI was the only other data available. Unfortunately, Hoover et al. (2008) did not have garnet samples of known composition to test how well the technique agreed with quantitative chemical analysis. Using selected samples from the large group studied by Manson and Stockton, this article compares garnet compositions from GIA's electron microprobe data to those inferred from the GIA-measured properties that were combined with the author's measured magnetic susceptibilities. The

accuracy of garnet compositions derived from the various properties is assessed.

MATERIALS AND METHODS

Materials. GIA initially supplied data for 539 garnets that included color, carat weight, RI, SG, cell constant, and variety, although the data set was incomplete for a number of the stones. The author then borrowed 28 of the samples for magnetic susceptibility measurements (see figure 1 table 2) that were selected to cover the full range of compositions and RI values. An additional constraint was that each stone be large enough for good susceptibility mea-

TABLE 1. Silicate garnet end-member species and their properties.^a

End member	Symbol	Formula	RI	SG	Cell constant (Å)	Volume susceptibility (×10 ⁻⁴ SI)
Pyrope	Prp	Mg ₃ Al ₂ Si ₃ O ₁₂	1.714	3.58	11.459	-0.2
Almandine	Alm	Fe ₃ Al ₂ Si ₃ O ₁₂	1.829	4.32	11.528	40.7
Spessartine	Sps	Mn ₃ Al ₂ Si ₃ O ₁₂	1.799	4.20	11.614	47.5
Grossular	Grs	Ca ₃ Al ₂ Si ₃ O ₁₂	1.734	3.59	11.851	-0.2
Andradite	Adr	Ca ₃ Fe ₂ Si ₃ O ₁₂	1.887	3.86	12.048	30.8
Uvarovite	Uv	Ca ₃ Cr ₂ Si ₃ O ₁₂	1.865	3.85	11.996	12.9
Goldmanite	Go	Ca ₃ V ₂ Si ₃ O ₁₂	1.834	3.77	12.070	6.9
Knorringite	Kn	Mg ₃ Cr ₂ Si ₃ O ₁₂	1.875	3.84	11.622	13.7

^a See text for sources of data.

TABLE 2. Garnet samples used in this study, their measured and calculated properties, and their compositions.^a

Sample no. ^b	Variety	Weight (ct)	Measured				Calculated (Locock)					
			RI	SG	Cell constant (Å)	Volume susceptibility ($\times 10^{-4}$ SI)	Composition	RI	SG	Cell constant (Å)	Volume susceptibility ($\times 10^{-4}$ SI)	Composition ^c
77	Rhodolite	2.42	1.752	3.83	11.493	16.0	Prp ₆₃ Alm ₂₂ Sps ₁₅	1.752	3.83	11.494	13.5	Prp ₆₃ Alm ₃₂ Grs ₃ Sps ₁
79	Color-change (pyralspite)	1.88	1.751	3.85	11.583	16.4	Prp ₆₃ Sps ₂₀ Alm ₁₇	1.752	3.82	11.571	15.9	Prp ₄₈ Sps ₂₃ Grs ₁₅ Alm ₁₂ Uv ₁
198	Mint green grossular	2.73	1.735	3.61	11.850	0.4	Grs ₉₉ Adr ₁	1.736	3.60	11.850	0	Grs ₉₄ Prp ₁ Adr ₁ Go ₁
234	Malaya	2.27	1.765	3.91	11.549	24.6	Prp ₄₇ Sps ₃₂ Alm ₂₁	1.766	3.93	11.545	23.7	Prp ₄₃ Sps ₃₄ Alm ₁₈ Grs ₂ Adr ₁
491	Malaya	1.53	1.762	3.90	11.555	24.7	Prp ₄₇ Sps ₃₆ Alm ₇	1.759	3.88	11.558	21.8	Prp ₄₅ Sps ₃₈ Alm ₈ Grs ₇ Adr ₁
996	Almandine-spessartine	6.78	1.810	4.22	11.580	44.9	Sps ₆₃ Alm ₃₇	1.811	4.24	11.580	44.4	Sps ₅₇ Alm ₄₀ Grs ₁
2211	Pyrope-almandine	2.14	1.762	3.87	11.530	16.2	Prp ₆₂ Alm ₄₀ Grs ₈	1.763	3.88	11.529	16.5	Prp ₅₀ Alm ₃₉ Grs ₉ Adr ₁ Sps ₁
2486	Rhodolite	2.20	1.762	3.85	11.509	15.7	Prp ₆₂ Alm ₃₆ Grs ₁₂	1.759	3.86	11.508	15.3	Prp ₅₇ Alm ₃₆ Grs ₄ Sps ₁ Adr ₁
2489	Hessonite	1.25	1.755	3.65	11.889	5.8	Grs ₈₃ Adr ₉ Alm ₁ or Grs ₄₁ Prp ₄₀ Adr ₁₉	1.760	3.64	11.882	5.0	Grs ₈₀ Adr ₁₆ Prp ₁
2491	Demantoid	1.45	1.881	3.84	—	29.7	Adr ₉₆ Grs ₄	1.887	3.86	12.048	30.8	Adr ₉₆
3429	Pyrope-almandine	3.55	1.784	4.02	11.508	22.9	Alm ₅₇ Grs ₃₃ Prp ₁₀	1.781	4.00	11.510	23.6	Alm ₅₅ Prp ₄₀ Sps ₂ Grs ₂
4967	Pyrope-almandine	3.18	1.750	3.82	11.534	12.1	Prp ₆₈ Alm ₃₀ Grs ₄	1.751	3.80	11.529	11.8	Prp ₅₉ Alm ₂₈ Grs ₁₁ Adr ₁
5821	Almandine-spessartine	2.52	1.810	4.19	—	46.6	(Outside the ternaries)	1.804	4.22	11.601	46.3	Sps ₈₃ Alm ₁₆
11089	Chromopyrope	1.96	1.744	3.70	11.537	6.2	Grs ₆₇ Prp ₂₇ Alm ₁₆	1.740	3.70	11.521	6.8	Prp ₇₂ Alm ₁₄ Grs ₇ Uv ₆ Adr ₁ Sps ₁
11090	Chromopyrope	5.37	1.742	3.72	—	8.0	Prp ₆₈ Grs ₂₂ Alm ₂₀	1.742	3.71	11.533	6.9	Prp ₇₁ Alm ₁₄ Grs ₇ Uv ₆ Adr ₁ Sps ₁
11568	Pyrope-almandine	3.39	1.807	4.15	—	31.3	Alm ₇₇ Grs ₁₉ Prp ₄	1.804	4.16	11.525	32.4	Alm ₇₄ Prp ₁₉ Sps ₄ Grs ₂
12487	Spessartine	1.41	1.800 ^d	4.23	—	47.0	Sps ₉₇ Alm ₃	1.805	4.22	11.580	45.6	Sps ₇₂ Alm ₂₆
12588	Almandine-spessartine	1.62	1.812	4.26	—	44.3	Sps ₅₃ Alm ₄₇	1.812	4.25	11.560	43.3	Alm ₅₂ Sps ₄₇ Grs ₁
13047	Spessartine	1.91	1.800 ^d	4.20	—	52.3	(Outside the ternaries)	1.805	4.22	11.581	45.4	Sps ₇₂ Alm ₂₆
13113	Chromopyrope	1.08	1.732 ^e	3.74	11.535	8.0	Prp ₆₈ Grs ₂₂ Alm ₂₀	1.744	3.73	11.530	7.9	Pyp ₆₈ Alm ₁₇ Grs ₇ Uv ₆ Adr ₁ Sps ₁
13234	Demantoid	1.79	1.882	3.87	—	28.8	Adr ₉₀ Uv ₇ Grs ₃	1.887	3.86	12.048	30.8	Adr ₉₈
25000 (35A)	Pyrope	1.27	1.744	3.77	11.492	10.9	Prp ₇₄ Alm ₂₃ Sps ₁	1.745	3.77	11.495	10.2	Prp ₆₈ Alm ₂₄ Grs ₃ Adr ₁
25867 (4097D)	Pyrope	0.18	1.730	—	—	4.5	Prp ₇₉ Alm ₁₂ Grs ₉	1.733	3.68	11.512	5.3	Prp ₇₇ Alm ₁₂ Grs ₈ Adr ₁ Uv ₁
26620 (5544A)	Almandine	3.06	1.791	4.13	11.534	27.8	Alm ₆₄ Prp ₃₂ Sps ₄	1.795	4.10	11.531	28.8	Alm ₆₇ Prp ₂₄ Grs ₅ Sps ₃
26767 (6673F)	Almandine	0.52	1.793	4.10	11.513	25.3	Alm ₆₂ Grs ₃₅ Prp ₃	1.798	4.13	11.513	30.4	Alm ₇₃ Prp ₂₄
27257 (12822A)	Spessartine	1.42	1.800 ^d	4.25	—	46.6	Sps ₉₇ Alm ₃	1.805	4.22	11.580	45.4	Sps ₈₉ Alm ₂₆
27352 (13122A)	Hessonite	9.82	1.754	3.64	—	4.3	Grs ₉₇ Adr ₁₃	1.757	3.64	11.875	4.8	Grs ₈₄ Adr ₁₂ Alm ₁ Sps ₁
27423 (13167A)	Hessonite	9.10	1.755	3.65	—	3.9	Grs ₉₆ Adr ₁₄	1.752	3.63	11.872	3.4	Grs ₈₆ Adr ₁₂

^a Data that was not available from GIA is indicated by “—”.

^b Numbers in parentheses are the former catalog numbers.

^c Note that calculations from the oxide chemistry seldom give end-member compositions that add to 100%.

^d These RI values are problematic; see text.

^e This RI was rechecked by the author and determined to be 1.742.

surements (e.g., >1 ct was preferred). When available, samples with measured SG and cell constant data were used; color was not part of the selection process.

Determination of End-Member Compositions. Silicate garnets have the general formula $X_3^2+Y_2^3+Si_3O_{12}$,

where X is commonly Ca^{2+} , Mn^{2+} , Fe^{2+} , and/or Mg^{2+} , and Y is commonly Al^{3+} , Fe^{3+} , Cr^{3+} , and/or V^{3+} . Because garnets form an isomorphous series, the X and Y positions can hold any combination of the respective ions listed; substitutions may also occur for Si.

There are two basic ways to determine the end-member composition of garnets: calculation from chemical data and derivation from measured properties. Chemical data (such as from an electron microprobe or wet chemical analysis) are typically expressed as wt.% oxides, and there are numerous (nonequivalent) ways to calculate end-member compositions from such data. A commonly used procedure from Rickwood (1968) was slightly modified by Manson and Stockton (1981). Rickwood (1968) discussed the variations that can arise from the different calculation methods, using a common metamorphic garnet composition of $\text{Prp}_{44}\text{Alm}_{42}\text{Grs}_{17}$ as an example, in which the pyrope content can vary by 3.4%, the almandine by 3.4%, and the grossular by 5.2%, depending on how the calculations are done. A more recent procedure by Locock (2008) incorporated advances in the understanding of the crystal chemistry of natural garnets through a

NEED TO KNOW

- Combined with RI or SG data, magnetic susceptibility is one more measureable property that is useful toward inferring garnet composition.
- Magnetic susceptibility of faceted gemstones can be measured nondestructively with a relatively simple apparatus.
- Susceptibility measurements are plotted against other properties on modified Winchell diagrams to derive garnet composition.
- A comparison of garnet compositions derived from measured properties versus chemical data showed a fairly good correlation.

measure of the quality of the analysis. For this paper, the author used the Locock procedure to

BOX A: MAGNETIC MATERIALS

All material substances react to the presence of a magnetic field: They develop an induced magnetic field in response to the applied field. The ratio of the induced field to the applied field is called the *volume susceptibility* (k) of the substance. It is a simple dimensionless ratio.

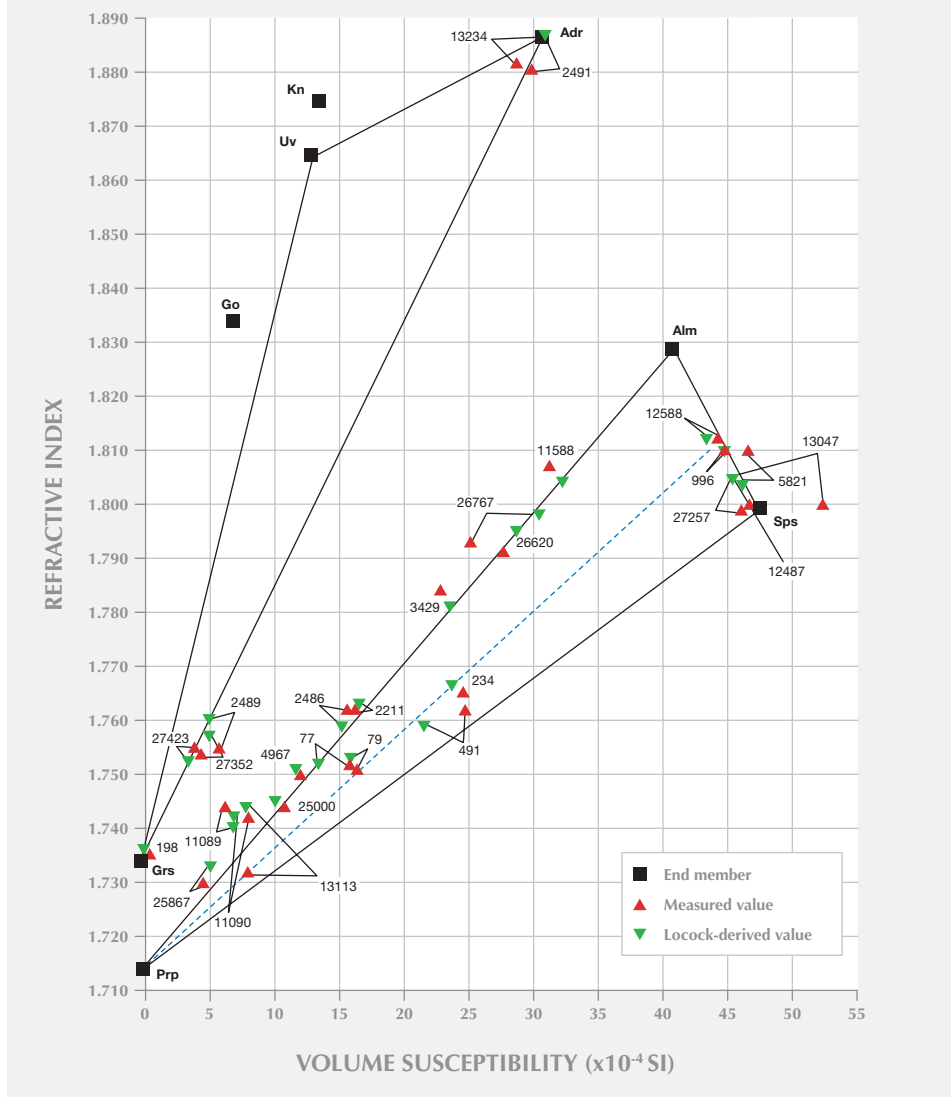
Materials react to a magnetic field in three different ways. Most materials are very weakly repelled, or *diamagnetic*. In this case, k is negative. A material with a sufficient number of atoms of the transition elements (Fe, Mn, Cu, Cr, etc.) or the rare-earth elements—depending on their valence state—may overcome the diamagnetic effects of the other atoms and be attracted to a magnet. For these materials, k is positive. If the value of k is independent of the strength of the applied field, the material is called *paramagnetic*. Here, k will be positive and of small to intermediate magnitude. If k changes with the strength of the applied magnetic field, the material is *ferromagnetic*, and k can be very large. Ferromagnetic materials are further divided into *true ferromagnetic*, *ferrimagnetic*, *antiferromagnetic*, and *canted antiferromagnetic*. These variations in behavior are due to interactions between the electrons in the material and the formation of what are called magnetic domains.

Of greatest interest to gemology are the paramagnetic materials and their susceptibilities, which can have some diagnostic value. By contrast, diamagnetic susceptibilities have little diagnostic value. Ferromagnetic materials, when present as inclusions in gems, can give anomalously high values of magnetic susceptibility for the host material.

Physicists have defined several different kinds of magnetic susceptibility. Although volume magnetic susceptibility is dimensionless, the numeric value will differ with the system of units being used, changing by a factor of 4π , or 12.57. Thus the system of units needs to be stated, even for this dimensionless number. This article uses the International System of Units (SI), which may be a possible source for confusion if one is not familiar with this peculiarity in some electromagnetic measurements. Another commonly used property is mass magnetic susceptibility, also called specific susceptibility. This measure has dimensions of inverse density (e.g., cubic centimeters per gram), and again one needs to be aware of a multiplier of 4π when other units of measurement are used. Molar magnetic susceptibility may also be expressed in units of cubic centimeters per mol, or their equivalent.

RIMS DIAGRAM

Figure 2. This plot of RI vs. magnetic susceptibility (RIMS diagram) compares measured properties (indicated by red triangles) against properties calculated from end-member compositions (green triangles, according to Locock [2008]) for the 28 GIA garnet samples. The black squares represent pure end-member properties (see table 1 for key to abbreviations). The pyralspite and ugrandite ternary triangles are shown by black lines connecting the corresponding end members.



obtain the end-member compositions from the GIA oxide chemical data.

The second way to determine garnet end-member composition is to use quantitative measured properties and solve a series of equations that are based on Vegard's law, which showed that garnet properties are additive functions of the molar proportions of end-member compositions (Hutchison, 1974). The equations are:

1. $RI_m = ARI_{EM1} + BRI_{EM2} + CRI_{EM3}$
2. $S_m = AS_{EM1} + BS_{EM2} + CS_{EM3}$
3. $A + B + C = 1$

where RI = refractive index, S = magnetic susceptibility, m = measured, EM = end-member values, and A, B, and C = percentages of end members. With two measured properties, one can solve for three possible end members. With three measured properties, the end members increase to four, and so on. As with compositions based on chemical analyses, the result is not unique; there will be several (similar) possibilities. Winchell (1958) showed how these equations can be solved graphically in a rather simple way, and his diagram of RI vs. unit cell dimensions (or cell constant) demonstrated the interrelation between the pure end members and a particular garnet. However, the cell constant of an unknown garnet is

not easily obtained by the gemologist because X-ray diffraction data is required, so Hoover et al. (2008) modified the Winchell diagram so that the composition of an unknown garnet can be determined—according to three or four end members—from quantitative measurements of properties such as magnetic susceptibility, RI, and SG. Box B describes how magnetic susceptibility was measured, both in this study and by Hoover et al. (2008).

Figure 2 is the modified Winchell diagram plotting RI vs. magnetic susceptibility (RIMS). Eight garnet end members of gemological importance (black squares) are shown on the diagram. The garnet ternaries pyrospite (pyrope, almandine, and spessartine) and ugrandite (uvarovite, grossular, and andradite) are shown as triangles outlined in black that connect each of the three corresponding end members. Other end members shown are goldmanite and

BOX B: MEASUREMENT OF MAGNETIC SUSCEPTIBILITY

While there are several ways to quantitatively measure magnetic susceptibility, volume susceptibility is routinely measured with a Gouy balance or the similar Evans balance (see www.geneq.com/catalog/en/msbalance.html). Susceptibility is measured by placing a sample on one arm of a laboratory balance and subjecting it to a strong magnetic field gradient. The weight loss or gain is measured and converted to susceptibility. Unfortunately, the sample must be in the form of a cylinder. In practice, the sample is often ground to a powder and placed in a cylindrical sample holder. This obviously is not practical for gem materials.

Hoover and Williams (2007) showed that if a very strong permanent magnet is used, and its pole face is smaller than the table (or other flat facet) of the gem to be measured, then the force of attraction between the magnet's pole face and the facet will be proportional to the gem's volume susceptibility. To calculate the gem's susceptibility, the magnet only needs to be calibrated with a material of known susceptibility. The apparatus used by Hoover and Williams (2007), Hoover et al. (2008), and in this study consisted of a biological microscope with the optics removed (figure B-1). In place of the optics, a small iron rod was fixed vertically to hold a variety of small ($\frac{1}{16}$ in. to $\frac{1}{4}$ in. diameter) cylindrical rare-earth magnets. The important components are the fine focus mechanism (for precise control of the magnet's vertical position) and the moveable X-Y stage that is used to align the gem's table with the magnet's pole face. A small digital scale was placed on the microscope stage, and a gem was placed on a pedestal in the weighing dish. The magnet's pole face was brought just into contact and parallel

with the gem's table. The gem was then slightly separated from the magnet to obtain a maximum change in weight (i.e., weight loss for a paramagnetic gem).

The procedure is no more complex than measuring specific gravity—and takes about as much time. The apparatus can be constructed at low cost using a surplus microscope.

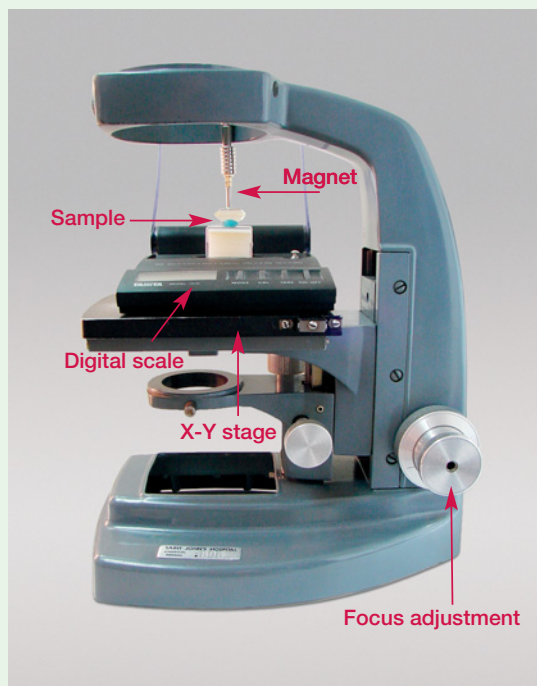


Figure B-1. This instrument was designed by Hoover and Williams (2007) for taking magnetic susceptibility measurements, and was used in the current study. Photo by Bear Williams.

knorringite. (Schorlomite is not shown because end-member property values are not available in the mineralogical literature, and in gem garnets this component may be present in only very small quantities.) The positions of all the garnets obtained for this study are also plotted: the green triangles represent the compositions calculated from microprobe analyses (using the Locock procedure), and the red triangles plot the RI and susceptibility data. The various garnet compositions can be recognized by their position with respect to the end members.

The process to determine the composition of the three garnet end members from any data point is simple. For example, for the green triangle representing the Locock five end-member composition of sample no. 234, which is plotted with an RI of 1.766 and a susceptibility of 23.7×10^{-4} SI:

- From the pyrope apex of the pyralspite ternary, draw a line through the center of the data point to intercept the opposite base of the triangle, shown by the blue dashed line.
- Next, measure the total length of the line, and then the length from the data point to the base of the triangle.
- Divide the line length from the data point to the base by the total length, which will give the percentage of pyrope end member.

For sample no. 234, the result is 47%. The process can be repeated for the other two apices, but it is simpler to measure the relative proportions of almandine and spessartine on the almandine-spessartine join where the blue line crosses it, and proportion them to the remaining percentage (53% for this example). Here it is at 60% spessartine, which yields 32% for spessartine and 21% for almandine, or $\text{Prp}_{47}\text{Sps}_{32}\text{Alm}_{21}$. By comparison, the Locock technique characterizes this stone, rounding to the nearest 1%, as $\text{Prp}_{43}\text{Sps}_{34}\text{Alm}_{18}\text{Grs}_4\text{Adr}_1$.

End-Member Properties. The properties of each garnet end member (table 1) are required to plot their positions in the various modified Winchell diagrams. For every end member but knorringite, the RI, SG, and cell constant used were reported by Meagher (1982). For knorringite, the calculated data from McConnell (table 50 in Deer et al., 1982) were used by Hoover et al. (2008), but the data do not agree well with the RI and cell dimension data measured

on synthetic samples by Ringwood (1977), or with the data presented by Nixon and Hornung (1968), who first defined knorringite. The McConnell data will continue to be used in this article, with the understanding that knorringite end-member values are subject to change.

Magnetic susceptibility values are not well known, either. Pure grossular and pyrope have no transition elements in their composition and are thus diamagnetic. Their susceptibilities are very small and slightly negative; they were assigned by Hoover et al. (2008) values of -0.2×10^{-4} SI, typical of diamagnetic materials. The other six end members are less easy to define. Frost (1960) measured the mass, or specific, susceptibilities of andradite, almandine, and spessartine, which (when converted to volume susceptibility) are 23.8, 36.9, and 42.7×10^{-4} SI, respectively. But the data are not robust. The four almandine-spessartine garnets Frost measured, ranging from $\text{Alm}_{65}\text{Sps}_{35}$ to $\text{Alm}_{10}\text{Sps}_{87}$, all had the same mass susceptibility. Nathan et al. (1965) measured spessartine's volume susceptibility as 44.3×10^{-4} SI, but the author's own measurements on spessartine suggested that this was slightly low. Hoover et al. (2008) were unable to find measured susceptibilities for the other three garnet end members. Approximate values, however, were calculated based on the magneton numbers of the constituent transition element ions present (Kittel, 1956), using the Langevin equation. This is how Hoover et al. (2008) obtained the values shown in the figures—30.8, 40.7, 47.5, 12.9, 6.9, and 13.7×10^{-4} SI, respectively—for andradite, almandine, spessartine, uvarovite, goldmanite, and knorringite.

Measured Properties. Except for the magnetic susceptibility measurements, all properties for the 28 study samples were supplied by GIA from the Manson-Stockton research. The volume susceptibility measurements were taken by the author, using the apparatus described in box B, with cobalt chloride as a susceptibility standard (described by Hoover et al., 2008).

RESULTS

RI vs. Magnetic Susceptibility Diagram. In the RIMS diagram (figure 2), the gem ugrandites plot on or very near the line joining grossular and andradite. The single mint green grossular (sample no. 198) is very close to the grossular end member. The three hesonites (2489, 27352, and 27423) are about 14% toward andradite. The two demantoids (2491 and 13234) are close to the andradite end member. For

the pyralspite garnets, a mixed almandine-spessartine group (996, 5821, and 12588) plots along the almandine-spessartine join, quite distinct from the rest. Spessartine samples (12487, 13047, and 27257) plot near their end-member composition. Three stones, consisting of two malaya (234 and 491) and one color-change garnet (79), are positioned within the pyralspite ternary. The rest of the garnets are arrayed near the pyrope-almandine join, or within the grossular-pyrope-almandine ternary; three chrome-pyropes (11089, 11090, and 13113) are included in the latter group.

Comparing the measured and calculated end-member data for most samples shows fair agreement (figure 2 and table 2). The variations between the two techniques are about what one would expect due to measurement error and some uncertainty in end-member properties. Not including sample 13113, for which the originally measured RI was incorrect, the average difference between measured and calculated RI values is 0.003. For volume susceptibility, there is a difference of 0.5×10^{-4} SI, if one disregards samples 13047 and 26767, which are anomalous. For specific gravity (figure 3), the average difference is 0.01.

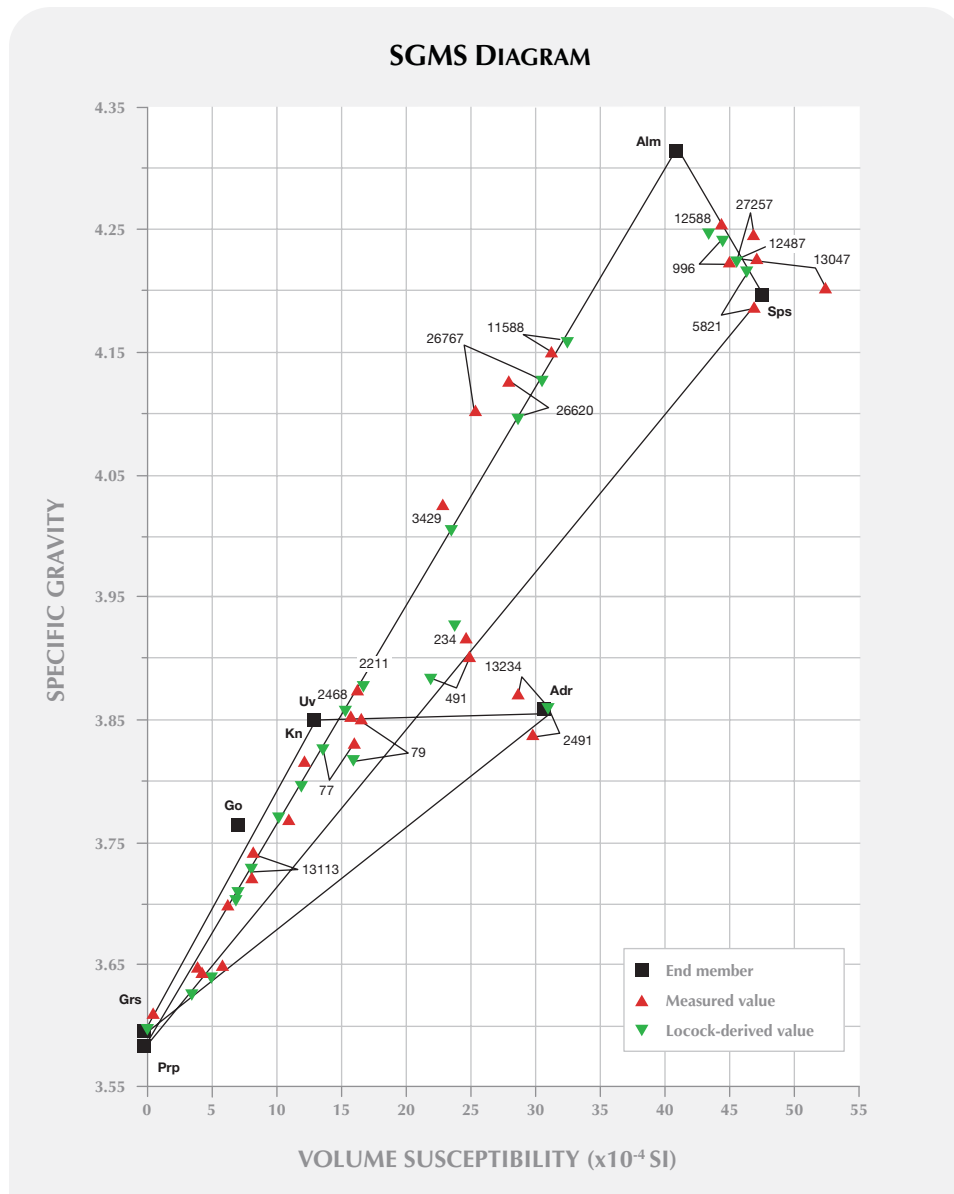


Figure 3. This plot shows SG vs. magnetic susceptibility (SGMS diagram) for the 27 GIA garnets for which the data were available. However, sample numbers are not shown for those samples that plot toward the pyrope and grossular end members, which overlap on this diagram.

To give a sense of how these variations are reflected in terms of garnet composition, let us assume a 3% difference in end-member composition of a $\text{Pyr}_{50}\text{Alm}_{50}$ garnet. This would produce a change of 0.004 in RI, 1.22×10^{-4} SI in volume susceptibility, and 0.02 in SG. Thus the average difference between these three measured properties and those calculated from the Locock procedure represents less than 3% compositional change in a mid-range pyrope-almandine. It is important to remember that such a derived composition will not be unique, and that any additional information, such as absorption spectra, may further reduce uncertainties in determining garnet composition.

The RIMS diagram shows the advantage of such plots in evaluating how accurate our property measurements need to be. Consider the various joins in the illustration. Those between pyrope or grossular and the other end members are relatively long, and therefore span a wide range in refractive index and susceptibility. A difference of a few percentage points in composition will have a measurable effect on these properties. By comparison, the almandine-spessartine join is quite short: a larger percentage change in composition is needed to produce a measurable change in properties.

Regarding the two samples with anomalous susceptibilities, no. 26767 had a small chip on the table below the magnet, which probably was responsible for its lower susceptibility. Sample 13047, a spessartine, had a high susceptibility. In the author's collection, a Brazilian spessartine shows a similarly high susceptibility. Neither shows evidence of ferromagnetic inclusions, such as magnetite, that could explain their anomalous susceptibilities. The author suspects that these are yttrium-bearing spessartines, with relatively enriched rare-earth contents that are responsible for their high susceptibilities. Note that sample 13047, in this property space, falls well beyond the expected measurement error from any ternary triangle using the eight more-common garnet end members.

Chrome-pyrope 13113 originally had an anomalously low measured RI, 1.732, compared to a calculated value of 1.744. Yet the other measured values of SG, cell constant, and susceptibility agreed well with calculated values. The refractive index is clearly questionable, which illustrates the utility of Winchell diagrams in checking the consistency between measured properties and chemical data. The sample's RI was rechecked by the author and found to be 1.742. The RIs of the three spessartines

(13047, 12487, and 27257) may also have been measured incorrectly. Each had a reported RI of 1.800 from the Manson-Stockton data set, and each had a very similar end-member composition. The calculated RIs are all 1.805. GIA, however, remeasured the RI of sample 13047 as >1.810 , or above the index of the refractometer liquid. The author checked these values with an experimental deviation angle refractometer and found all three to be 1.809, but the error range of the instrument is no better than 0.004. These stones remain problematic.

SG vs. Magnetic Susceptibility Diagram. Another modified Winchell diagram, plotting specific gravity vs. magnetic susceptibility (SGMS), holds some promise. This diagram (figure 3) shows the 27 garnets for which SG data were available. Stockton and Manson (1985) did not consider specific gravity in their characterization of garnet, though they measured it for many of the samples:

There is so much overlap in specific gravity ranges for the various types of garnets that the usefulness of this property is questionable. Moreover the difficulty of accurately measuring density as well as the considerable variability introduced by the presence of inclusions suggests that this is not a reliable characteristic for the identification and classification of gems. (Stockton and Manson, 1985, p. 212)

However, figure 3 suggests otherwise. Note the positions of samples 996, 11588, 26767, 26620, 3429, 234, 491, 2211, and 2486 with respect to the pyral-spilite ternary in this figure, compared to their positions in figure 1. They indicate very similar chemical composition, whether RI or specific gravity is used with magnetic susceptibility. Of particular importance for the practicing gemologist is that RI values that cannot be obtained on a conventional refractometer can now be measured by substituting SG for RI to infer composition in a manner similar to using a RIMS plot. This possibility was suggested by Hoover et al. (2008), assuming SG values were accurate enough. The Manson-Stockton data clearly demonstrate the usefulness of SG data for stones that are not too included. For example, metamorphic garnets of high almandine content can be easily distinguished from typical pegmatitic almandine-spessartine compositions.

Unfortunately, the SGMS plot also shows that the specific gravity and magnetic susceptibility of pyrope and grossular are almost identical, and that the pyrope and grossular ends of the pyral-spilite and

ugrandite ternaries overlap. Clearly there are problems in distinguishing a pyrope-almandine-spessartine from a grossular-almandine-spessartine. It should be no surprise, then, that using SG to add a fourth end member to inferred compositions from RI and susceptibility is questionable.

RI vs. SG Diagram. Figure 4 is the modified Winchell plot of RI vs. SG (RISG), using the 27 stones shown previously. Jackson (2006) used such a diagram for characterization, but noted the lack of robustness for garnets of multiple end-member compositions. Stockton and Manson (1985) also plotted

an RISG diagram for 202 stones used in their studies, but did not show the end-member positions. Notice that chrome pyrope no. 13113 is again anomalous in this diagram, but not in the SGMS plot of figure 3.

There is a significant problem with using the RISG diagram: The pyralspite and ugrandite ternaries are very narrow, indicating that within either, the relationship between the two properties is nearly linear. This is a consequence of the Gladstone-Dale relationship between the two properties (Larsen and Berman, 1934). Thus we are unable to distinguish—in the case of a pyralspite, for example—the proportions of each of the three components based only on these

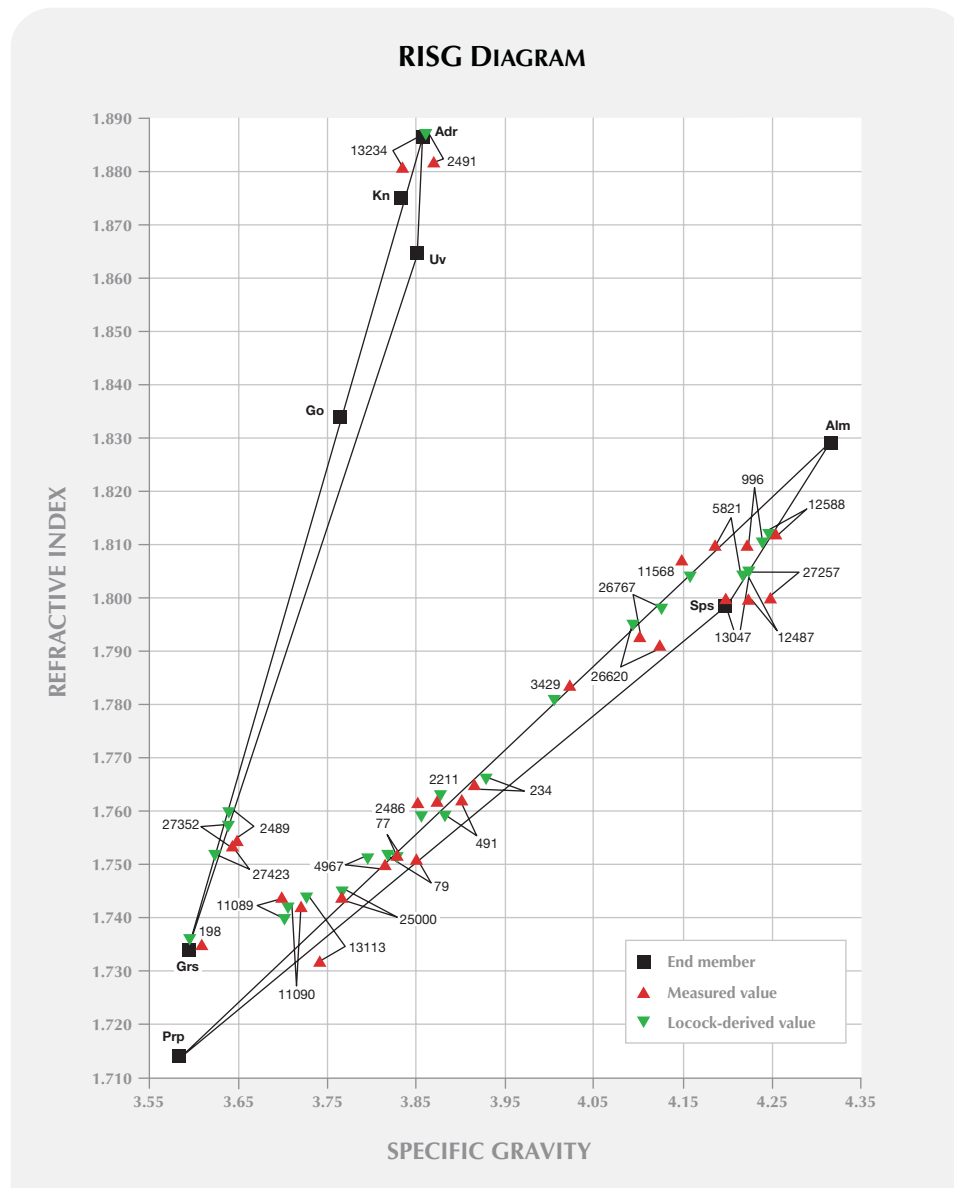


Figure 4. This plot shows RI vs. SG (RISG diagram) for the 27 GIA garnets with data available.



Figure 5. These garnets show similar color but have different compositions. From left to right: GIA sample nos. 79 (pyralspite), 37369 (hessonite), and 25000 (pyrope-almandine). Photo by Robert Weldon.

two properties, unless we have extremely accurate measurements of both properties. It is interesting to note that for these particular stones, the measured RI and SG values agree reasonably well with the calculated values. This is further evidence that Manson and Stockton were able to measure SG adequately to provide useful data for Winchell-type diagrams.

Multiple End Members and Compositional Possibilities. A few garnet varieties, such as tsavorite and demantoid, are often characterized by a single end member, but most other garnets require more. Figures 2 and 3 show that the malaya (nos. 234 and 491) and color-change (no. 79) garnets are the only pyralspites studied that plot well within the pyralspite ternary. The others are either close to the almandine-spessartine or pyrope-almandine joins, or within the grossular-pyrope-almandine ternary. The malaya and color-change garnets are best described by a combination of the pyralspite end members, plus significant grossular. Thus they are very useful for comparing the inferred three or four end members by applying Winchell diagrams to the microprobe composition.

Sample no. 79 is particularly useful because of its relatively high grossular component. The Locock procedure yields a composition of $\text{Prp}_{48}\text{Sps}_{23}\text{Grs}_{15}\text{Alm}_{12}\text{Uv}_1$, with less than 1% consisting of other components. From figure 2 the composition can be derived as (1) $\text{Prp}_{63}\text{Sps}_{20}\text{Alm}_{17}$ or (2) $\text{Sps}_{35}\text{Grs}_{34}\text{Prp}_{31}$. Either of these compositions gives an RI of 1.751 and a susceptibility of 16.4×10^{-4} SI. Note that neither PrpGrsAlm nor GrsAlmSps fits the two properties. The calculated SGs from these two composi-

tions are 3.83 and 3.80, respectively, a difference of less than 1%, which is very slight for such a large difference in composition. The measured SG for this 1.88 ct stone is 3.85. Clearly, this value does not fit, so one cannot calculate a mixed PrpSpsGrsAlm garnet from these measured data. For this stone, a rather accurate SG (of 3.817) is needed to derive a four end-member composition obtained with the Locock method. This example demonstrates the problem with adding SG to determine a fourth end member for distinguishing between some pyralspite garnets. A photo of sample no. 79 is shown in figure 5, along with no. 25000 and a hessonite that resembles the latter in color.

Garnet no. 25000 is also an interesting stone. From the Locock procedure, its composition is $\text{Prp}_{68}\text{Alm}_{24}\text{Grs}_3\text{Adr}_1$. GIA had classified it as a pyrope. Interestingly, the stone's color matches that of many hessonites. But its measured susceptibility is close to its calculated properties, and the stone is clearly not hessonite (figure 2). The measured properties indicate $\text{Pyp}_{75}\text{Alm}_{25}$, if it is assumed to have only pyrope and almandine components, and this composition would have RI and SG values of 1.743 and 3.77, respectively. However, this sample can also be fit with a composition of $\text{Grs}_{51}\text{Prp}_{26}\text{Sps}_{23}$ and RI and SG values of 1.744 and 3.77, respectively. These properties fall within the measurement error of $\text{Prp}_{75}\text{Alm}_{25}$. This example shows that very minor differences in measured properties may tip the composition to one side or the other of the pyrope-almandine join. The author suspects there are other such pyropes that could masquerade as hessonites.

RI vs. Cell Constant Diagram. While Manson and Stockton did not use cell constant in their articles, they did measure it for a number of their samples. This makes it possible to compare the modified Winchell RIMS plot against a standard Winchell plot of RI vs. cell constant (RICC), as well as four other variations, when four quantitatively measurable properties are available.

Figure 6 shows a conventional Winchell plot for 16 of the 28 GIA samples for which cell constant was measured. Note that the differences between the calculated and measured values are about the same as those shown for the RIMS plots in figure 2. Comparing these two plots shows distinct differences in the positioning of some stones within the pyralspite ternaries.

Consider the stones arrayed near the pyrope-almandine join. In figure 2 they are positioned, on

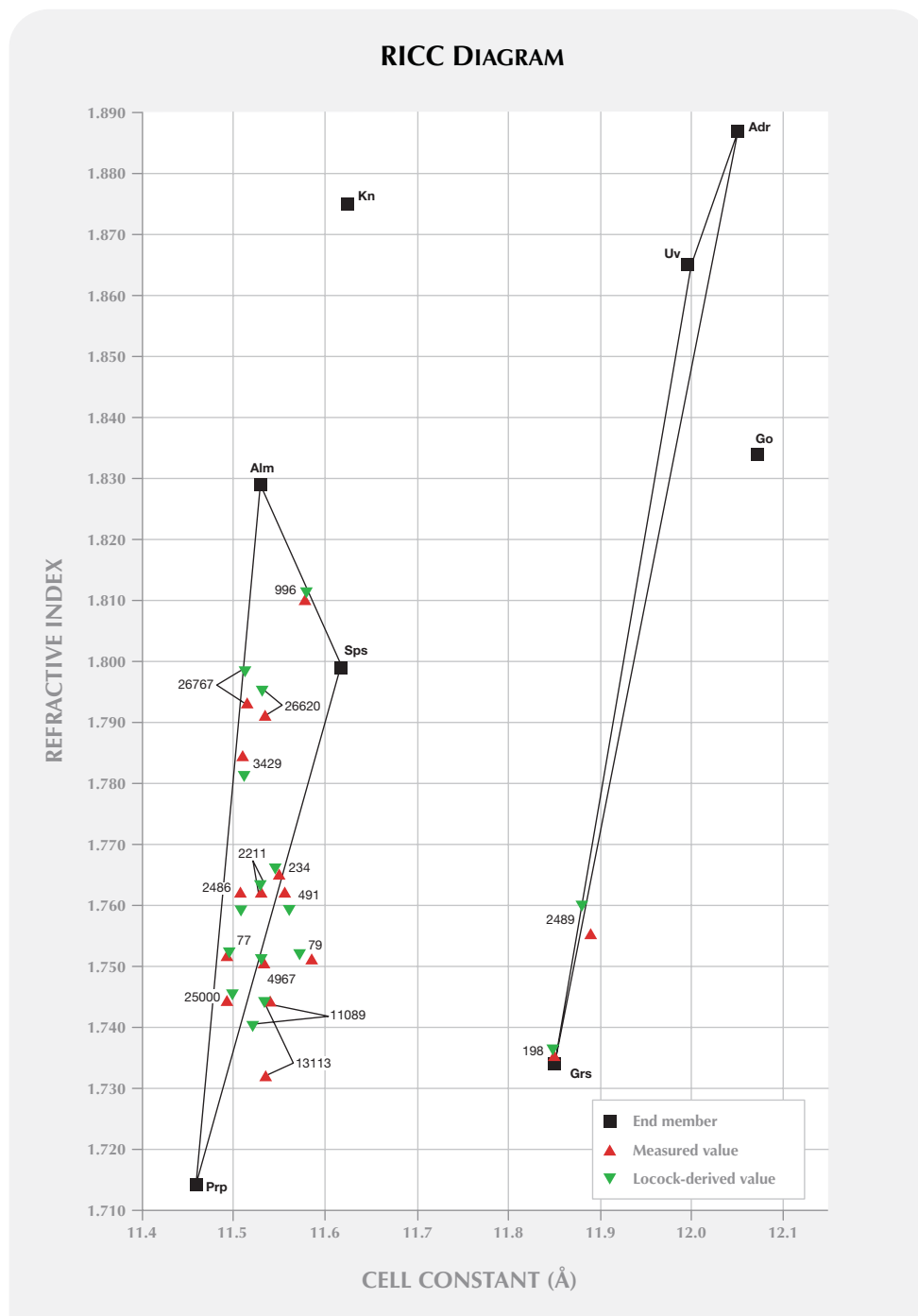


Figure 6. This conventional Winchell plot shows the RI vs. cell constant (RICC diagram) for 16 GIA garnet samples.

average, slightly to the left of the join (nos. 26767, 3429, 2211, 2486, 77, and 25000). In figure 6 they are within the pyralspite ternary. But the malaya (no. 491) and color-change (79) garnets are outside the pyralspite ternary. These differences reflect the effects of end members other than pyralspite's on the measured properties. If the composition of a garnet is purely pyralspite, its position within the ternary would not change according to the particular

Winchell diagram used. In these cases, the differences are due to grossular and/or uvarovite components. Note that in the RICC plot the ugrandite ternary is very narrow, indicating that a ugrandite with all three end members as major components cannot be well characterized by this type of diagram.

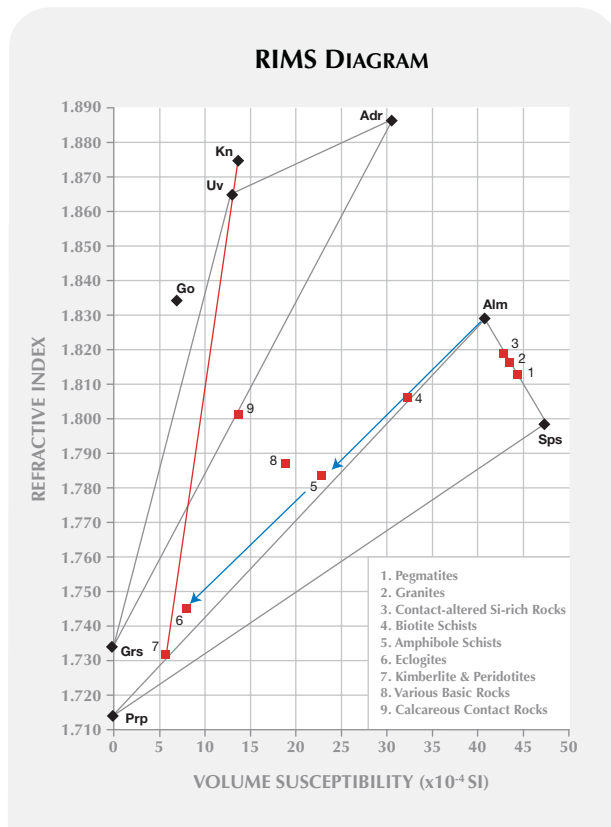
Usefulness of Modified Winchell Diagrams. These diagrams provide a simple but powerful demonstra-

tion of the relationship between garnet properties and composition. Any garnet with properties that plot near an end member will have a preponderance of that end member in its composition. A sample positioned toward the center of a given ternary will be composed of similar quantities of each end member. One can also estimate the effect that adding or subtracting any end member will have on the various properties. The effect on properties is directly related to the garnet's distance from the end member.

In addition to offering compositional information, the modified Winchell diagrams can also provide insights into garnet paragenesis. Figure 7 is a RIMS plot of data from Wright (1938) showing the average compositions of garnets from various rock

types. The RIs and susceptibilities were calculated from Wright's average compositions. The plot shows that garnets associated with felsic igneous rocks (nos. 1, 2, and 3) such as the granitic pegmatites are essentially almandine and spessartine. Metamorphic garnets (nos. 4, 5, and 6) show higher pyrope/grossular as the metamorphic grade increases (blue arrows), with the highest grade (eclogitic; no. 6) approaching the composition of peridotitic garnet (no. 7). The red line shows the change in properties of an average peridotitic pyrope toward the knorringite component as chromium is added. Comparing figure 7 with figure 2, correlations are evident between many of the garnet samples and their probable genetic origins. Malaya and color-change garnets are not represented in the Wright data, but the present author suspects they represent metamorphosed, subducted, high-Mn oceanic sediments.

Figure 7. This RIMS diagram shows the average garnet compositions from various rock associations, as given by Wright (1938). The RI and susceptibility data are plotted from compositions that include the average proportions of five major garnet end members. The blue arrows show the compositional change for metamorphic garnets as the metamorphic grade increases.



CONCLUSION

Gem garnets (e.g., figure 8) encompass a broad range of compositions and properties. Because most gemologists lack the capability to obtain quantitative chemical data, garnet composition must be inferred from measured/observed properties. In the past, RI and possibly SG were the only quantitative measures for deriving chemical composition. Yet these properties are not sufficiently independent of each other for such determinations. By measuring magnetic susceptibilities on selected garnets with well characterized compositions, the author has demonstrated a technique for inferring garnet composition from measurements of two or more quantitative properties.

Inferring chemical composition in this way should not be considered equivalent to the results obtained from a microprobe or other chemical analysis. While chemical data typically give the percentages of oxides in a sample, these data are not of prime interest to the gemologist, who seeks the proportion of ideal end members. This proportion may be obtained from either oxide chemistry or garnet properties, but neither method gives unique results. When oxide percentages are used, the number of ideal end members will vary according to the number of elements analyzed. Using garnet properties to infer end-member composition limits the number of properties measured. Using RI and magnetic susceptibility, then, we can infer a three end-member composition.



Figure 8. Gem garnets, such as these examples from the Dr. Edward J. Gübelin Collection, show a variety of properties and compositions. Magnetic susceptibility is one more measurable property the gemologist can use to help estimate garnet composition. Shown clockwise from the top: 44.28 ct pyrope-spessartine from Madagascar (GIA Collection no. 34387a), 19.12 ct pyrope-almandine from Sri Lanka (34769), 4.24 ct demantoid (33303), 3.65 ct tsavorite from Tanzania (35569), and 19.90 ct spessartine from Brazil (33238); photo by Robert Weldon.

REFERENCES

- Deer W.A., Howie R.A., Zussman J. (1982) *Rock Forming Minerals*, Vol. 1A—Orthosilicates. Longman, London, pp. 469–697.
- Frost M.J. (1960) Magnetic susceptibility of garnets. *Mineralogical Magazine*, Vol. 32, pp. 573–576, <http://dx.doi.org/10.1180/minmag.1960.032.250.07>.
- Hoover D.B., Williams B. (2007) Magnetic susceptibility for gemstone discrimination. *Australian Gemmologist*, Vol. 23, No. 4, pp. 146–159.
- Hoover D.B., Williams C., Williams B., Mitchell C. (2008) Magnetic susceptibility, a better approach to defining garnets. *Journal of Gemmology*, Vol. 31, No. 3/4, pp. 91–103.
- Hutchison C.S. (1974) *Laboratory Handbook of Petrographic Techniques*. John Wiley & Sons, New York, 527 pp.
- Jackson B. (2006) The garnets. In M. O'Donoghue, Ed., *Gems*, 6th ed., Elsevier, Oxford, UK, pp. 195–237.
- Kittel C. (1956) *Introduction to Solid State Physics*, 2nd ed. John Wiley & Sons, New York, 617 pp.
- Larsen E.S., Berman H. (1934) The microscopic determination of the nonopaque minerals. *U.S. Geological Survey Bulletin 848*, 2nd ed., U.S. Government Printing Office, Washington, DC, 266 pp.
- Locock A.J. (2008) An Excel spreadsheet to recast analyses of garnet into end-member components, and a synopsis of the crystal chemistry of natural silicate garnets. *Computers @ Geosciences*, Vol. 34, pp. 1769–1780, <http://dx.doi.org/10.1016/j.cageo.2007.12.013>.
- Manson D.V., Stockton C.M. (1981) Gem garnets in the red-to-violet color range. *G&G*, Vol. 17, No. 4, pp. 191–204, <http://dx.doi.org/10.5741/GEMS.17.4.191>.
- Meagher E.P. (1982) Silicate garnets. In *Reviews in Mineralogy*, Vol. 5, 2nd ed., Orthosilicates, Mineralogical Society of America, Washington, DC, pp. 25–66.
- Nathan Y., Katz A., Eyal M. (1965) Garnets from the Eilat area, southern Israel. *Mineralogical Magazine*, Vol. 35, pp. 386–392, <http://dx.doi.org/10.1180/minmag.1965.035.270.12>.
- Nixon P.H., Hornung G. (1968) A new chromium garnet end member, knorringite, from kimberlite. *American Mineralogist*, Vol. 53, pp. 1833–1840.
- Rickwood P.C. (1968) On recasting analyses of garnet into end-member molecules. *Contributions to Mineralogy and Petrology*, Vol. 18, pp. 175–198, <http://dx.doi.org/10.1007/BF00371808>.
- Ringwood A.E. (1977) Synthesis of pyrope-knorringite solid solution series. *Earth and Planetary Science Letters*, Vol. 36, pp. 443–448, [http://dx.doi.org/10.1016/0012-821X\(77\)90069-3](http://dx.doi.org/10.1016/0012-821X(77)90069-3).
- Stockton C.M., Manson D.V. (1985) A proposed new classification for gem-quality garnets. *G&G*, Vol. 21, No. 4, pp. 205–218, <http://dx.doi.org/10.5741/GEMS.21.4.205>.
- Winchell H. (1958) The composition and physical properties of garnet. *American Mineralogist*, Vol. 43, pp. 595–600.
- Wright W.I. (1938) The composition and occurrence of garnets. *American Mineralogist*, Vol. 23, pp. 436–449.

The various modified Winchell diagrams give the gemologist new insight into garnet chemical composition and its relation to measured properties. They can be a useful educational tool—showing the range of RIs possible where pyrope is the principal component, for example. In addition, Winchell diagrams can yield information on a garnet's probable geologic environment.

ABOUT THE AUTHOR

Dr. Hoover (dbhoover@aol.com) is a retired research geophysicist with the U.S. Geological Survey who now pursues independent geological research in Springfield, Missouri.

ACKNOWLEDGMENTS

The author thanks GIA for providing access to the enormous amount of data collected in the 1980s by D. Vincent Manson and Carol M. Stockton for their classic series of *Gems & Gemology* articles on the garnet group. Particular thanks go to Terri Ottaway, museum curator, for supplying samples from GIA's Museum Collection in Carlsbad, and to Ms. Stockton for providing her raw data. Without their cooperation, this work would not have been possible. The author is also grateful to Bear and Cara Williams (Bear Essentials, Jefferson City, Missouri) and Claire Mitchell (Gem-A, London) for innumerable discussions on the nature and identification of the garnet group.

GIA'S SYMMETRY GRADING BOUNDARIES FOR ROUND BRILLIANT CUT DIAMONDS

Ron H. Geurts, Ilene M. Reinitz, Troy Blodgett, and Al M. Gilbertson

Grade boundary limits are presented for 10 symmetry parameters of the round brilliant cut diamond. Starting in early 2012, these values will be used to support and constrain visual symmetry grading on GIA diamond reports. For manufacturers, the boundaries provide useful predictions of symmetry grades. Other symmetry features of faceted diamonds will continue to be evaluated visually.

Since 2006, GIA has used certain proportion measurements obtained with non-contact optical scanners to grade the cut of round brilliant diamonds. Improvements in the operation and accuracy of these instruments now enable us to also measure some symmetry parameters during the grading process. Although both Excellent and Very Good symmetry grades meet GIA's criteria for an Excellent cut grade (Moses et al., 2004), there is a premium for what the trade calls a "triple Excellent": an Excellent grade for cut, polish, and symmetry. Therefore, many diamond manufacturers would like to be able to predict GIA symmetry grades from measurement data, so they can apply these consider-

ations during planning and cutting. Likewise, makers of non-contact optical scanners have been interested in guidelines for how measurable symmetry parameters affect the GIA symmetry grade. The grade boundaries presented here offer a substantive estimate of the symmetry grade for any round brilliant cut diamond.

In GIA's laboratory, polished diamonds are measured with a non-contact optical scanner early in the grading process. Later, polish and symmetry are evaluated visually at 10× magnification, using a standard procedure. As described in Gillen et al. (2005), specific parameter- and facet-related features are considered in grading symmetry. This article presents numerical grade limits for 10 important symmetry parameters that can be measured accurately enough to support visual symmetry grading. Although measured values have been available to graders as a guide for several years, beginning in 2012 GIA will use measured values and apply these boundary limits strictly when grading symmetry for round brilliant cut diamonds. Facet-related symmetry features, and the manner in which multiple features combine, may also affect the symmetry grade, and these aspects will continue to be evaluated visually, as they are presently beyond reproducible instrument measurement.

Compared to visual assessment, instrumental measurements provide a more consistent way of establishing a symmetry grade, especially when a diamond has very subtle symmetry deviations. Figure 1 shows a diamond with several symmetry flaws: a wavy and uneven girdle (resulting in an uneven crown height), a table not parallel to the girdle, and uneven bezel facets. In the past, the only means of

See end of article for About the Authors.
GEMS & GEMOLOGY, Vol. 47, No. 4, pp. 286–295,
<http://dx.doi.org/10.5741.GEMS.47.4.286>.
© 2011 Gemological Institute of America



Figure 1. This 0.69 ct standard round brilliant cut diamond displays several obvious symmetry features that can be quantified. Photo by Robert Weldon.

determining this diamond's symmetry grade would have been the judgment and experience of the grader. Quantifying these features by instrumental measurement provides a more consistent basis for symmetry grading, and gives cutters the details needed to improve their diamonds' symmetry.

BACKGROUND

The repeated measurement of any attribute, such as weight or size, is accompanied by a certain degree of uncertainty. For example, the repeated measurement of a diamond's weight, or its total depth, yields results that vary slightly within a certain range. For the most accurate results, the measured value itself and the variation in repeated measurements—the uncertainty of that value—are both important.

The U.S. National Institute of Standards and Technology (NIST) notes that "a measurement result is complete only when accompanied by a quantitative statement of its uncertainty" ("Uncertainty of measurement results," 1998). Whatever the tool or method, measurement results fall within a certain allowable range of values—the *tolerance*. For our purposes, the tolerance of a measuring device describes its contribution to the overall uncertainty of the measured values (GIA Research, 2005).

Statistical examination of repeated independent measurements provides one way to estimate their uncertainty. The distribution of these measurements also reveals information about reproducibility and defensible precision. For example, a device might

measure crown angle to three decimal places, but if repeated measurements demonstrate an uncertainty in the first decimal place, the two additional digits offer no meaningful precision (Reinitz et al., 2005).

Even detailed knowledge of the uncertainty does not tell us whether measurements are accurate. Accuracy can only be determined relative to the measurement of a known standard, such as an object with NIST-traceable values and reported uncertainties. Box A describes some basic metrology concepts, including measurement uncertainty.

The proportion values used to determine a diamond's cut grade are normally the average of eight measurements; these are not greatly affected by a single outlying value. In contrast, symmetry parameters examine the range (the largest and smallest) of those values, and they are much more affected by a single poor measurement. This means a higher level of confidence in the reproducibility and accuracy of each measured value is needed to predict a symmetry grade, or to reinforce visual grading. GIA has achieved this confidence through advances in the devices used to measure polished diamonds, coupled with efforts to ensure the diamonds are thoroughly cleaned. For example, suppose eight crown angles are individually measured at 34.1°, 34.5°, 34.9°, 35.3°, 34.2°, 34.3°, 34.0°, and 34.1°. The average is 34.43°, and the difference in values (maximum minus minimum) is 1.3°. A second set of measurements yields values of 34.1°, 34.5°, 34.5°, 34.8°, 34.2°, 34.3°, 34.0°, and 34.1°. The second average is 34.31°,

BOX A: BASIC MEASURING CONCEPTS

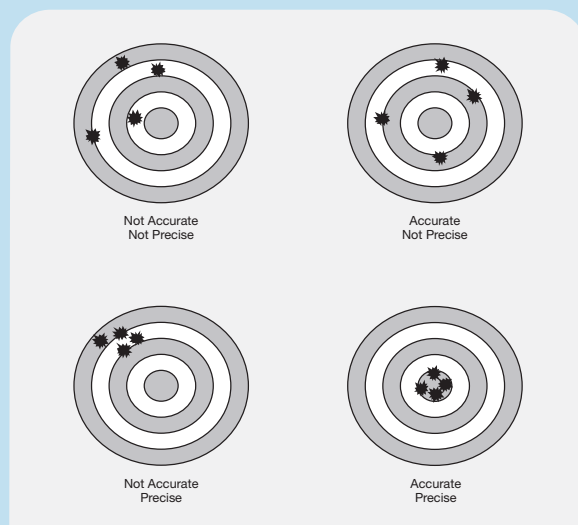
Taking several independent measurements of the same characteristic illustrates the difference between precision and accuracy, as shown in figure A-1. Accuracy refers to how close the measured values are to the reference value, shown here as the center of the target. Precision refers to how close the values are to each other, and in practice this affects how many significant figures should be used when reporting the measurement.

When the difference between two measured values is less than or equal to the measurement uncertainty, the values are *within tolerance* of each other, and by definition not readily distinguishable from one another. Figure A-2 shows six measurements of the total depth of one round brilliant, each with an uncertainty of ± 0.015 mm. The average value of those measurements is 5.015 mm. Trial 4, with a value of 5.00 mm, is just within tolerance of that average. Trial 6, with a value of 5.04 mm, is not within tolerance of the average. This is described as an *outlying* value.

Most gemologically important parameters for the round brilliant cut diamond, such as the crown or pavilion angle, represent averages rather than single measurements. In metrology, averages of multiple measurements are used to reduce measurement uncertainty. But a quantity such as average crown angle is calculated from eight values obtained from different facets, rather than eight measurements of the same facet. As a result, this average has its own uncertainty that is no smaller than the uncertainties

of the eight individual values. In a round brilliant of lower symmetry, the eight crown angle values may vary by several degrees. The uncertainty of a symmetry assessment for such variation among the crown angles

Figure A-1. A measurement is accurate when it agrees with an independently obtained reference value (here, the center of the bull's-eye). Measurements are precise when they can be reproduced with small uncertainties. The ideal situation is to have measurements that are both accurate and precise.



only 0.12° below the previous average. But the difference in values is now 0.8° , considerably smaller than the 1.3° from the first set of measurements. In other words, the average changes less than the difference in values when one or two of the eight values is marred by dirt or some other measuring problem not specifically related to that particular diamond.

Higher-quality measurements have a smaller uncertainty, but even the best measuring systems have some tolerance for each parameter. Box A shows an example of measurement uncertainty at the border between Very Good and Excellent. Even measurements of clean diamonds made on devices of proven accuracy and precision can produce one or more values that fall within tolerance of a symmetry

grade boundary. Multiple measurements, on one device or on different devices, can yield slightly different results. All devices have a margin of error (within the tolerance of the device) that could yield two different grades when one or more parameters are near a border. Since no measurement is exact, prudent cut planning acknowledges measuring tolerances and avoids placing parameters too close to the borders.

MEASURABLE SYMMETRY PARAMETERS AND ADDITIONAL FACTORS

Ten symmetry parameters are illustrated in figure 2. GIA has developed procedures to measure these

COMPARING VALUES WITH UNCERTAINTIES

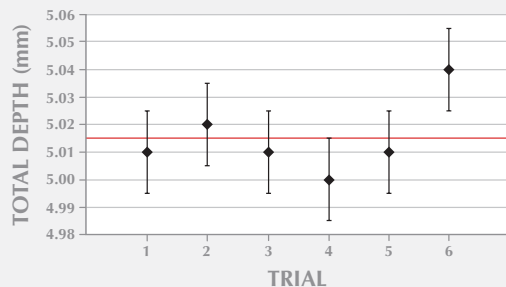


Figure A-2. These total-depth measurements are shown with error bars that represent measurement uncertainty. These bars overlap the average value of 5.015 mm for the first five trials, but not the sixth. It is important to recognize the distinction between (1) measurements within tolerance of each other, and (2) measurements that clearly differ from each other beyond the tolerance. If the error bars overlap each other, the measurements can be considered the same; if they do not overlap, the measurements are different.

is also no smaller than the individual uncertainties.

The uncertainty associated with a measured value can be thought of as a “bubble” around it. Overlap among these bubbles in a group of measurements indicates agreement with each other. A fixed boundary, such as a limit for symmetry grading, can cut through such uncertainty bubbles, separating a group of measurements that agree with each other

UNCERTAINTY VS. A SYMMETRY BOUNDARY

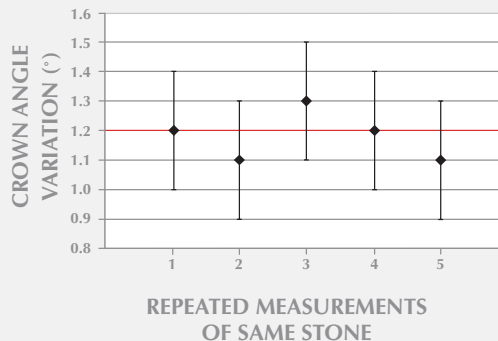


Figure A-3. A round brilliant measured five times yields crown angle–variation values with uncertainties that cross the symmetry grade limit for this parameter (1.2°). Although the third measurement of 1.3° would indicate Very Good symmetry, the most reproducible value—the one most often obtained—is within the limits for Excellent.

into two differing results. Figure A-3 shows such an example, where all five measurements are within tolerance of each other, but one generates a symmetry grade of Very Good, based on this one parameter, while the other four would score in the Excellent range. From basic metrological principles, if the measuring device is sound, the more reproducible value is the correct one.

parameters with sufficient accuracy to determine the symmetry grade of round brilliant cut diamonds. Additional parameters have been identified, such as the symmetry of the star facets and the upper and lower girdle facets, but numerical boundaries for these are still under review.

The 10 symmetry parameters are calculated as follows:

- 1. Out-of-round:** the difference between the maximum and minimum diameter, as a percentage of the average diameter
- 2. Table off-center:** the direct distance between the table center and the outline center projected into the table plane, as a percentage of the average diameter

NEED TO KNOW

- Starting in early 2012, GIA will apply boundary limits for 10 symmetry parameters measured by non-contact optical scanners when grading the symmetry of round brilliant cut diamonds.
- Additional measurable parameters, aspects arising from combinations of these parameters, and facet-related symmetry variations will continue to be assessed visually.
- Manufacturers should strive to attain values that are 20% lower than the symmetry boundary limits, to account for measurement uncertainty and features that may combine to lower the symmetry grade.

QUANTIFIED SYMMETRY FEATURES

Out-of-round: deviation from the circular shape of a round diamond

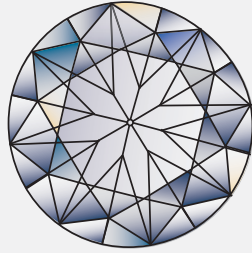
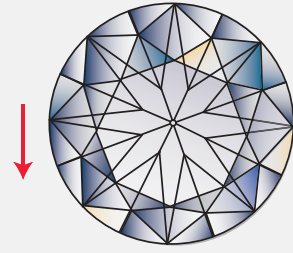
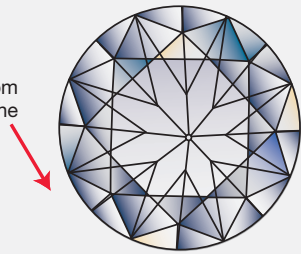


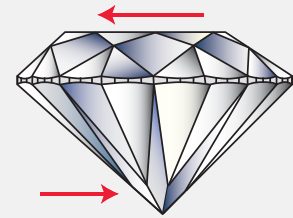
Table off-center: deviation of the table from the central position on the crown



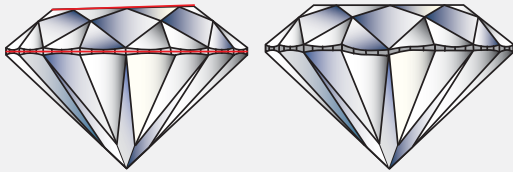
Culet off-center: deviation of the culet from the central position on the pavilion



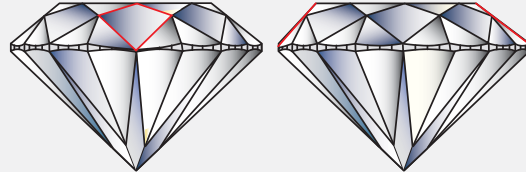
Table/culet alignment: displacement of the table facet and culet in opposite directions



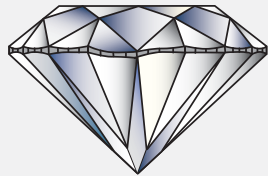
Crown height variation: differing crown height measurements indicating a wavy girdle or table/girdle not parallel



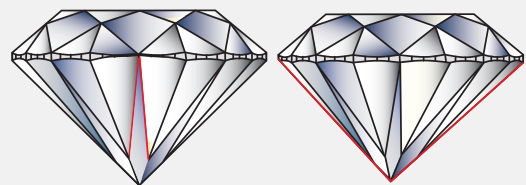
Crown angle variation: crown angles are unequal; typically related to table off-center



Pavilion depth variation: differing pavilion depth measurements indicating a wavy girdle



Pavilion angle variation: pavilion angles are unequal; typically related to culet off-center



Girdle thickness variation: variation of the girdle thickness at bezel positions

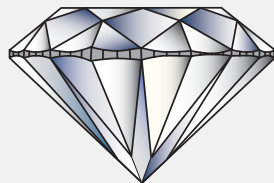


Table size variation: differing table size measurements indicating non-octagonal table

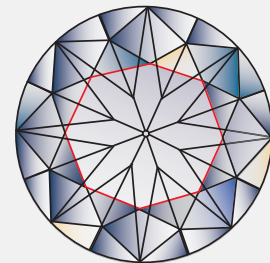


Figure 2. These 10 symmetry features can be measured reliably enough by non-contact optical scanners to determine the symmetry grade of round brilliant cut diamonds.



Figure 3. Three vertical lengths (A1–A3) in this close-up of the 0.69 ct diamond in figure 1 illustrate girdle thickness differences. Region B (green circle) shows where the facet edges of the upper and lower girdle do not meet (crown and pavilion misalignment). Region C (yellow circle) shows the junction where three facets fail to meet (pointing fault). Photo by Robert Weldon.

3. **Culet off-center:** the direct distance between the culet center and the outline center projected into any horizontal plane such as the table plane, as a percentage of the average diameter
4. **Table/culet alignment:** the direct distance between the table center and the culet center projected into the table plane, as a percentage of the average diameter
5. **Crown height variation:** the difference between the maximum and minimum crown height values, as a percentage of the average diameter
6. **Crown angle variation:** the difference between the maximum and minimum crown angle values, in degrees
7. **Pavilion depth variation:** the difference between the maximum and minimum pavilion depth values, as a percentage of the average diameter
8. **Pavilion angle variation:** the difference between the maximum and minimum pavilion angle values, in degrees
9. **Girdle thickness variation:** the difference between the maximum and minimum girdle thickness values, as a percentage of the average diameter, measured at the bezel-main junctions (see also features A1–A3 in figure 3)
10. **Table size variation:** the difference between the maximum and minimum table size values, as a percentage of the average diameter

Because the facets of a round brilliant are connected to each other, these symmetry features frequently occur in combination. All of the symmetry features combine to produce a general face-up visual impression, so the symmetry grade is established by looking at the face-up diamond. Depending on where they occur, and how they combine, different symmetry features can visually amplify or compensate for one another, as discussed in box B. This

interaction plays a large role in determining the overall symmetry grade for round brilliants with lower symmetry. But for those with high symmetry, the magnitude of a single feature may dominate the evaluation.

Facet-related symmetry features also play a role in determining the symmetry grade (e.g., figure 3, features B and C), but they are not part of the grading procedure described here. A full description of facet-related symmetry features can be found in Blodgett et al. (2009). Open or short facets (non-pointing), misalignment between the bezels and pavilion mains, and prominent naturals or extra facets are readily observed, but they may occur independently of the 10 measurable symmetry parameters listed above. Misshapen or uneven facets usually relate to a combination of the 10 parameters, but the relationships can be complex.

RECOMMENDED SYMMETRY BOUNDARIES

The limits given below were derived from a statistical comparison of measured values for the 10 parameters and the final symmetry grades assigned to the diamonds. This comparison was repeated four times over a period of 10 years, each time on newly acquired data sets from several thousand diamonds. Each analysis examined several sets of limits for the 10 parameters to identify robust matches with visual symmetry grading.

Table 1 presents the ranges of allowed values for individual symmetry features, measured in percentage or degrees, that GIA uses to support and constrain visual symmetry grading. The limits dividing Fair from Poor symmetry are not presented here because of the small number of round brilliants with such low symmetry. Measured values should be rounded to the indicated precision, if necessary, before calculating the differences. If the value for any one parameter falls into a range associated with a lower grade, the overall symmetry grade will be low-

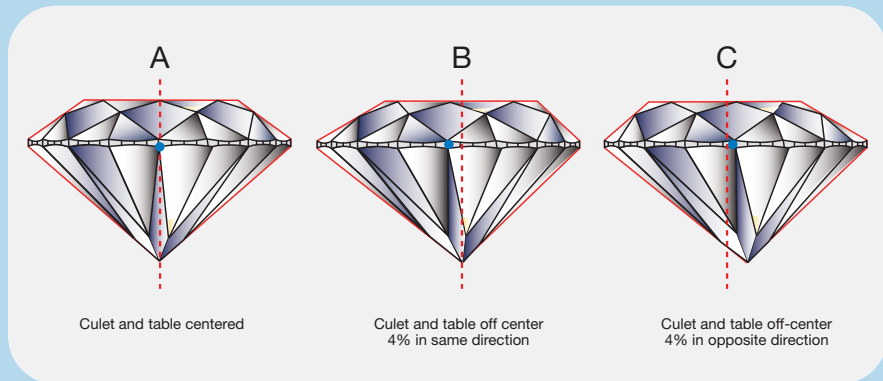
BOX B: COMBINATIONS OF SYMMETRY FEATURES

The red dashed lines in the drawings in figure B-1 show the position of the table center, and the blue dot shows the center of the stone outline. Consider two round brilliants, each with a 4% off-center table and culet (cases B and C). The measured values for table and culet being off center are equal, and each feature would be easily noticed individually, in profile as well as face-up. When the culet and table are off center in the same direction (case B), the two symmetry features compensate for each other visually. But when the table and culet are shifted off center in different directions (case C), the negative visual impression is amplified considerably.

When uneven crown height and girdle thick-

ness are added to the off-center table and culet, the visual difference between various combinations of these features becomes even more pronounced. In figure B-2 (top), the table and culet are off center in the same direction, and the girdle and crown height are uneven along this same A-B axis. Arranged in this way, these features tend to compensate each other visually, particularly in the face-up view. In contrast, figure B-2 (bottom) shows a table and culet that are off center in opposite directions, and the girdle thickness and crown height are uneven in a different direction (along the G-H axis). This combination amplifies the visual impression of asymmetry.

Figure B-1. A culet and table that are off center in different directions produce a more asymmetrical appearance (case C) than when they are off center in the same direction (case B). Note that the degree of asymmetry is extreme, down to the Fair range.



ered accordingly. Combinations of symmetry features, as well as facet-related features that are not measured, will still be evaluated visually, which may also contribute to a lower symmetry grade.

For example, if nine of the parameters are within the Excellent range but the table is off-center by 0.7%, the best possible symmetry grade is Very Good. If all 10 parameters are within the Excellent range, the expected symmetry grade would be Excellent. But consider a round brilliant that is out of round by 0.7%, with crown angle variation of 1.1° and girdle thickness variation of 1.1%. Even though all three parameters are within the limits for

TABLE 1. Limits used by GIA to grade the symmetry of round brilliant cut diamonds.

Parameter	Excellent	Very Good	Good
Out-of-round (%)	0–0.9	1.0–1.8	1.9–3.6
Table off-center (%)	0–0.6	0.7–1.2	1.3–2.4
Culet off-center (%)	0–0.6	0.7–1.2	1.3–2.4
Table/culet alignment (%)	0–0.9	1.0–1.8	1.9–3.6
Crown height variation (%)	0–1.2	1.3–2.4	2.5–4.8
Crown angle variation (°)	0–1.2	1.3–2.4	2.5–4.8
Pavilion depth variation (%)	0–1.2	1.3–2.4	2.5–4.8
Pavilion angle variation (°)	0–0.9	1.0–1.8	1.9–3.6
Girdle thickness variation (%)	0–1.2	1.3–2.4	2.5–4.8
Table size variation (%)	0–1.2	1.3–2.4	2.5–4.8

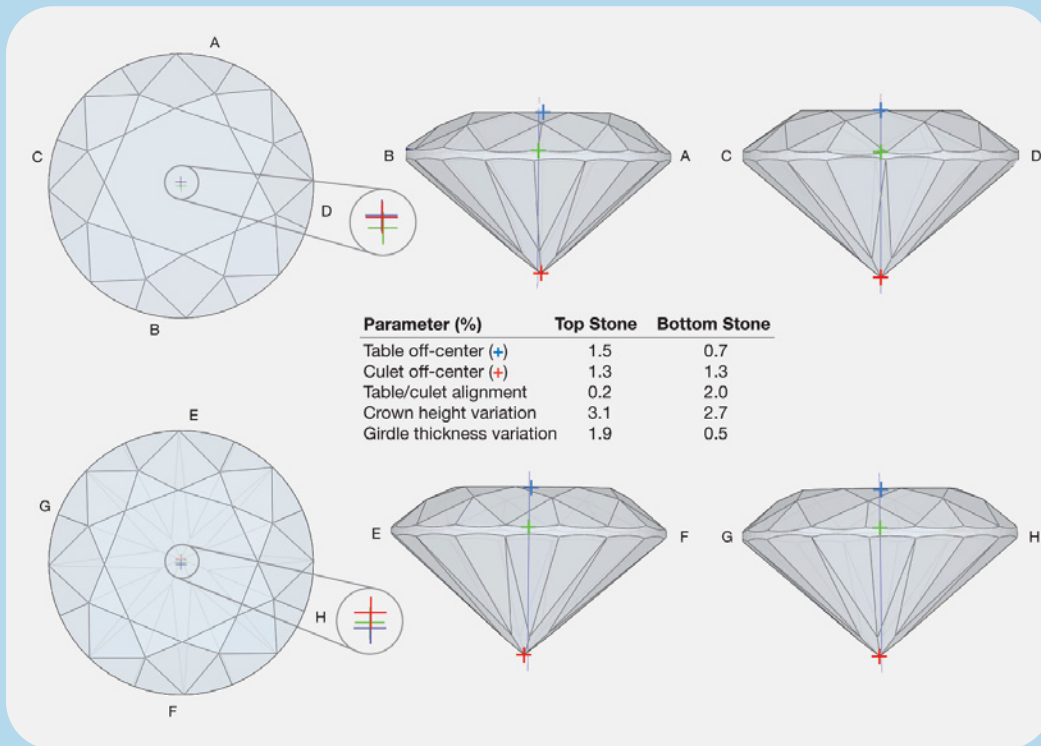


Figure B-2. These two round brilliants have multiple measurable symmetry faults that limit them to no better than a Good symmetry grade. Although both stones have equal culet off-center values, the appearance of overall symmetry is different because of the relative placement of the various symmetry faults. The green crosshair indicates the center of the outline, blue is the center of the table, and red denotes the center of the culet. When the faults are aligned, the asymmetry appears less pronounced (top). By comparison, when symmetry faults occur in different directions, the visual impression of asymmetry is amplified (bottom). In either combination, these displacements are considerably more subtle than those shown in figure B-1.

TABLE 2. Recommended limits for estimating the symmetry grade of round brilliant cut diamonds.

Parameter	Excellent	Very Good	Good
Out-of-round (%)	0–0.7	0.8–1.4	1.5–2.8
Table off-center (%)	0–0.5	0.6–1.0	1.1–1.9
Culet off-center (%)	0–0.5	0.6–1.0	1.1–1.9
Table/culet alignment (%)	0–0.7	0.8–1.4	1.5–2.8
Crown height variation (%)	0–1.0	1.1–2.0	2.1–3.9
Crown angle variation (°)	0–1.0	1.1–2.0	2.1–3.9
Pavilion depth variation (%)	0–1.0	1.1–2.0	2.1–3.9
Pavilion angle variation (°)	0–0.7	0.8–1.4	1.5–2.8
Girdle thickness variation (%)	0–1.0	1.1–2.0	2.1–3.9
Table size variation (%)	0–1.0	1.1–2.0	2.1–3.9

Excellent, the combination of these three symmetry features (and any others found on the diamond) may result in either an Excellent or a Very Good symmetry grade, depending on the visual assessment.

Because every measurement contains uncertainty, and symmetry features may combine to lower the symmetry grade, we recommend a “safety margin” for the trade to use in estimating the symmetry grade. Accordingly, the values shown in table 2 are 20% lower than those in table 1. When the values for all 10 parameters fall within these narrower recommended borders, there is a strong likelihood that the visual symmetry assessment will agree with the

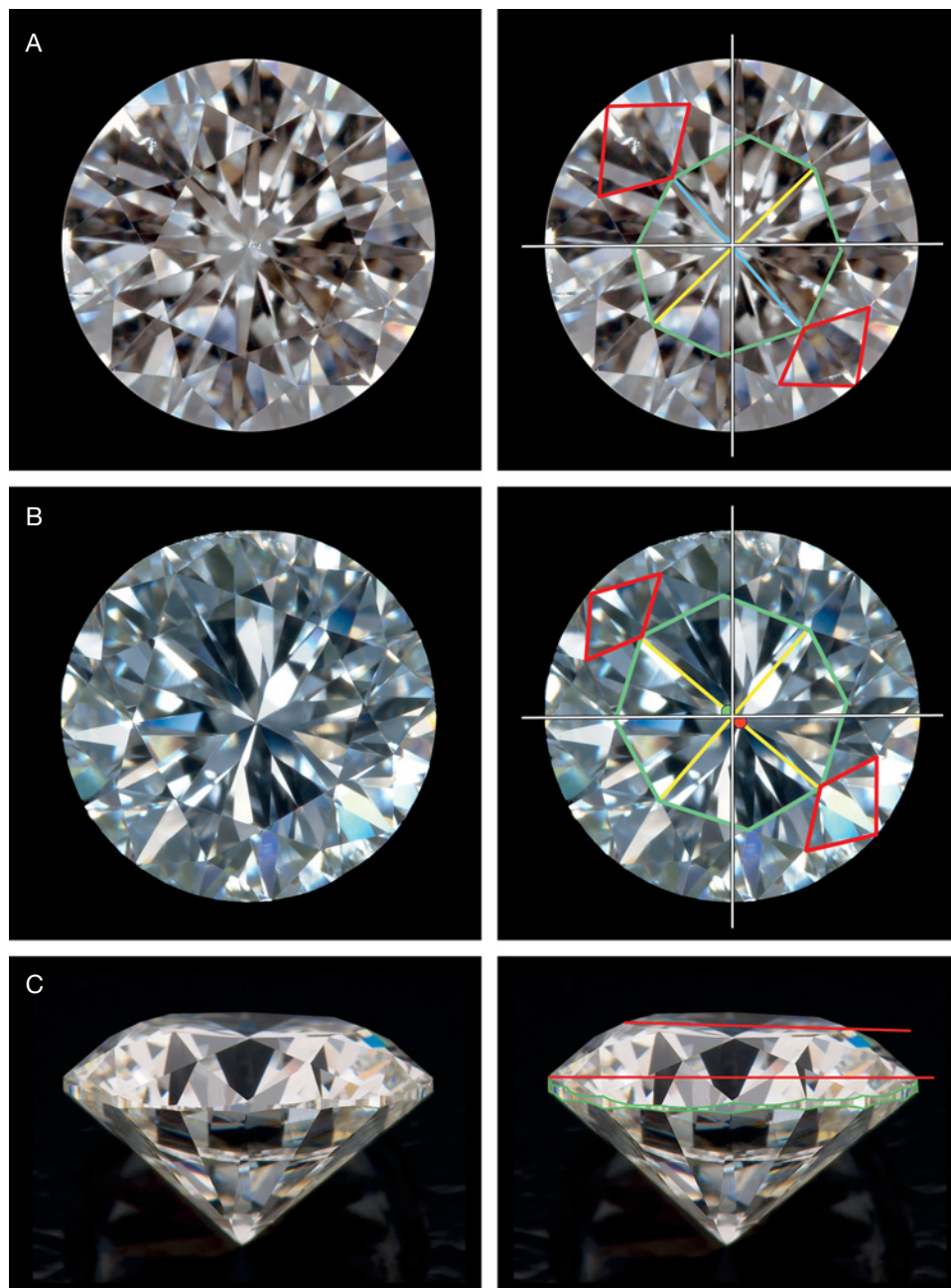


Figure 4. These three round brilliants each display a combination of symmetry faults. (A) The table of this 1.00 ct diamond (Fair symmetry) is not an octagon (6.1% table size variation, as shown by the blue and yellow lines) and the table is off-center by 2.5%. The asymmetry of the table is associated with crown angle variations and uneven bezels (marked red). (B) The culet of this 0.83 ct diamond (Fair symmetry) is off-center by 2.9% (red dot). The table is also off-center in an opposing direction (green dot), yielding a value for table/culet alignment of 3.4%. These symmetry faults are associated with uneven bezels (marked red) and pavilion mains. Unlike the diamond in A, the nearly equal quadrants defined by the yellow lines show that the table is octagonal. (C) In this 0.69 ct diamond (also shown in figures 1 and 3; Good symmetry), the girdle is wavy and not parallel to the table. Photos by GIA (A and B) and Robert Weldon (C).

measurement. Within these recommended limits, it is unlikely that a combination of measurable symmetry features would lead to a lower symmetry grade. Note that the second example in the previous paragraph exceeds two of these recommended limits.

The boundary values presented for these 10 symmetry features are most useful along the Excellent–Very Good symmetry border, where a single feature often dominates the final grade determination. These individual parameter limits are also relevant for the border between Very Good and Good. When symmetry problems become severe,

though, it is more likely that multiple symmetry features will limit the grade, because the interactions among symmetry factors become more pronounced (again, see box B). Because combinations of minor symmetry features can create a significant visual impact, the limits in the tables must be viewed only as a guide.

DISCUSSION

During the analysis of laboratory grading results, we observed some variation in how strictly symmetry was evaluated by our graders, particularly for mea-

sured features near the border between Excellent and Very Good. A common set of fixed numerical limits for these parameters can only improve the consistency of symmetry grading for such stones. Diamonds with at least one parameter beyond the limits shown in table 1 will receive the lower symmetry grade. Symmetry features not captured by these 10 parameters will continue to be evaluated visually. If these additional facet-related features are sufficiently prominent—an extra facet polished at the corner of the table, for instance—they will reduce the symmetry grade even if all measured parameters fall within the narrower limits in table 2. Visual symmetry observations cannot raise a symmetry grade, but they can reveal instances when a cleaner, more correct measurement of the diamond is needed.

Measured values can be of great help for diamonds with multiple symmetry faults, such as the three shown in figure 4. In such cases, some of the symmetry features are more easily noticed visually, while others are captured more accurately by measurement. In figure 4A, the asymmetry of the table leads to variation in crown angles and uneven bezel facets. In other cases, similar faults with the table might be associated with a wavy girdle that takes up the uneven aspects of the crown and allows little variation in the crown angles. Under both sets of circumstances, the uneven bezels are a prominent feature that does not describe the underlying symmetry faults as clearly as the measured values for crown angle variation, crown height variation, and girdle thickness variation.

In figure 4B, the off-center culet and table lead to uneven bezels and pavilion mains. The displacement between the table center and the culet

emphasizes the visual impact of the off-center culet (again, see box B), but the measured values—that is, Good for table-culet alignment, but Fair for table off-center—provide a context for evaluating the severity of the combination. In figure 4C, the most prominent symmetry fault is displayed for the diamond shown in figure 3. The table and girdle are not parallel, a fault that is more severe than the uneven girdle thickness or the facet-related symmetry features.

CONCLUSION

Measurement is a process full of inherent uncertainties, but GIA's efforts to achieve smaller uncertainties have been successful. Starting in early 2012, the measurable values presented in table 1 will be used to attain greater consistency than is possible through visual assessment alone. Additional measurable parameters, aspects arising from combinations of these parameters, and facet-related symmetry variations will continue to be assessed visually. A more restrictive set of limits is recommended for manufacturers, to help ensure that the final symmetry grade will not be undermined by combination effects or measuring tolerances.

ABOUT THE AUTHORS

Mr. Geurts is a manager of research and development at GIA in Antwerp. Dr. Reinitz is a project manager at GIA in New York. Dr. Blodgett is a research scientist, and Mr. Gilbertson a research associate, at GIA in Carlsbad.

REFERENCES

- Blodgett T., Geurts R., Gilbertson A., Lucas A., Pay D., Reinitz I., Shigley J., Yantzer K., Zink C. (2009) Finish, culet size and girdle thickness; Categories of the GIA Diamond Cut Grading System. www.gia.edu/diamondcut/pdf/poster_finish_culet_girdle_highres.pdf [date accessed: June 14, 2011].
- GIA Research (2005) Measurement tolerances: Accuracy and precision in the gem industry. *Rapaport Diamond Report*, Vol. 28, No. 13, pp. 183–185, www.gia.edu/diamondcut/pdf/4_05_RDR_pg183_185.pdf.
- Gillen D.B., Lanzl B.F., Yantzer P.M. (2005) Polish and symmetry. *Rapaport Diamond Report*, Vol. 28, No. 39, pp. 80–87, www.gia.edu/diamondcut/pdf/polish_and_symmetry.pdf.
- Moses T.M., Johnson M.L., Green B., Blodgett T., Cino K., Geurts R.H., Gilbertson A.M., Hemphill T.S., King J.M., Kornylak L., Reinitz I.M., Shigley J.E. (2004) A foundation for grading the overall cut quality of round brilliant cut diamonds. *G&G*, Vol. 40, No. 3, pp. 202–228, <http://dx.doi.org/10.5741/GEMS.40.4.202>.
- Reinitz I., Yantzer K., Johnson M., Blodgett T., Geurts R., Gilbertson A. (2005) Proportion measurement: Tolerances for the GIA Diamond Cut Grading System. *Rapaport Diamond Report*, Vol. 28, No. 30, pp. 34–39, www.gia.edu/diamondcut/pdf/0805_pg34_39.pdf.
- Uncertainty of measurement results (1998) *The NIST Reference on Constants and Uncertainty*. <http://physics.nist.gov/cuu/Uncertainty/international1.html> [date accessed: June 14, 2011].

A HISTORIC TURQUOISE JEWELRY SET CONTAINING FOSSILIZED DENTINE (ODONTOLITE) AND GLASS

Michael S. Krzemnicki, Franz Herzog, and Wei Zhou

A set of six antique brooches, set with diamonds and light blue cabochons, was investigated with microscopy, Raman analysis, and EDXRF spectroscopy. Most of the cabochons proved to be fossilized dentine, also known as odontolite (mineralogically, fluorapatite). The brooches also contained turquoise and artificial glass.

The Swiss Gemmological Institute SSEF recently received a set of six antique brooches for identification (figure 1). These same pieces had already been presented in Bennett and Mascetti (2003, p. 102) as turquoise jewelry. They were set with numerous small rose-cut diamonds and a few larger old-cut diamonds, but most prominent were a number of light blue to greenish blue cabochons that appeared to be turquoise. Visual examination quickly revealed otherwise. Considering the historic background of these brooches, we were interested in examining the blue gems in greater detail to shed light on early turquoise imitations.

Turquoise, a copper-bearing hydrated aluminum phosphate with the chemical formula

$\text{Cu}(\text{Al}, \text{Fe}^{3+})_6(\text{PO}_4)_4(\text{OH})_8 \cdot 4\text{H}_2\text{O}$, has been known since prehistoric times. It has been widely used in jewelry in the Middle East (Egypt and Persia), the Far East (Tibet, Mongolia, and China), and by native North Americans (Ahmed, 1999; Chalker et al., 2004). Yet turquoise was once very fashionable in Europe, especially during the 18th and 19th centuries (Bennett and Mascetti, 2003), so it is not surprising that imitations were used when genuine turquoise was not available. The wide range of turquoise imitations includes secondary minerals from copper deposits such as chrysocolla, dyed minerals such as magnesite or howlite, and artificial materials such as glass or sintered products (Arnould and Poirot, 1975; Lind et al., 1983; Fryer, 1983; Kane, 1985; Hurwit, 1988; Salanne, 2009).

In this study, we report on a historic turquoise substitute—fossilized dentine, also known as *odontolite*, *ivory turquoise*, *bone turquoise*, or *French turquoise*. Much of this material consists of fossilized mastodon ivory from Miocene-age (13–16 million years old) sedimentary rocks of the Gers District between the Aquitaine and Languedoc regions of southwestern France (Reiche et al., 2001). The tusks are hosted by alluvial sediments (molasse alternating with fine sand and clay facies) that accumulated in basins during the erosion of the nearby Pyrenees Mountains (Crouzel, 1957; Antoine et al., 1997). The fossilized dentine consists mainly of fluorapatite, $\text{Ca}_5(\text{PO}_4)_3\text{F}$; since medieval times, local Cistercian monks have used a heating process to turn the material light blue (de La Brosse, 1626; Réaumur, 1715; Fischer, 1819), which they thought to be turquoise. These “stones” were originally set in medieval religious artifacts, but came into fashion in the early to mid-19th century (Brown, 2007),

See end of article for About the Authors and Acknowledgment.

GEMS & GEMOLOGY, Vol. 47, No. 4, pp. 296–301,
<http://dx.doi.org/10.5741.GEMS.47.4.296>.

© 2011 Gemological Institute of America



Figure 1. These six brooches are set with 313 light blue stones, the majority of which proved to be fossilized dentine (odontolite), mixed with a few turquoise and glass cabochons. Photo by Luc Phan, Swiss Gemmological Institute SSEF.

when fossilized dentine was recovered commercially in southwestern France.

A similar set of brooches containing odontolite was described by Crowningshield (1993). The present study offers further data on this material. Odontolite is rarely encountered in the market today, although it is occasionally present in historic jewels from private collections or museums. Gemologists seldom have the opportunity to test this material in the laboratory.

MATERIALS AND METHODS

Six brooches, all of very similar style (figure 1), were investigated. Their ornamental patterns of folded and knotted bands are characteristic of early to mid-19th century design (Bennett and Mascetti, 2003). Several French assay marks were seen on the metal mounting. In total, the brooches contained 313 opaque light blue cabochons from approximately 2 to 11 mm long, set with numerous small rose-cut diamonds and three old-cut diamond center-stones. The brooches ranged from approximately 2.5 to 14 cm long and from 6.6 to 53.6 g in weight.

All of the pieces were observed microscopically with 10–50× magnification. A few stones were very difficult to investigate due to the complexity of the mounting. Many of the cabochons were also examined at high

magnification (200×) using an Olympus microscope coupled with our Renishaw Raman system. For identification, Raman spectra were taken on a large number of stones, using a 514 nm argon-ion laser (Hänni et al., 1998). The spectra were collected from 1800 to 100 cm^{-1} Raman shift, to include the vibrational range of organic compounds, such as wax and artificial resin, used for turquoise impregnation. In a few cases, spectra were collected up to 5000 cm^{-1} to check for OH bands in the dentine.

We also conducted semiquantitative energy-dispersive X-ray fluorescence (EDXRF) chemical analysis of two cabochons, using a Thermo Fisher Scientific Quant’X unit. These analyses, carried out using a series of excitation energies from 4 to 25 kV, covered a large range of elements, from Na to those with high atomic number.

RESULTS

The 313 light blue cabochons in the brooches (table 1) were categorized into three groups: odontolite (288

TABLE 1. Gems identified in the historic “turquoise” brooches.

Brooch	Location in figure 1	No. cabochons	No. analyzed by Raman	Odontolite ^a	Turquoise	Glass
A	Top left	94	88	87	7	0
B	Center	59	52	57	0	2
C	Top right	57	52	52	0	5
D	Bottom right	54	44	52	0	2
E	Bottom left	24	24	21	1	2
F	Bottom center	25	24	19	2	4
Total		313	284	288	10	15

^a Due to the mountings, a few of the odontolites could only be identified by microscopic examination; these are also included here.

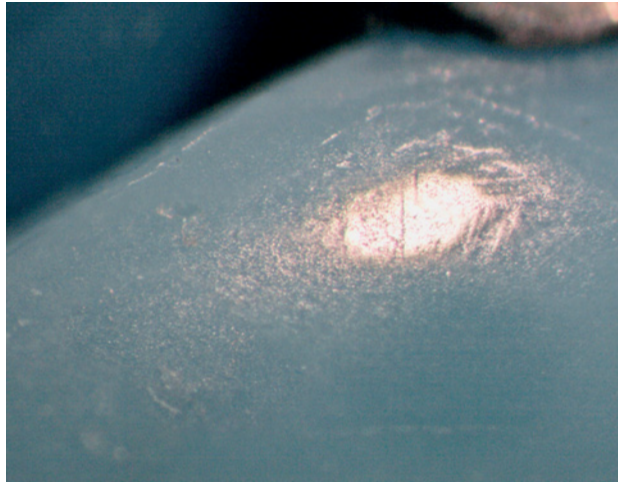
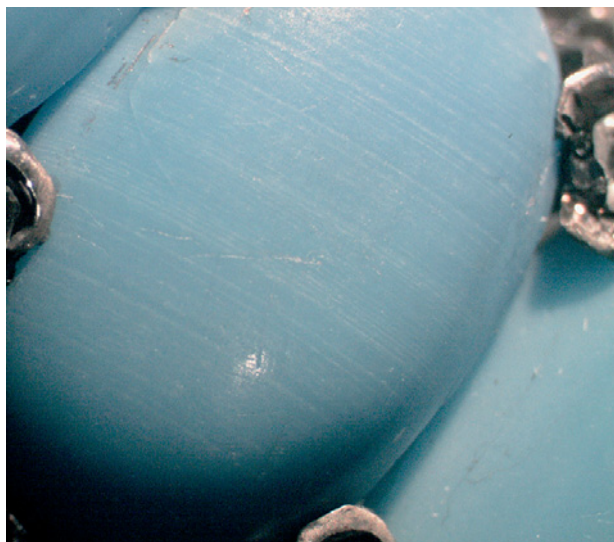


Figure 2. Micropores were observed on the surface of the odontolite cabochons. Photomicrograph by M. S. Krzemnicki; magnified 30x.

stones), turquoise (10), and artificial silica glass (15).

The odontolite cabochons all showed a microgranular surface covered with a dense pattern of micropores. These very tiny pores were either rounded in outline (figure 2) or occurred as longitudinal channels, depending on how they were intersected by the curved surface of the cabochon. On a macro scale, these cabochons often showed weak banding (figure 3), and in some cases a very distinct pattern of curved intersection banding (figure 4), described as

Figure 3. The odontolite displayed weak banding. Photomicrograph by M. S. Krzemnicki; magnified 15x.



characteristic for elephant, mammoth, and mastodon ivory (Campbell Pedersen, 2010).

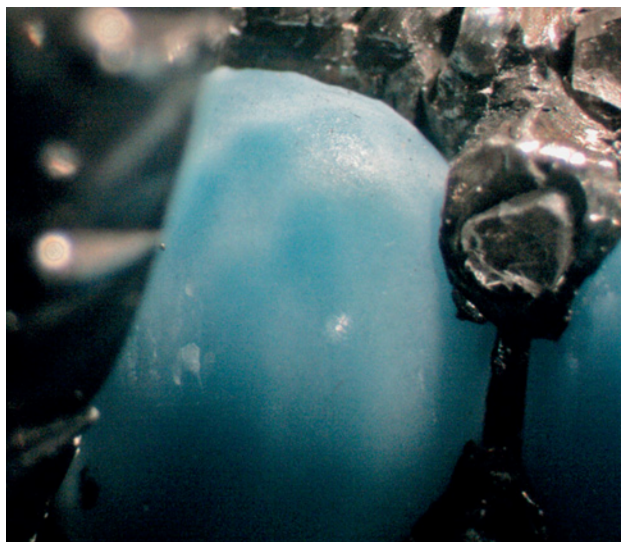
The Raman spectra of the odontolite revealed a distinct peak at 964 cm^{-1} and smaller peaks at about 1090 , 580 , and 430 cm^{-1} Raman shift (figure 5), and only a weak, broad OH band at about 3540 cm^{-1} . This pattern showed a perfect correlation with fluorapatite spectra taken from the SSEF reference mineral collection and with the published literature (Reiche et al., 2000; Campillo et al., 2010). EDXRF analyses of two cabochons confirmed their identity as apatite, revealing Ca and P as major elements and low concentrations of S, Cl, Sr, and Mn. Both analyses also revealed traces of Cu.

The turquoise cabochons showed a smoothly pol-

NEED TO KNOW

- Odontolite is fossilized dentine (mastodon ivory) from France that has been heat treated to produce its blue coloration.
- This historic turquoise substitute was identified in a set of six antique brooches set with diamonds.
- A combination of microscopic observation and Raman spectroscopy was effective for separating odontolite from the turquoise and artificial silica glass also present in the brooches.

Figure 4. Characteristic curved intersection bands were visible on several of the odontolite cabochons. Photomicrograph by M. S. Krzemnicki; magnified 20x.



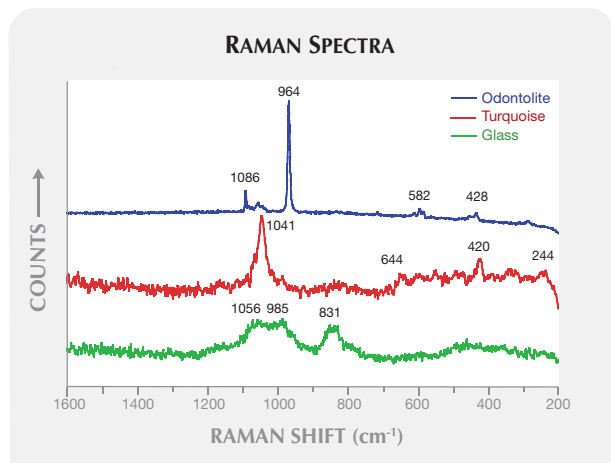


Figure 5. Raman spectra are shown for odontolite, turquoise, and blue silica glass.

ished surface and even color; some also had fine irregular brown veins (figure 6). They had a slightly more greenish blue color than the odontolite. Their Raman spectra were characterized by a general increase in Raman signal, with a distinct doublet at $\sim 1040\text{ cm}^{-1}$ Raman shift and a series of smaller peaks between 650 and 200 cm^{-1} , typical for turquoise. We found no peak in the $1800\text{--}1400\text{ cm}^{-1}$ range that would be expected for turquoise treated with wax and/or stabilized with artificial resin (Kiefert et al., 1999).

The silica glass cabochons showed a smooth surface, with some scratches and small but distinctly spherical gas bubbles (figure 7). They revealed only a very weak, indistinct Raman signal characterized by three broad bands at about 1060 , 985 , and 830 cm^{-1} , attributable to the Si-O vibrational modes of silica glass (McMillan, 1984).

DISCUSSION

The brooches exemplify the fashionable use of odontolite as a turquoise imitation in mid-19th century period jewelry. This was especially true in France, the source of the material.

Figure 8 shows the distribution of odontolite and turquoise in the largest brooch. It contained only seven pieces of turquoise, together with 87 odontolite cabochons. The turquoise specimens were small and rather hidden, whereas the odontolite occupied the most prominent positions. In contrast to the other brooches, we found no silica glass in this item. In general, the distribution of turquoise cabochons in the brooches seemed rather random, and three of the



Figure 6. Fine brown veins are visible in this turquoise specimen. The two neighboring cabochons are odontolite. Photomicrograph by M. S. Krzemnicki; magnified 15 \times .

pieces did not contain any turquoise at all.

Bennett and Mascetti (2003, p. 89) pictured an antique brooch set with diamonds and blue cabochons described as odontolite and turquoise. One of the cabochons in the photo shows a distinctly greenish blue color, suggesting to the present authors that it is turquoise, mixed with seven odontolite cabochons. We presume that mixing of these similar-looking materials was common at that time. It is not clear how much the jewelers actually knew about the materials they were using.

Figure 7. A gas bubble is apparent in this glass cabochon in one of the brooches. Photomicrograph by M. S. Krzemnicki; magnified 25 \times .

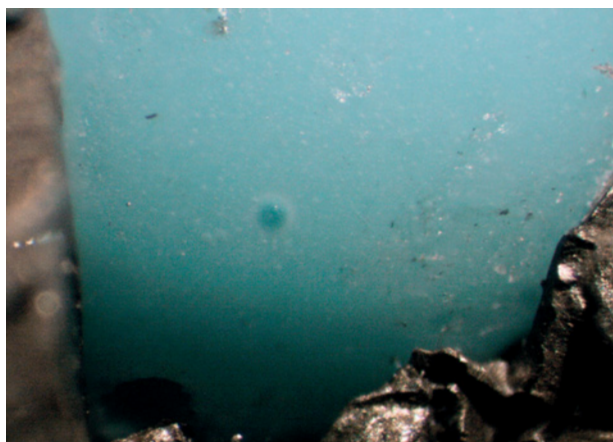
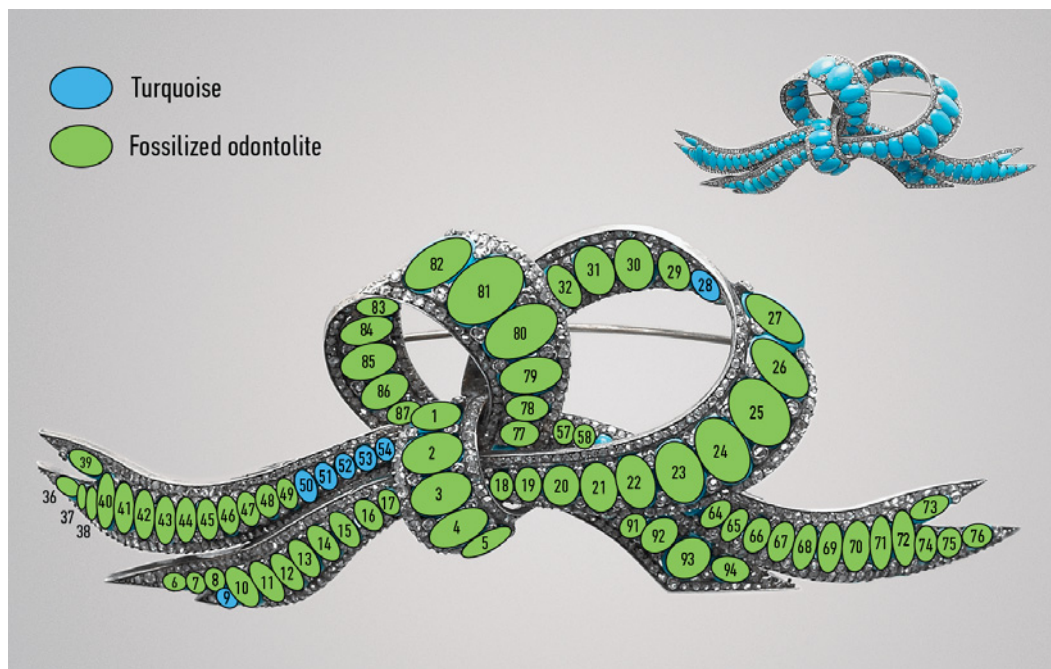


Figure 8. The largest brooch (~14 cm long) contained mostly odontolite with a few turquoise cabochons. Photo by M. S. Krzemnicki.



Based on its appearance and historical availability, we presume that the turquoise in this jewelry originated from classical sources in the Middle East, such as Persia. They showed no indications of any treatment (waxing, stabilization, or dyeing), as expected for the time period of the jewelry.

With its attractive light blue color, odontolite has been used as a turquoise simulant since the Middle Ages (Reiche et al., 2001). Although the heat-induced coloration was described in the early 18th century (Réaumur, 1715; Fischer, 1819), the cause of the blue color has been a subject of debate. Reiche et al. (2000, 2001) only recently showed that the oxidation of manganese traces within the fluorapatite during a heating process is responsible for the blue hue of the originally light gray odontolite. Using X-ray absorption spectroscopy, these authors found that heating to about 600°C under oxidizing conditions transforms octahedrally coordinated Mn^{2+} into tetrahedrally coordinated Mn^{5+} , which substitutes for phosphorous in the fluorapatite (Reiche et al., 2002).

The traces of Cu that we detected in the two odontolite cabochons using EDXRF spectroscopy may result from contamination during polishing.

There was no visual indication on any of the investigated samples of artificial blue color concentrations, as would be expected for dyeing with a copper-bearing solution (e.g., copper sulfate).

The glass imitations were uncommon in these brooches. Whether they were set during the crafting or during subsequent repair is not known. Similar glass, however, has a long history as a substitute (Hänni et al., 1998), and is often found in fashion jewelry from the 19th century.

CONCLUSIONS

What started as routine testing of a set of brooches ultimately shed light on the widespread use of a rare turquoise imitation—odontolite—in mid-19th century jewelry that was much in fashion in Western Europe. The odontolite cabochons were mixed with turquoise and also set with glass either at the manufacturing stage or during subsequent repair. The most useful approach to identifying these materials is a combination of microscopic observation and Raman spectroscopy. Both methods are fully nondestructive so they can be readily applied to valuable historic objects.

ABOUT THE AUTHORS

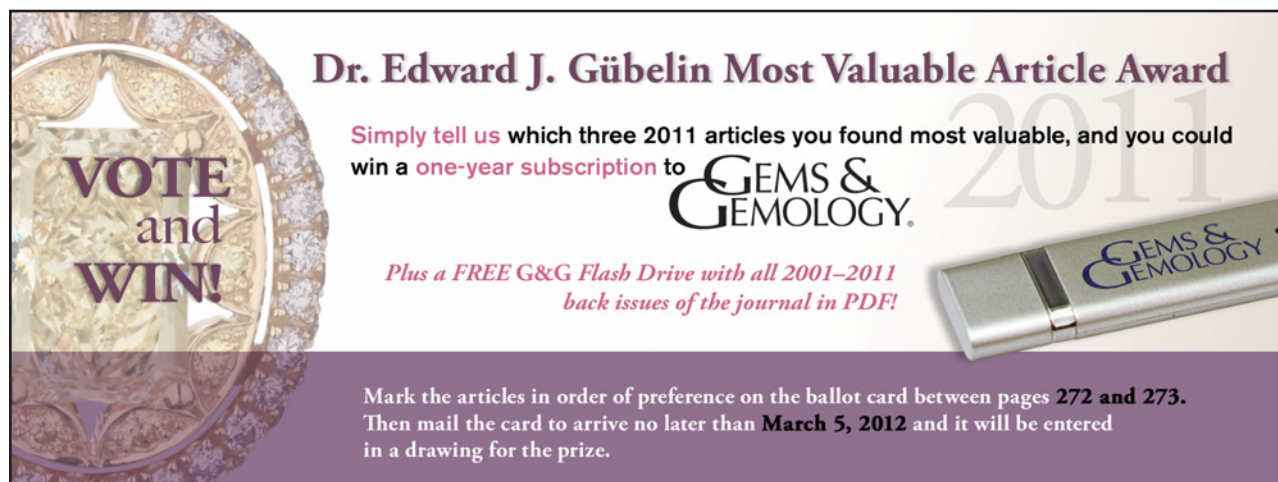
Dr. Krzemnicki (gemlab@ssef.ch) is director, Dr. Herzog is analytical technician, and Dr. Zhou is a gemologist at Swiss Gemmological Institute SSEF, Basel, Switzerland.

ACKNOWLEDGMENT

The authors thank Thomas and Ida Färber (Färber Collection, Geneva) for loaning these brooches for our research, and for fruitful discussions about these historic jewels.

REFERENCES

- Ahmed A. (1999) Türkis aus dem ägyptischen Sinai. *extraLapis* No. 16: *Türkise—Der Edelstein mit der Farbe des Himmels*, Christian Weise Verlag, Munich, Germany, pp. 76–81.
- Antoine P.-O., Duranthon F., Tassy P. (1997) L'apport des grandes mammifères (Rinocéros, Suoïdes, Proboscidiens) à la connaissance des gisements du Miocène d'Aquitaine (France). In J.-P. Aguilar, S. Legendre., and J. Michaux, Eds., *Actes du Congrès BiochoM'97*, Mémoires Travaux E.P.H.E., Institut Montpeillier, Vol. 21, pp. 581–591.
- Arnould H., Poirot J.-P. (1975) Infra-red reflection spectra of turquoise (natural and synthetic) and its substitutes. *Journal of Gemmology*, Vol. 14, pp. 375–377.
- Bennett D., Mascetti D. (2003) *Understanding Jewellery*. Antique Collectors Club Ltd., Woodbridge, Suffolk, England, 494 pp.
- Brown G. (2007) Rare ivories—Challenging identifications. Lecture presented at the Federal Conference of the Gemmological Association of Australia, Hobart, Tasmania, May 19, www.australiangemmologist.com.au/images/rareivories.pdf.
- Campbell Pedersen M. (2010) *Gem and Ornamental Materials of Organic Origin*. NAG Press, London.
- Campillo M., Lacharaise P.D., Reparaz J.S., Goni A.R., Valiente M. (2010) On the assessment of hydroxyapatite fluoridation by means of Raman scattering. *Journal of Chemical Physics*, Vol. 132, No. 24, article no. 244501 [5 pp.], <http://dx.doi.org/10.1063/1.3428556>.
- Chalker K., Dubin L.S., Whiteley P.M. (2004) *Totems to Turquoise: Native North American Jewelry Arts of the Northwest and Southwest*. Published in association with the American Museum of Natural History by Harry N. Abrams, New York, 224 pp.
- Crouzel F. (1957) Le Miocène continental du Bassin d'Aquitaine. *Bulletin du Service de la Carte Géologique de la France*, Vol. 54, No. 248, 264 pp.
- Crowningshield G.R. (1993) Gem Trade Lab Notes: Odontolite. *G&G*, Vol. 29, No. 2, p. 127.
- de La Brosse G. (1626) *Livre sur la Nature, vertu et Utilité des Plantes*. Bibliothèque Interuniversitaire de Médecine et d'Odontologie, Paris.
- Fischer G. (1819) Essay on the turquoise and the calcite. In T. Thomson, Ed., *Annals of Philosophy*, Vol. 14, pp. 406–420.
- Fryer C.W. (1983) Gem Trade Lab Notes: Turquoise imitation. *G&G*, Vol. 19, No. 2, p. 117.
- Hänni H.A., Schubiger B., Kiefert L., Häberli S. (1998) Raman investigations on two historical objects from Basel Cathedral: The Reliquary cross and Dorothy monstrance. *G&G*, Vol. 34, No. 2, pp. 102–113, <http://dx.doi.org/10.5741/GEMS.34.2.102>.
- Hurwit K.N. (1988) Gem Trade Lab Notes: Imitation turquoise with “veins” and pyrite. *G&G*, Vol. 24, No. 1, p. 52.
- Kane R.E. (1985) Gem Trade Lab Notes: Turquoise simulant, dyed magnesite. *G&G*, Vol. 21, No. 1, pp. 47–48.
- Kiefert L., Hänni H.A., Chalain J.-P., Weber W. (1999) Identification of filler substances in emeralds by infrared and Raman spectroscopy. *Journal of Gemmology*, Vol. 26, No. 8, pp. 501–520.
- Lind T., Schmetzer K., Bank H. (1983) The identification of turquoise by infrared spectroscopy and X-ray powder diffraction. *G&G*, Vol. 19, No. 3, pp. 164–168, <http://dx.doi.org/10.5741/GEMS.19.3.164>.
- McMillan P. (1984) Structural studies of silicate glasses and melts—Applications and limitations of Raman spectroscopy. *American Mineralogist*, Vol. 69, pp. 622–644.
- Réaumur R. (1715) Observations sur les mines de turquoises du royaume; sur la nature de la matière qu'on y trouve, et sur la manière dont on lui donne la couleur. *Mémoires de l'Académie Royale des Sciences*, pp. 174–202.
- Reiche I., Vignaud C., Menu M. (2000) Heat induced transformation of fossil mastodon ivory into turquoise ‘odontolite’: Structural and elemental characterisation. *Solid State Sciences*, Vol. 2, No. 6, pp. 625–636, [http://dx.doi.org/10.1016/S1293-2558\(00\)01067-0](http://dx.doi.org/10.1016/S1293-2558(00)01067-0).
- Reiche I., Vignaud C., Champagnon B., Panczer G., Brouder C., Morin G., Solé V.A., Charlet L., Menu M. (2001) From mastodon ivory to gemstone: The origin of turquoise color in odontolite. *American Mineralogist*, Vol. 86, pp. 1519–1524.
- Reiche I., Morin G., Brouder C., Solé V.A., Petit P.-E., Vignaudi C., Calligaro T., Menu M. (2002) Manganese accommodation in fossilised mastodon ivory and heat-induced colour transformation: Evidence by EXAFS. *European Journal of Mineralogy*, Vol. 14, pp. 1069–1073, <http://dx.doi.org/10.1127/0935-1221/2002/0014-10693>.
- Salanne C. (2009) Etude de la Turquoise, de ses Traitements et Imitations. Diplôme d'Université de Gemmologie, University of Nantes, France, 88 pp.



Dr. Edward J. Gübelin Most Valuable Article Award

Simply tell us which three 2011 articles you found most valuable, and you could win a one-year subscription to **GEMS & GEMOLOGY**.

Plus a FREE G&G Flash Drive with all 2001–2011 back issues of the journal in PDF!

Mark the articles in order of preference on the ballot card between pages 272 and 273. Then mail the card to arrive no later than **March 5, 2012** and it will be entered in a drawing for the prize.

THE RADIOACTIVE DECAY PATTERN OF BLUE TOPAZ TREATED BY NEUTRON IRRADIATION

Jian Zhang, Taijin Lu, Manjun Wang, and Hua Chen

A systematic study of 15 neutron-irradiated blue topaz samples was conducted using high-purity germanium (HPGe) digital gamma-ray spectroscopy. The specific activity of the detected radionuclides (^{134}Cs , ^{182}Ta , ^{46}Sc , and/or ^{160}Tb) was measured, and the decay pattern of the irradiated topaz was determined. Based on the time elapsed since their removal from the nuclear reactor, the amount of time required for the residual radioactivity to decay to safe levels was calculated. Most of the samples were safe at the time of the first measurement (95 days after irradiation), but higher concentrations of radionuclide impurities in some samples will require them to be quarantined for several years.

Radioactivity is one of the most discussed topics surrounding blue topaz (figure 1), which is commonly treated by irradiation from near-colorless starting material. To maintain consumer confidence, it is important to ensure that these gems do not contain dangerous levels of residual radioactivity. Three major irradiation methods are used: gamma (γ), neutron, and electron-beam irradiation (Nassau, 1985; Ashbaugh, 1988). Of these, neutron irradiation creates perhaps the most beautiful medi-

um blue color, called "London Blue." Unfortunately, this treatment also produces radioactivity from the nuclides of trace-element impurities in topaz (Crowningshield, 1981; Ashbaugh, 1988), such as Fe, Mn, Co, Zn, Sb, Ta, Cs, Sc, and Tb (Foord et al., 1988; Northrup and Reeder, 1994). These radioactive nuclides, which have various half-lives (table 1), may emit γ -rays and beta (β) particles of varying radiation intensity (Ashbaugh, 1991; Nelson, 1991). While a high dose of γ -rays and β -particles poses danger, a very low dose is not harmful. Therefore, blue topaz colored by neutron irradiation requires a quarantine period to allow the residual radioactivity to reach a safe level (referred to, e.g., as the exemption level) of less than 74 becquerels per gram (Bq/g) or 2 nanocuries per gram (nCi/g; Ashbaugh, 1988).

Investigations of blue topaz have focused mainly on irradiation methods and the cause of the coloration, with less emphasis on the detection of residual radioactivity. Ashbaugh (1988) discussed the radioactivity of colored stones treated by irradiation, as well as potential health hazards and government regulations. Based on these findings, GIA offered testing services for irradiated gems from 1991 through 2006. However, that article did not address blue topaz treated by neutron irradiation. Guo et al. (2000) measured the specific activity of the total alpha (α) and β radioactivity of crushed blue topaz after irradiation using an FJ-2603 low-level α - and β -radiation measuring device and a BH1216A low-background measuring instrument. While that effort was helpful in exploring the radioactive decay of irradiated blue topaz, the specific nuclides involved were not determined. Helal et al. (2006) analyzed the trace elements in topaz samples before and after neutron irradiation using ICP-MS and a high-purity germanium (HPGe) detector. This study proved that radioactivity in blue topaz colored by neutron irradiation is related to variations in the trace elements in the topaz. However, the decay pattern of the radionuclides was unclear. This article studies the residual radioactivity in blue topaz treated by neutron irradiation, identifies the specific radionuclides

See end of article for About the Authors and Acknowledgments.

GEMS & GEMOLOGY, Vol. 47, No. 4, pp. 302–307,
<http://dx.doi.org/10.5741/GEMS.47.4.302>.

© 2011 Gemological Institute of America



Figure 1. Most blue topaz on the market is irradiated to enhance its color. These stones (~4–10 ct) were treated by neutron irradiation. Photo by J. Zhang.

TABLE 1. Half-lives of radioactive nuclides in irradiated blue topaz.

Radionuclide	Half-life (days)
⁵⁹ Fe	44.51
¹²⁴ Sb	60.20
¹⁶⁰ Tb	72.30
⁴⁶ Sc	83.81
¹⁸² Ta	114.4
⁶⁵ Zn	243.8
⁵⁴ Mn	312.2
¹³⁴ Cs	753.7
⁶⁰ Co	1,924

involved, and calculates quarantine periods for the most highly radioactive samples to reach the exemption level.

MATERIALS AND METHODS

Fifteen samples of cut but unpolished near-colorless topaz (weighing 0.75 to ~2.0 g) of pegmatite origin from China's Guangdong Province were studied. EDXRF chemical analy-

sis was performed on all 15 samples (after irradiation) and on one additional untreated sample from the same locality, using an ARL Quant'X spectrometer at the National Gemstone Testing Center in Beijing.

The important color centers in topaz are produced after 12 hours of irradiation at 1.2×10^{19} neutrons/(cm² × sec). These conditions were used in this study to produce the colors shown in figure 2. The irradiation was conducted in a "light water" (ordinary water) nuclear reactor at the China Institute of Atomic Energy in Beijing. The samples were placed in cadmium-lined containers to reduce the amount of the thermal neutrons caused by absorption, and also to increase the amount of the fast, color-producing neutrons.

A GEM-30185-Plus Despec HPGe digital gamma-ray spectrometer (figure 3) was used to measure the residual radioactivity of the irradiated blue topaz. The Ge semiconductor detector had a relative efficiency of 25%, an energy resolution of 1.96 keV at 1332.5 keV for ⁶⁰Co, and a peak ratio of 48. The values measured represent the combined radioactivity of specific nuclides in the process of decay. The measurements were semiquantitative, obtained for 40,000 seconds of active time.



Figure 2. These irradiated topaz samples (weighing 0.75 to ~2.0 g) were used in this study. From left to right, the top row shows samples numbered Topaz-1 to Topaz-7, and the bottom row shows Topaz-8 to Topaz-15. Photo by J. Zhang.



Figure 3. The HPGe digital spectrometer at the China Institute of Atomic Energy in Beijing was used in this study. Photo by J. Zhang.

To explore the decay pattern of the irradiated blue topaz, we conducted four measurements of the residual radioactivity in the 15 samples. The samples were removed from the reactor on September 28, 2005, and gamma-ray spectroscopy was subsequently performed on January 1, 2006 (day 95); March 14 (day 167); April 19 (day 203); and November 30 (day 428). We tested all samples at day 95, and then focused on four samples (figure 4) with residual radioactivity higher than the exemption value (74 Bq/g).

TABLE 2. Residual radioactivity (Bq/g) of irradiated blue topaz samples after four periods of decay.^a

Sample no.	Nuclide	Decay time (days)			
		95	167	203	428
Topaz-8	¹³⁴ Cs	417.6	392.1	379.2	309.3
	¹⁸² Ta	19,800	12,800	10,290	2,668
	Total	20,218	13,192	10,669	2,977
Topaz-9	¹³⁴ Cs	1,617	1,512	1,462	1,187
	⁴⁶ Sc	296.3	162.1	120.7	18.4
	¹⁸² Ta	495.9	321.1	258.1	66.8
	Total	2,409	1,996	1,840	1,273
Topaz-10	¹⁸² Ta	195,000	125,800	100,800	25,750
	Total	195,000	125,800	100,800	25,750
Topaz-15	¹³⁴ Cs	106.2	100.2	96.5	78.7
	⁴⁶ Sc	237.9	132.1	98.6	15.0
	¹⁶⁰ Tb	3,909	1,961	1,389	160.5
	Total	4,253	2,193	1,585	254.2

^a Although Fe was detected in the samples by EDXRF analysis, no iron radionuclides were detected by gamma-ray spectroscopy.

RESULTS AND DISCUSSION

EDXRF spectroscopy showed traces of Mg, Ca, Na, K, and Cl in all samples, while Fe, Cs, Sr, Sc, Ta, and Tb were detected in some of them. Gamma-ray spectroscopy revealed the variable presence of four radionuclides in the irradiated topaz: ¹³⁴Cs, ¹⁸²Ta, ⁴⁶Sc, and/or ¹⁶⁰Tb (table 2). When the samples were first tested 95 days after irradiation, four of them showed residual radioactivity above the exemption level. The residual radioactivity of the other 11 samples had decayed below the exemption level or the detection limit of the spectrometer.

NEED TO KNOW

- Neutron irradiation is commonly used to create an attractive “London Blue” color in near-colorless topaz.
- Topaz may contain trace impurities that become radioactive after neutron irradiation.
- Gamma-ray spectroscopy showed that irradiated topaz samples from China contained up to four radionuclides.
- Most of the samples were safe to handle when measured 95 days after irradiation, but some will require several years to “cool down.”

The goal of studying the decay pattern of irradiated blue topaz is to determine the time needed for the residual radioactivity to decay to a safe level (Miraglia, 1986; Miraglia and Cunningham, 1988). The half-life decay formula of radioactive nuclides is necessary for these calculations. De Soete et al. (1972) defined the formula as follows: If the probability of decay for radioactive elements in unit time is $1/\tau$, and if the number of radioactive elements is N , then the number of decayed radioactive elements in the time span of dt should be dN , where

$$dN/N = -1/\tau dt \quad (1)$$

In formula (1), the negative sign indicates a reduction in the number of subatomic particles that constitute ionizing radiation. Integrating both sides of the equation yields:

$$N = N_0 e^{-t/\tau} \quad (2)$$

In formula (2), N_0 is the original value of radioactivity from a given nuclide, and τ represents the decay time constant, after which the element has been reduced to e^{-1} of the original value of radioactivity. The relationship between τ and half-life ($T_{1/2}$) can be expressed as:

$$T_{1/2} = 0.693\tau \quad (3)$$

Applying formula (3) to formula (2), we can derive the half-life decay formula of radioactive nuclides:

$$N = N_0 e^{-0.693t/T_{1/2}} \quad (4)$$



Figure 4. These four samples (9.5–16.5 mm long) had residual radioactivity higher than the exemption level when initially measured after 95 days. From left to right: Topaz-8, Topaz-9, Topaz-10, and Topaz-15. Photo by J. Zhang.

In formula (4), N_0 is the initial value of radioactivity and N is the unknown value of radioactivity, expressed in units of Bq. $T_{1/2}$ is the half-life of the nuclide, and t is its decay time.

The specific activity of each radionuclide present in a given sample was calculated. The values obtained at the first stage of radiation detection (after 95 days) can be set as the initial values. Values for each subsequent stage can then be calculated and compared with the detected values, as shown in table 3. In addition, the radioactivity of the samples upon their removal from the reactor (day 0) can be

calculated. Most importantly, the time required for the residual radioactivity to decay below the exemption level (74 Bq/g) can be derived using the formula; these times are shown in table 4 for the four samples.

CONCLUSIONS

Blue topaz (e.g., figure 5) typically takes two to three years to decay below the exemption level after neutron irradiation. The actual quarantine time necessary for specific samples depends on several factors. There are three scenarios that can contribute to high levels of residual radioactivity in irradiated gems.

The first is the presence of activated impurities with a long half-life (i.e., a comparatively slow rate of decay). For example, ^{134}Cs has a half-life of 2.06 years. This radionuclide was present in three of the four topaz samples showing residual radioactivity, and for Topaz-9 the time required to decay below the exemption level was calculated at 3,440 days (~9.4 years).

Second, high concentrations of activated impurities (even those that do not have a long half-life) may produce high residual radioactivity. Sample Topaz-10, for example, contained a large amount of ^{182}Ta (half-life of 114 days). Consequently, the sample's radioactivity upon removal from the reactor was 347,600 Bq/g, and it took 1,391 days (~3.8 years) for the sample to decay below the exemption level.

The third scenario contributing to high levels of residual

TABLE 3. Detected and calculated specific activity (Bq/g) of radionuclides in irradiated blue topaz.

Sample no.	Nuclide	Method	Decay time (days)				
			0	95	167	203	428
Topaz-8	^{134}Cs	Detected		417.6	392.1	379.2	309.3
		Calculated	455.8		390.8	378.0	307.2
	^{182}Ta	Detected		19,800	12,800	10,290	2,668
		Calculated	35,280		12,780	10,270	2,664
Topaz-9	^{134}Cs	Detected		1,617	1,512	1,462	1,187
		Calculated	1,764		1,513	1,464	1,190
	^{46}Sc	Detected		296.3	162.1	120.7	18.4
		Calculated	650.0		163.4	121.3	18.9
	^{182}Ta	Detected		495.9	321.1	258.1	66.8
		Calculated	877.7		320.1	257.2	66.5
Topaz-10	^{182}Ta	Detected		195,000	125,800	100,800	25,750
		Calculated	347,600		125,900	101,100	25,770
Topaz-15	^{134}Cs	Detected		106.2	100.2	96.5	78.7
		Calculated	115.7		99.2	96.0	78.0
	^{46}Sc	Detected		237.9	132.1	98.6	15.0
		Calculated	521.8		131.1	97.4	15.1
	^{160}Tb	Detected		3,909	1,961	1,389	160.5
		Calculated	9,717		1,960	1,388	160.6

TABLE 4. Decay time needed for irradiated blue topaz samples to reach the exemption level of 74 Bq/g.

Sample no.	Nuclide	Decay time (days)						
		0	95	428	703	1,391	1,975	3,440
Topaz-8	¹³⁴ Cs	455.8	417.6	309.3	238.4	139.8	73.8	
	¹⁸² Ta	35,280	19,800	2,668	491.5	14.5	0.2	
	Total	35,736	20,218	2,997.3	729.9	154.3	74.0	
Topaz-9	¹³⁴ Cs	1,764	1,617	1,187.3	922.5	540.7	285.6	74.0
	⁴⁶ Sc	650.0	296.3	18.4	1.9	0	0	0
	¹⁸² Ta	877.7	495.9	66.8	12.2	0.4	0	0
	Total	3,291	2,409	1,272	936.6	541.1	285.6	74.0
Topaz-10	¹⁸² Ta	347,600	195,000	25,750	4,843	73.9		
	Total	347,600	195,000	25,750	4,843	73.9		
Topaz-15	¹³⁴ Cs	115.7	106.2	78.7	60.5			
	⁴⁶ Sc	521.8	237.9	15.0	1.6			
	¹⁶⁰ Tb	9,717	3,909	160.5	11.5			
	Total	10,350	3,434	254.2	73.6			



radioactivity is the presence of activated impurities with a long half-life combined with relatively high concentrations.

The Chinese topaz studied for this article should be assumed to contain different trace-element impurities than starting material from other sources (e.g., Brazil), and therefore the decay times presented in this study are not representative of all neutron-irradiated topaz on the market. Still, the procedure and data presented here provide useful information for evaluating the residual radioactivity in topaz treated by neutron irradiation, regardless of locality.

Figure 5. Treated blue topaz (here, 85.79–243.66 ct) is commonly encountered in the global gem market, and neutron-irradiated samples must undergo appropriate safeguards to ensure that they do not contain dangerous levels of residual radioactivity. Photo by Robert Weldon; from top to bottom, GIA Collection nos. 16203, 30886, 31942, 30889, and 31947.

ABOUT THE AUTHORS

Mr. Zhang (zj7975@sina.com) is an engineer, Dr. Lu is chief researcher, Ms. Wang is a professor, and Ms. Chen is director of the research department, at the National Gems & Jewellery Technology Administrative Center, in Beijing, China.

ACKNOWLEDGMENTS

The authors thank Ms. Xiuqing Gao for irradiating the topaz samples, and Mr. Yongbao Gao for performing the gamma-ray spectroscopy; both are located at the China Institute of Atomic Energy in Beijing.

REFERENCES

- Ashbaugh C.E. (1988) Gemstone irradiation and radioactivity. *G&G*, Vol. 24, No. 4, pp. 196–213, <http://dx.doi.org/10.5741/GEMS.24.4.196>.
- Ashbaugh C.E. III (1991) Radioactive and radiation treated gemstones. *Radioactivity & Radiochemistry*, Vol. 2, No. 1, pp. 42–57.
- Crowningshield R. (1981) Irradiated topaz and radioactivity. *G&G*, Vol. 17, No. 4, pp. 215–217, <http://dx.doi.org/10.5741/GEMS.17.4.215>.
- Foord E.E., Jackson L.L., Taggart J.E., Crock J.G., King T.V.V. (1988) Topaz: Environments of crystallization, crystal chemistry, and infrared spectra. *Mineralogical Record*, Vol. 26, pp. 69–70.
- Guo Y.C., Liu X.L., Huang J.Z. (2000) Radioactivity and decay pattern of topaz colored by neutron radiation. *China Occupational Medicine*, Vol. 27, No. 2, pp. 19–21 [in Chinese].
- Helal A.I., Zahran N.F., Goma M.A.M., Salama S. (2006) Irradiated topaz in the reactor. *VIII Radiation Physics & Protection Conference*, Beni Suef - Fayoum, Egypt, November 13–15, pp. 447–451.
- Miraglia F.J. (1986) Distribution of Products Irradiated in Research Reactors. U.S. Nuclear Regulatory Commission Generic Letter 86-11, June 25.
- Miraglia F.J., Cunningham R.E. (1988) Distribution of Gems Irradiated in Research Reactors. U.S. Nuclear Regulatory Commission Generic Letter 88-04, February 23.
- Nassau K. (1985) Altering the color of topaz. *G&G*, Vol. 21, No. 1, pp. 26–34, <http://dx.doi.org/10.5741/GEMS.21.1.26>.
- Nelson K.L. (1991) Health Risk Assessment of Irradiated Topaz. Unpublished PhD thesis, University of Minnesota.
- Northrup P.A., Reeder R.J. (1994) Evidence for the importance of growth-surface structure to trace element incorporation in topaz. *American Mineralogist*, Vol. 79, pp. 1167–1175.
- de Soete D., Gijbels R., Hoste J. (1972) *Neutron Activation Analysis*. John Wiley & Sons, New York.

THANK YOU, REVIEWERS



GEMS & GEMOLOGY requires that all articles undergo a peer review process in which each manuscript is evaluated by at least three experts in the field. This process is vital to the accuracy and readability of the published article. Because members of our Editorial Review Board cannot have expertise in every area, we sometimes call on other experts to share their intellect and insight. In addition to the members of our Editorial Review Board, we extend a heartfelt thanks to the following individuals who reviewed manuscripts for *G&G* in 2010–2011.

Dr. Ilaria Adamo * Dr. Vladimir Balitsky * Dudley Blauwet * Bill Boyajian * Dr. Christopher M. Breeding * Maggie Campbell-Pedersen * Dr. Francois Farges * Dr. David Fisher * Dr. Harald Gabasch * Dr. Eloïse Gaillou * Rui Galopim de Carvalho * Al Gilbertson * Dr. Gaston Giuliani * Dr. Lee Groat * Dr. John Gurney * Thomas Hain-schwang * Hertz Hasenfeld * Richard Hughes * Dr. Stefanos Karampelas * John King * William Larson * Elise Misiorowski * Vincent Pardieu * Dr. Adolf Peretti * Dr. Federico Pezzotta * John Pollard * Dr. Ilene Reinitz * Dr. Benjamin Rondeau * Dr. Andy Shen * Russell Shor * Elisabeth Strack * Carol Stockton * Ursula Wehrmeister

EDITORS

Thomas M. Moses | Shane F. McClure | GIA Laboratory

DIAMOND

A Rare Fancy Vivid Purple Diamond

In GIA's colored diamond grading system, predominantly purple diamonds can occur in the red-purple, reddish purple, and purple hue ranges. While none of these are common, diamonds in the unmodified purple range are the rarest.

GIA first encountered purple diamonds in the 1970s. Their color is due to plastic deformation of the crystal structure that occurred during their geologic history, resulting in parallel glide planes (referred to as *graining*). This graining exhibits pink and brown dichroism, observed under magnification (see S. Titkov et al., "Natural-color purple diamonds from Siberia," Spring 2008 *G&G*, pp. 56–63). It is extremely rare to see a pure purple hue resulting from such plastic deformation.

The New York laboratory recently had the opportunity to examine a 0.81 ct purple diamond with unusually strong color (figure 1). The cut-cornered rectangular modified brilliant was faceted so the graining reflected the purple color throughout the stone, maximizing its intensity. With magnification and diffused lighting, well-defined parallel glide planes were vis-



Figure 1. This extremely rare 0.81 ct diamond was color graded Fancy Vivid purple.

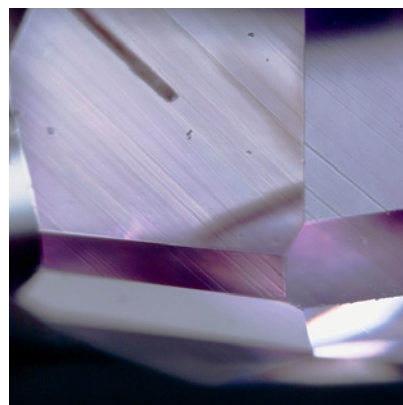
ible through the pavilion (figure 2). These planes showed a strong concentration of purple color, while the surrounding area appeared nearly colorless. The stone fluoresced weak yellow to long-wave UV radiation and was inert to short-wave UV. Under the very strong short-wave UV of the DiamondView, the glide planes displayed clear green fluorescence, which is attributed to the localized distribution of the H3 optical center. The H3 center was also present in the UV-Vis absorption spectrum taken at liquid-nitrogen temperature, along with a strong absorption band centered at ~550 nm, which clearly contributed to the predominantly purple

color. FTIR spectroscopy showed the diamond was a type IaA with a very high concentration of aggregated nitrogen, predominantly in the A form. We also noted a very weak absorption at 3107 cm^{-1} , attributed to hydrogen.

The outstanding feature of this diamond was its depth of color, which placed it in the Fancy Vivid range. On the rare occasions the lab has seen purple diamonds, they typically have a dark or unsaturated color, resulting in color grades modified by "gray" or "grayish." It is unusual for GIA to encounter more than a handful of purple diamonds, regardless of their depth of color, in any given year. The rarity is exponentially greater for a diamond with a very strong purple hue.

Jason Darley, Paul Johnson, and John King

Figure 2. The purple coloration in the diamond was concentrated along parallel glide planes. Magnified 60 \times .



Editors' note: All items were written by staff members of the GIA Laboratory.

GEMS & GEMOLOGY, Vol. 47, No. 4, pp. 308–315, <http://dx.doi.org/10.5741/GEMS.47.4.308>.

© 2011 Gemological Institute of America

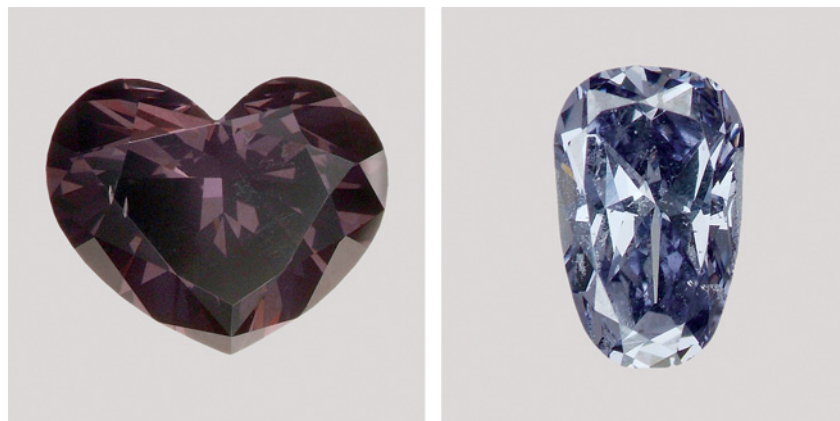


Figure 3. These two diamonds, a 0.85 ct Fancy black heart shape (left) and a 0.20 ct Fancy grayish blue modified pear shape (right), had similar hydrogen-related spectroscopic properties but dramatically different color.

A Strongly Purple-Colored Black Diamond

Hydrogen-rich diamonds with gray to blue to violet colors are rare, but they are well documented in the literature (see, e.g., C. H. van der Bogert et al., “Gray-to-blue-to-violet hydrogen-rich diamonds from the Argyle mine,

Australia,” Spring 2009 *G&G*, pp. 20–37). The New York lab recently tested such a diamond with an unusually dark tone.

The 0.85 ct type Ia heart shape (figure 3, left) showed extremely strong hydrogen-related features (e.g., 3107 cm^{-1}) in its mid-infrared absorption spectrum. The high concentra-

tion of hydrogen produced such a dark appearance that the diamond received a Fancy black color grade.

We compared this heart shape to a 0.20 ct modified pear shape (figure 3, right) with similar overall spectroscopic properties, also type Ia, that received a Fancy grayish blue color grade. In this diamond, however, the hydrogen impurity did not cause such a strong absorption. The difference between the two stones was also clearly displayed in their Vis-NIR absorption spectra in the 400–900 nm range. Both showed typical absorptions for gray to blue to violet diamonds, such as bands near 500 and 700 nm, attributed to hydrogen. The much stronger absorption in the heart shape blocked most of the light return, making it appear virtually black. Its spectrum was very noisy because of the absorbance, and the spectrometer detected only a very weak signal (figure 4). Only with magnification and fiber-optic illumination could we observe fine clouds associated with hydrogen in such diamonds (figure 5); the stone’s true deep purple bodycolor was also seen.

This rare diamond provides a good example of an extreme end of the color range of hydrogen-rich diamonds, in which the purple color was so deep that the stone appeared black.

Paul Johnson

Figure 4. The Vis-NIR absorption spectrum of the Fancy black heart shape showed a weak signal and significant noise.

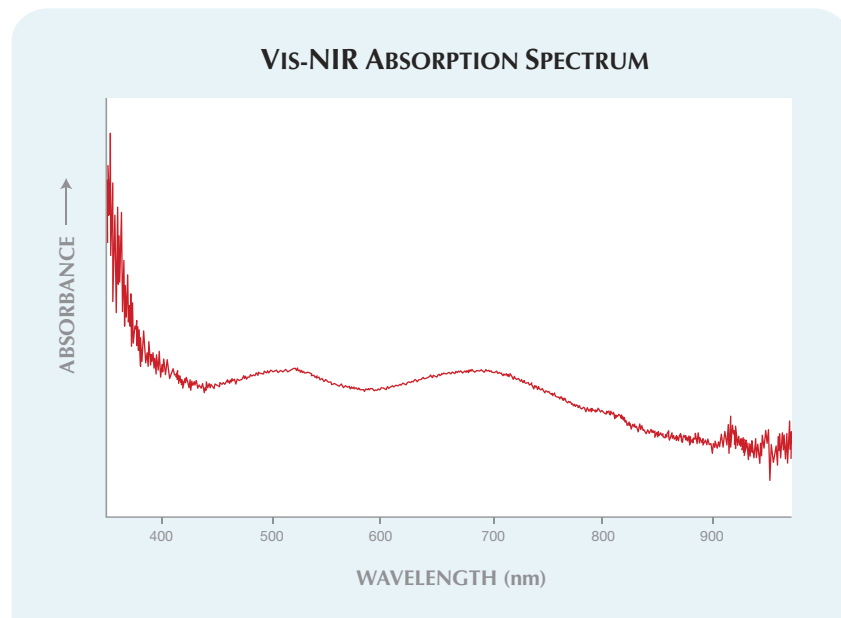


Figure 5. With magnification and fiber-optic illumination, the heart-shaped diamond’s deep purple bodycolor became apparent.



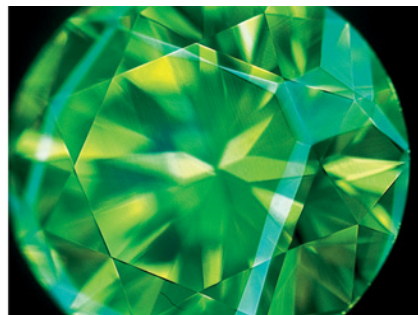
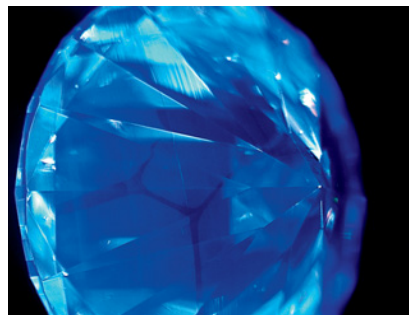


Figure 6. In the DiamondView, this 0.99 ct HPHT-treated diamond (left) shows four-fold symmetry that appears similar to the cross pattern typically encountered in HPHT synthetics (right, 1.00 ct).

HPHT-Treated Diamond with the Fluorescence Pattern of an HPHT-Grown Synthetic

Synthetic diamonds grown at high-pressure, high-temperature (HPHT) conditions are no longer rare in the market. One method to distinguish them from natural diamonds is imaging their growth patterns with ultraviolet-activated fluorescence, such as with the DiamondView instrument.

The growth structure of HPHT synthetics is typically quite distinctive and, in most cases, eloquently displayed in their fluorescence images. Because HPHT synthetic diamonds form under different conditions than their natural counterparts, the growth rates of their various crystal faces are generally quite different. The resulting morphology of HPHT products is typically cubo-octahedral, whereas natural diamonds grow as octahedra. The overwhelming majority of HPHT synthetics show a diagnostic cross shape in their luminescence pattern. Sometimes, however, natural diamonds exhibit four-fold symmetry that may be confused with this cross pattern.

One such instance was seen recently in the Carlsbad laboratory. A 0.99 ct F-color type IIa round brilliant underwent advanced testing to determine if it was natural, treated, or synthetic. The stone's DiamondView image (figure 6, left) showed a configuration resembling the cross pattern (figure 6, right), and its photoluminescence (PL) spectra indicated the

sample had been subjected to HPHT conditions, therefore suggesting it was an HPHT-grown synthetic. Nevertheless, microscopic examination with crossed polarizers revealed a mottled strain pattern typical of natural type IIa diamonds (figure 7), and additional peaks in the PL spectra confirmed it was an HPHT-treated natural diamond.

DiamondView imaging can be diagnostic for synthetic diamonds, particularly those of HPHT origin. But careful consideration of both DiamondView images and spectral data (particularly PL) is usually necessary to definitively identify natural or synthetic origin. The cross-shaped growth pattern in the present diamond may be due to formation under different conditions (i.e., lower temperatures) than those typically experienced by natural diamonds, which led

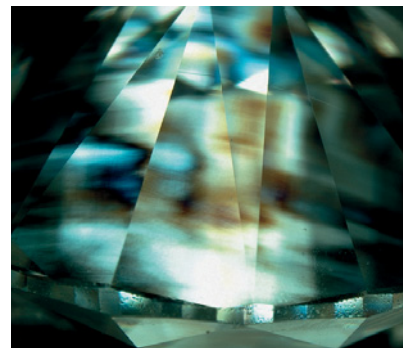


Figure 7. The HPHT-treated diamond's mottled strain pattern indicated natural origin. Image width: 4.35 mm.

to its altered morphology. The fact that this diamond was chosen for HPHT treatment was an interesting coincidence.

Sally Eaton-Magaña

Type IIb Diamond with Long Phosphorescence

It is well known that type II synthetic diamonds and some natural diamonds (including type IIb) are phosphorescent. In natural diamonds the effect usually lasts for only a few seconds. However, a 4.23 ct emerald cut (figure 8) recently submitted to the Carlsbad laboratory proved to be an exception. Identified as an untreated type IIb diamond with D color and IF clarity, it

Figure 8. This 4.23 ct type IIb diamond is shown before (left) and after (right) exposure to short-wave UV radiation for 10 seconds. The photo on the right shows the diamond's strong blue phosphorescence.



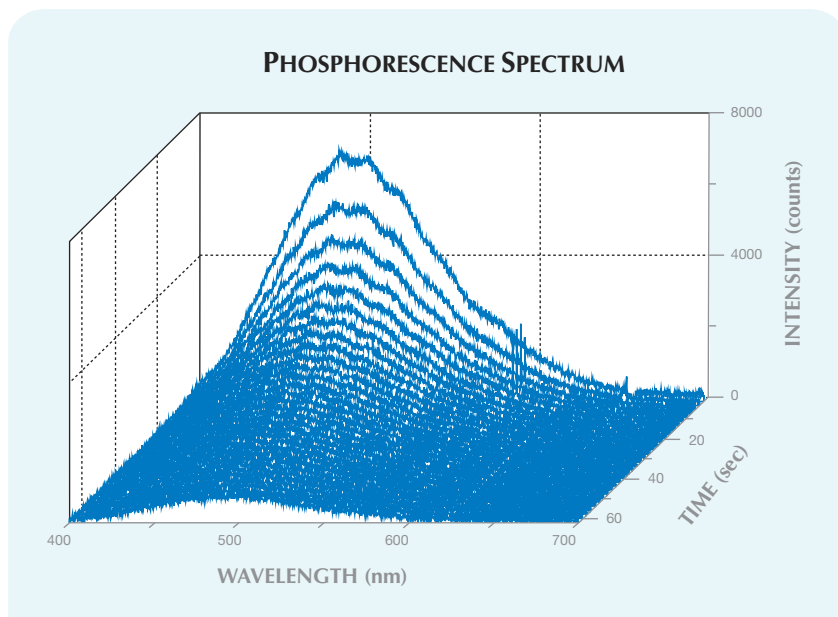


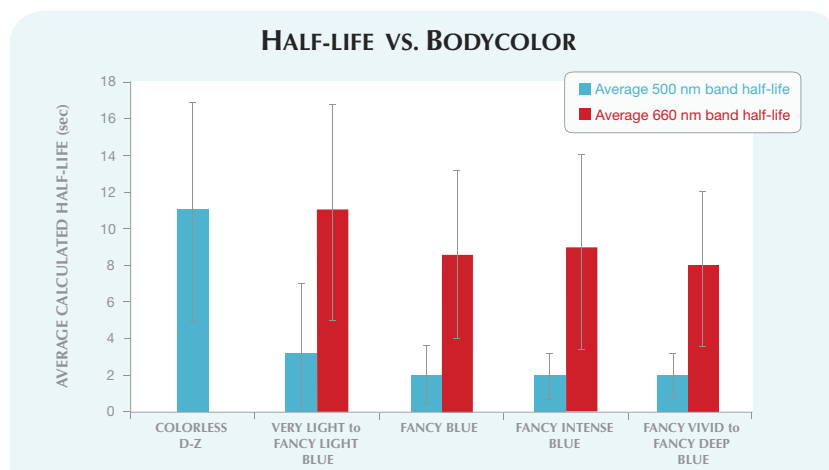
Figure 9. The three-dimensional spectral plot for the diamond in figure 8 shows its long-lasting phosphorescence corresponding to the 500 nm band. The diamond was exposed to UV radiation for 20 seconds and data were collected over one second intervals.

displayed very weak to weak greenish blue fluorescence to long- and short-wave UV radiation. During UV exposure, the fluorescence appeared to intensify due to the sample's strong phosphorescence. After 5 seconds of exposure to short-wave UV radiation, the diamond displayed bright blue phosphorescence (see video in the *G&G* Data Depository at gia.edu/gandg), and it continued to luminesce for several minutes.

Phosphorescence spectroscopy revealed a band at 500 nm (also documented in type IIb diamonds by S. Eaton-Magaña et al., "Luminescence of the Hope diamond and other blue diamonds," Fall 2006 *G&G*, pp. 95–96) that was responsible for the blue phosphorescence. Figure 9 shows the spectra collected over a period of 60 seconds in a three-dimensional plot. At the end of 60 seconds, the 500 nm phosphorescence band was still visible. The calculated half-life of this band was 8.4 seconds. By comparison, the Hope diamond's 500 nm band half-life is only 1.8 seconds (S. Eaton-

Magaña et al., "Using phosphorescence as a fingerprint for the Hope

Figure 10. Data compiled for 300 natural type IIb diamonds show variations in the average half-life of phosphorescence bands (with error bars showing standard deviations) at 500 and 660 nm according to their bodycolor. Colorless type IIb diamonds generally do not show a red phosphorescence band at 660 nm, and their blue 500 nm band has a long half-life. Type IIb diamonds with stronger blue coloration have both 500 and 660 nm bands, and the half-life of their blue phosphorescence is much shorter.



and other blue diamonds," *Geology*, Vol. 36, No. 1, 2008, pp. 83–86). Figure 10 shows the relationship between apparent bodycolor and phosphorescence half-life in 300 natural type IIb diamonds examined in the GIA laboratory. The present diamond's 500 nm band had a much longer half-life and a stronger intensity than most natural type IIb diamonds; this combination produced the unusually long phosphorescence.

This diamond also exhibited thermoluminescence, as described in the Spring 2011 Lab Notes (pp. 50–51). It was immersed in a liquid-nitrogen bath (-196°C) and simultaneously exposed to short-wave UV. After removal from the bath, it warmed up rapidly and displayed a flash of blue thermoluminescence. After a few seconds of additional warming, it exhibited the long-lasting phosphorescence described above. A second video documenting both luminescence behaviors is available in the *G&G* Data Depository.

Andy H. Shen and
Sally Eaton-Magaña

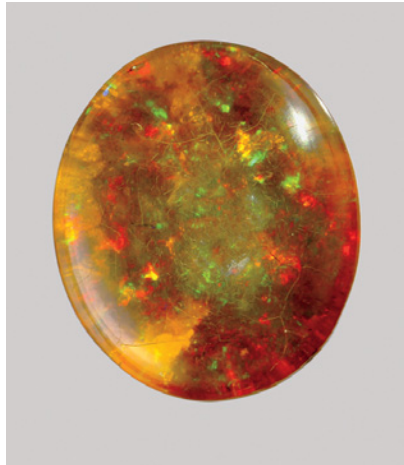


Figure 11. This 67.17 ct opal was clarity enhanced with some type of oil.

OPAL

Clarity-Enhanced, with Artificial Matrix

The Carlsbad laboratory recently received a 67.17 ct opal cabochon (figure 11) for identification. The stone showed an orangy yellow bodycolor and moderate play-of-color. It also had an unusual mottled gray “matrix” on the back and felt slightly greasy to the touch. In reflected light, a network of fine lines on the surface revealed a large amount of crazing, but these lines were not easily seen upon initial examination.

Gemological examination produced measurements consistent with

natural opal. The refractive index was 1.45, but we did not test specific gravity because of the presence of the “matrix.” The sample was inert to long-wave UV radiation and gave a weak greenish yellow reaction to short-wave UV. Notably, the fractures fluoresced weak yellow to both long- and short-wave UV.

Microscopic examination revealed a somewhat columnar structure and bodycolor similar to material from Wollo Province, Ethiopia. A dense network of very low-relief fractures was also seen throughout the stone; their subtle appearance immediately suggested clarity enhancement. Closer examination showed flattened gas bubbles in many of the fractures from incomplete filling (figure 12, left). When exposed to a relatively low temperature thermal probe, the fractures began to sweat (figure 12, right). Because of the mobile nature of the clarity enhancing substance, we concluded that the stone was treated with some variety of oil rather than an epoxy resin.

The “matrix” on the back of the cabochon consisted of a hard gray resin-like material that showed swirl marks and also some grinding marks, indicating it had been applied during or after the lapidary process. This layer added significant weight and likely helped hold the highly fractured stone together.

While we do not know for certain if this stone was from the Wollo

deposit, this seems likely given its appearance and the high volume of material recently mined there. Although this opal did not show hydrophane character, in one of these contributors’ (NR) experience, not all Wollo opal is hydrophane type. In addition, some of the orangy yellow Wollo opal seems to be prone to crazing.

As with any new source, artificially enhanced lesser-quality material will eventually make its way to the market as treatments are developed to create salable products. Even though very high-quality untreated Ethiopian opal is readily available, buyers should be aware that an increasing amount of treated material is appearing in the trade, including clarity-enhanced samples such as this one and others subjected to forms of color modification (see, e.g., N. Renfro and S. F. McClure, “A new dyed purple opal,” www.gia.edu/research-resources/news-from-research). As with all treatments, these are acceptable as long as proper disclosure is given to the buyer.

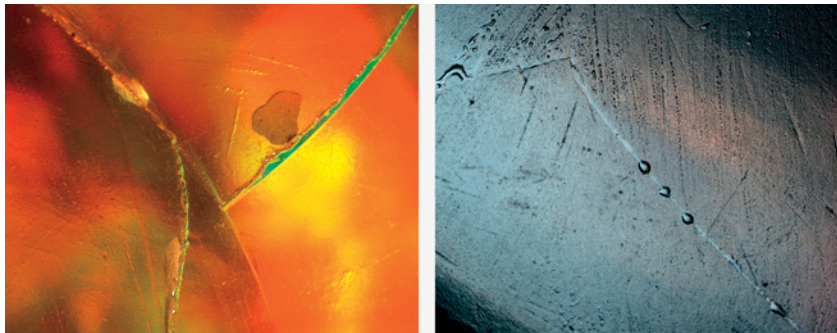
Nathan Renfro and Phil York

Ethiopian Black Opal

The Carlsbad laboratory recently examined a 10.67 ct black opal (figure 13), reportedly from the Wollo Province of Ethiopia. Because black is not a common bodycolor for opal from this important locality, and there are increasing reports of this material being treated (e.g., the article by N. Renfro and S. F. McClure in this issue, pp. 260–270), we sought to determine the cause of color in this sample. Also submitted was an approximately 1 kg parcel of opal nodules, on which the client permitted destructive testing to investigate the cause of the bodycolor.

Standard gemological properties from the cabochon were consistent with those expected for opal, including an RI of 1.45 and a hydrostatic SG of 2.05. It was inert to long- and short-wave UV radiation. Microscopic examination revealed small brown dendritic inclusions, a “digit-pattern”

Figure 12. Low-relief fractures were seen throughout the opal, many of which showed flattened gas bubbles near the surface (left). Droplets of oil readily sweated out of the fractures when exposed to low temperature heat from a thermal probe (right, reflected light). Magnified 40 \times .



columnar structure, and nonphenomenal patch areas with a greenish cast. These microscopic observations and physical properties are consistent with features seen in other colors of Wollo opal.

The rough material had the same general appearance and gemological properties as the cabochon, except that the nodules displayed color zoning. One of the rough pieces was sliced in half, revealing a dark brown to black core with a light brown to near-colorless perimeter (figure 14). This structure suggested natural color, as the reverse pattern (dark perimeter with light core) would be expected if the dark color had been artificially introduced.

We performed LA-ICP-MS chemical analysis of one slice, and Mn was the only element that showed distinct variations between the dark core (average 261 ppmw) and light rim (average 23 ppmw). The elevated Mn in the core is consistent with the dark color, as black manganese oxides have been observed on Wollo opal. If Mn was present during opal formation, it is reasonable to conclude that man-

Figure 13. This 10.67 ct opal cabochon is reportedly from the Wollo Province of Ethiopia. The black bodycolor is caused by natural manganese oxides incorporated during formation.

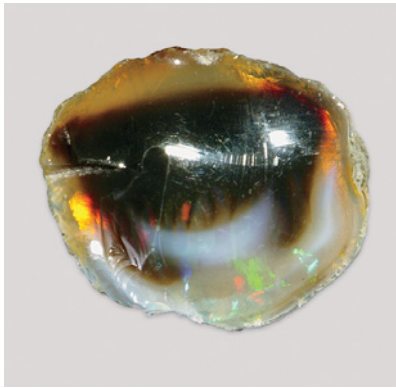


Figure 14. This 8.37 ct slice from a black opal nodule shows a dark core with a near-colorless to light brown perimeter, suggestive of natural color. LA-ICP-MS analysis of the core revealed high concentrations of Mn, which is responsible for the bodycolor.

ganese oxides would be incorporated into the opal and impart a dark bodycolor. Qualitative analysis by EDXRF also showed relatively high levels of Mn when compared to a white opal from Wollo.

Figure 15. This strand contains 17 large (up to 29.46 mm), coated, baroque-shaped, bead-cultured freshwater pearls.



While treated black Ethiopian material has been documented (e.g., www.stonegroup.com/SmokeTreatmentinWolloOpal.pdf), opal enthusiasts will certainly appreciate these natural-color gems from the Wollo Province.

Nathan Renfro

Coated Bead-Cultured Freshwater PEARLS

In September 2011, a strand of unusually large white baroque “pearls” was submitted to the New York laboratory for identification. The 17 pieces measured 22.43 × 17.60 × 14.17 mm to 29.46 × 19.64 × 16.50 mm. They had a noticeably unnatural color and surface appearance, yet their baroque shape was typical of some freshwater cultured pearls seen in the marketplace (figure 15).

Microscopic inspection revealed a surface structure that lacked the characteristic platelet structure of nacreous pearls. Instead, the surfaces had a “glittery” painted appearance and unnaturally distributed orient, fea-

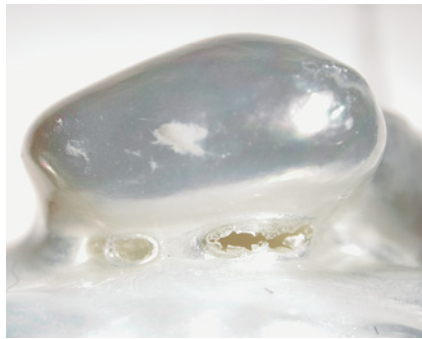


Figure 16. Microscopic examination of the cultured pearls reveals air bubbles trapped in folds within the surface (left, magnified 20×). A close-up of a drill hole shows puckering and peeling of the outer surface, as well as the underlying nacreous surface of the cultured pearl (right, magnified 20×).

tures commonly found in imitation pearls. Also, air bubbles were trapped in the folds and crevices throughout the strand (e.g., figure 16, left). Puckering at the drill holes, as well as noticeable chipping and peeling, further indicated a pearl imitation. In addition, some of the drill holes revealed an underlying nacreous layer (figure 16, right). These observations suggested the strand consisted of nacreous pearls with a thick coating, which would explain their organic-appearing shape despite their artificial appearance.

Most of the samples showed obvious uniformly round bulges like those seen in baroque bead-cultured pearls. Examination of these areas with fiberoptic lighting showed distinct banding that is typical of shell beads. X-radiography revealed that the entire strand was indeed bead cultured (figure 17). No distinct boundary between the very thin nacre and the coating could be observed in the X-ray images.

The long-wave UV reaction was relatively inert across the body of the cultured pearls but strong bluish white along the narrower areas where the coating was most concentrated. When exposed to X-rays, the strand showed moderate yellow luminescence (which was visible through the coating), typical of a freshwater origin. This was confirmed by LA-ICP-

MS chemical analysis of an exposed nacreous layer, which showed high concentrations of Mn and Sr. Both EDXRF and LA-ICP-MS detected significant amounts of bismuth in the coating. Bismuth is often used in artificial coatings to create a pearlescent appearance (J. V. Koleske, Ed., *Paint and Coating Testing Manual: 14th*

Figure 17. X-radiography of the strand reveals a bead-cultured structure and very thin nacre layers around the beads.



Edition of the Gardner-Sward Handbook, American Society for Testing and Materials, Philadelphia, 1995, pp. 229–230). Natural saltwater pearls with a bismuth-bearing coating were reported in a Fall 2005 Gem News International entry (pp. 272–273).

This strand proved unusual for two reasons: Bead-cultured freshwater pearls are not common in the market, and the pearl coatings we have examined have tended to consist of clear silicone polymers applied to improve luster or protect the underlying nacre (see Lab Notes: Spring 2000, p. 65; Spring 2002, pp. 83–84). The coating on the present strand created the illusion of thick, luminous nacre, and was probably applied to reinforce the precariously thin nacre layer on these cultured pearls.

Akira Hyatt

Tenebrescent ZIRCON

Only a few gem varieties are known to exhibit reversible photochromism, also known as tenebrescence. This phenomenon is most notable in hackmanite a variety of sodalite. Recently we learned about another gem showing tenebrescence: zircon. Our source indicated that five such stones had been discovered approximately 25 years ago in central Australia. When left in the dark for a few hours, the specimens reportedly turned orange, which would fade to near-colorless within a few minutes of exposure to light (figure 18).

Two of the Australian samples were provided for examination in September, 2011: a 3.07 ct piece of rough and a 1.80 ct faceted round brilliant. Both samples had fairly typical properties for zircon: RI—over the limits of the refractometer (>1.81); SG—4.72; and fluorescence—very weak orange to long-wave UV radiation, and moderate orangy yellow to short-wave UV. Microscopic examination revealed reflective disk-like inclusions. LA-ICP-MS chemical analysis did not show anything out of the ordinary for zircon.

When first taken out of the dark environment, the stones were orange.

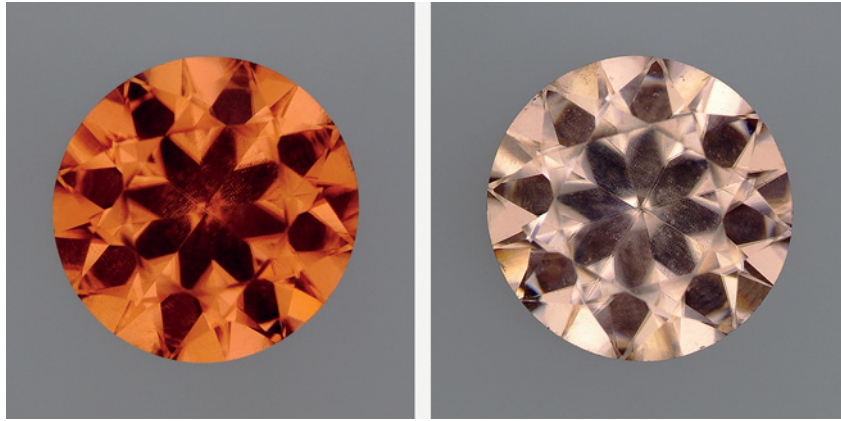


Figure 18. This 1.80 ct tenebrescent zircon is shown just after it was taken out of the dark (left), and after exposure to a fiber-optic light for several minutes (right).

Placed under a standard 13.3 watt incandescent desk lamp, they faded within a couple of minutes to a light, slightly pinkish brown. The color did not appear to change any further under indirect office lighting. Additional exposure to a 150-watt fiber-optic light for approximately one minute caused them to fade to pale pinkish brown. Longer exposure to the fiber-optic light did not cause any more fading. After being stored in the dark overnight, the stones returned to their original color. We repeated this process several times with the same results.

Some tenebrescent stones change back to their original color by exposure to short-wave UV radiation or heat. Attempts to restore the orange

color of these zircons with short-wave UV were unsuccessful. We also tried low heat without success, but this may be because the samples were not heated enough; they were not heated further out of concern for potential damage.

A search of the literature by GIA's Richard T. Liddicoat Library and Information Center found no mention of "tenebrescent" zircon, although several books described zircons with such behavior. The oldest reference found was in Max Bauer's *Precious Stones* (1904), which noted: "Zircon—The colour and luster of some hyacinths [probably referring to brownish or pinkish orange material] is liable to change even at ordinary

temperatures if the stones are exposed to light. . . . In some cases the colour becomes pale. . . . Such altered stones, if kept in darkness, will recover their original colour. . . ." Interestingly, several other references gave fairly similar descriptions of this phenomenon, but it was never referred to as tenebrescence—even though it fits the definition. Likewise, a Fall 1986 Lab Note (pp. 188–189) documented reversible color-change in a blue zircon, which changed to an undesirable grayish brown with exposure to long-wave UV radiation.

Several online retailers are selling this material as tenebrescent zircon. The stones are reported to be from Tanzania, Australia, Cambodia, or Nigeria; one site says it was found 10 years ago. It remains unclear whether any of this information is reliable, but one thing is certain: tenebrescent zircon exists, and it is a wonder that this interesting material has been so little reported in the contemporary literature.

Shane F. McClure

PHOTO CREDITS

Sood Oil (Judy) Chia—1; Paul Johnson—2 and 5; Jian Xin (Jae) Liao—3 and 15; Sally Eaton-Magaña—6; David Nelson—7; C. D. Mengason—8 and 18; Robison McMurtry—11, 13, and 14; Nathan Renfro—12; JaeWon Chang—16.

For online access to all issues of **GEMS & GEMOLOGY** from 1981 to the present, visit:

store.gia.edu

Editor

Brendan M. Laurs (blaur@gia.edu)

Contributing Editors

Emmanuel Fritsch, CNRS, Team 6502, Institut des Matériaux Jean Rouxel (IMN), University of Nantes, France (fritsch@cnsr-immn.fr)

Michael S. Krzemnicki, Swiss Gemmological Institute SSEF, Basel, Switzerland (gemlab@ssef.ch)

Franck Notari, GGTL GemLab–GemTechLab, Geneva, Switzerland (franck.notari@gemtechlab.ch)

Kenneth Scarratt, GIA, Bangkok, Thailand (ken.scarratt@gia.edu)

COLORED STONES AND ORGANIC MATERIALS

Chondrodite from Mahenge, Tanzania. At the 2011 Tucson gem shows, Dudley Blauwet (Dudley Blauwet Gems, Louisville, Colorado) showed GIA some samples of chondrodite that were found near Mahenge, Tanzania, in early 2010. Chondrodite, $(\text{Mg,Fe}^{2+})_5(\text{SiO}_4)_2(\text{F,OH})_2$, is a fairly rare monoclinic silicate mineral that typically occurs as small grains ranging from yellow to red and brown; well-formed crystals and gem-quality material are rare. Faceted chondrodite was previously reported from Tanzania, though from a different locality, Sumbawanga (see Winter 2007 Gem News International [GNI], pp. 377–378).

Mr. Blauwet was aware of ~100 g of rough material being produced at Mahenge, which consisted of small waterworn pebbles and larger broken fragments. He bought a few small samples in 2010, and the cut stones from this parcel yielded 121 pieces totaling 19.06 carats. Later, during the 2011 Tucson shows, he purchased about 50 g of clean rough. This parcel produced 99 cut stones totaling 55.57 carats. It included five gems weighing >1.5 ct; the largest one was ~2.0 ct.

Gemmological examination by GIA in Tucson yielded the following properties from a 0.34 ct faceted sample (figure 1, left): $\text{RI}-n_c = 1.594$, $n_b = 1.602$, $n_g = 1.621$; birefringence—0.027; optic character—biaxial positive; pleochroism—weak yellow to near colorless; UV fluorescence—inert to long-wave, and slightly chalky yellow to short-wave UV; and no lines visible with the desk-model spec-



Figure 1. These chondrodites (left, 0.34 ct) are from Mahenge, Tanzania. Photo by Robert Weldon.

troscope. Inclusions consisted of numerous transparent reflective particles and fine oriented short needles, some appearing rusty orange. Compared to the Sumbawanga chondrodite, the Mahenge material had a slightly higher RI, but the same birefringence. The needle-like inclusions were not seen in the Sumbawanga material.

Mr. Blauwet reported that, to his knowledge, no additional gem-quality chondrodite has been produced from Mahenge since 2010.

Thomas W. Overton (gandg@gia.edu)
Carlsbad, California

Editor's note: Interested contributors should send information and illustrations to Brendan Laurs at blaur@gia.edu or GIA, The Robert Mouawad Campus, 5345 Armada Drive, Carlsbad, CA 92008. Original photos will be returned after consideration or publication.

GEMS & GEMOLOGY, Vol. 47, No. 4, pp. 316–335,
<http://dx.doi.org/10.5471.GEMS.47.4.316>.

© 2011 Gemological Institute of America

Blue dolomite from Colombia. Dolomite, a calcium-magnesium carbonate $[\text{CaMg}(\text{CO}_3)_2]$, is the second most important carbonate mineral after calcite. Although dolomite is sometimes used as an ornamental stone, it is rarely seen as a gem due to its low hardness (Mohs 3½–4) and lack of transparency. However, in late 2010, GIA was informed by Farooq Hashmi (Intimate Gems, Glen Cove, New York) about a new find of gem-quality blue dolomite from the famous Muzo emerald mine in Colombia. The



Figure 2. This 1.13 ct oval brilliant is a rare blue dolomite from the Muzo mine, Colombia. Photo by Brad Payne.

material was reportedly produced in mid-2010 from veins in black shale. Less than 2 kg of gem-quality rough were found, as crystals up to 2.5 cm across (mostly ~1 cm). Mr. Hashmi arranged for some of the rough material to be donated to GIA by Greg Turner (Sacred Earth Minerals, Asheville, North Carolina), and Brad Payne (The Gem Trader, Surprise, Arizona) also loaned a 1.13 ct oval brilliant (figure 2) for examination.

All of the samples were transparent light blue without any color zoning. Their gemological properties were consistent with dolomite, which was confirmed by Raman analysis. Microscopic observation revealed two- and three-

phase inclusions with jagged edges (figure 3, left), along with other fluid and transparent crystalline inclusions. Healed feathers containing tiny crystals were found in most samples. A wavy strain pattern was observed with cross-polarized light. Dolomite's high birefringence (0.180) was evident from the strong doubling. An albite inclusion, identified by Raman and LA-ICP-MS analysis, broke the surface of one rough sample (figure 3, right). Pyrite, commonly associated with dolomite at Muzo, was also seen on the surface of a few rough samples, all of which were rhombohedral twinned aggregates with reentrant corners. The surfaces also showed numerous etch features. One crystal contained three large, flat fractures parallel to rhombic faces, consistent with the perfect rhombohedral cleavage of dolomite.

A UV-Vis spectrum of the cut stone revealed Fe^{3+} absorption bands at 450, 460, and 470 nm, along with a large broad band centered at ~580 nm. Qualitative EDXRF spectroscopy detected Ca and Mg, as well as traces of Fe and Mn. LA-ICP-MS analysis revealed many additional trace elements, including Sc, Ti, V, Cr, Ni, Zn, Sr, Y, and rare-earth elements. A pure dolomite crystal is expected to be colorless, and the blue color shown by this Colombian material may be due to natural radiation. Blue color in carbonate minerals (i.e., calcite) that contain twinning and dislocations is thought to be related to natural radiation (T. Calderon et al., "Relationship between blue color and radiation damage in calcite," *Radiation Effects*, Vol. 76, 1983, pp. 187–191, <http://dx.doi.org/10.1080/01422448308209660>).

Transparent (colorless) dolomite has been documented from Spain (see M. O'Donoghue, Ed., *Gems*, 6th ed., Butterworth-Heinemann, Oxford, UK, 2006, p. 406), but

Figure 3. The dolomite contained tiny jagged three-phase inclusions associated with other fluid inclusions (left, magnified 110 \times). An albite inclusion broke the surface of one rough dolomite sample (right, magnified 80 \times). Photomicrographs by K. S. Moe.





Figure 4. This unusual pendant, measuring ~3 × 8 cm, contains a slab of Namibian fluorite that is surrounded by a piece of brushed silver. It is shown in reflected light (left) and transmitted light (right). Courtesy of Goldideas, Windhoek; photos by Jo-Hannes Brunner.

we believe this is the first report of blue dolomite being used as a gemstone.

Kyaw Soe Moe (kmoe@gia.edu) and Wai L. Win
GIA, New York

Fluorite from Namibia. The Klein Spitzkoppe area in Namibia is known as a source of attractive crystals of topaz, aquamarine, and other minerals from miarolitic cavities (see, e.g., B. Cairncross et al., “Topaz, aquamarine, and other beryls from Klein Spitzkoppe, Namibia,” Summer 1998 *G&G*, pp. 114–125). In mid-2011, GIA was informed by Jo-Hannes Brunner (Pangolin Trading,

Windhoek, Namibia) about a new find of fluorite located several kilometers from Klein Spitzkoppe toward the Khan River. The material shows distinctive color zoning and inclusions, and Mr. Brunner reported that only a small amount has been mined so far. He indicated that a few dozen polished slabs have been produced in sizes up to 10+ cm in longest dimension, and some of them have been set in silver pendants (e.g., figure 4). Mr. Brunner donated to GIA one polished slab (89.47 ct, or 37.05 × 39.75 × 5.60 mm) and seven rough pieces of this fluorite (9.83 to 45.97 g) for examination.

Gemological examination of the slab revealed the following properties: RI—1.434; hydrostatic SG—3.12; Chelsea filter reaction—none; fluorescence—inert to long-wave UV radiation, and weak yellow to short-wave UV in the yellow to orangy yellow portions; and no clear absorption lines visible with the desk-model spectroscope. These properties are consistent with fluorite, and the identity of all the samples was confirmed by Raman spectroscopy.

The fluorite was distinctly color zoned, with cubic violet zones inside yellow to orangy yellow areas. Whitish, prismatic inclusions with generally square cross-sections (figure 5) appeared opaque in transmitted light and were predominantly hosted by the violet areas of the fluorite. These inclusions were identified by Raman spectroscopy as dickite, a clay mineral with the formula $Al_2Si_2O_5(OH)_4$. Many of them consisted of partially hollow tubes, apparently created when some of the soft dickite weathered away or was removed during the polishing of the slab. A few yellow areas within the dickite inclusions were identified as sulfur, and Raman analysis also detected quartz inclusions in the fluorite. In addition, microscopic examination revealed reflective, iridescent fluid inclusions with geometric patterns.

LA-ICP-MS analysis of both the yellow and violet portions of the fluorite showed trace amounts of Ti, Sr, La, and Ce. The violet area tended to show higher concentra-

Figure 5. Color zoning and several prismatic inclusions containing dickite are visible in this Namibian fluorite slab (gift of Jo-Hannes Brunner; GIA Collection no. 38388). Photomicrograph by C. Ito; magnified 16×.

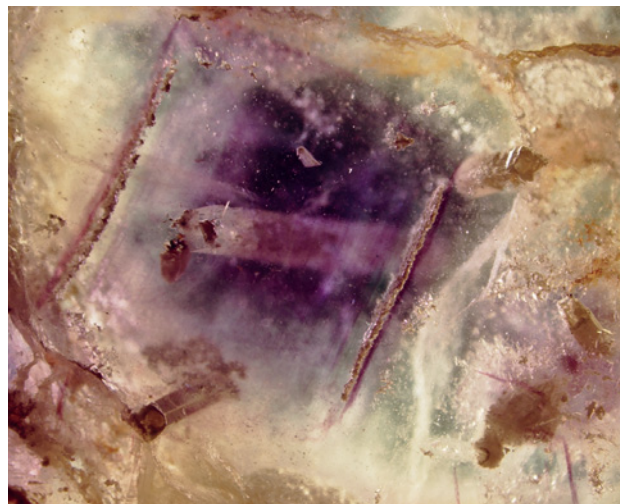




Figure 6. Shown here are rough and cut opals from Laverton, Western Australia. The faceted stones weigh 0.50–4.39 ct. Photo by V. Pardieu.

tions of these elements, as well as trace amounts of additional rare-earth elements.

UV-Vis-NIR spectroscopy of a yellow portion of the slab showed a broad band at 434 nm, while a violet section displayed a 306 nm peak with broad bands at approximately 410 and 570 nm. The band in the yellow region is consistent with the “yellow center” attributed to an O_3^- ion replacing two adjacent F^- ions (H. Bill and G. Calas, “Color centers, associated rare-earth ions and the origin of coloration in natural fluorites,” *Physics and Chemistry of Minerals*, Vol. 3, 1978, pp. 117–131). The violet portion showed an absorption spectrum similar to those of purple fluorites in that article, with a 570–580 nm band (possibly attributed to colloidal calcium) and other possible Y- or Ce-associated F-center features.

Absorption spectra of the fluorite and Raman spectra of the inclusions are available in the *G&G* Data Depository at gia.edu/gandg. The delicate color patterns and interesting inclusion scene displayed by this fluorite makes it an attractive option for jewelry use when cut as slabs.

Claire Ito (cito@gia.edu)
GIA, New York

Common opal from Laverton, Western Australia. In early 2011, Peter Piromanski from Holdfast Exploration Pty. Ltd., Wannero, Western Australia, showed this contributor some attractive patch opals (e.g., figure 6), to be marketed as Piroman Opal, that were reportedly from a new deposit 31 km north of the town of Laverton, near the Great

Central Road at coordinates 28°22'10" S, 122°35'59" E. According to local geologic maps, this region consists mainly of weathered biotite monzogranite or kaolinized granites. The opal seam appears to be associated with a fault trending northeast/southwest. In September 2008, Holdfast Exploration was granted a five-year exploration license, and prospecting has been carried out since November 2008. Pits were excavated up to about 1.5 m deep in six different areas using mainly hand tools, a jackhammer, and an excavator.

Samples of opal in host rock, loose pieces of rough, and faceted stones were donated to GIA in December 2010. Eight samples weighing 0.49–4.39 ct studied for this report represented the color range of the Laverton material: two rough specimens (yellow and brownish orange) and six faceted stones (two colorless, two yellow, and two brownish orange). Some of the matrix specimens contained colorless, yellow, and brownish orange opal within the same piece. Most of the opal in matrix showed some unhealed surface-reaching fissures that were present before the stones were brought to GIA. Observations over an 11-month period showed some evidence of crazing in one of them, the colorless round brilliant shown in figure 6.

Gemological properties of the opal are summarized in table 1. Most of the samples showed some turbidity and flow patterns. One of the two colorless pieces contained clusters of minute crystals (figure 7, top left). In most of the yellow material, small spheres were seen individually (figure 7, top right) or in groups (figure 7, bottom left). In the

TABLE 1. Properties of opal from Laverton, Western Australia.

Color	Colorless to saturated yellow and brownish orange. Some stones showed orange and colorless color zoning.
Diaphaneity	Transparent to translucent
RI	1.40–1.44
SG	1.99–2.01
Mohs hardness	5–6
UV fluorescence	Yellow and brownish orange opal: inert Colorless opal: strong white (with 2–3 seconds of phosphorescence) to short-wave UV
Spectroscope spectrum	Colorless to yellow opal: no features Brownish orange opal: strong absorption in the blue region

brownish orange opal, the most common inclusions were tiny angular, often reddish crystals associated with randomly oriented reflective (sometimes iridescent) discoid tension fissures, reminiscent of the “lily pads” seen in peridot (figure 7, bottom right). We have been unable to identify any of these inclusions with Raman microspectroscopy.

EDXRF analysis of five opals (colorless, yellow, and brownish orange) showed traces of Cu and Zr in all samples, while Ca, Fe, and Sr were detected in all but the colorless pieces. The three darker brownish orange stones contained the highest Fe contents, as expected from the literature (E. Fritsch et al., “Découvertes récentes sur l’opale,”

Revue de Gemmologie, No. 138–139, 1999, pp. 34–40). Raman spectroscopy of the same five samples showed a rather broad asymmetric band centered at about 350 cm^{-1} with smaller bands at 1220, 1075, 965, and 780 cm^{-1} . Such spectra are typical of opal-CT (M. Ostrooumov et al., “Spectres Raman des opales: Aspect diagnostique et aide à la classification,” *European Journal of Mineralogy*, Vol. 11, 1999, pp. 899–908), which is usually found in a volcanic setting.

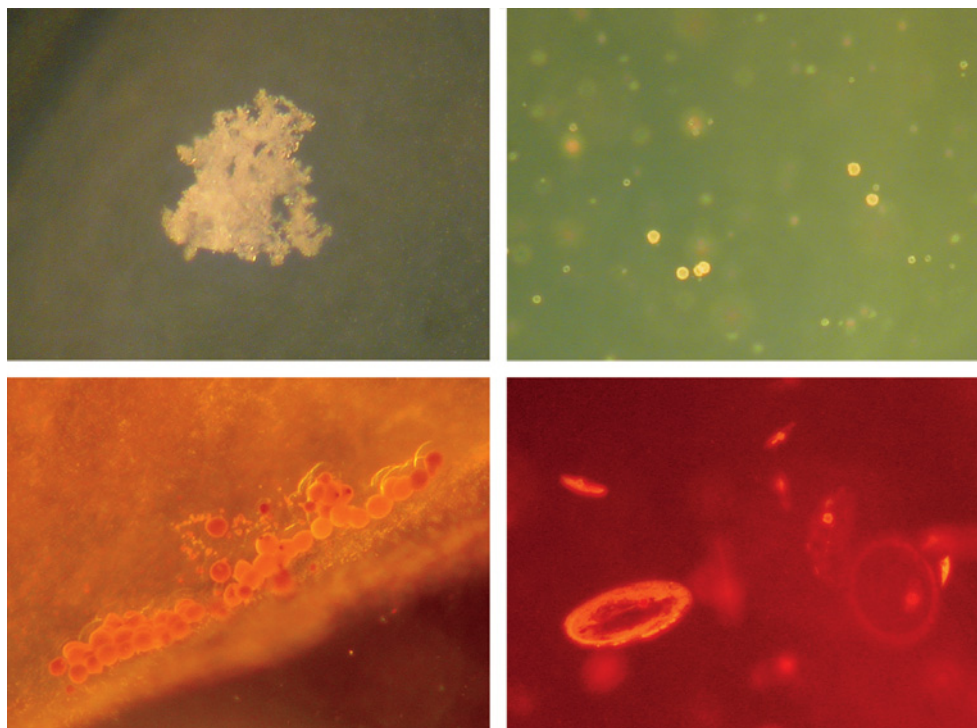
The discovery of fire opal in Western Australia, a part of the country not usually associated with opal, is an interesting development. Prospecting is ongoing, and updates and additional information on this opal will be posted at www.piromanopal.com.au. These attractive gems could make a welcome addition to Australian opal production.

Vincent Pardieu (vpardieu@gia.edu)
GIA, Bangkok

A bicolor, bi-pattern hydrophane opal. The Laboratoire Français de Gemmologie in Paris recently examined an unusual 17.15 ct opal cabochon, measuring approximately 20.95 × 15.96 × 11.69 mm. Play-of-color in the full rainbow of hues was visible throughout the stone (figure 8, left), but the bodycolor was not even. One end of the cabochon was medium brown, while the rest of the gem had a translucent whitish color (figure 8, right). The color boundary formed a well-defined line along the base of the stone. Such a zoning pattern has been occasionally seen in common opal but is unusual for play-of-color opal.

To better characterize the opal, we weighed it after 12

Figure 7. Inclusions seen in the Laverton opals included a cluster of minute unknown crystals (top left) and tiny spherical inclusions (top right), which sometimes occurred in clusters (bottom left). Randomly oriented crystals associated with lily pad-like tension fissures were also seen (bottom right). Photomicrographs by V. Pardieu, magnified ~40×.



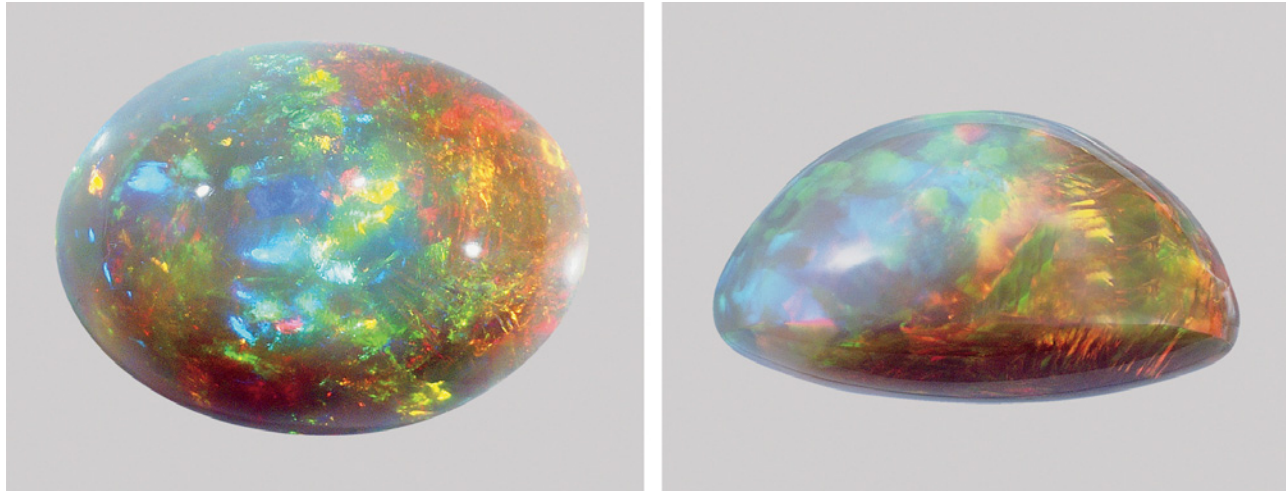


Figure 8. This 17.15 ct bicolor, bi-pattern opal is likely from Ethiopia's Wollo Province. The opal's color zoning is best viewed from the side. One end has a translucent whitish color, and the other is medium brown. Photos by A. Droux.

hours of drying in air in the laboratory, and again after immersion in water. Water fills the pores of opals that show hydrophane character. After immersion the stone weighed 17.99 ct, which clearly indicated a hydrophane character, but its appearance remained unaltered.

To avoid introducing foreign substances into the porous opal, we did not test for RI or SG. The gem emitted a weak whitish fluorescence to long-wave UV radiation, with a slightly less intense reaction to short-wave UV. The emission was zoned, with the brown portion nearly inert. The cap of the white zone at the top of the cabochon had a

stronger fluorescence than the rest of the opal.

Another peculiarity was that the two color zones showed different patterns in their play-of-color. The brown zone had fairly large patches and a striated appearance, sometimes referred to as a "straw" or "chaff" pattern (figure 9). This feature is due to polysynthetic twinning of the network of silica spheres found in many opals, particularly those from Ethiopia. This pattern was absent from the light-colored portion, which had smaller patches, less-visible borders, and somewhat "rolling" color flashes.

The base of the cabochon showed a cellular pattern of

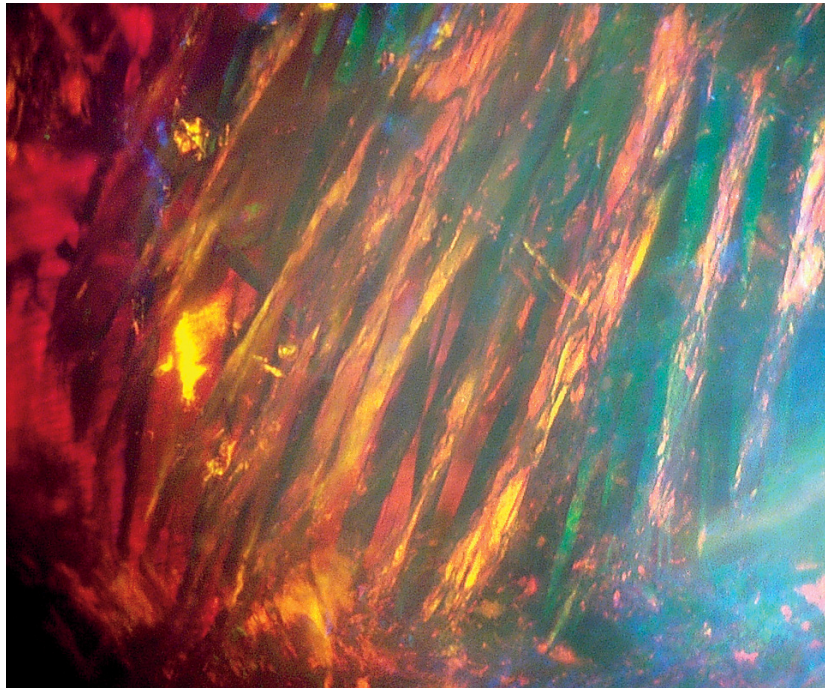


Figure 9. The "straw" or "chaff" pattern in the brown zone is due to polysynthetic twinning of the network of silica spheres constituting the opal. Photomicrograph by A. Droux; magnified 55x.



Figure 10. This 4.56 ct quartz cabochon displayed vivid red coloration and subtle chatoyancy. Photo by B. Rondeau.

well-formed “digits” that is typical of some opals from Wollo, Ethiopia, along with the abundance of twinning in the brown portion of the stone. Whitish play-of-color opal is common from Wollo but not from Ethiopia’s Shewa area. We concluded that this gem is likely from the Wollo deposits.

*Alexandre Droux
Laboratoire Français de Gemmologie, Paris
Emmanuel Fritsch*

Figure 11. The chatoyancy or star effect in the quartz is due to numerous oriented short needles of cinnabar. Photomicrograph by B. Rondeau; magnified 50×.

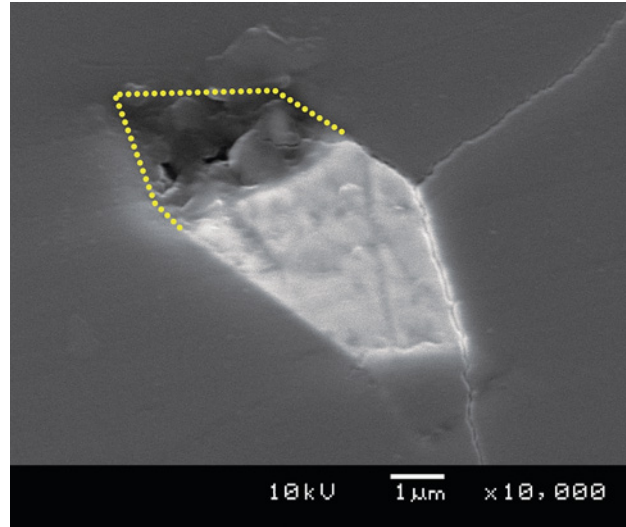
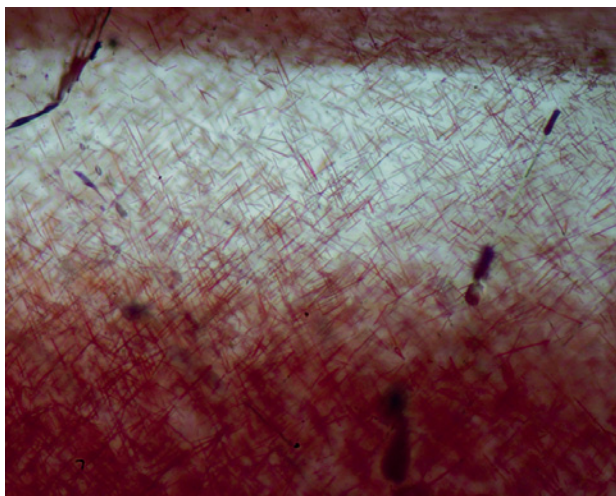


Figure 12. This surface-reaching cinnabar inclusion shows a six-fold euhedral shape in cross-section. The upper left portion of the inclusion has broken away, and the original trace is outlined. Image by B. Rondeau.

Chatoyant quartz with cinnabar inclusions. While on a buying trip to Jaipur, India, one of these contributors (TP) purchased a 4.56 ct cabochon of what appeared to be quartz with iron oxide inclusions, such as those seen in “strawberry” quartz from Kazakhstan. The cabochon measured 10.4 × 8.7 × 6.8 mm and had a vitreous luster (figure 10). Its spot RI of ~1.54, SG of 2.64, and inert reaction to long- and short-wave UV were all consistent with quartz. The gem was vivid red under reflected light except for a narrow linear near-colorless band. Most interestingly, it displayed chatoyancy in fiber-optic light, appearing as a four-rayed star in some positions. Microscopic examination revealed that the phenomenon was due to numerous red inclusions. These were short (<1 mm) acicular crystals oriented mainly along four directions (figure 11). When viewed with a scanning electron microscope (SEM), they showed a euhedral shape, with six-fold symmetry in cross-section, and were about 3 µm wide in narrowest dimension (figure 12). Since their morphology did not resemble that of iron oxide, we investigated them further.

Chemical analysis of surface-reaching inclusions using a JEOL 5800 SEM equipped with an energy-dispersive spectrometer detected only mercury and sulfur, a composition consistent with cinnabar. This identification is also consistent with their hexagonal symmetry. Cinnabar inclusions in quartz have been documented previously, especially in material from China (J. Hyršl and G. Niedermayr, *Magic World: Inclusions in Quartz*, Bode Verlag, Haltern, Germany, 2003, p. 53; E. J. Gübelin and J. I. Koivula, *Phototlas of Inclusions in Gemstones*, Vol. 3, Opinio Verlag, Basel, Switzerland, 2005, pp. 592, 627). To the best of our



Figure 13. This 45.85 ct quartz cabochon was unusual for its eye-visible inclusions of elongated emerald crystals. Photo by G. Choudhary.

knowledge, however, cinnabar has not been reported as oriented inclusions responsible for chatoyancy or a star effect, which makes this an unusual and attractive specimen.

Thierry Pradat (tp@gems-plus.com)
G-Plus, Lyon, France

Benjamin Rondeau
Laboratoire de Planétologie et Géodynamique,
CNRS, Team 6112, University of Nantes, France

Emmanuel Fritsch

Quartz with acicular emerald inclusions. Quartz with randomly distributed tourmaline or rutile needles is widely available in the market. These gems are often described as

“tourmalinated” or “rutilated” quartz, respectively. Recently, the Gem Testing Laboratory in Jaipur examined a quartz specimen that contained eye-visible emerald crystals (figure 13). Although intergrowths of emerald and quartz and a notable emerald-in-quartz specimen have been reported previously (e.g., Lab Notes: Summer 2000, pp. 164–165; Fall 2008, p. 258), this was quite different.

The slightly smoky 45.85 ct marquise-shaped cabochon measured 37.60 × 18.26 × 11.57 mm. The prominent green inclusions displayed an acicular habit (figure 14, left). Their green color and hexagonal profile (figure 14, right) strongly suggested emerald, but their acicular habit raised some doubts, as emeralds typically show a more columnar form. Most of the crystals also displayed basal parting planes, reminiscent of the actinolite blades found in emeralds from the Ural Mountains of Russia. Some also displayed color zones following the prism faces, while others contained rain-like inclusions.

To conclusively identify the inclusions, we examined the sample under a desk-model spectroscope. It revealed a spectrum consistent with emerald, featuring a doublet in the red region and an absorption band in the yellow-green region. Further confirmation was obtained by FTIR, which displayed a typical emerald spectrum. IR spectroscopy also confirmed the host material as quartz, which was supported by a spot RI of 1.54 and a hydrostatic SG of 2.65.

Textural relationships indicated that the emerald crystals formed before the host quartz (i.e., they are protogenetic). Emerald is known to occur within quartz, but this sample was quite unusual for the crystals’ acicular habit and their occurrence as inclusions, not merely in association with the quartz or as an intergrowth.

Gagan Choudhary (gagan@gjpecindia.com)
Gem Testing Laboratory, Jaipur, India

Figure 14. The inclusions displayed an acicular habit (left, magnified 32×), which is usually not associated with emeralds. However, their green color and hexagonal profile (right, magnified 48×) helped identify them as emerald. (The green material in some quartz fractures is polishing powder.) Photomicrographs by G. Choudhary.

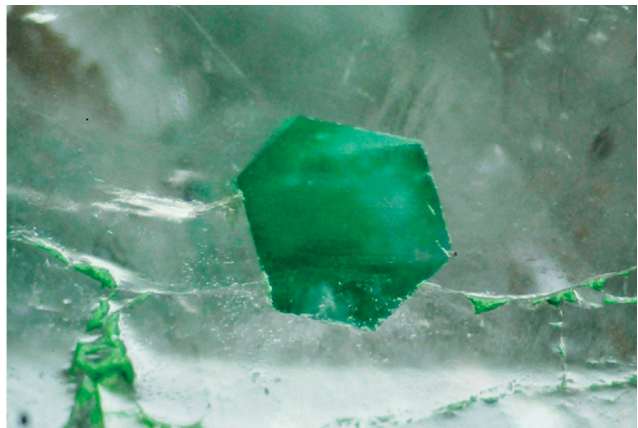
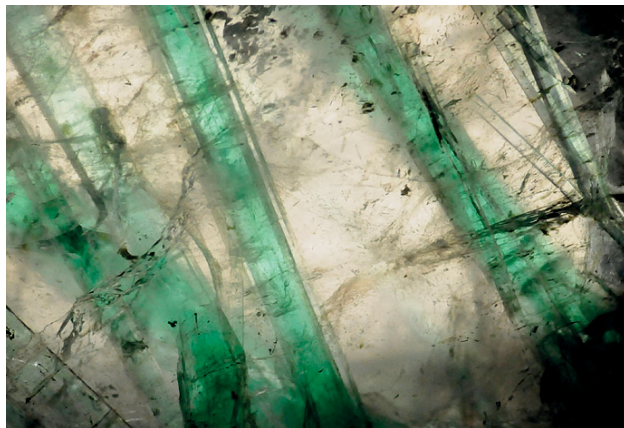




Figure 15. This life-size quartz skull carving contains inclusions of the rare mineral izoklakeite. Courtesy of Harold Van Pelt; photo by Erica Van Pelt.

Quartz carving with inclusions of izoklakeite. These contributors recently examined a life-size quartz skull (figure 15) carved by noted gem photographer and lapidary Harold Van Pelt (Los Angeles). The hollowed skull contained two articulated pieces and a jaw hinge that opened and closed. Starting with a 250 lb. colorless quartz crystal, Mr. Van Pelt produced this 6.5 lb. (2.9 kg) sculpture.

One of the carving's interesting features was its abundance of conspicuous submetallic silver-gray inclusions (e.g., figure 16). These were initially believed to be jamesonite, a lead-iron-antimony sulfide mineral often found in fibrous form. Initial analyses with a scanning electron microscope (SEM) quickly determined otherwise. No iron was detected, which meant the fibers consisted of a different material.

A more detailed SEM and electron microprobe investigation at Caltech revealed a lead-antimony-bismuth sulfide with a minor amount of copper. Its formula was initially determined as $(\text{Pb}_{2.65}\text{Cu}_{0.25})(\text{Sb}_{1.14}\text{Bi}_{0.95})\text{S}_6$. Areas of some of the fibers also consisted of several alteration products: galena (PbS), bismuthinite (Bi_2S_3), some $\text{CuPb}(\text{Sb,Bi})\text{S}_3$ minerals, and small amounts of native bismuth.

To identify the original lead-antimony-bismuth sulfide, we obtained a $\sim 1 \text{ cm}^3$ piece of the quartz from which the skull was originally carved. It was cooled in liquid nitrogen to make it brittle and immediately shattered in a

percussion mortar. This freed numerous fragments of the silver-gray included crystals. Powder X-ray diffraction analysis at the Natural History Museum of Los Angeles County pointed to either izoklakeite or giessenite, and an electron back-scattered diffraction pattern done at Caltech,

Figure 16. Izoklakeite and possibly other sulfides form these inclusions in the quartz used in the carving from figure 15. Photomicrograph by G. R. Rossman; image width 3.2 mm.

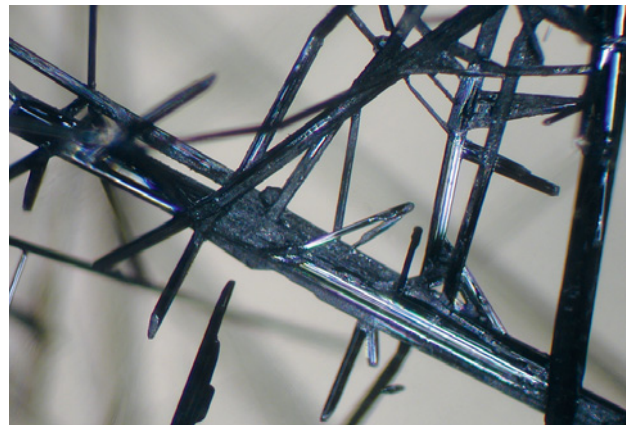




Figure 17. A Pakistani miner breaks marble to collect rubies at Datumbaresho, in the Hunza Valley. Photo by V. Pardieu.

together with the chemical analyses, confirmed that the phase was izoklakeite.

Izoklakeite is the antimony member of a solid-solution series with giessenite, the bismuth-dominant member. It was first described from a sulfide body near Izok Lake, Canada (D. C. Harris et al., "Izoklakeite, a new mineral species from Izok Lake, Northwest Territories," *Canadian Mineralogist*, Vol. 24, 1986, pp. 1–5). The mineral was later found in Sweden and as inclusions in quartz crystals from Switzerland. Its ideal chemical formula is $\text{Cu}_4\text{Pb}_{54}\text{Sb}_{38}\text{S}_{114}$.

The quartz skull, named "Izok" in honor of its unusual inclusions, is part of an exhibit of Harold Van Pelt's carvings on display at the Houston Museum of Natural Science through October 2012.

George R. Rossman (*grr@gps.caltech.edu*) and Chi Ma
California Institute of Technology
Pasadena, California

Anthony R. Kampf
Natural History Museum of Los Angeles County

Update on ruby and sapphire mining in Pakistan. In August and September 2011, these contributors visited Pakistan to collect reference samples for GIA's laboratory. With the support of gem merchant Syed Iftikhar Hussein

(Syed Trading Co., Peshawar, Pakistan), we traveled first to northern Pakistan to visit ruby deposits near Hunza and Bisil. Author VP, with assistance from Zulfiqar Ali Abbas (Kashmir Gems Ltd., Abbottabad, Pakistan), then proceeded to the ruby and sapphire deposits in the Kaghan Valley near Batakundi. This report provides an update on the mining and production at some of the Pakistani deposits described in the Fall 2007 (pp. 263–264) and Winter 2010 (pp. 319–320) GNI entries.

About 100 miners and local dealers were involved with ruby mining and trading around the Hunza Valley, at several deposits that initially started producing in the 1960s and 1980s. The rubies are found in marbles, sometimes associated with mica and blue and pink spinel. The deposits are located north of the valley, from Datumbaresho (figure 17) in the northwest to the Aliabad and Karimabad areas (Bajoring, Gharei Chhar, Phudan Daar, Gafinas), Altit, Ahmedabad, and Dong-e-Das (also known as Ganesh) in the east. Most of the workings are located 500–1,000 m above the villages at an elevation around 3,000 m (nearly 10,000 feet), and they are difficult to access because of the steep terrain. The color of the ruby generally ranges from deep red at Datumbaresho to pinkish red at Aliabad/Karimabad to pinkish and bluish red around Dong-e-Das. The size of the stones appears to



Figure 18. These rubies are from the Bisil area, in the Basha Valley of Pakistan. The largest piece, on the far right, is ~1 cm long. Photo by V. Pardieu.

increase in that same direction, from <0.4 g to 20+ g. Most Hunza ruby is cabochon quality at best, though mineral specimens are also important. Much of the region's production is apparently exported to China.

The Bisil ruby deposit is located near 35°52'53" N, 75°23'52" E, in the Basha Valley north of Skardu. It was discovered in 2003 by a local prospector. Rubies from Bisil (figure 18) are also found in marble, within veins or pods, typically in association with diopside and mica. We saw about 10 mining pits, up to 20 m deep. The deposits appear to extend from just above Bisil village (elevation ~2,800 m) to the top of the mountains at an elevation above 3,500 m, and may extend more than 10 km in an east-west direction. About 15 miners were working the area using simple tools, jackhammers, and dynamite. Small stones ranging from pink to deep red are mined year-round, but production is very limited.

The Batakundi ruby deposit is located in the Kaghan Valley at 34°52'41" N, 73°48'05" E, at an elevation of 4,190 m. Marble-hosted rubies, most of them small and deep red, have been recovered there since 2000. Rough stones larger than 0.6 g are very rare, with most of the production smaller than 0.2 g. A group of seven miners led by Haider Ali have been working in the current area since 2006. As at Bisil, the miners use a jackhammer, dynamite, and hand

tools; production is extremely limited.

Also in the Batakundi area, the Besar (also known as Basil or Besel) sapphire mines were being worked by about 50 miners using jackhammers and explosives at two sites, located at 35°02'41" N, 73°52'56" E, and 35°02'58" N, 73°53'19" E (e.g., figure 19). The elevation of these sites is 4,020 m and 3,780 m, respectively. Several kilograms of pink to purple sapphires were being extracted from the graphite-rich veins on a daily basis; less than 5% was of gem quality.

The overall ruby production from Pakistan is very low compared to other primary-type deposits in Asia and Africa. Most of the ruby production in Central Asia comes from the Murgab area in eastern Tajikistan and from Jegdalek, Afghanistan. Pakistani rubies are typically more included and smaller. Although Pakistan's ruby mines are rarely affected by the political instability and security issues present elsewhere in the country, the deposits are located high in mountainous areas that are difficult to access.

Vincent Pardieu
Stephane Jacquat
Piat Co., Bangkok

Figure 19. At the Besar deposits, in the Batakundi area of Pakistan's Kaghan Valley, several miners use jackhammers and explosives to break the hard rock in search of sapphires. Photo by V. Pardieu.



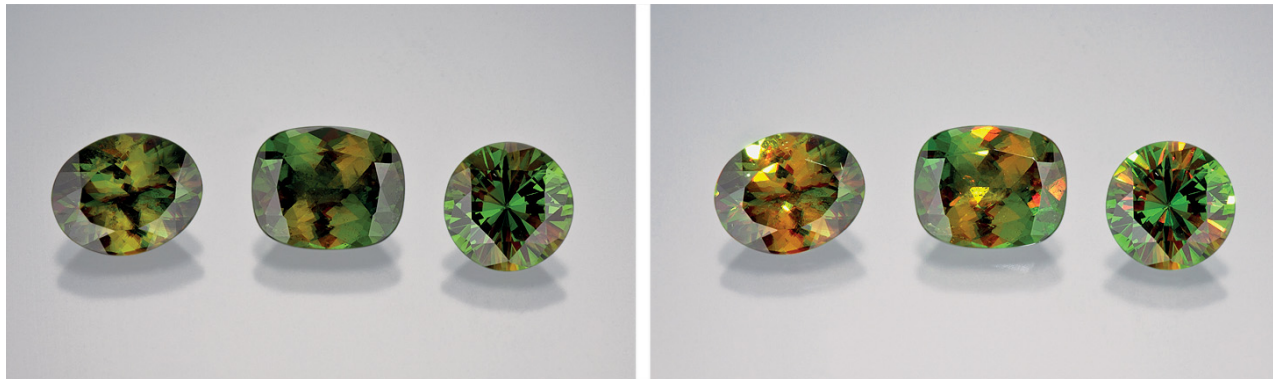


Figure 20. Sphene from the Pakistan/Afghanistan border area may contain a significant amount of V, which is presumably responsible for its color-change behavior. The oval gem on the left (2.76 ct) shows a noticeable color change from mainly yellowish green in daylight-equivalent lighting (left) to brownish orange in incandescent light (right). Photos by Robert Weldon.

Vanadium-bearing color-change sphene from Pakistan/Afghanistan. Recently seen in the Carlsbad laboratory was a parcel of rough and cut sphene (e.g., figure 20) loaned for examination by Eric Braunwart (Columbia Gem House, Vancouver, Washington). According to him, the sphene originated near the Pakistan/Afghanistan border. The most interesting feature of this material was that many of the stones showed a slight to moderate color change. In daylight-equivalent lighting, the sphene was dominantly vivid green to yellowish green, changing to brownish orange or brown under incandescent light (again, see figure 20). However, strong pleochroism was responsible for the multiple colors seen in the faceted stones.

The rough consisted of well-formed blade-like crystals, so it is apparent that the material was mined from a primary deposit. Rough production as of July 2011 was estimated by Mr. Braunwart to be around 600 g, from which approximately 200 carats of finished material have been produced. The cut stones ranged from calibrated sizes as small as 3 mm in diameter up to larger stones weighing several carats. The largest faceted stone from the production so far was a 5.45 ct oval brilliant.

Gemological properties of the material were consistent with sphene. The RI was over-the-limit of the refractometer, and the average SG (measured hydrostatically) was 3.54. A strong red reaction was observed with a Chelsea filter. Microscopic observation revealed strong doubling and numerous included crystals. These were identified by Raman microspectroscopy as transparent near-colorless apatite and dark elongated needle-like crystals of an amphibole mineral (figure 21). Several stones also contained fluid “fingerprints.” A few rough pieces showed prominent zoning, and the color change was less apparent across these zoned areas.

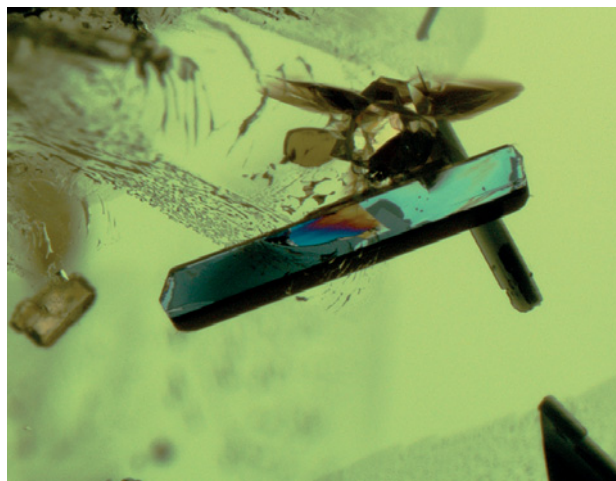
EDXRF spectroscopy of all samples showed major amounts of Ca, Ti, and Si that are expected for sphene, as well as traces of V, but no Cr. LA-ICP-MS measurements of several spots on a faceted sample detected an average of

more than 2400 ppmw V (and no Cr), which is presumably the cause of the color change. The visible spectrum showed a broad absorption feature centered at approximately 603 nm (figure 22). Transmission windows on either side of this broad band are consistent with the spectrum expected for a color-change gem.

The coloration of this sphene is much different from the typically “golden” orange material previously described from Pakistan’s North West Frontier Province (Spring 2006 GNI, pp. 68–69), and also from the yellow sphene known from Badakhshan, Afghanistan (Summer 2006 GNI, pp. 180–182).

Nathan Renfro (nrenfro@gia.edu)
GIA, Carlsbad

Figure 21. The most notable inclusions in the sphene were crystals of near-colorless apatite and dark elongated amphibole. Also present were numerous fluid fingerprints. Photomicrograph by N. Renfro; magnified 35 \times .



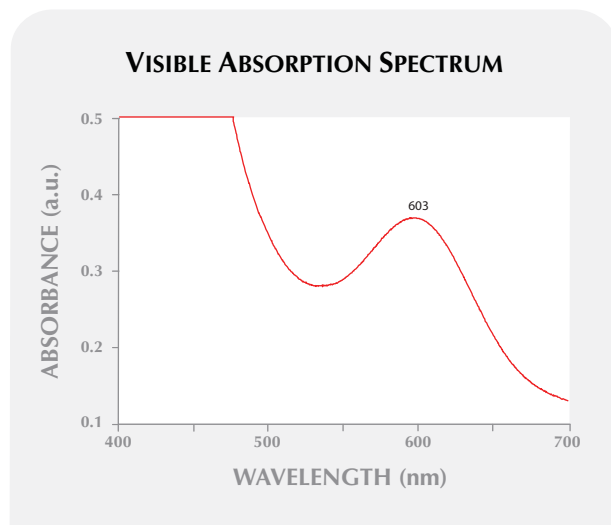


Figure 22. The visible spectrum of the color-change sphen showed a broad absorption feature centered at 603 nm that is presumably due to V, as this was the only significant trace element detected by LA-ICP-MS analysis.

Cobalt blue-colored spinel from Khuoi Ngan, Vietnam.

Blue spinel has been reported from several localities in the An Phu–Luc Yen area of northern Vietnam, though highly saturated material is quite rare (e.g., C. P. Smith et al., “A closer look at Vietnamese spinel,” *InColor*, Spring 2008, pp. 11–13; J. B. Senoble, “Beauty and rarity—A quest for Vietnamese blue spinel,” *InColor*, Summer 2010, pp. 18–23; Spring 2011 GNI, pp. 60–61). Testing has shown that the blue color is due to various amounts of cobalt and iron impurities (Smith et al., 2008).

Gem and mineral dealer Dudley Blauwet recently visited one of the Vietnamese blue spinel deposits and provided some information on the mining and production of this material. The site was located just east of the village of Khuoi Ngan and approximately 2.5 km southeast of An Phu, where a few local villagers were mining secondary deposits in shallow pits along the edges of rice paddies (figure 23). Work at the site began in 2008, and a number of pits were excavated with hand tools to a depth of 2–3 m. The gem-bearing material was taken to a nearby area for washing and hand picking (figure 24).

The spinel rough was quite small but intensely colored. Mr. Blauwet obtained four small parcels ranging from 0.4 to 5 g over the course of four days in Luc Yen. In addition, he purchased a fifth lot of rough in An Phu on the day that he visited Khuoi Ngan. The individual pieces of rough were mostly <0.2 ct but suitable for cutting melee because of the high color saturation. All of the lots were said to be from Khuoi Ngan, except one that was reportedly from Bai Ruong (which may be an alternative



Figure 23. At Khuoi Ngan, near An Phu in northern Vietnam, bright blue spinel is mined from shallow pits by local villagers. Photo by Dudley Blauwet.

name for Khuoi Ngan, as it refers to the same area of rice fields). The largest piece of rough Mr. Blauwet purchased yielded a faceted oval weighing 0.80 ct (figure 25). During his latest visit to Vietnam, in November 2011, he reported very limited production of the intense blue spinel from Khuoi Ngan, in small sizes that would cut stones expected to weigh <0.15 ct.

Mr. Blauwet mentioned that buyers continue to see glass and synthetics in rough and cut gem parcels in Vietnam. After receiving his first shipment of blue spinels from the cutting factory, a 0.26 ct sample was found to be glass. Such imitations can be difficult to identify in the field since the rough material commonly has been tumbled to give the appearance of alluvial pebbles, which also disguises any obvious bubbles or swirl marks. He reported that a Chelsea filter is helpful in such situations: Co-bearing spinel appears pink to red, while glass shows no reaction.

Three faceted samples of Mr. Blauwet’s intense blue



Figure 24. The spinel-bearing soil from Khuoi Ngan is washed and carefully sorted by hand to extract the small pieces of spinel. Photo by Dudley Blauwet.

Khuoi Ngan spinel (0.24–0.80 ct) were examined at GIA’s Carlsbad laboratory. SG values ranged from 3.50 to 3.57, and the RI of the largest stone was 1.716. LA-ICP-MS analyses showed 60–290 ppmw Co. Iron was 7,400–10,500 ppmw, and significant traces of Zn, Ga, Ni, Mn, V, and Li also were recorded. As expected, all three samples appeared red in the Chelsea filter.

Thomas W. Overton
 Andy H. Shen
 GIA, Carlsbad

Trapiche spinel from Mogok, Myanmar. Trapiche growth structure, most commonly observed in emerald, has also been seen in ruby, sapphire, tourmaline, quartz, and andalusite. In January 2011, Bill Larson (Palagems.com, Fallbrook, California) loaned five samples to GIA that were represented as trapiche spinel from Mogok, Myanmar. They were polished into round tablets that ranged from 1.2 to 3.0 cm, and all showed a subtle radiating texture that was more visible with transmitted light. Two pieces (3.64 and 6.76 ct) were characterized by this contributor for this report.

The samples were translucent and ranged from pinkish orange to red with “arms” that were dark gray (e.g., figure 26). Gemological properties of both samples were

consistent with spinel, except for an inert reaction to UV radiation. Raman spectroscopy confirmed the spinel identification. Six arms were easily recognized in each tablet, though the trapiche structure was not well defined. Rather than a core, the 3.64 ct sample contained a point where the arms intersected. The 6.76 ct tablet had an

Figure 25. These spinels from Khuoi Ngan weigh up to 0.80 ct. Photo by Robert Weldon.



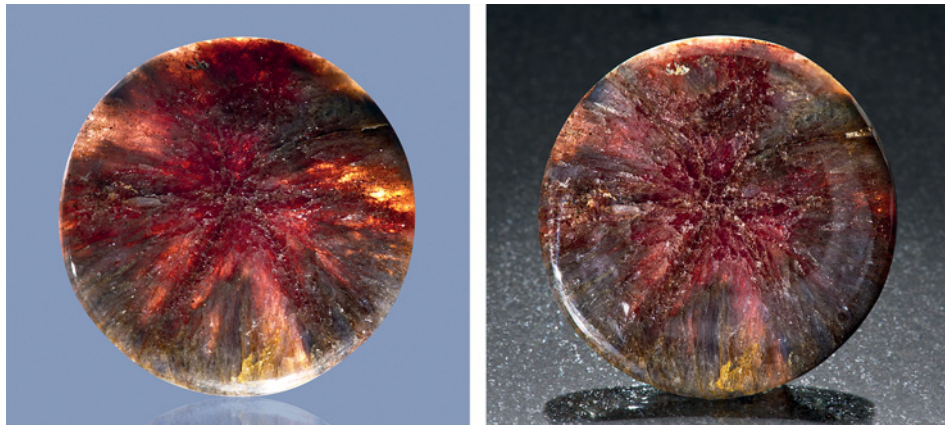


Figure 26. This 6.76 ct tablet of trapiche spinel, reportedly from Mogok, may represent a spinel pseudomorph after ruby. The trapiche structure is not well defined, but the arms are easily recognized, particularly in transmitted light (left). Photos by Robert Weldon.

indistinct core that was cloudy and full of cracks. The arms were created by concentrations of gray wispy clouds and a denser network of cracks than in the surrounding material.

In both tablets, tiny black graphite inclusions (identified by Raman analysis) were visible throughout with a gemological microscope. In the 3.64 ct tablet, minute inclusions of molybdenite, magnesite, goethite, and hematite were detected in the arms (e.g., figure 27; see the *G&G* Data Depository for more images). Hematite crystals were found between the arms, and hematite, magnesite, molybdenite, and calcite were found along the outer rim of the samples. In the 6.76 ct tablet, dolomite crystals were detected in the core and the arms; goethite crystals were identified between the arms and in the rim. Notably, Cr³⁺ photoluminescence bands at 692 and 694 nm, which are characteristic of ruby, were detected in one tiny included crystal along the rim of this sample (figure 28).

Numerous cracks and cavities were observed throughout the tablets. DiamondView images revealed bright blue and purple zones in the cracks, while the host spinel showed a faint blue color. In the 3.69 ct tablet, orange-red stains were seen with the microscope inside the fractures between the arms. Qualitative EDXRF analysis revealed Mg, Al, Ti, V, Cr, Fe, Zn, Ga, Ca, and Mn in both samples.

The spinels had not been exposed to heat treatment, as confirmed by their PL spectrum, which featured a sharp band at 685 nm.

Similar samples of trapiche spinel from Myanmar were characterized by M. Okano and A. Abduriyim ("Trapiche spinel," *Gemmology*, Vol. 41, No. 485, Issue 2, 2010, pp. 14–15 [in Japanese]), who suggested that the trapiche structure formed during the growth of tabular spinel crystals. A pseudomorphic origin of this trapiche spinel after ruby is also possible, and is supported by the remnant ruby inclusion detected in one of the samples.

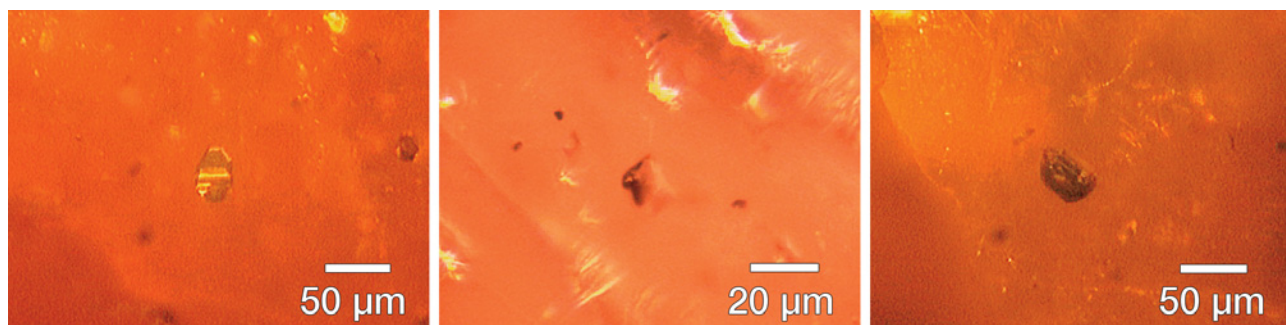
Editor's note: Consistent with its mission, GIA has a vital role in conducting research, characterizing gemstones, and gaining knowledge that leads to the determination of gemstone origins. The samples studied in this report are not subject to the Tom Lantos Block Burmese JADE Act of 2008, and their import was in accordance with U.S. law.

Kyaw Soe Moe

SYNTHETICS AND SIMULANTS

"Cat's-eye pearls": Unusual non-nacreous calcitic pearl imitations. Imitations of non-nacreous pearls are abundant in the market. They can be made of just about any materi-

Figure 27. Micro-inclusions in the trapiche spinel identified using Raman spectroscopy included a molybdenite crystal along the rim (left), a rhombohedral magnesite crystal in an arm (center), and a dark-appearing calcite crystal along the rim (right). Raman microscope photomicrographs by K. S. Moe.



PHOTOLUMINESCENCE SPECTROSCOPY

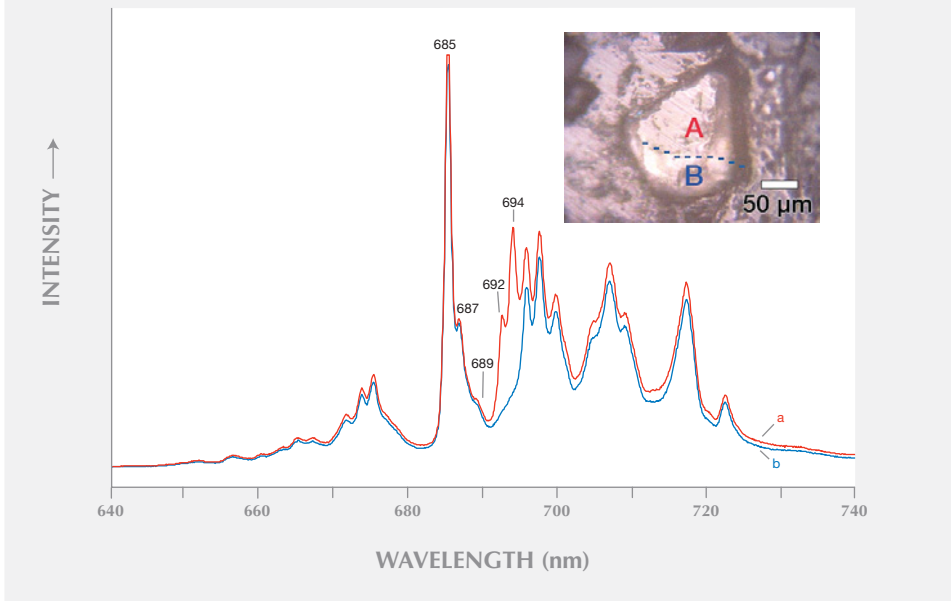


Figure 28. Photoluminescence spectroscopy detected remnants of ruby in the 6.76 ct trapiche spinel. In the Raman microscope image (inset, by K. S. Moe), the light reflected from region A is slightly different from region B. Interestingly, region A showed ruby PL bands at 692 and 694 nm in addition to spinel PL bands at 685, 687, and 689 nm; region B showed only spinel PL bands, as recorded at several other spots on the sample.

al but are usually sculpted from shell. Shells thick enough to yield such pearl imitations are rather common, though generally they are restricted to aragonitic mollusks such as *Strombus sp.*, *Tridacna sp.*, and *Cassis sp.* Calcitic shells, including those of *Pinna sp.* and *Atrina sp.*, tend to be thin and are therefore not suitable. Shell imitations show a layered structure when viewed with strong transmitted light,

making them easy to identify.

This contributor recently received for testing six unusual black “pearls” (figure 29) from two different clients. Represented as non-nacreous natural pearls, the pieces weighed between 2.52 and 10.26 ct and exhibited chatoyancy when illuminated with an intense light source. The chatoyancy was displayed all around the

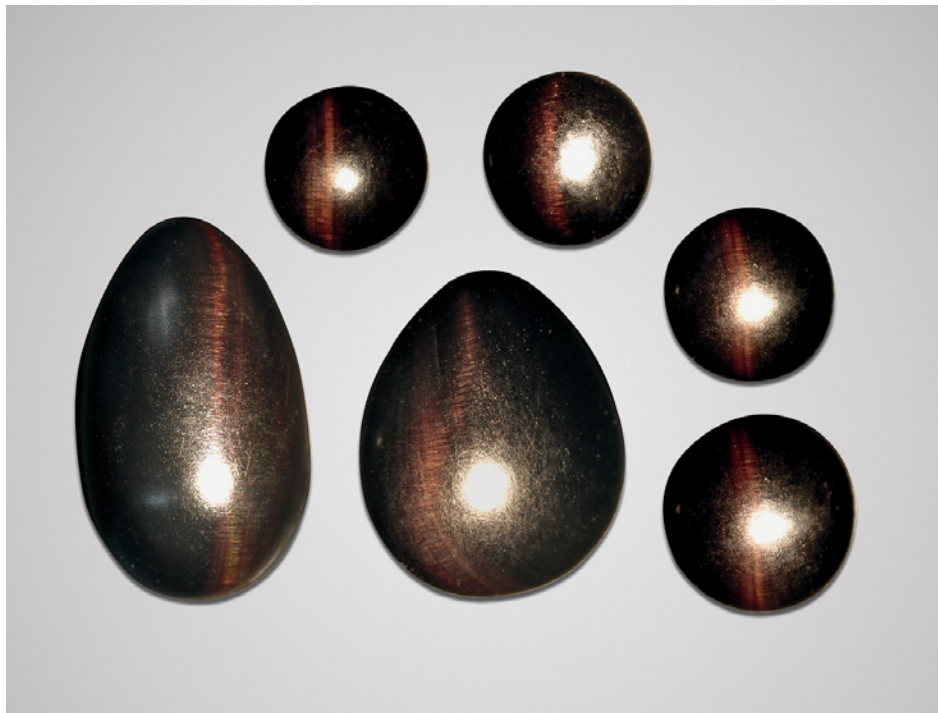


Figure 29. Represented as non-nacreous natural pearls, these sculpted pieces of shell (2.52–10.26 ct) exhibit distinct chatoyancy. Photo by T. Hainschwang.

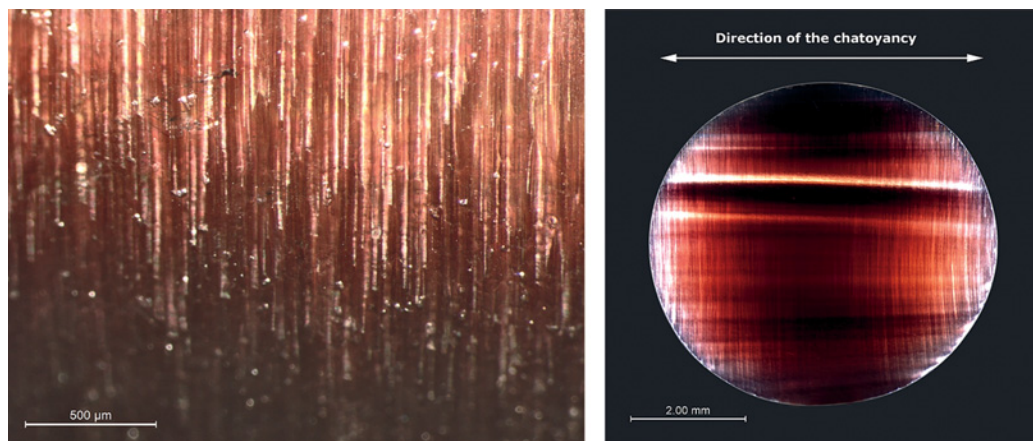


Figure 30. The sculpted shell's fibrous structure is clearly visible with magnification (left). The thin polished section on the right displays a layered appearance in transmitted light that is expected for shell. Photomicrographs by T. Hainschwang.

samples when they were rotated about an axis perpendicular to the band, but it was not visible along this axis. The phenomenon was caused by light reflections from their fibrous structure (figure 30, left). Viewed from the side, no fibrous structure was visible, but hexagonal outlines of the fibers could be seen. These parallel layers of very fine hexagonal prisms are characteristic of calcitic pearls and shell. As expected, reflectance infrared spectroscopy identified the samples as calcite. Distinct concentrations of Sr, detected by EDXRF chemical analysis, confirmed that they were of marine origin.

The surface of the samples showed obvious polishing lines, a common feature in polished and worked non-nacreous natural pearls. The telltale layered structure of sculpted shell was not visible since the samples were practically opaque to strong fiber-optic light. X-radiographs did not reveal any structure, which is very unusual for brown to black calcitic natural pearls; those from Pinnidae mollusks typically show distinct concentric structures.

Because the orientation of the prismatic fibers and the resulting chatoyancy clearly indicated a layered structure, and none of the properties were consistent with natural pearls, these objects could only be sculpted shell. To more closely examine the layered structure of these "cat's-eye pearls," we were granted permission to grind down one of the smaller samples until it was transparent. This section displayed a distinct layered structure perpendicular to the direction of the fibrous prismatic calcite crystals (figure 30, right), as expected for shell.

Having confirmed that these "cat's-eye pearls" were sculpted from calcitic shell, the question remained: Which mollusk could form a dark brown to black shell thick enough to cut a 10 mm pearl imitation? After some research, we found a private collection with a few massive shells from *Atrina vexillum* (a pen shell) that were thick enough to cut pearl imitations such as the ones described in this report.

Thomas Hainschwang
(thomas.hainschwang@ggtl-lab.org)
GGTL Gemlab–GemTechLab
Balzers, Liechtenstein

Large synthetic quartz. Recently, the Gübelin Gem Lab received four large gems (figure 31) submitted for analysis by Erwin Walti (Oetwil am See, Switzerland). They were represented as amethyst (surprising for a dark green gem), aquamarine (greenish blue and light blue concave cuts), and citrine (yellow oval cut), and they weighed 162.00, 33.20, 36.30, and 38.40 ct, respectively. To improve workflow, the laboratory occasionally puts stones through more advanced analyses, such as FTIR and EDXRF spectroscopy, prior to gemological testing. Such was the case with these samples.

We noticed immediately that the analytical data did not match either natural quartz or aquamarine. All four FTIR spectra showed total absorption below approximately 3600 cm^{-1} and only a weak, broad absorption band at 5196 cm^{-1} (e.g., figure 32). These IR features are consistent with those reported for some synthetic quartz (e.g., P. Zecchini and M. Smaali, "Identification de l'origine naturelle ou artificielle des quartz," *Revue de Gemmologie a.f.g.*, Vol. 138–139, 1999, pp. 74–83). EDXRF spectroscopy of all four stones showed major amounts of Si with traces of Fe. The dark green sample also contained small but significant amounts of cobalt (0.005 wt.% Co_3O_4), indicative of synthetic origin, while the yellow sample showed traces of calcium (0.068 wt.% CaO). All other measured elements were below the detection limit.

Microscopic examination of the dark green gem showed a colorless seed plate with fine particles on each side (figure 33) and parallel green banding. The other gems were very clean, with only the light blue one showing reflective breadcrumb-like particles. No growth or color zoning was observed in those stones. Refractive indices were 1.54–1.55, consistent with quartz, and Raman analysis of the light blue and the yellow samples confirmed this identification. We therefore identified all four samples as synthetic quartz. While synthetic citrine is well known, dark green synthetic quartz is less common, and the aquamarine-like color varieties reported here are not often seen in the market.

Lore Kiefert (l.kiefert@gubelingemlab.ch)
Gübelin Gem Lab, Lucerne, Switzerland

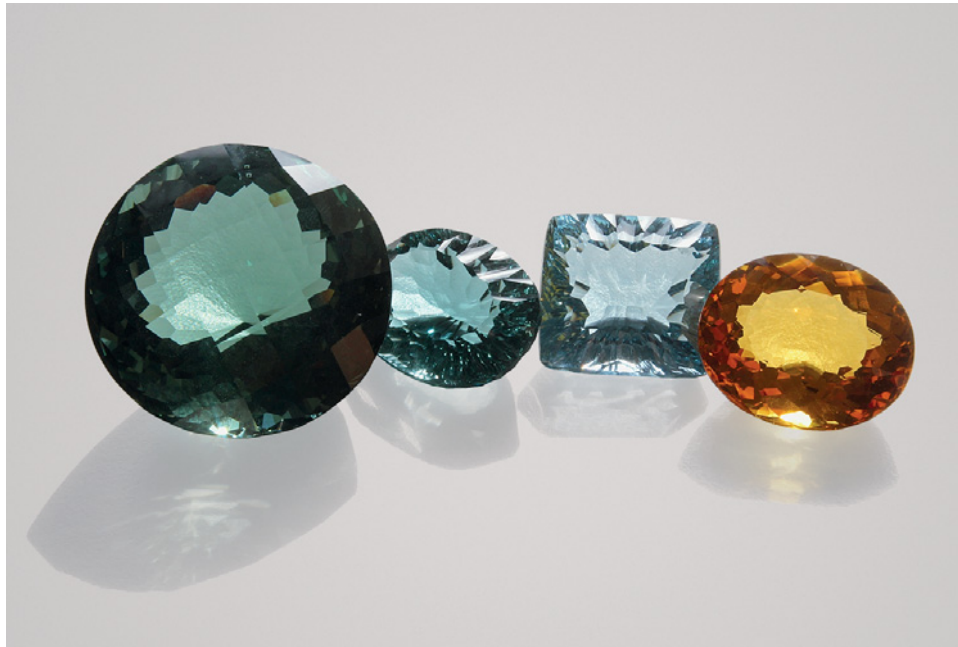


Figure 31. These large faceted samples, submitted as amethyst (even though dark green), aquamarine, and citrine, proved to consist of synthetic quartz. The largest weighs 162 ct. Photo by Evelyne Murer, © Gübelin Gem Lab.

TREATMENTS

Sugar-acid treatment of opal from Wollo, Ethiopia. Several gemological laboratories have recently identified “black” opals from Ethiopia’s Wollo Province as smoke treated (e.g., www.stonegrouplabs.com/SmokeTreatmentinWolloOpal.pdf). The effectiveness of the smoke treatment is probably related to the hydrophane character that is commonly shown by Wollo opal. The porosity allows the smoke to penetrate the opal structure deep enough to create a dark bodycolor. Accordingly, one of us (FM) investigated the possibility of treating Wollo opal using a sugar-

acid process similar to that used for matrix opal from Andamooka, Australia.

For this experiment, we chose 12 mostly low-grade

Figure 32. This FTIR spectrum of the synthetic citrine is representative of all the synthetic quartz samples. It shows a cutoff at $\sim 3600\text{ cm}^{-1}$ and a small band at 5196 cm^{-1} .

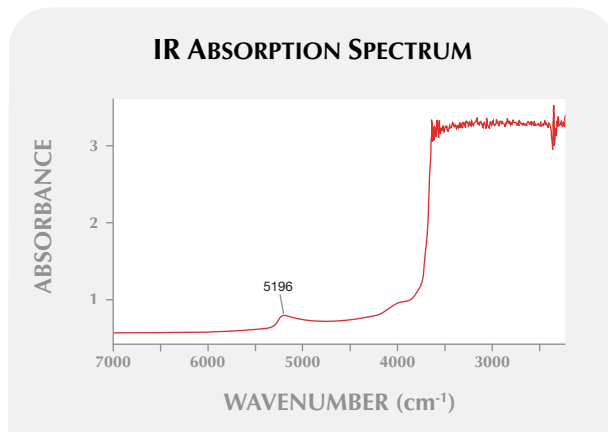


Figure 33. A close-up view of the dark green sample shows a seed plate (defined by arrows) and numerous fine particles. Photomicrograph by Lore Kiefert, © Gübelin Gem Lab; magnified 20 \times .

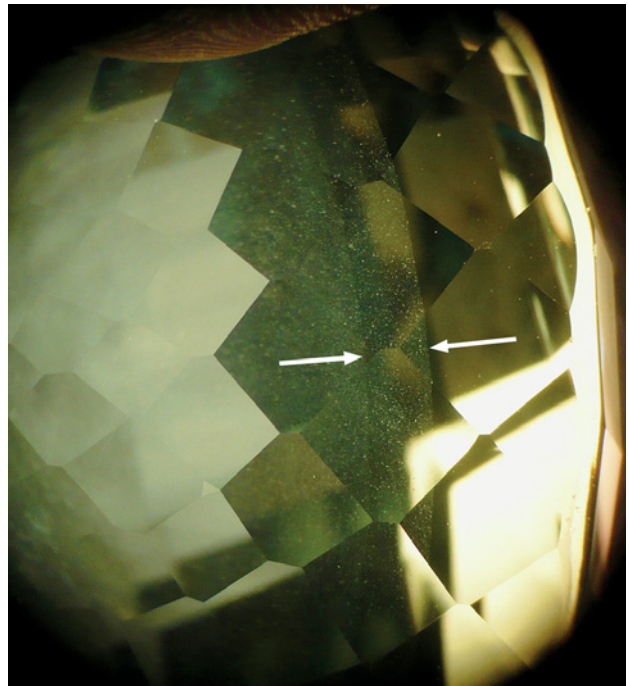




Figure 34. These opals from Wollo, Ethiopia, are shown before (left) and after (right) sugar-acid treatment. Darker bodycolors were produced in samples with a greater hydrophane character. The broken opals (center-right and bottom-left) show the shallow penetration depth of the treatment. The samples measure from 13 × 9 × 7 mm (lower right) to 29 × 16 × 10 mm (upper left). Photos by F. Mazzero.

opals tumbled as irregular pebbles, with a white to yellowish white bodycolor typical for opals from Wollo (figure 34, left). The samples were first heated at 90°C for 2 hours in a solution containing 25% sugar by weight. Next they were heated at 100°C for 3 hours in a 60% solution of hydrochloric acid. All the opals turned a darker color (figure 34, right). Some acquired a homogeneous, opaque, black bodycolor, while others darkened unevenly from grayish brown to gray. The play-of-color became more intense in some samples and less vivid in others. Two of the opals were broken open, revealing that the dark coloration penetrated only a few millimeters into the stones. The samples with the greatest hydrophane character (as indicated by their ability to stick to the tongue) showed the darkest colors after treatment. Conversely, the more transparent and least hydrophane-like opals were least affected by the treatment (e.g., inner portion of the upper-right sample in figure 34). As expected, the hydrophane character appears to have facilitated the penetration of the sugar and acid solutions into the opal.

Even darker coloration in hydrophane opal may be attainable by varying the carbon source and its concentration, the nature of the acid and its concentration, and finally the temperature and duration of heating in both solutions. Such experiments are in progress, and the results will give gemologists a better idea of what to expect for future treatments of this prolific type of opal.

Benjamin Rondeau (benjamin.rondeau@univ-nantes.fr)

Emmanuel Fritsch

Francesco Mazzero

Opalinda, Paris

Jean-Pierre Gauthier

Centre de Recherches Gemmologiques, Nantes, France

CONFERENCE REPORTS

32nd International Gemmological Conference. The biennial IGC was held July 13–17, 2011, in Interlaken, Switzer-

land. More than 70 gemologists from 31 countries gathered to discuss developments in the field. The organizing committee was led by Dr. Michael Krzemnicki, in collaboration with colleagues at the Swiss Gemmological Institute SSEF, the Swiss Gemmological Society, George and Anne Bosshart, and Dr. Henry A. Hänni. The conference featured 12 sessions on topics ranging from colored stones to pearls and diamonds, analytical methods and gem treatments, and special sessions on Canadian gems, rare stones, and organic materials. The 48 talks and 14 interactive poster presentations covered a wide range of topics and regions. The conference proceedings and excursion guides are available at www.igc2011.org; some of the presentations are summarized below.

Dr. Thomas Armbruster (University of Bern, Switzerland) delivered the opening keynote address on gemology's position at the interface of mineralogy and crystallography. Using the beryl group as an example, he demonstrated the similarities and differences in the crystal structures within this group of minerals. **Dr. Karl Schmetzer** (Petershausen, Germany) described chemical zoning in trapiche tourmaline from Zambia, which is characterized by a strong negative correlation between Ca and Na. **Dr. Jürgen Schnellrath** (Centro de Tecnologia Mineral, Rio de Janeiro) discussed unusual fiber distribution patterns in Brazilian cat's-eye quartz. **Dr. Shang-i Liu** (Hong Kong Institute of Gemmology) presented results of a study on Cs- and Li-rich beryl from Madagascar, using electron microprobe, LA-ICP-MS, FTIR, Raman analysis, and electron paramagnetic resonance spectroscopy.

The pearl session included presentations by **Dr. Michael S. Krzemnicki** on formation models for Tokki cultured pearls, which form as attachments to larger beaded cultured pearls; **Nick Sturman** (GIA, Bangkok) on separating natural from cultured Queen conch pearls (*Strombus gigas*); and **Federico Bärlocher** (Farlang, Cernobbio, Italy) on the production and trade of Melo pearls from Myanmar.

Walter Balmer (Department of Geology, Chulalongkorn University, Bangkok) addressed the characterization of rubies from marble deposits in Myanmar (Mogok), Vietnam (Luc Yen) and Tanzania (Morogoro and Uluguru Mountains) using UV-Vis spectroscopy. **John Koivula** (GIA, Carlsbad) showed how high-temperature fusion of corundum mimics residues in heat-treated rubies and sapphires. **Terry Coldham** (Sapphex, Sydney) advocated greater cooperation between researchers and producers in shedding light on the genesis of basaltic sapphires. **Edward Boehm** (RareSource, Chattanooga, Tennessee) offered insight into current colored stone market trends, and **Brad Wilson** (Alpine Gems, Kingston, Canada) described a wide variety of recent finds on Baffin Island, Canada.

Dr. Thomas Pettke (University of Bern) gave the conference's second keynote talk, in which he reviewed LA-ICP-MS applications and offered an outlook on the potential of this method in gemology. The poster sessions gave insights into current research, including presentations on jadeite trading in China (**Elizabeth Su**, DuaSun Collection, Shanghai) and rare-earth coloration in bastnäsite (**Dr. Franz Herzog**, Swiss Gemmological Institute SSEF, Basel).

The conference was preceded by excursions to the Natural History Museum in Bern and mineral localities in the Ticino Alps. A three-day trip to the Binn Valley and Zermatt immediately followed the conference. Both tours took participants to areas of mineralogical and geological interest in Switzerland. Adopting Dr. Nguyen Ngoc Khoi's proposal, the delegates unanimously decided to hold the 2013 IGC in Vietnam.

*Laurent Cartier (igcswitzerland@gmail.com)
Swiss Gemmological Institute SSEF, Basel*

2011 NAG Institute of Registered Valuers Conference. The National Association of Goldsmiths IRV 23rd annual conference took place September 24–26 at its usual venue, Loughborough University, Leicestershire, UK. Approximately 150 delegates attended the various presentations, including hands-on workshop sessions.

Market trends and industry issues were discussed by **Richard Drucker** of Gemworld International (Glenview, Illinois). He explained how the market is changing locally and internationally with China and India now becoming

the predominant buyers, and how these global influences are pushing some diamond and gem prices to new heights. A round-up of the auction market, including information on commissions and insurance, as well as recommendations on how to best work in the auction world, was presented by **Stephen Whittaker** of Fellows & Sons (Birmingham, UK). He also explained the use and costs of technology in the auction business.

The focal point of the conference was introducing a new valuation qualification, CAT (Certificate of Appraisal Theory), which was presented by **Heather McPherson**, a Fellow of the NAG Institute of Registered Valuers (Coalville, UK). This training program is intended to replace the JET (Jewellery Education & Training) valuation course and will be launched by spring 2012 as a new requirement to become an Institute Registered Valuer.

Harry Levy, president of the London Diamond Bourse, explained the valuation of diamonds and colored stones, with information on nomenclature, treatments, and origins. The importance of treatment disclosure was the main theme of his presentation. **Steve Bennett** of GemsTV (Worcestershire, UK) described how education, training, and vertical integration have been the key factors in his family-run business.

*Mehdi Saadian (mehdi@gialondon.co.uk)
GIA, London*

ERRATA

1. For figure 1 of the Fall 2011 CVD synthetic diamond article by B. Willems et al. (pp. 202–207), the correct photographer of the images in this composite photo was Jian Xin (Jae) Liao.
2. Figure 18 of the Fall 2011 Vietnamese corundum article by N. N. Khoi et al. (pp. 182–195) shows the absorption spectrum of a sapphire, rather than a ruby. *G&G* thanks Nathan Renfro for this correction.
3. The Fall 2011 GNI entry by D. Beaton (pp. 247–248) should have indicated that the strong absorption peaks at 376 and 386 nm were attributed to Fe³⁺ pairs (376 nm) and Fe³⁺ (386 nm). *G&G* apologizes for introducing errors in the peak assignments, and thanks Nathan Renfro for the correction.

EDITORS

Susan B. Johnson
Jana E. Miyahira-Smith

G&G

Online Book Reviews

The Diamond Compendium

By DeeDee Cunningham, 888 pp.,
illus., publ. by NAG Press, London,
2011. US\$225.00

This hardcover tome of nearly 900 pages is filled with pertinent illustrations. The book is comprised of 20 chapters divided into sections that cover all aspects of diamonds: origin, crystallography, global occurrences, exploration, mining methods, cutting, polishing, grading, and identification. Simulants and synthetic diamonds are also reviewed.

The compendium is not meant to be read cover to cover; it is a reference work to be consulted on specific topics, some of which are explored in greater scientific depth. As expected from a highly skilled gemologist and jeweler, the sections on crystallography, physical properties, cutting, polishing, and grading are the strongest, while the text on global occurrences contains a few inaccuracies. For instance:

- The Lomonosov kimberlite cluster, 100 km north of Arkhangelsk in northwestern Russia, is not close to the Finnish border but 500 km to the east of it.
- The Golconda alluvial diamond field is not located near the ancient Golconda fortress but at least 250 km to the southeast.
- No kimberlites or other primary diamondiferous rocks have ever been found in Guyana, and certainly not the 14 kimberlites quoted on page 119.

There is also a slight problem on page 207, in the paragraph on airborne prospecting. Most airborne prospecting is carried out to detect local differences in the earth's magnetic field caused by mineral deposits (such a survey is shown in photo 5.1). The two sentences about Falcon technolo-

gy for airborne gravity gradient surveying are out of place and should be reworked to avoid confusion with magnetic surveying. Apart from these items, the information is well researched and clearly written.

The author takes great care in presenting the correct terminology. She explains the different meanings of *form* and *habit* in crystallography, and why lonsdaleite (a hexagonal polymorph of diamond) is not a kind of diamond but a different mineral. The chapters on evaluating carat weight, clarity, color, and cut offer useful tips on how to hold and angle the diamond for best results. The chapter on color examines how color is perceived, while others review color treatments and recutting to enhance brilliance. The chapters on identification of natural diamond, simulants, and synthetic diamond are very good.

The Diamond Compendium took seven years to compile, and the information is up to date to 2007. The wide range of topics makes it an important reference source and handbook with practical tips for use in gemology.

A. J. A. (BRAM) JANSE
*Archon Exploration
Carine, Western Australia*

Precious Objects: A Story of Diamonds, Family, and a Way of Life

By Alicia Oltuski, 370 pp., publ. by
Scribner, New York, 2011. US\$24.00

Book editors often say every story has been told before, so the secret of a good book lies in the telling. Certainly, the past two decades have seen numerous books describing how diamonds are formed deep within the earth, how De Beers gained control of rough diamond production, how stones are bought and sold, and their

role in the corridors of luxury—and in civil conflict. But Ms. Oltuski, whose father and grandfather were both diamond dealers, understands the book editors' maxim and manages to capture all of these topics honestly and in a deeply personal way to create an engaging, well-written work.

Ms. Oltuski is a skilled writer who can transform the everyday dealings of a diamond office into entertaining stories, without resorting to the sensationalist tales of chasing multimillion dollar stones and dodging international jewel thieves that other authors have created to pack drama into an essentially mundane buy-and-sell world. The result is a realistic account of New York's diamond community, down to the duct-taped jewelry cases.

The early chapters focus on the art of the deal. Stories are told of her father's negotiations with clients (who's fibbing and who's really offering genuine prices), her mother's stops to help with stone deliveries on the way to her own job, the weight her grandparents' reputation still carried years later, and a childhood where security and secrecy came home from the office.

In the middle chapters she artfully weaves in personal anecdotes and observations to transform the oft-told clichés about New York's diamond industry into fresh, appealing reading. The accounts of how diamonds are formed deep beneath the earth, the workings of De Beers's sight system (albeit a bit out of date in today's multi-source environment), the mores of the Hasidic Jewish community, and 47th Street's love-hate relationship with Martin Rapaport's price list—they are all here, but in a new dress.

Her portrait of her grandfather Yankel ("Jack" to the New Yorkers) is an intimate account of how diamond families came into being after the

upheavals of World War II. Yankel was a natural trader, scratching a living in post-war Europe by scrounging scarce items and swapping them for merchandise he could swap for even more goods. That led him to diamonds. Yankel's story is one of survival, like that of many New Yorkers from his generation who had come there to begin life anew and raise a family. The stories of those who experienced the horrors of war, the Holocaust, and mass displacements cannot be told often enough before they pass on.

In the end, Ms. Oltuski's book is an honest look at the diamond trade. And in telling this story, it becomes obvious that the book's real precious objects are not the gemstones, but her family members and the other men and (few) women who inhabit New York's diamond district.

RUSSELL SHOR

*Gemological Institute of America
Carlsbad, California*

Diamonds in Nature: A Guide to Rough Diamonds

*By Ralf and Michelle C. Tappert,
142 pp., illus., publ. by Springer
Verlag, Heidelberg, Germany, 2011.
US\$60.00*

Husband-and-wife team Ralf and Michelle Tappert offer a prime example of how a scientific text should be written and illustrated. The subject matter is handled in clear, concise sentences accompanied by Mr. Tappert's superb photographs. As it says in the foreword, there are many books that discuss diamond's optical, physical, and gemological properties, but few on rough diamonds and how they appear in nature. *Diamonds in Nature* does exactly this and does it admirably well.

This book is not for the general reader but for diamond gemologists and geologists. It gives a comprehensive account of every feature of rough diamonds, including their origin, morphology, colors, surface textures, and

mineral inclusions. The glossy text is accompanied by photos and diagrams, more than 300 references, and a helpful index. The authors avoid confusing and excruciating detail and provide references to relevant literature for further particulars.

Everything gets a mention. The "Origin" chapter, for instance, discusses cratons, diamonds from lithospheric mantle roots to upper parts of the lower mantle, types of diamond, diamonds in metamorphic crustal rocks from Kokchetav to Jack Hills, diamonds in impact structures and meteors, and presolar specimens. The "Morphology" chapter recognizes three major types: monocrystalline, fibrous, and polycrystalline (including types of carbonado). Habits are divided into regular, irregular, twins, and macles, and photos show representative crystals. In the "Colors" chapter there are details on colorless, yellow, blue, brown, pink, purple, green, and brown-spotted diamonds. Well-chosen photos in the "Surface Textures" chapter show various surface features occurring preferentially on certain crystal faces, such as terraces, hill-ocks, micro-disks and micro-pits, frosting, ruts, edge abrasion, scratches, and percussion marks. The "Inclusions" chapter recognizes three types by origin (protogenetic, syngenetic, and epigenetic) and four types by mineralogy (peridotitic and eclogitic suites as lithospheric inclusions, an asthenosphere/transition zone suite, and a lower mantle suite as sublithospheric inclusions).

The volume also contains a list of unconfirmed and rare mineral inclusions, with a selected reference for each. Mineral inclusions of all types are covered in the text, accompanied by beautiful color illustrations. Carbon isotopes and the sources of carbon (organic, mantle, or carbonates) are discussed briefly, as are the ages of diamonds.

In summary, I recommend this thoroughly informative text to all readers interested in the subject of rough diamonds.

A. J. A. (BRAM) JANSE

MEDIA REVIEW

What's Hot in Tucson 2010. DVD (three discs), approx. 6 hours, released by Blue Cap Productions [www.bluecapproductions.com], Marina del Rey, CA, 2011. \$39.95

What's Hot in Tucson 2010—Gems & Jewelry. DVD, approx. 2 hours, released by Blue Cap Productions [www.bluecapproductions.com], Marina del Rey, CA, 2011. \$24.99

What's Hot in Tucson 2010 is the fourth in Blue Cap's series of videos that take viewers behind the scenes of the city's major mineral shows. The three DVDs, cohosted by David Wilber and Bob Jones, provide hours of interviews with mineral dealers at five different venues: the InnSuites hotel, the Pueblo Inn Gem & Mineral Show, the Fine Minerals International house, the Westward Look resort, and the TGMS Main Show at the Tucson Convention Center.

The program highlights the newest and finest minerals in the market, showing superb examples of exotic and classic mineral specimens. The cohosts are subject experts, and the interviews provide valuable information about the specimens, such as locality, formation, and mining techniques. The production values are high, allowing the viewer to appreciate the minerals' beauty and details.

This video series also includes the first installment of *What's Hot in Tucson—Gems & Jewelry*, which offers an insider's look at the American Gem Trade Association show at the Tucson Convention Center. The AGTA GemFair is where many of the year's trends and new products debut. This segment is hosted by Delphine Leblanc, who conducts interviews on the floor with some of the biggest names at the show, including cutters, designers, and dealers in estate jewelry, specialty colored gemstones, pearls, and colored diamonds.

From novice to expert, there is something for everyone in this eight-hour DVD package.

MICHELE KELLEY

Monmouth Beach, New Jersey

EDITOR

Brendan M. Laurs

REVIEW BOARD

Edward R. Blomgren
Owl's Head, New York

Annette Buckley
Austin, Texas

Jo Ellen Cole
Vista, California

R. A. Howie
Royal Holloway, University of London

Edward Johnson
GIA, London

Michele Kelley
Monmouth Beach, New Jersey

Guy Lalous
Academy for Mineralogy, Antwerp, Belgium

Kyaw Soe Moe
GIA, New York

Keith A. Mychaluk
Calgary, Alberta, Canada

Joshua Sheby
New York, New York

James E. Shigley
GIA, Carlsbad

Russell Shor
GIA, Carlsbad

Jennifer Stone-Sundberg
Portland, Oregon

Rolf Tatje
Duisburg, Germany

Dennis A. Zwigart
State College, Pennsylvania

COLORED STONES AND ORGANIC MATERIALS

Geographical origin classification of gem corundum using elemental fingerprint analysis by laser ablation inductively coupled plasma mass spectrometry. M.-M. Pornwilard, R. Hansawek, J. Shiowatana, and A. Siripinyanond [scasp@mahidol.ac.th], *International Journal of Mass Spectrometry*, Vol. 306, No. 1, 2011, pp. 57–62, <http://dx.doi.org/10.1016/j.ijms.2011.06.010>.

Various market sectors are increasingly asking for origin identification of rubies and sapphires. Because the chemical composition of corundum reflects its geographic origin, fingerprinting techniques based on trace-element analysis are of great interest. Several methods have been used—particle-induced X-ray emission/proton-induced gamma-ray emission (PIXE/PIGE), micro-PIXE, laser-induced breakdown spectrometry (LIBS), and energy-dispersive X-ray fluorescence (EDXRF) analysis—but these techniques are either time-consuming or provide insufficient detection limits.

This study employed laser ablation–inductively coupled plasma–mass spectrometry (LA-ICP-MS), combined with multivariate data analysis, to classify the origin of 58 gem corundum samples. Trace-element concentrations were analyzed by LA-ICP-MS to construct a data matrix, with columns representing the concentration of 10 elements (B, Si, Zn, Ga, Sn, Mg, Ti, V, Cr, and Fe) in each stone. Two multivariate statistical techniques—principal-component analysis from factor analysis and linear discriminant analysis (LDA)—were employed to differentiate and classify the samples.

This approach identified the geographic origin of both homogeneously colored and multicolored corundum samples from six countries. LDA provided good differentiation between rubies from Southeast Asia and Africa, as well as blue sapphires

This section is designed to provide as complete a record as practical of the recent literature on gems and gemology. Articles are selected for abstracting solely at the discretion of the section editors and their abstractors, and space limitations may require that we include only those articles that we feel will be of greatest interest to our readership.

Requests for reprints of articles abstracted must be addressed to the author or publisher of the original material.

The abstractor of each article is identified by his or her initials at the end of each abstract. Guest abstractors are identified by their full names. Opinions expressed in an abstract belong to the abstractor and in no way reflect the position of Gems & Gemology or GIA.

© 2011 Gemological Institute of America

from Madagascar and Nigeria. LDA mapping, with the use of a normalization factor, identified the origin of variously colored corundum with 80% accuracy. *ERB*

Nomenclature of the tourmaline-supergroup minerals. D.

J. Henry, M. Novak, F. C. Hawthorne, A. Ertl, B. L. Dutrow, P. Uher, and F. Pezzotta, *American Mineralogist*, Vol. 96, 2011, pp. 895–913, <http://dx.doi.org/10.2138/am.2011.3636>.

Tourmaline is a chemically complex mineral group that presents challenges for both chemical analysis and mineralogical classification. Tourmalines are typically not differentiated according to mineral species by gemologists because they cannot be distinguished by normal gem testing methods (and in many cases, gem tourmalines are elbaïtes). This mineral supergroup is comprised of 18 species currently recognized by the International Mineralogical Association, represented by the generalized structural formula $XY_3Z_6(T_6O_{18})(BO_3)_3V_3W$. The most common constituents of each site are:

X = Na⁺, Ca²⁺, K⁺, vacancy
Y = Fe²⁺, Mg²⁺, Mn²⁺, Al³⁺, Li⁺, Fe³⁺, Cr³⁺
Z = Al³⁺, Fe³⁺, Mg²⁺, Cr³⁺
T = Si⁴⁺, Al³⁺, B³⁺
B = B³⁺
V = OH⁻, O²⁻
W = OH⁻, F⁻, O²⁻

The tourmaline supergroup can be divided into several groups and subgroups. Alkali, calcic, and X-vacant primary groups are recognized on the basis of their X-site occupancy. Because cations with different valence states can occupy the same site, coupled substitutions of particular cations are required to relate the compositions of the groups. Within a relevant site, the dominant ion of the dominant valence state is used as the basis of nomenclature.

The article describes the major tourmaline groups and the recognized and prospective mineral species they encompass. It defines the concepts central to tourmaline classification and provides a hierarchical approach to determining species nomenclature according to the amount of information available on a specimen's chemical composition. Finally, the authors discuss each of the recognized tourmaline species, providing lists of color-based varietal names as well as obsolete, discredited, or misidentified species. *JES*

Organic gems protected by CITES. S. Karamelas and L.

Kiefert, *InColor*, No. 15, Fall/Winter 2010, pp. 20–23. Organic gems, defined as those formed through biological processes, are often the product of endangered animal or plant substances. Among numerous conventions and treaties governing the local, national, and international trade in endangered species materials, the most widely recognized is the Convention on International Trade in Endangered Species of Wild Fauna and Flora (CITES). Three

appendices in the CITES regulations organize and list the species. Appendix I covers species that are greatly threatened with extinction. Materials from these species (e.g., tortoise shell) can only be traded for exceptional purposes, such as scientific research. Appendix II species are not necessarily facing extinction, but their trade must be controlled to avoid threatening their survival. Elephant ivory is an example of an Appendix II material, and some argue that it should be listed in Appendix I. To meet CITES requirements for legal trade, Appendix II species require a certificate issued by an authority of the country or state of export/import. Species listed in Appendix III are protected in at least one country that has requested other CITES parties' assistance in controlling the trade of that species.

As countries become more familiar with these regulations, many gemological laboratories are seeing an increase in organic gems submitted to determine if they are protected. The distinction can sometimes be made just by using magnification. The presence of Schreger (also known as "engine turn") lines indicates either elephant or mammoth ivory. Mammoth ivory is not protected by CITES because the animal is already extinct, and the angle at which the Schreger lines intersect can be diagnostic for separating it from elephant ivory. The lines are not always apparent under magnification, and more sophisticated (and expensive) instruments such as X-ray computed microtomography can be used for more challenging ivory/mammoth separations. Similar distinctions are needed between *Corallium* vs. *Stylaster* red or pink corals. Growth structures observed with magnification are diagnostic, but these are not always visible. Raman spectroscopy is useful for making this separation.

A large percentage of the protected species currently used as gem materials can be easily identified by well-equipped gemological laboratories. The addition of other species to the CITES appendices will require the use of more sophisticated nondestructive testing methods to separate them. *JEC*

The role of matrix proteins in the control of nacreous layer deposition during pearl formation. X. J. Liu, J. Li, L.

Xiang, J. Sun, G. L. Zheng, G. Y. Zhang, H. Z. Wang, L. P. Xie, and R. Q. Zhang, *Proceedings of the Royal Society B*, 2011, pp. 1–8, <http://dx.doi.org/10.1098/rspb.2011.1661>.

Formed by a biomineralization process, pearl nacre is composed of aragonite platelets and biological macromolecules. The platelets are arranged in continuous parallel layers separated by interlamellar organic sheets and intercrystalline organic membranes. This study focused on the deposition of the platelets on pearl nuclei, and the gene expression of five nacre matrix proteins in the pearl sac during early stages of formation. The authors found that pearls begin forming with irregular CaCO₃ deposition on the nucleus, followed by further deposition that becomes more and more regular until the mature nacreous layer has formed.

The low-level expression of matrix proteins during the irregular CaCO_3 deposition suggests that the process may not be initially controlled by the organic matrix. Instead, significant expression of matrix proteins in the pearl sac was detected 30–35 days after nucleus implantation. This was accompanied by a change in aragonite deposition from large, irregular crystals to smaller, ordered crystals. This ordered deposition was controlled by the organic matrix.

These results suggest that the bioactivities of matrix proteins are critical for nacre formation and pearl development, by controlling the shape, size, nucleation, and aggregation of CaCO_3 crystals. *JES*

Study of structural and valence state of Cr and Fe in chrysoberyl and alexandrite with EPR and Mössbauer spectroscopy. V. S. Urasov, N. A. Gromalova, S. V. Vyatkin, V. S. Rusakov, V. V. Maltsev, and N. N. Eremin, *Moscow University Geology Bulletin*, Vol. 66, No. 2, 2011, pp. 102–107.

The authors investigated the valence and structural distributions of chromium and iron in chrysoberyl. The samples consisted of alexandrite from the Ural Mountains and an unknown deposit, chrysoberyl from Tanzania, and synthetic alexandrite produced by Czochralski, flux, and hydrothermal methods. EPR and Mössbauer spectroscopy were used to determine the valence states, and limited annealing studies in air and argon were performed to determine their impact on structural distributions.

The two Al^{3+} sites in the chrysoberyl structure, M1 and M2, are slightly distorted octahedral voids with differing symmetries and volumes. The authors cite earlier studies to establish that Fe^{3+} cations substitute for Al^{3+} ions in the (larger) M2 sites exclusively. The present work shows that while Fe^{2+} enters the chrysoberyl structure, only some Fe^{3+} enters the structure and the balance exists in other phases such as Fe_2O_3 . The wide range of Fe^{2+} to Fe^{3+} ratios in the various samples indicates crystal formation under a variety of redox conditions.

From the annealing studies, the authors suggest that the proportion of Cr^{3+} occupancy between the M1 and M2 sites is dependent in part on the crystallization temperature. At higher temperatures such as those achieved with synthetic growth techniques or annealing, the ratio of M2 to M1 occupancy increases. One possible rationale the authors propose is thermal diffusion of Cr^{3+} from the M1 site to the M2 site. *JSS*

Tourmaline: The kaleidoscopic gemstone. F. Pezzotta [fpezzotta@yahoo.com] and B. M. Laurs, *Elements*, Vol. 7, No. 5, 2011, pp. 333–338, <http://dx.doi.org/10.2113/gselements.7.5.333>.

This article examines one of the most popular and spectacular colored stones (and this abstractor's favorite gem). Tourmalines are found in virtually every color of the rainbow, including complex and beautifully zoned and occasionally chatoyant crystals. The gem is well suited for a

broad commercial market because it combines beauty, durability, rarity, a variety of sizes and shapes, and an attractive range of price points.

The authors provide a list of tourmaline colors, causes of color, varietal names, and probable species. Due to tourmaline's pronounced and variable dichroism, optimal color is achieved during the cutting process. Further influencing color is natural or laboratory irradiation of some pale tourmalines, which commonly produces vivid pink and red stones, and heat treatment of dark blue or green stones to lighten or intensify their color. Interestingly, gem tourmaline has not yet been synthesized, probably due to its chemical complexity.

Copper-bearing gem tourmaline was discovered in the 1980s in the Brazilian state of Paraíba, and has become one of the world's most desirable gems, largely due to its vivid "neon" blue-to-green and purple hues. The article overviews the geographic locales, coloring mechanisms, and absorption spectra of this tourmaline variety, which can rival diamonds in cost.

Gem tourmalines form in magmatic, pegmatitic environments and in metamorphic rock, with variable geological ages—as recent as 6 million years to between 100 and 550 million years ago. Inclusions mainly consist of trapped fluids, randomly arranged capillary-like tubes, partially healed fractures, and occasional growth tubes.

The article touches on the gem's distinguished and colorful history, including its role in the jewels of royalty. Of particular note are a huge "ruby" (actually red tourmaline) in the great Czech crown of Saint Wenceslas, the specimens in the Kremlin's Treasure Room, and the Dowager Empress Tz'u Hsi's passion for carved pink tourmaline. *ERB*

On the words used as names for ruby and sapphire. L. A. Lytvynov, *Functional Materials*, Vol. 18, No. 2, 2011, pp. 274–277.

This article examines the trade names of ruby and sapphire from different cultures and historical periods. In fact, many names that contain the noun "ruby" preceded by an adjective are not rubies at all, but other varieties of minerals. The author gives the etymology of many of these trade names and a comprehensive chart. *JS*

DIAMONDS

Bistable N_2 -H complexes: The first proposed structure of a H-related colour-causing defect in diamond. J. P. Goss, C. P. Ewels, P. R. Briddon, and E. Fritsch, *Diamond and Related Materials*, Vol. 20, No. 7, 2011, pp. 896–901, <http://dx.doi.org/10.1016/j.diamond.2011.05.004>.

For some time, scientists have thought that hydrogen-related defects in diamond, detectable by spectroscopy, might contribute to their coloration, but the exact nature of these defects has remained unclear. The hydrogen content of diamonds varies widely. In this article, the authors propose a

model for a hydrogenated substitutional nitrogen pair defect (N₂-H), which they predict will exhibit optical absorption above 600 nm and thus contribute to diamond coloration. They suggest that this defect is one of a family of nitrogen-hydrogen defects, which due to covalent nitrogen-hydrogen bonding might explain several absorptions observed in the spectra of diamonds. This defect could exist in both neutral and negative charge states. Structural differences associated with these states may also contribute to the thermochromic and photochromic behavior exhibited by so-called chameleon diamonds. *JES*

Deep mantle cycling of oceanic crust: Evidence from diamonds and their mineral inclusions. M. J. Walter, S. C. Kohn, D. Araujo, G. P. Bulanova, C. B. Smith, E. Gaillou, J. Wang, A. Steele, and S. B. Shirey, *Scienceexpress*, Vol. 334, No. 6052, 2011, pp. 54–57, <http://dx.doi.org/10.1126/science.1209300>.

In plate tectonics, basaltic oceanic crust subducts on lithospheric slabs into the mantle. Seismological studies extend this subduction process down into the lower mantle (>600 km depth), and geochemical observations indicate the return of some subducted oceanic crustal material to the upper mantle (~200–500 km depth) in convective mantle plumes. On the basis of their mineral inclusions, geologists believe that most diamonds found at the earth's surface originated in the lithosphere at depths of less than 200 km.

In this article, the authors analyzed mineral inclusions in “superdeep” type IIa diamonds from the Juina-5 kimberlite in Mato Grosso, Brazil. These unusual diamonds host inclusions with compositions comprising the entire assemblage of mineral phases expected to crystallize from basalt in the lower mantle. Mineralogical evidence indicates that originally homogeneous silicate phases (trapped in the diamonds as inclusions during growth) exsolved into composite mineral assemblages. This unmixing is interpreted as having occurred at a later time during the convective ascent of the diamonds from the lower to the upper mantle. These diamonds record a history of upward transport on the order of 500–1,000 km in the mantle, long before being sampled by kimberlite magmas and brought to the surface. Since the carbon isotopic signature of these superdeep diamonds is consistent with a surface-derived source of carbon, the authors conclude that the deep carbon cycle extends all the way from the crust to the lower mantle. *JES*

Diamond resorption: Link to metasomatic events in the mantle or record of magmatic fluid in kimberlitic magma? Y. Fedortchouk and Z. H. Zhang, *Canadian Mineralogist*, Vol. 49, No. 3, 2011, pp. 707–719, <http://dx.doi.org/10.3749/canmin.49.3.707>.

Because of their lengthy and complex history of growth and dissolution in the earth, diamond crystals display a tremendous variation in their morphology and surface fea-

tures. Based on a study of 330 gem-quality crystals from the Ekati mine in the Northwest Territories of Canada, the authors developed a methodology to distinguish between dissolution events that took place in the mantle versus those occurring in the ascending kimberlitic magma. The authors inferred that the majority of the samples (~72%) exhibited resorption features produced within kimberlite. Approximately 13% experienced resorption in the mantle, while the remainder displayed resorption features produced in both environments.

The diamonds with mantle-generated resorption features had a different thermal history, as evidenced by their lower nitrogen content and greater degree of nitrogen aggregation. The diamonds with kimberlite-induced resorption could be subdivided into two categories: resorption in the presence of either an aqueous fluid or kimberlitic magma. The authors provide photos of diamond crystals that illustrate the various resorption styles. They suggest that diamonds from kimberlite pipes (even those separated by geologic space or time) would be expected to have similar mantle-generated resorption, but might display different magma-generated resorption features depending on the retention or loss of aqueous fluid from the ascending magma. *JES*

Nano and sub-micro inclusions as probes into the origin and history of natural diamonds. J. Purushothaman, P. R. Sajanlal, M. Ponnavaikko, and T. Pradeep, *Diamond and Related Materials*, Vol. 20, No. 7, 2011, pp. 1050–1055, <http://dx.doi.org/10.1016/j.diamond.2011.06.003>.

Of five diamonds examined, one contained a group of micro-inclusions. Non-diamond Raman peaks at 514, 510, and 490 cm⁻¹ were detected in different areas of the stone, suggesting a group of micro-inclusions with various constituents. This was confirmed by a Raman intensity image, which showed bright and dark zones in the range from 750 to 100 cm⁻¹. Energy-dispersive chemical analysis gave the composition of a pyroxene (Fe, Mg, and Ca silicate) with a ternary perovskite structure. It also detected uneven distributions of Cr, Ru, Nb, Co, and Ni throughout the micro-inclusion assemblage. Fe and Cr were clearly observed in mass spectra using laser desorption ionization–mass spectrometry (LDI-MS).

The authors concluded that this diamond was of peridotitic origin, as evidenced by the presence of ferromagnesian pyroxene minerals and Cr, and the absence of aluminum, alkalis, and rare-earth elements. This nondestructive micro-inclusions study showed potential for defining the genesis of not only diamonds but also of other gem materials. *KSM*

Seismic architecture of the Archean North American mantle and its relationship to diamondiferous kimberlite fields. S. Faure, S. Godey, F. Fallara, and S. Trépanier, *Economic Geology*, Vol. 106, No. 2,

2011, pp. 223–240, <http://dx.doi.org/10.2113/econgeo.106.2.223>.

The architecture of the base of the lithosphere beneath cratons in Canada and the United States has been defined for the first time in three dimensions using a high-resolution, Rayleigh wave-phase-velocity, tomographic model of the upper mantle (30–250 km depth). There is remarkable agreement between data obtained from mantle xenoliths and the lithospheric base obtained from this geophysical model. The inferred base also corresponds to the petrologic definition of the boundary between the lithosphere and the asthenosphere.

An important conclusion of this study is that diamondiferous kimberlites are not located over the deepest parts of the cratonic roots (~180–240 km). Rather, they seem to occur most often over the sloping edges of the lithosphere-asthenosphere boundary that surround the deepest part of the cratonic root zone. The starting point for kimberlite magma ascension to the surface originates from these areas at depths of 160–200 km. This depth interval delineates the region of the upper mantle where diamonds should have been stable since the Archean, and over which all known existing and potential future diamond mines in Canada are located. *JES*

A secondary ion mass spectrometry (SIMS) re-evaluation of B and Li isotopic compositions of Cu-bearing elbaite from three global localities. T. Ludwig, H. R. Marschall, P. A. E. Pogge von Strandmann, B. M. Shabaga, M. Fayek, and F. C. Hawthorne, *Mineralogical Magazine*, Vol. 75, No. 4, 2011, pp. 2485–2494.

Copper-bearing elbaite is recovered from pegmatite-related deposits in Brazil, Mozambique, and Nigeria. Chemical analyses of 10 samples from these three geographic sources using the SIMS technique revealed distinct differences in boron and lithium isotope compositions, which offer valuable tourmaline provenance information. The isotopic compositions for these two elements are relatively homogeneous even across chemical- and color-zoned samples. The two isotopes are also within the range of previously published data for granitic and pegmatitic tourmalines. *JES*

Spectroscopic research on ultrahigh pressure (UHP) macrodiamond at Copeton and Bingara NSW, eastern Australia. L. Barron, T. P. Mernagh, B. J. Barron, and R. Pogson, *Spectrochimica Acta A*, Vol. 80, No. 1, 2011, pp. 112–118, <http://dx.doi.org/10.1016/j.saa.2011.03.003>.

Since the 19th century, an estimated one million carats of diamonds (average weight ~0.25 ct) have been mined from numerous secondary placer deposits along the eastern coast of Australia, the vast majority from the Copeton-Bingara area of New South Wales. Most were recovered between 1867 and 1922. The absence of typical indicator minerals in these sedimentary deposits has hampered geologists' efforts to identify the primary sources of the diamonds. Unlike

deposits in other parts of the world, these diamonds apparently did not originate from the subcratonic lithosphere.

Approximately 3,000 diamonds were characterized for this study. Raman spectroscopy of mineral inclusions indicates the diamonds formed under high-pressure conditions in the lower mantle at the termination of subduction of oceanic crust by continental collision. Using IR spectroscopy, the authors distinguished two groups of diamonds according to their nitrogen abundance and aggregation state. They suggest that these two groups originated from different mantle sources and propose the following delivery mechanism. After subduction, the eclogitic host rocks were stranded for a period in the lower mantle under high-pressure conditions where diamond formation took place, and were then exhumed to the upper mantle/lower crust. At some later time, diamonds (along with garnet and pyroxene) were transported to the surface by alkali basaltic intrusions.

The diamonds exhibit evidence of pervasive deformation during growth, resulting in crystal imperfections, strongly aggregated nitrogen, a reduction of the second-order Raman peak that normally would be more intense, and exceptional durability in industrial applications. *JES*

Start of the Wilson cycle at 3 Ga shown by diamonds from the subcontinental mantle. S. B. Shirey and S. H. Richardson, *Science*, Vol. 333, No. 6041, 2011, pp. 434–436, <http://dx.doi.org/10.1126/science.1206275>.

The Wilson cycle describes the set of major plate tectonic processes whereby continental plates were dispersed and then reassembled on the earth's surface. These processes are associated with crustal growth, mountain building, and the occurrence of ore deposits. This multistage cycle has repeated itself throughout geologic time, and its operation since the Precambrian is apparent in the geologic record of crustal rocks. The timing of the start of this cycle has been uncertain, however. Mineral inclusions, encapsulated in diamonds billions of years ago during their formation in the subcontinental lithosphere, may provide information on this fundamental geologic event.

The authors analyzed existing data on 4,287 silicate and 112 sulfide inclusions in diamonds recovered from ancient cratons in Australia, southern Africa, and Siberia. These inclusions were classified, on the basis of their chemical composition, as either peridotitic or eclogitic. Only peridotitic inclusions formed prior to 3.2 billion years ago (Ga), while diamonds with eclogitic inclusions became more prevalent after 3.0 Ga. The researchers concluded that the change in inclusion mineralogy at this time resulted from the capture of eclogite and diamond-forming fluids in the subcontinental mantle due to subduction and continental collision associated with the onset of plate tectonics. The start of the Wilson cycle at 3.0 Ga marked a change from crustal modification by recycling and other near-surface processes to plate tectonics, a shift that has continued to the present day. *JES*

GEM LOCALITIES

Different origins of Thai area sapphire and ruby, derived from mineral inclusions and co-existing minerals.

S. Saminpanya and F. L. Sutherland, *European Journal of Mineralogy*, Vol. 23, No. 4, 2011, pp. 683–694, <http://dx.doi.org/10.1127/0935-1221/2011/0023-2123>.

The authors used SEM-EDS analysis to identify and measure the chemical composition of mineral inclusions in gem corundum from Thailand. The mineral phases in the sapphires included alkali feldspar (sanidine), nepheline, zircon, and spinel (hercynite and magnetite-hercynite). Those identified in rubies included pyrope, diopside (fassaite), and sapphirine.

Based on the composition of these inclusions, the authors conclude that Thai rubies crystallized in the upper mantle in high-pressure metamorphic rocks of ultramafic or mafic composition (they suggest a garnet pyroxenite or granulite). The sapphires had higher Ga, Ti, Fe, Ta, Nb, and Sn contents than the rubies. The authors suggest that the sapphires crystallized in high-grade metamorphic rocks (gneisses), or from magmas of highly alkaline composition, at shallower levels in the lithosphere than the rocks that hosted the rubies. JES

Distinction of gem spinels from the Himalayan mountain belt.

A. Malsy (a.malsy@gubelingemlab.ch) and L. Klemm, *CHIMIA International Journal for Chemistry*, Vol. 64, No 10, 2010, pp. 741–746, <http://dx.doi.org/10.2533/chimia.2010.741>.

Gem spinel deposits in Myanmar (Mogok), Vietnam (Luc Yen), and Tajikistan formed in association with Himalayan orogenesis. Samples from these deposits were investigated by standard gemological testing and LA-ICP-MS. In most of the Mogok spinels, microscopic examination identified apatite and calcite inclusions together with octahedral negative crystals. Dislocation systems and sphene inclusions distinguished samples from Luc Yen. A yellow surface fluorescence to short-wave UV radiation was observed only in samples from Tajikistan. Due to their similar formation conditions, spinels from these sources display few origin-specific characteristics in their trace-element pattern, but Ti, Fe, Ni, Zn, Zr, and Sn differ slightly. The highest Zn concentrations were observed in Mogok material, while samples from Luc Yen had the highest Fe content. Spinel from these deposits can therefore be distinguished by trace-element chemistry. This is especially helpful for gems that show few or no inclusion features. GL

Emeralds from South America—Brazil and Colombia. D.

Schwarz (d.schwarz@gubelingemlab.ch), J. C. Mendes, L. Klemm, and P. H. S. Lopes, *InColor*, No. 16, Spring 2011, pp. 36–46.

Brazil's emerald mines are located in the states of Minas Gerais, Bahia, Goiás, and Tocantins. Most deposits of economic interest are hosted by mica schists. The emeralds' gemological properties directly reflect the geological-mineralogical environment in which they formed. The geologic conditions in the various Brazilian deposits have many similarities, so the emeralds' properties may also overlap. Colombian emeralds have distinctive three-phase inclusions and growth structures, while mica inclusions (biotite-phlogopite) are the most common solid inclusions found in Brazilian stones. Growth phenomena are normally not well developed in Brazilian emeralds.

Chemical analyses of Brazilian and Colombian specimens were acquired by LA-ICP-MS, and several elements (Cr, V, Fe, Na, Mg, Ga, and Cs) are discussed. The V/Cr ratio provides a reliable indication of the origin of color. The absorption spectra of Colombian emeralds normally show variable contributions from both Cr³⁺ and V³⁺. Colombian specimens contain very little iron and generally do not contain bands related to Fe³⁺. Brazilian emeralds have “combination spectra” composed of (Cr³⁺ + V³⁺) and Fe³⁺-related features, as their iron concentration is moderate to high. GL

Host rock characteristics and source of chromium and beryllium for emerald mineralization in the ophiolitic rocks of the Indus Suture Zone in Swat, NW Pakistan. M. Arif, D. J. Henry, and C. J. Moon, *Ore Geology Reviews*, Vol. 39, No. 1/2, 2011, pp. 1–20, <http://dx.doi.org/10.1016/j.oregeorev.2010.11.006>.

The Swat Valley region of northern Pakistan has been an important source of emeralds for the past five decades. The stones have been reported from a number of localities in this area, with the main deposits near Mingora and Gujar Kili. The emeralds are hosted by magnesite-talc-quartz-dolomite assemblages that form part of the extensive sequence of metamorphosed sedimentary and igneous rocks along the tectonic collision zone between the Asian and Indian continental plates. These magnesite-rich rocks are mostly distributed along contacts between serpentized ultramafic rocks and carbonate±graphite-bearing metasedimentary rocks. From their field association and petrographic evidence, they apparently resulted from alteration by carbonate-bearing metamorphic fluids. Late-stage hydrothermal activity in the fissile magnesite-rich rocks produced quartz veins that locally contain emerald, Cr-tourmaline, and Cr,Ni-rich muscovite. Petrographic and mineralogical analysis suggests that the Cr, Ni, and Mg in these minerals were derived by alteration of the original ultramafic rocks. In contrast, the Be and B appear to have been introduced by hydrothermal solutions of igneous origin that invaded the magnesite-rich host rocks. JES

Laos: Land of a million elephants...and sapphires. R. Hughes, A. Ishmale, F. Isatelle, and P. Wang, *InColor*, No. 16, Spring 2011, pp. 12–19.

Near the infamous Golden Triangle, the point where Laos, Myanmar, and Thailand meet, lies the Ban Huay Xai sapphire deposit. The deposit has been a point of geologic interest since 1890, and it saw a brief surge of activity in the 1960s as various mining companies took a passing interest in recovering its small rough material.

In 2006, though, the Lao government partnered with Sino Resources Mining Co., which staked a handful of claims and is now obtaining 200 kg of rough sapphires per month. Mining is done on a shallow level, with most stones uncovered beneath 30 cm of topsoil and 1–1.5 m of overburden. The majority of the stones are small (<3 mm), but their color is exceptional.

Sino Resources is aware that its open-pit mining can be destructive for the environment and the primarily farming-based community. The company has adopted a stance of stewardship and is restoring mined land to its natural state, negotiating with farmers, and investing in training and employing the local community for more than 95% of its labor force. AB

Microstructure and origin of colour of chrysoprase from Haneti (Tanzania). H. A. Graetsch [heribert.graetsch@rub.de], *Neues Jahrbuch für Mineralogie, Abhandlungen*, 2011, Vol. 182, No. 2, pp. 111–117, <http://dx.doi.org/10.1127/0077-7757/2011/0187>.

The green color of chrysoprase is known to originate from a Ni-containing compound incorporated within the microcrystalline structure of chalcedony. However, the nature of the admixed Ni-containing phase is not known precisely, due to the lack of direct evidence from X-ray diffraction or microscopy.

To address this issue, the authors studied chrysoprase from the Haneti-Itiso area in central Tanzania, and comparison samples from Poland and Australia, using optical reflectance spectroscopy, near-infrared absorption spectroscopy, and powder X-ray diffraction. The results showed that the green color of Haneti chrysoprase is caused by the incorporation of trace amounts of gaspeite (a Ni-carbonate mineral) in the microstructure of the chalcedony. Chrysoprase samples from the comparison sources did not show any gaspeite diffraction peaks; their color seems to originate from a different pigment (i.e., inclusions of poor crystallinity). The Haneti chrysoprase has a higher crystallinity of both the microcrystalline quartz matrix and the gaspeite pigment. ERB

Mines and minerals of the Southern California pegmatite province. J. Fisher, *Rocks & Minerals*, Vol. 86, No. 1, 2011, pp. 14–34, <http://dx.doi.org/10.1080/00357529.2011.537167>.

Granitic pegmatites in Southern California have long yielded a variety of gems, including some notable recent discoveries. This nontechnical summary provides an excellent mining history of the region. It is liberally illustrated with impressive specimens of tourmaline, beryl (morganite),

topaz, garnet (spessartine), and spodumene (kunzite). Although much has been written about the district and its legendary discoveries, this article reports on recent finds rivaling those of bygone decades. In particular, considerable gem rough and mineral specimens have emerged from the Cyro-Genie and Oceanview mines in the past 10 years. The region clearly is not depleted, though production is typically cyclical with long intervals of inactivity. KAM

Oscillatory zoned liddicoatite from Anjanaboina, central Madagascar. II. Compositional variation and mechanisms of substitution. A. J. Lussier and F. C. Hawthorne, *Canadian Mineralogist*, Vol. 49, No. 1, 2011, pp. 89–104, <http://dx.doi.org/10.3749/canmin.49.1.89>.

For more than a century, granitic pegmatites at Anjanaboina (~60 km west of Antsirabe) have produced exceptional color-zoned crystals of liddicoatite tourmaline. Slices of these crystals cut perpendicular to the c-axis that exhibit banded, triangular-shaped, or other color zoning patterns are much sought-after by both mineral collectors and jewelry manufacturers. This study was undertaken to analyze by electron microprobe one of these tourmaline slices from core to rim to better understand the changes in chemical composition that accompany the color zoning.

Over the bulk of the crystal, the compositional variation corresponds to two substitution mechanisms:

1. ${}^X\text{Na} + {}^Y\text{M}^* \rightarrow {}^X\text{Ca} + {}^Y\text{Li}$
2. ${}^Y\text{M}^* + {}^Y\text{M}^* \rightarrow {}^Y\text{Li} + {}^Y\text{Al}$

where $\text{M}^* = \text{Fe} + \text{Mg} + \text{Mn}$, and X and Y represent different crystallographic sites in the tourmaline structure.

The analyses reveal a smooth monotonic variation in the concentrations of the principal constituents of the tourmaline, and a superimposed oscillatory variation in several elements—particularly Fe, Mg, Mn, Na, and Ca. This oscillation is manifested as a decrease in the amount of an element until a color zone boundary is reached, at which the concentration rises abruptly, with this same pattern repeated at each boundary. The compositional and color variations are different in the pyramidal and prismatic growth sectors. The authors suggest specific chemical substitutions based on the two mechanisms shown above to explain the observed variations in chemical composition. They conclude that current models for oscillatory zoning in minerals do not fully explain the internal color patterns seen in this tourmaline, and a more appropriate model needs to be developed. JES

Raman microspectroscopy of organic inclusions in spodumenes from Nilaw (Nuristan, Afghanistan). A. Weselucha-Birczynska [birczyns@chemia.uj.edu.pl.], M. Słowakiewicz, L. Natkaniec-Nowak, and L. M. Proniewicz, *Spectrochimica Acta Part A: Molecular and Biomolecular Spectroscopy*, Vol. 79, No. 4, 2011, pp. 789–796, <http://dx.doi.org/10.1016/j.saa.2010.08.054>.

Spodumene crystals from the Nuristan region are among the finest examples of this mineral ever found. Gem spodumene occurs in two main color varieties in Afghanistan: pink to violet (kunzite) and yellowish green. Samples from the Nilaw mine were investigated by microthermometry and Raman spectroscopy. Microthermometry of the primary fluid inclusions indicated crystallization ranges of 300–650°C and 1.5–2.5 kbar. The brine concentration in the fluid inclusions varied from 4.3 to 6.6 wt.% NaCl equivalent salinity. Raman spectra of selected fluid, organic, and solid inclusions were collected in linear or rectangular arrays as well as depth profiles to study their size and contents. The phases documented were calcite, beryl, topaz, and spodumene accompanied by fluid and/or organic inclusions (liquid and gas hydrocarbons) with bands at 2900 cm⁻¹ (C₂H₆-CH₃), 2550 cm⁻¹ (H₂S), and 2350 cm⁻¹ (CO₂, N₂). Also confirmed was the presence of carbonaceous matter (D-band at ~1320 cm⁻¹ and/or G-band at ~1600 cm⁻¹), which developed in the course of transformation of the original hydrocarbons. *GL*

INSTRUMENTS AND TECHNIQUES

Use of the Raman spectrometer in gemological laboratories: Review. L. Kiefert and S. Karamelas (s.karamelas@gubelingemlab.ch), *Spectrochimica Acta Part A: Molecular and Biomolecular Spectroscopy*, Vol. 80, No. 1, 2011, pp. 119–124, <http://dx.doi.org/10.1016/j.saa.2011.03.004>.

The Raman effect was first reported in 1928, and for decades it was used mainly in physics and chemistry. With the availability of Raman microscopes in the mid-1970s, the technique became better suited for geosciences, including gemology. In the 1990s, Raman spectrometers became smaller, more sensitive, and more affordable, expanding their use in gemological laboratories. The technique is now routinely used to establish the identity of an unknown gem, study inclusions, identify treatments, and characterize natural or artificial color in pearls and corals.

Raman spectroscopy offers a nondestructive means of gem identification that does not require any contact with the sample. Identification of subsurface inclusions is also possible in some cases. In the area of gem treatments, the method is used for the detection of emerald fillers; the identification of lead-, barium-, or zirconium-rich glass-fillings (or the presence of fluxes) in corundum; and the detection of heat-treated corundum and HPHT-annealed diamonds.

The authors conclude that Raman spectroscopy has become an indispensable tool for gemological laboratories, and that many new applications are waiting to be found. Future possibilities include the use of the Raman photoluminescence spectroscopy for characterizing colored diamonds and studying the role of rare-earth elements in colored stones. *DAZ*

JEWELRY HISTORY

Emeralds, sapphires, pearls and other gemmological materials from the Preslav gold treasure (X century) in Bulgaria. E. Strack (info@strack-gih.de) and R. I. Kostov, *Bulgarian Academy of Sciences, Bulgarian Mineralogical Society*, Vol. 48, 2010, pp. 103–123.

The Preslav gold treasure was found in 1978 near the town of Veliki Preslav, the second Bulgarian capital during the end of the First Bulgarian Kingdom. The 10th-century treasure belonged to a female member of the royal family and is believed to be of Byzantine origin. Among the gem materials identified are emerald, violet sapphire, pearl, reddish violet garnet, rock crystal, amethyst, and carnelian. The average dimensions of the emeralds in two medallions were 0.5 cm long and 0.6 cm wide; their origin is suspected to be Egyptian or Austrian based on the deposits known at the time and similarities in their morphology, internal features, and inclusions. Fine rutile silk inclusions were identified in the sapphire. As the Indian subcontinent was the main source of gem corundum in antiquity and Early Medieval times, it can be assumed that the sapphires in the Preslav treasure are of an Indian or Sri Lankan origin. The barrel- and baroque-shaped saltwater pearls (average 0.4 cm long and 0.5 cm in diameter), some of them partly decomposed, are thought to originate from the Persian Gulf and the coastal areas of the Indian Ocean. *GL*

JEWELRY RETAILING

Watches and jewellery retailing, executive summary – UK – September 2011. Mintel, www.mintel.com, 10 pp.

This report, available only to Mintel subscribers, forecasts sales of watches and jewelry (not including costume jewelry) in the UK at £4.2 billion (US\$6.6 billion) in 2011, a growth of 3% since 2006. The value of the market shrank by 1% between 2007 and 2009. Mintel suggests that sales will increase by 8% between 2011 and 2016 to reach £4.6 billion (US\$7.2 billion), but there are challenges for both the watch and jewelry sectors.

The watch market faces competition from portable electronic devices that display the time. Based on their consumer research, Mintel calculates the average price people would spend on a watch for themselves in 2011 is £87, a notable 17% decline from £102 in 2010.

The precious metal jewelry market, which accounts for three-quarters of market value, is affected by the soaring gold price, which has decreased volume sales. The volatile price of gold is the main reason behind a 77% reduction in the weight of gold pieces hallmarked in UK assay offices between 2001 and 2010.

Marriages have ebbed to the lowest rate since records began nearly 150 years ago, according to the UK's Office of National Statistics. Demand for engagement and wedding rings have therefore dropped. But gift giving and

receiving remains popular, and the permanence of watches and jewelry will continue to drive sales. *EJ*

PRECIOUS METALS

Determination of gold in jewellery alloys via potentiometric titration: Procedure standardization and results benchmarking. G. Pezzatini, M. Caneschi, M. Innocenti, S. Bellandi, E. Lastraioli, L. Romualdi, and S. Caporali, *Current Analytical Chemistry*, Vol. 7, No. 4, 2011, pp. 277–285, <http://dx.doi.org/10.2174/157341111797183065>.

Potentiometric titration is a volumetric method in which the electrical potential between two solutions is measured as a function of the added reagent volume. The authors recommend this method for the accurate determination of the gold content of jewelry alloys rather than traditional cupellation (i.e., fire assay), which presents serious health and environmental risks.

A wide variety of gold jewelry alloys were dissolved in acid, and the resulting solutions were used in an optimized titration procedure developed by the authors. To evaluate the proposed method, the authors performed experiments in three different laboratories. The results were consistent with data obtained by cupellation, demonstrating that potentiometric titration is a robust and affordable alternative to classic fire assay for testing gold alloy jewelry. *JES*

Microstructure analysis of selected platinum alloys. P. Battaini, *Platinum Metals Review*, Vol. 55, No. 2, 2011, pp. 74–83, <http://dx.doi.org/10.1595/147106711X554008>.

Optical metallography involves the microscopic examination of polished or etched surfaces of metal. The technique can be employed to describe a metal's microstructures both qualitatively and quantitatively. It is often supplemented by other methods, such as SEM-EDS analysis, to more fully characterize a material. In this article, the author describes the metallographic analysis of the internal microstructure of platinum metal alloys similar to those used for jewelry and industrial applications. A number of examples illustrate the visual distinction between these various alloys, and whether the alloy sample was merely crystallized ("as cast") or had been work-hardened and annealed. *JES*

MISCELLANEOUS

Gemstone mining as a development cluster: A study of Brazil's emerald mines. J. A. Puppim de Oliveira, S. Ali, *Resources Policy*, Vol. 36, 2011, pp. 132–141.

Most Brazilian emerald mining is clustered in three areas within the country. The vast majority of mining is small

scale, bringing little direct benefit to local government, while environmental damage and the effects of overpopulation during an emerald "rush" can create lasting problems. And without tax revenues from mining, local governments have no incentive to offer improved health and living standards to miners. The authors propose several solutions to mitigate these conditions, including: (1) bringing in outside investors who are accountable to international standards, and possess technology for more efficient and less destructive mining; (2) introducing corporate governance standards; (3) encouraging miners' cooperatives that will pay taxes and provide incentive for governments to create services; and (4) developing local markets to realize higher returns. *RS*

Potential for modernization of small-scale gemstone miners—The case of the tsavorite mines in southeast Kenya. C. Simonet, *InColor*, No. 16, Spring 2011, pp. 22–27.

The exact location of colored stone mineralization is hard to predict, even by applying drilling methods. Thus it is extremely difficult to mechanize the mining of colored stones, especially for primary deposits. The low percentage of high-grade material produced from most deposits also contributes to the inability to sustain mechanized mining. Thus, gem miners are still using crude methods that do not meet international standards.

Kenya is one of the leading producers of tsavorite. Mining is mostly done with basic equipment, such as compressors and jackhammers. Challenges include the lack of technical knowledge, the irregularly spaced tsavorite concentrations, and the steeply dipping mineralized zones, resulting in a series of narrow tunnels. As a consequence, gem production is unpredictable and the prices are low. Kenya has many tsavorite deposits with similar structural geometry and geologic characteristics, and this presents a good opportunity to modernize small-scale mining. This initiative would require standard mining procedures, properly defined equipment, and detailed geologic surveys using remote sensing, geophysics, and geochemistry. Other aspects include training miners; providing expertise from geologists, gemologists, and mine engineers; improving access to funding; and branding. Modernization of tsavorite mining would promote market stability and compliance with proper health, safety, and environmental standards.

In recent years, two major gem mining companies have been listed on stock exchanges. This ensured their compliance with international standards of scientific work, mining methods, planning, and governance, including publication of resource estimates and technical studies. This trend is an encouraging sign for the modernization of the colored stone mining industry. *KSM*

SUBJECT INDEX

This index gives the first author (in parentheses), issue, and inclusive pages of the article in which the subject occurs for all feature articles, Notes & New Techniques, and Rapid Communications that appeared in Volume 47 of *Gems & Gemology*. Also included are abstracts of presentations from the Summer 2011 (S11) issue, the proceedings of the Fifth International Gemological Symposium. For the Gem News International (GNI) and Lab Notes (LN) sections, inclusive pages are given for the item. The Book Reviews section is available only as an online supplement, with the page numbers preceded by S. The Author Index (p. S19) provides the full title and coauthors of the articles cited.

A

Afghanistan

- afghanite from Badakhshan (GNI)F11:235
- emerald mining in (GNI)F11:238-239
- sapphire from, beryllium- and tungsten-bearing (LN)Sp11:53-54
- scapolite from (GNI)Sp11:65-66
- sphene from border area with Pakistan, color-change (GNI)W11:327-328

Afghanite

- from Afghanistan (GNI)F11:235

Agate

- dendritic, in jewelry (GNI)Sp11:62-63
- and reconstituted turquoise doublet, marketed as Coral Sea (GNI)Sp11:62

Amethyst

- separation from synthetic, using infrared spectroscopy (Karampelas)F11:196-201
- from southern Brazil (Juchem)Su11:137-138

Amethyst, synthetic

- separation from natural, using infrared spectroscopy (Karampelas)F11:196-201

Ametrine [amethyst-citrine]

- from Bolivia, Anahí mine (Weldon)Su11:163-164

Ammonite

- iridescent, from Madagascar (GNI)F11:235-236

Analytical techniques [general]

- to characterize gem materials (Rossman)Su11:124-125

Andesine

- reportedly from Tibet (Rossman)Sp11:16-30, (Abduriyim)Su11:167-180

Andradite

- demitoid from northern Madagascar (Pezzotta)Sp11:2-14

Annealing, see Diamond treatment

Aquamarine

- from Thanh Hoa, Vietnam (Huong)Sp11:42-48, (GNI)F11:236-237

Aquamarine simulants

- synthetic quartz (GNI)W11:332-333

Argon isotope analysis

- of andesine, from Tibet and other claimed localities (Rossman)Sp11:16-300

Argyle diamond mine

- colored diamonds from (Chapman)Su11:130

Assembled gem materials

- agate and reconstituted turquoise doublet, marketed as Coral Sea agate (GNI)Sp11:62
- corundum and lead-glass triplet (GNI)F11:251-252
- glass triplet imitation of "mystic" treated topaz (GNI)F11:252-253
- opal with artificial matrix (LN)W11:312

Asterism

- artificial (Steinbach)Su11:152-153
- in quartz, caused by cinnabar inclusions (GNI)W11:322-323

Auctions

- of luxury jewelry (Luke)Su11:100-102

Australia

- colored diamonds from Argyle (Chapman)Su11:130
- opal from—Laverton, Western Australia (GNI)W11:319-320; nomenclature and characterization (Beattie)Su11:116
- zircon from, exhibiting tenebrescence (LN)W11:314-315

B

Beryl, see Aquamarine, Emerald

Beryllium

- natural, in blue sapphire—(LN)F11:232-233; from Afghanistan (LN)Sp11:53-54

Beryllium diffusion, see Diffusion treatment

Bolivia

- ametrine from the Anahí mine (Weldon)Su11:163-164

Book reviews

- Collectors Guide to Granite Pegmatites* (King)F11:S4
 - Collectors Guide to Silicate Crystal Structures* (Lauf)F11:S4
 - Colour of Paradise: The Emerald in the Age of Gunpowder Empires* (Lane)Sp11:S2-S3
 - The Diamond Compendium* (Cunningham)W11:S1
 - Diamond Math* (Glasser)F11:S4
 - Diamonds in Nature: A Guide to Rough Diamonds* (Tappert and Tappert)W11:S2
 - The Extraordinary World of Diamonds* (Norman)F11:S1-S2
 - Gems and Gemology in Pakistan* (Khan and Kausar)F11:S4
 - Jewellery from the Orient: Treasures from the Bir Collection* (Siewert)Sp11:S3
 - Living Jewels: Masterpieces from Nature* (Peltason)F11:S1
 - Mineral Treasures of the World* (The Geological Museum of China and The Collector's Edge Minerals Inc.)F11:S4
 - Pearls* (Bari and Lam)Sp11:S1
 - Precious Objects: A Story of Diamonds, Family, and a Way of Life* (Oltuski)W11:S1-S2
 - Terra Spinel Terra Firma* (Yavorsky and Hughes)Sp11:S1-S2
 - Twentieth-Century Jewellery: From Art Nouveau to Contemporary Design in Europe and the United States* (Cappellieri)Sp11:S3
 - What's Hot in Tucson 2010* (Blue Cap Productions)W11:S2
 - The Workbench Guide to Jewelry Techniques* (Young)F11:S2
 - World Hallmarks, Volume I: Europe, 19th to 21st Centuries, 2nd ed.* (Whetstone, Niklewicz, and Matula)F11:S3-S4
- Boxes [article sidebars]**
- andesine from Tibet and other claimed localities—feldspar nomenclature (Rossman)Sp11:16-30; samples and

- experimental details (Rossman)Sp11:16-30
- diamond symmetry—basic measuring concepts (Geurts)W11:286-295; combinations of symmetry features (Geurts)W11:286-295
- magnetic susceptibility—and magnetic materials (Hoover)W11:272-285; measurement of (Hoover)W11:272-285
- Brazil**
- diamond from, black, nature of coloration (Vasilyev)Su11:135
- gemstones from southern (Juchem)Su11:137-138
- opal (or cristobalite?) from, blue (Schnellrath)Su11:142
- spodumene from, green cat's-eye (GNI)F11:249-250
- tourmaline from Pederneira, Minas Gerais (Pezzotta)Su11:141-142
- Burma**, see Myanmar
- C**
- California**, see United States
- Canada**
- diamonds from (Stachel)Su11:112-114
- Carving**, see Lapidary arts
- Cat's-eye**, see Chatoyancy
- "Cat's-eye pearls"**
- non-nacreous calcitic pearl imitations (GNI)W11:330-332
- Cavansite**
- faceted (GNI)Sp11:56-57
- Chalcedony**
- purplish blue and red-brown, from Peru (GNI)F11:237-238
- "Challenge,"** see *Gems & Gemology*
- Chatoyancy**
- in quartz—caused by tourmaline needle inclusions (GNI)F11:245-246; with cinnabar inclusions (GNI)W11:322-323
- in spodumene, green (GNI)F11:249-250
- Chemical composition**
- of andesine, reportedly from Tibet (Rossman)Sp11:16-30, (Abduriyim)Su11:167-180
- of demantoid from northern Madagascar (Pezzotta)Sp11:2-14
- of garnet—(Henderson)Su11:148; determined using magnetic susceptibility (Hoover)W11:272-285
- of zircon, brownish red, from China (Chen)Sp11:36-41
- Chemical vapor deposition [CVD]**, see Diamond, synthetic
- Chemometrics**
- of corundum, in determining geographic origin (Yetter)Su11:157
- China**
- andesine, reportedly from Tibet (Rossman)Sp11:16-30, (Abduriyim)Su11:167-180
- development and tax policy of gem industry in (Jia)Su11:159-160
- freshwater cultured pearls from—beaded with baroque freshwater cultured pearls (GNI)F11:244-245; with exotic metallic colors (Beavers)Su11:144; treatments and their detection (Strack)Su11:120
- nephrite from, natural and treated (Zhang)Su11:122
- sapphire, blue and pink, from Muling (Chen)Su11:136-137
- topaz, neutron-irradiated blue, from Guangdong (Zhang)W11:302-307
- zircon, brownish red, from Muling (Chen)Sp11:36-41
- Chondrodite**
- from Tanzania (GNI)W11:316
- Chrysocolla**, see Chalcedony
- Citrine simulants**
- large synthetic quartz (GNI)W11:332-333
- Clinohumite**
- unusually large (LN)F11:222-223
- Coating**
- on bead-cultured freshwater pearls (LN)W11:313-314
- on diamond—black (LN)F11:223-224; with spectroscopic features of a natural-color pink (LN)F11:224-225
- Colombia**
- dolomite, blue, from Muzo (GNI)W11:316-318
- Color, cause of**
- in natural-color and treated colorless and colored diamonds (Epelboym)Su11:133
- in tanzanite (Smith)Su11:119-120
- in tourmaline from Mt. Marie, Maine (GNI)Sp11:67-68
- Color change**
- sphene, vanadium-bearing, from Pakistan/Afghanistan (GNI)W11:327-328
- Color grading**
- of diamond, nomenclature (Tashey)Su11:163
- dual integrating sphere spectrometer with artificial intelligence (Liu)Su11:154
- Color zoning**
- in andesine, reportedly from Tibet (Rossman)Sp11:16-30, (Abduriyim)Su11:167-180
- in low-grade diamonds (Kwon)Su11:134
- in opal, bicolored (GNI)W11:320-322
- in topaz, yellowish to greenish brown (GNI)F11:250-251
- Colored stones**
- from Brazil, southern (Juchem)Su11:137-138
- discriminant analysis for identifying geographic origin of (Blodgett)Su11:145
- examined at the Gem Testing Laboratory in Jaipur, India (Choudhary)Su11:145-146
- market for (Drucker)Su11:158-159
- marketing of (Overlin)Su11:97-99
- from Mexico, review of (Ostrooumov)Su11:141
- world production of (Yager)Su11:142-143
- Conch pearl**
- large (LN)F11:230-231
- Conferences**
- ICA Congress 2011 (GNI)F11:253-254
- International Gemmological Conference (GNI)W11:334-335
- International Gemological Symposium (Proceedings issue)Su11:79-166
- NAG Institute of Registered Valuers Conference (GNI)W11:335
- Scottish Gemmological Conference 2011 (GNI)F11:254
- Sinkankas Symposium 2011—Diamond (GNI)F11:254-255
- Conflict diamonds**
- debate on (Symposium Debate Center)Su11:126-128
- Congo, Democratic Republic of the**
- andesine reportedly from (Rossman)Sp11:16-30
- Conoscopy**
- technique for identifying interference figures in gem materials (Gumpesberger)Su11:147
- Coral**
- conservation of (Carmona)Su11:158
- Coral Sea agate**
- agate and reconstituted turquoise doublet (GNI)Sp11:62
- Corundum**
- mining in Pakistan (GNI)W11:325-326
- triplet with lead glass (GNI)F11:251-252
- see also Ruby, Sapphire
- Country of origin**, see Geographic origin
- Cristobalite**
- or blue opal(?) from Brazil (Schnellrath)Su11:142
- Cultured pearl**, see Pearl, cultured
- CVD [chemical vapor deposition]-grown synthetic diamonds**, see Diamond, synthetic
- D**
- Demantoid**, see Andradite
- Dentine**, see Odontolite
- Diamond**
- brooch from September 11 attacks (GNI)F11:255-256
- cleaning technology (Vins)Su11:136
- color grading of, nomenclature (Tashey)Su11:163
- color origin, determination of (Epelboym)Su11:133
- color zoning in low-grade diamonds (Kwon)Su11:134
- crystal descriptions, for use in explo-

ration (Klettke)Su11:139
 inclusions in low-grade diamonds (Kwon)Su11:134
 length-to-width ratios among fancy-shapes (Blodgett)Su11:129
 localities, alluvial (Janse)Su11:110
 with luminescent cleavage (LN)F11:226-227
 marketing of (Overlin)Su11:97-99
 mining of—(Coopersmith)Su11:108; in Canada (Stachel)Su11:112-114; in Liberia (GNI)Sp11:63-64
 phosphorescence, long-lasting (LN)W11:310-311
 polished supplies from secondary market sources (Shor)Su11:163
 postage stamp collection (Overlin)F11:214-219
 from Russia's Nurbinskaya pipe, mineralogical characteristics of (Solodova)Su11:134-135
 strain in colorless untreated (LN)F11:224-225
 symmetry grading of—assessments and metrics (Caspi)Su11:153-154; GIA boundaries (Geurts)W11:286-295
 thermoluminescence in type IaB (LN)Sp11:50
 with 3H and H3 defects resulting from radiation damage (Choi)Su11:131
 from Zimbabwe, naturally irradiated (Breeding)Su11:129-130, (Crepin)Su11:105
 see also Diamond, colored; Diamond, cuts and cutting of; Diamond, inclusions in; Diamond, synthetic; Diamond treatment; DiamondView imaging

Diamond, colored
 from the Argyle mine, studies of (Chapman)Su11:130
 black—from Brazil, nature of coloration (Vasilyev)Su11:135; coated (LN)F11:223-224; colored by strong plastic deformation (LN)F11:223; strongly purple-colored (LN)W11:309
 color grading of, nomenclature (Tashey)Su11:163
 color origin, determination of (Epelboym)Su11:133
 Fancy Vivid purple (LN)W11:308
 greenish brown, with a color shift (LN)F11:234-235
 see also Diamond, synthetic; Diamond treatment

Diamond, cuts and cutting of
 to exhibit inclusions (LN)Sp11:50-52
 preferences in length-to-width ratios (Blodgett)Su11:129

Diamond, inclusions in
 in low-grade diamonds (Kwon)Su11:134
 manufactured to exhibit (GNI)Sp11:50-52
 3D mapping systems (Caspi)Su11:153

Diamond, synthetic
 chemical vapor deposition [CVD]—from Gemesis (LN)F11:227-228; luminescent regions in

(Willems)F11:202-207; optical properties of silicon-related defects (D'Haenens-Johansson)Su11:131-132
 HPHT-grown—donor nitrogen aggregation in (Vins)Su11:135-136; pink (Johnson)Su11:133-134
 marketing of (Overlin)Su11:97-99
 treated, with pink color intensified by fluorescence (LN)F11:228-229

Diamond treatment
 characterization of (Epelboym)Su11:133
 coating—black (LN)F11:223-224; with spectroscopic features of a natural-color pink (LN)F11:224-225
 HPHT—discriminant analysis in distinguishing (Blodgett)Su11:145; with fluorescence pattern of an HPHT-grown synthetic (LN)W11:310; large brownish yellowish orange (LN)Sp11:49; large colorless (LN)Sp11:49-50; large pink (LN)F11:227; observation of strain in detecting (Eaton-Magaña)Su11:132; subtle color enhancement (LN)F11:225-226
 irradiation, producing green and orangy brown spots (Nasdala)Su11:105-106
 of synthetics—donor nitrogen aggregation in (Vins)Su11:135-136; pink (Johnson)Su11:133-134; (LN)F11:228-229

DiamondView imaging
 of CVD-grown synthetic diamonds, luminescent regions in (Willems)F11:202-207
 of HPHT-grown pink synthetic diamonds (Johnson)Su11:133-134
 of HPHT-treated diamond with fluorescence pattern of an HPHT-grown synthetic (LN)W11:310

Diffusion treatment
 experiments performed on andesine (Rossman)Sp11:16-30, (Abduriyim)Su11:167-180
 of sapphire with Be—durability and safety testing (Sutthirat)Su11:121; experiments (Wathanakul)Su11:153; pink (LN)F11:232

Discriminant analysis
 of andesine, reportedly from Tibet (Abduriyim)Su11:167-180
 to identify geographic origin of colored stones and HPHT treatment in diamonds (Blodgett)Su11:145

Dolomite
 blue, from Colombia (GNI)W11:316-318

Doublets, see Assembled gem materials

Durability
 of Be-diffused sapphire (Sutthirat)Su11:121
 of lead-glass-filled ruby (Sutthirat)Su11:121

Dyeing
 of Chinese freshwater cultured pearls, detection of (Strack)Su11:120
 of opal from Ethiopia, purple (Renfro)W11:260-270

E

Economy
 global, GIA Symposium keynote address on (Overlin)Su11:80-82

Editorials
 "GIA Symposium 2011: Advancing the Science and Business of Gems" (Kimmel and Keller)Su11:79
 "Great Expectations" (Iverson)W11:259
 "New Beginnings" (Iverson)F11:181

EDXRF, see Spectroscopy, energy-dispersive X-ray fluorescence

Electron-microprobe analysis
 of andesine from various claimed localities (Rossman)Sp11:16-30
 of aquamarine from Vietnam (Huong)Sp11:42-48
 of demantoid from northern Madagascar (Pezzotta)Sp11:2-14
 of ruby and sapphire from Vietnam (Khoi)F11:182-195
 of zircon, brownish red, from China (Chen)Sp11:36-41
 see also Chemical composition

Emerald
 from Afghanistan, mining update (GNI)F11:238-239
 formation of (Giuliani)Su11:108-110
 geographic origin of (de Corte)Su11:147
 inclusions in quartz (GNI)W11:323
 market for (Drucker)Su11:158-159
 separation from synthetic (de Corte)Su11:147
 from Zambia, mining of (GNI)Sp11:63-65

Emerald simulants
 plastic-coated quartz (GNI)Sp11:71-72
 trapiche (GNI)Sp11:68-69

Emerald, synthetic
 separation from natural (de Corte)Su11:147

Enhancement, see Coating; Diamond treatment; Diffusion treatment; Dyeing; Filling, fracture or cavity; Heat treatment; Irradiation; Treatment; specific gem materials

EPR, see Spectroscopy, electron paramagnetic resonance

Errata
 to "CVD synthetic diamond luminescent regions" (Willems)F11:202-207—incorrect photographer (GNI)W11:335
 to "Extreme conoscopy" (Gumpesberger)Su11:147—incorrect caption (GNI)F11:256
 to "Gem treatments retrospective" (McClure)F10:218-240—description of topaz treatment methods (GNI)Sp11:73
 to "Natural-color tanzanite" (Smith)Su11:119—incorrect caption (GNI)F11:256
 to "Sapphire and zircon from Ethiopia" (GNI)F11:247-248—errors in absorption peak assignments (GNI)W11:335
 to "Vietnamese ruby and sapphire"

- (Khoi)F11:182-195—incorrect caption (GNI)W11:335
- Ethics**
debate on (Symposium Debate Center)Su11:126-128
- Ethiopia**
opal from Wollo—black (LN)W11:312-313; dyed purple (Renfro)W11:260-270; play-of-color (Rondeau)Su11:112; sugar-acid treatment of (GNI)W11:333-334
sapphire from (GNI)F11:247-248
zircon from (GNI)F11:247-248
- F**
- Faceting**, see Diamond, cuts and cutting of
- Fair trade practices**
debate on (Symposium Debate Center)Su11:126-128
examples and case studies (Luke)Su11:103-104
- Fakes**, see specific gem materials simulated
- Feldspar**
sunstone from Oregon, comparison of two deposits (McClure)Su11:150-151
see also Andesine
- Filling, fracture or cavity**
of ruby with a lead glass—durability and safety testing (Sutthirat)Su11:121; trapiche (GNI)Sp11:72
- Fluorescence, ultraviolet [UV]**
applications in gemology (Taylor)Su11:125
of an HPHT-treated diamond, with pattern resembling an HPHT-grown synthetic diamond (LN)W11:310
- Fluorite**
from Namibia (GNI)W11:318-319
- France**
odontolite (fossilized mastodon ivory) from (Krzemnicki)W11:296-301
- Fuchsite**
deep green rock (GNI)F11:239-240
- G**
- Garnet**
chemical composition, determination of—using Raman spectroscopy (Henderson)Su11:148; using magnetic susceptibility (Hoover)W11:272-285
color-change, from Tanzania (GNI)F11:240-241
hydrogrossular, green cabochon resembling jadeite (LN)Sp11:52-53
see also Andradite, Grossular
- Gemesis**
CVD-grown synthetic diamonds (LN)F11:227-228
- Geological Institute of America**
Gübelin gem collection, online resource (Shigley)Su11:151-152
Symposium 2011 (Kimmel and Keller)Su11:79
- Gems & Gemology**
“Challenge”—Sp11:75-76; winners and answers F11:220
Edward J. Gübelin Most Valuable Article Award Sp11:1-2
- Geographic origin**
of colored gemstones, determination of (Abduriyim)Su11:114-116
of corundum, determination using LIBS and advanced chemometrics (Yetter)Su11:157
discriminant analysis, application of in determining—(Blodgett)Su11:145; of andesine (Abduriyim)Su11:167-180; of emerald (de Corte)Su11:147
Materialytics Sequencing System (McManus)Su11:155-156
of peridot (Thoresen)Su11:121-122
- Geology**
of Canadian diamond deposits (Stachel)Su11:112-114
- Glass**
triplet imitation of “mystic” treated topaz (GNI)F11:252-253
- Grossular**
green, from Tanzania (GNI)Sp11:57-58
- Guatemala**
jadeite from, lavender (Harlow)Su11:116
- Gübelin gem collection**
online resource of (Shigley)Su11:151-152
- H**
- Halite**
submitted for identification (LN)Sp11:52-53
- Hallmarking**
of precious metals, benefits of (Niklewicz)Su11:160-161
- Heat treatment**
of Chinese freshwater cultured pearls, detection of (Strack)Su11:120
of odontolite, blue, in antique brooches (Krzemnicki)W11:296-301
of ruby, pretreatment (Lee)Su11:148-149
of zircon, brownish red, from China (Chen)Sp11:36-41
- High-pressure, high-temperature [HPHT] synthesis**, see Diamond, synthetic
- High-pressure, high-temperature [HPHT] treatment**, see Diamond treatment
- History**
of diamonds, in themed postage stamp collection (Overlin)F11:214-219
- Hydrogrossular**, see Garnet
- Hydrophane**
bicolor, bi-pattern opal (GNI)W11:320-322
dyed purple opal from Wollo, Ethiopia (Renfro)W11:260-270
- I**
- Illumination methods**
in the buying, selling, and grading of gemstones (Eickhorst)Su11:123
- Imitations**, see specific gem materials imitated
- Inclusions**
in andesine, reportedly from Tibet (Rossman)Sp11:16-30, (Abduriyim)Su11:167-180
of cinnabar in chatoyant quartz (GNI)W11:322-323
in dyed purple opal from Ethiopia (Renfro)W11:260-270
of emerald in quartz (GNI)W11:323 and geographic origin of colored gemstones (Abduriyim)Su11:114-116
of izoklakeite in quartz skull carving (GNI)W11:324-325
of spessartine in quartz (GNI)F11:245
of tourmaline in cat’s-eye quartz (GNI)F11:245-246
of trolleite and lazulite in blue quartz (GNI)Sp11:57-58
see also Diamond, inclusions in
- India**
agate from, dendritic (GNI)Sp11:62-63
Gem Testing Laboratory in Jaipur, remarkable gems encountered at (Choudhary)Su11:145-146
quartz from, with spectral interference (GNI)Sp11:58-59
scapolite from (GNI)Sp11:59
- Infrared spectroscopy**, see Spectroscopy, infrared
- Instruments**
dual integrating sphere for color grading and measurement (Liu)Su11:154
inclusion mapping system for diamonds (Caspi)Su11:153
spectral analysis, automated real-time (Magaña)Su11:154-155
symmetry grading system for diamonds (Caspi)Su11:153-154
ultra-deep diamond cleaning technology (Vins)Su11:136
see also Argon isotope analysis; Chemometrics; Conoscopy; DiamondView imaging; Electron-microprobe analysis; Fluorescence, ultraviolet; Illumination methods; Magnetic susceptibility; Microscopy; Oxygen isotope analysis; Scanning electron microscopy; Spectral analysis; Spectrometer; Spectrometry [various]; Spectroscopy [various]; X-radiography; X-ray diffraction
- Interference**
spectral, in quartz from India (GNI)Sp11:58-59
- International Gemological Symposium, 5th [2011]**
proceedings of (Kimmel and Keller)Su11:79
- Internet**
and jewelry retailing (Overlin)Su11:95-96
- Irradiation**
of diamond—producing green and orangy brown spots on surface (Nasdala)Su11:105-106; producing 3H

and H3 defects (Choi)Su11:131
natural, of diamonds from Zimbabwe—
(Crepin)Su11:105; hydrogen-rich
(Breeding)Su11:129-130
of sapphire, with electron-beam
(Seo)Su11:151
of topaz, blue (Zhang)W11:302-307

Isotopes, see Argon isotope analysis,
Oxygen isotope analysis

Ivory
mastodon, fossilized (odontolite), heat-
ed blue (Krzemnicki)W11:296-301

Izoklakeite
inclusions in quartz skull carving
(GNI)W11:324-325

J

Jade, see Jadeite, Nephrite

Jadeite

green cabochon (LN)Sp11:52-53
lavender, from Myanmar, Guatemala,
and Japan (Harlow)Su11:116
sales at the 2010 Myanmar Gem
Emporium (GNI)Sp11:72-73

Japan

jadeite from, lavender (Harlow)Su11:116

Jewelry

antique and estate, selling of
(Luke)Su11:100-102
design overview (Luke)Su11:92-94
luxury trends (Overlin)Su11:89-91

L

LA-ICP-MS, see Spectrometry, laser abla-
tion—inductively coupled plasma—mass
[LA-ICP-MS]

Lapidary arts

quartz skull carving with inclusions of
izoklakeite (GNI)W11:324-325
rhodochrosite carving of ancient Indian
sage (GNI)F11:246-247
see also Diamond, cuts and cutting of

Liberia

diamond mining in (GNI)Sp11:63-64
ruby from (Kiefert)Su11:138

LIBS, see Spectroscopy, laser-induced
breakdown

Lighting

and the buying, selling, and grading of
gemstones (Eickhorst)Su11:123

Luminescence

of gem materials (Fritsch)Su11:123,
(Rossman)Su11:124-125
see also DiamondView imaging,
Fluorescence, ultraviolet [UV]

M

Madagascar

ammonite from, iridescent
(GNI)F11:235-236
demantoid and topazolite from
Antetezambato (Pezzotta)Sp11:2-14

tourmaline from, correlation of man-
ganese and iron (Ahn)Su11:143-144

Magnetic susceptibility

as a means of determining garnet com-
position (Hoover)W11:272-285

Maine, see United States

Marketing and distribution

abbreviated jewelry descriptions
(Root)Su11:161-162
of ametrine from the Anahí mine,
Bolivia (Weldon)Su11:163-164
and China's gem industry
(Jia)Su11:159-160
of colored stones (Drucker)Su11:158-
159, (Overlin)Su11:97-99
of coral jewelry (Carmona)Su11:158
of cultured pearls (Overlin)Su11:97-99
of diamonds—(Overlin)Su11:97-99;
color grading (Tashey)Su11:163; from
secondary market sources
(Shor)Su11:163
digital-age (Overlin)Su11:95-96
hallmarking of precious metals, bene-
fits of (Niklewicz)Su11:160-161
lectures, gem and jewelry (Serras-
Herman)Su11:162
in the mineral collector market
(Johnson)Su11:160
of ruby—perception of rarity
(Robertson)Su11:161; "pigeon's
blood" (Atichat)Su11:157-158

Materialytics Sequencing System

quantitative process to determine geo-
graphic origin of gem materials
(McManus)Su11:155-156

Mauritania

Nummrite from (GNI)F11:242-243

Measurement

concepts and uncertainty of
(Geurts)W11:286-295

Meteorites

pallasite with gem-quality peridot—
(Shen)F11:208-213; mounted in jew-
elry (GNI)F11:243-244

Mexico

colored gemstones from, review of
(Ostrooomov)Su11:141
opal, blue, from Sinaloa (GNI)F11:243

Microscopy

polarized light and fluorescence, to
establish origin of color in natural
diamonds (Epelboym)Su11:133

Mining and exploration

of colored gemstones worldwide
(Yager)Su11:142-143
concrete mixer to sort gem-bearing
gravels (Limsuwan)Su11:139
of corundum in Pakistan
(GNI)W11:325-326
for diamond—(Coopersmith)Su11:108;
in Canada (Stachel)Su11:112-114; in
Liberia (GNI)Sp11:63-64
for emerald—(Giuliani)Su11:108-110;
in Afghanistan (GNI)F11:238-239; in
Zambia (GNI)Sp11:63-65
for sapphire in Sri Lanka (GNI)F11:248-
249

Moissanite, synthetic

with crystalline silicon intergrowth
(LN)Sp11:54-55

Moonstone

synthetic star spinel imitation of
(LN)Sp11:54-55

Most valuable article, see *Gems @
Gemology*

Myanmar

colorless gems from (GNI)F11:241-242
gem sales and production
(GNI)Sp11:72-73, (GNI)F11:256
jadeite from, lavender
(Harlow)Su11:116
ruby overgrowth on painite, from
Mogok (Nissinboim)Su11:140-141
spinel, trapiche, from Mogok
(GNI)W11:329-330

N

Namibia

fluorite from Klein Spitzkoppe region
(GNI)W11:318-319

Nassau, Kurt

obituary (GNI)Sp11:73

Nephrite

from China, natural and treated
(Zhang)Su11:122
rough, imitation of (GNI)Sp11:69-70

Neutron irradiation, see Irradiation

Nomenclature and classification

abbreviated jewelry descriptions
(Root)Su11:161-162
of diamond—color grades
(Tashey)Su11:163; crystals, for use
in geology and exploration
(Klettke)Su11:139
"pigeon's blood" ruby, standards for
(Atichat)Su11:157-158
"royal blue" sapphire, standards for
(Atichat)Su11:157-158
of ruby, effect on perception of rarity
(Robertson)Su11:161

Nummrite

from Mauritania (GNI)F11:242-243

O

Obituary

Kurt Nassau (GNI)Sp11:73

Odontolite

fossilized dentine (mastodon ivory),
blue, identified in antique brooches
(Krzemnicki)W11:296-301

Oiling

of opal with artificial matrix
(LN)W11:312

Omphacite

green cabochon resembling jadeite
(LN)Sp11:52-53

Opal

from Australia—common
(GNI)W11:319-320; nomenclature
and characterization

(Beattie)Su11:116
bicolor, bi-pattern hydrophane
(GNI)W11:320-322
blue—(or cristobalite?) from Brazil
(Schnellrath)Su11:142; from Mexico
(GNI)F11:243
clarity-enhanced, with artificial matrix
(LN)W11:312
from Ethiopia—black (LN)W11:312-
313; dyed purple (Renfro)W11:260-
270; play-of-color (Rondeau)Su11:112
sugar-acid treatment of, from Wollo,
Ethiopia (GNI)W11:333-334

Oregon, see United States

Oxygen isotope analysis
to characterize gem materials
(Rossman)Su11:124-125

P

Painite
from Myanmar, with ruby overgrowth
(Nissinboim)Su11:140-141

Pakistan
corundum mining in (GNI)W11:325-
326
sphene from border area with
Afghanistan, color-change
(GNI)W11:327-328

Pallasite, see Peridot

Pargasite
from Tanzania (GNI)Sp11:65

Pearl
identification of (Scarratt)Su11:117-119
non-nacreous, from *Tridacna gigas*
(Bidwell)Su11:144-145

Pearl, cultured
characterization of, using analytical
techniques (Lu)Su11:149-150
Chinese freshwater—beaded with
baroque freshwater cultured pearls
(GNI)F11:244-245; with exotic metal-
lic colors (Beavers)Su11:144; treat-
ments and their detection
(Strack)Su11:120
coated bead-cultured freshwater
(LN)W11:313-314
grafting methods (Ito)Su11:148
identification of (Scarratt)Su11:117-119
marketing of (Overlin)Su11:97-99
from *P. margaritifera*, absorption fea-
tures of (Karampelas)Sp11:31-35
with plastic bead nuclei (LN)F11:229-230
quality factors of (Ito)Su11:148
sales at the 2010 Myanmar Gem
Emporium (GNI)Sp11:72-73
separation of natural-color saltwater,
from *P. margaritifera* and *P. sterna*,
using spectral differentiation
(Karampelas)Su11:117
treatments and their detection
(Strack)Su11:120

Pearl, non-nacreous
imitation—calcitic “cat’s-eye pearls”
(GNI)W11:330-332; skillfully crafted
(GNI)Sp11:70-71

natural, from *Tridacna gigas*
(Bidwell)Su11:144-145

Pearl simulants
non-nacreous—(GNI)Sp11:70-71; cal-
citic “cat’s-eye pearls”
(GNI)W11:330-332

Pegmatites
gem pockets in (Lyckberg)Su11:111-112
Pederneira, in Minas Gerais, Brazil
(Pezzotta)Su11:141-142
Stewart, in Pala, California
(Morton)Su11:140

Peridot
from pallasitic meteorites—identifica-
tion of (Shen)F11:208-213; jewelry
(GNI)F11:243-244
from Zabargad, history of
(Thoresen)Su11:121-122

Peru
variscite from (GNI)F11:251

Phosphorescence
in diamond, long-lasting (LN)W11:310-
311

Photoluminescence spectroscopy, see
Spectroscopy, photoluminescence

Plagioclase, see Andesine, Feldspar

Plastic
coating of quartz, imitating emerald
(GNI)Sp11:68-69

Play-of-color, see Opal

Postage stamps
diamond-themed collection
(Overlin)F11:214-219

Q

Quartz
blue, with trolleite and lazulite inclu-
sions (GNI)Sp11:57-58
carving of skull, with inclusions of
izoklakeite (GNI)W11:324-325
chatoyant—with cinnabar inclusions
(GNI)W11:322-323; pink, with tour-
maline needle inclusions
(GNI)F11:245-246
with emerald inclusions (GNI)W11:323
from India, spectral interference in
(GNI)Sp11:58-59
plastic-coated, imitating emerald
(GNI)Sp11:71-72
spectroscopic differentiation of natural
and synthetic (Choudhary)Su11:146-
147
with spessartine inclusions (GNI)F11:245
see also Amethyst; Ametrine
[amethyst-citrine]; Quartz, synthetic

Quartz, synthetic
large, represented as amethyst, aquama-
rine, and citrine (GNI)W11:332-333

R

Radioactivity
of blue topaz, neutron-irradiated
(Zhang)W11:302-307

Rhodochrosite
carving of ancient Indian sage
(GNI)F11:246-247

Rock
fuchsite-rich, deep green (GNI)F11:239-
240

Ruby
geographic origin of (Yetter)Su11:157
lead-glass-filled—durability and safety
testing (Sutthirat)Su11:121; trapiche
(GNI)Sp11:72-73
from Liberia (Kiefert)Su11:138
market for (Drucker)Su11:158-159
from Myanmar—color similarity to
Van Gogh’s *The Night Café*
(Dubinsky)Su11:159; overgrowth on
painite (Nissinboim)Su11:140-141
from Pakistan, mining of
(GNI)W11:325-326
“pigeon’s blood,” standards for
(Atichat)Su11:157-158
rarity of, with regard to treatment and
nomenclature (Robertson)Su11:161
from Vietnam, northern (Khoi)F11:182-
195

Russia
diamonds from the Nurbinskaya pipe,
mineralogical characteristics of
(Solodova)Su11:134-135

S

St. John’s Island, see Zabargad

Sapphire
from Afghanistan, beryllium- and tung-
sten-bearing (LN)Sp11:53-54
from China, blue and pink
(Chen)Su11:136-137
blue, with natural Be—(LN)F11:232-233;
from Afghanistan (LN)Sp11:53-54
diffusion-treated with Be—blue, experi-
ments on (Wathanakul)Su11:153;
pink (LN)F11:232; safety and durabil-
ity testing of (Sutthirat)Su11:121
from Ethiopia (GNI)F11:247-248
geographic origin of (Yetter)Su11:157
green, distinct color caused by iron
(LN)F11:231-232
irradiation of, electron-beam
(Seo)Su11:151
market for (Drucker)Su11:158-159
from Pakistan, mining of
(GNI)W11:325-326
“royal blue,” standards for
(Atichat)Su11:157-158
from Sri Lanka, mining of
(GNI)F11:248-249
star, with blue color similar to Van
Gogh’s *The Starry Night*
(Dubinsky)Su11:159
from Vietnam, northern (Khoi)F11:182-
195

Sapphire, synthetic
green, distinct color caused by cobalt
(LN)F11:231-232
recent advances in growth of (Stone-
Sundberg)Su11:156

- Scanning electron microscopy [SEM]**
of andesine, reportedly from Tibet (Rossman)Sp11:16-30, (Abduriyim)Su11:167-180
- Scapolite**
from Afghanistan (GNI)Sp11:65-66
from India (GNI)Sp11:59
- Simulants**, see specific gem materials simulated
- Social media**
and jewelry retailing (Overlin)Su11:95-96
- Spectralysis**
automated real-time spectral analysis system (Magaña)Su11:154-155
- Spectrometer**
dual integrating sphere, for color grading and measurement (Liu)Su11:154
- Spectrometry, laser ablation-inductively coupled plasma-mass [LA-ICP-MS]**
of andesine, reportedly from Tibet (Abduriyim)Su11:167-180
of aquamarine from Vietnam (Huong)Sp11:42-48
of colored gemstones, and country of origin determination— (Abduriyim)Su11:114-116, and application of discriminant analysis (Blodgett)Su11:145
of cultured pearls (Lu)Su11:149-150
of demantoid from northern Madagascar (Pezzotta)Sp11:2-14
of gem materials (Rossman)Su11:124-125
of lavender jadeite from Myanmar, Guatemala, and Japan (Harlow)Su11:116
of peridot from meteorites, identification of (Shen)F11:208-213
of ruby, filled with lead glass (Sutthirat)Su11:121
of sapphire—Be-diffused (Sutthirat)Su11:121; green, distinct color caused by iron (LN)F11:231-232
of synthetic sapphire, green (LN)F11:231-232
of zircon, brownish red, from China (Chen)Sp11:36-41
see also Chemical composition
- Spectroscopy, electron paramagnetic resonance [EPR]**
to characterize gem materials (Rossman)Su11:124-125
- Spectroscopy, energy-dispersive X-ray fluorescence [EDXRF]**
of cultured pearls (Lu)Su11:149-150
- Spectroscopy, gamma ray**
of topaz, neutron-irradiated blue (Zhang)W11:302-307
- Spectroscopy, infrared**
of aquamarine from Vietnam (Huong)Sp11:42-48
of diamonds, low-grade, with distinctive color zoning and inclusions (Kwon)Su11:134
of emerald, natural and synthetic (de Corte)Su11:147
of quartz, natural and synthetic— (Choudhary)Su11:146-147; amethyst (Karampelas)F11:196-201
reflectance, of saltwater cultured pearls from *P. margaritifera* (Karampelas)Sp11:31-35
of tourmaline from Madagascar, spectral correlation of manganese and iron (Ahn)Su11:143-144
- Spectroscopy, laser-induced breakdown [LIBS]**
of corundum (Yetter)Su11:157
of gem materials (Rossman)Su11:124-125
- Spectroscopy, phosphorescence**
of a diamond with long-lasting phosphorescence (LN)W11:310-311
- Spectroscopy, photoluminescence**
of cultured pearls, natural-color, *P. margaritifera* and *P. sterna* (Karampelas)Su11:117
of diamond—to establish origin of color (Epelboym)Su11:133; HPHT-treated, to identify strain (Eaton-Magaña)Su11:132
- Spectroscopy, Raman**
of aquamarine from Vietnam (Huong)Sp11:42-48
of garnet (Henderson)Su11:148
of odontolite in antique brooches (Krzemnicki)W11:296-301
of pearls—Chinese freshwater cultured (Strack)Su11:120; natural and cultured (Scarratt)Su11:117-119
of zircon, brownish red, from China (Chen)Sp11:36-41
- Spectroscopy, UV-Vis-NIR**
of andesine (Rossman)Sp11:16-30
of colored gemstones, and country of origin determination (Abduriyim)Su11:114-116
of diamond, strongly purple-colored black (LN)W11:309
of emerald, natural and synthetic (de Corte)Su11:147
of garnet, color-change, from Tanzania (GNI)F11:240-241
of ruby from Vietnam (Khoi)F11:182-195 [erratum W11:335]
of tourmaline—(Sriprasert)Su11:152; from Madagascar, spectral correlation of manganese and iron (Ahn)Su11:143-144
of zircon, brownish red, from China (Chen)Sp11:36-41
- Spessartine**
inclusions in quartz (GNI)F11:245
- Sphene [titanite]**
color-change, from Pakistan/Afghanistan (GNI)W11:327-328
- Spinel**
trapiche, from Mogok, Myanmar (GNI)W11:329-330
from Vietnam—(GNI)Sp11:60-61; cobalt blue (GNI)W11:328-329
- Spinel, synthetic**
star, imitation of moonstone (LN)Sp11:54-55
- Spodumene**
green cat's-eye, from Brazil (GNI)F11:249-250
- Sri Lanka**
sapphire from, mining update (GNI)F11:248-249
- Strain**
in colorless untreated diamonds (LN)F11:224-225
in HPHT-treated diamonds (Eaton-Magaña)Su11:132
- Sunstone**, see Feldspar
- Sustainability**
Anahí ametrine mine, Bolivia (Weldon)Su11:163-164
of coral jewelry (Carmona)Su11:158
- Symmetry grading**
assessments and metrics for polished diamonds (Caspì)Su11:153-154
GIA boundaries for round brilliant diamonds (Geurts)W11:286-295
- Synthetics**, see specific gem materials
- T**
- Tanzania**
chondroite from Mahenge (GNI)W11:316
garnet from—color-change (GNI)F11:240-241; green grossular (GNI)Sp11:57-58
gems from Tunduru (Limsuwan)Su11:110-111
pargasite from (GNI)Sp11:65
see also Tanzanite
- Tanzanite**
natural-color, identification of (Smith)Su11:119-120
- Tenebrescence**
in zircon from Australia (LN)W11:314-315
- Thermoluminescence**
in type IaB diamonds (LN)Sp11:50
- Tibet**
andesine reportedly from (Rossman)Sp11:16-30, (Abduriyim)Su11:167-180
- Titanite**, see Sphene
- Topaz**
color-zoned, yellowish to greenish brown (GNI)F11:250-251
imitation of “mystic” treated topaz (GNI)F11:252-253
neutron-irradiated blue, radioactive decay pattern of (Zhang)W11:302-307
- Topazolite**
from northern Madagascar (Pezzotta)Sp11:2-14
- Tourmaline**
from Brazil, Pederneira pegmatite (Pezzotta)Su11:141-142
inclusions in cat's-eye quartz (GNI)F11:245-246
from Madagascar, spectral correlation of manganese and iron (Ahn)Su11:143-144

spectroscopic characteristics of (Sriprasert)Su11:152
from the United States—California, Stewart pegmatite (Morton)Su11:140; Maine (GNI)Sp11:66-68

Trapiche

emerald imitation (GNI)Sp11:68-69
ruby, lead-glass-filled (GNI)Sp11:72-73
spinel, from Mogok, Myanmar (GNI)W11:329-330

Treatment

ancient (Lule)Su11:150
irradiation of blue topaz (Zhang)W11:302-307
lead-glass-filling of ruby—and corundum triplet (GNI)F11:251-252; trapiche (GNI)Sp11:72-73
pretreatment and heat treatment of ruby (Lee)Su11:148-149
sugar-acid, of opal from Ethiopia (GNI)W11:333-334
see also Coating; Diamond treatment; Diffusion treatment; Dyeing; Filling; fracture or cavity; Heat treatment; Irradiation; specific gem materials

Tucson gem shows

highlights of (GNI)Sp11:56-63

Turquoise simulants

odontolite, in set of antique brooches (Krzemnicki)W11:296-301

U

Ultraviolet fluorescence, see Fluorescence, ultraviolet [UV]

United States

Stewart pegmatite, Pala, California (Morton)Su11:140
sunstone from Oregon, comparison of two deposits (McClure)Su11:150-151
tourmaline from Mt. Marie, Maine—(GNI)Sp11:66-68; origin of color (GNI)Sp11:67-68

V

Variscite

from Peru (GNI)F11:251

Vietnam

aquamarine from Thanh Hoa (Huong)Sp11:42-48, (GNI)F11:236-237
ruby and sapphire from Tan Huong-Truc Lau (Khoi)F11:182-195
spinel from—cobalt blue, from Khuoi Ngan (GNI)W11:328-329; northern Vietnam (GNI)Sp11:60-61

W

Winchell diagrams

use in determining garnet composition (Hoover)W11:272-285

X

X-radiography

of coated bead-cultured freshwater pearl (LN)W11:313-314
of pearls, natural and cultured (Scarratt)Su11:117-119

X-ray diffraction

of andesine, reportedly from Tibet (Abduriyim)Su11:167-180

Z

Zabargad [St. John's Island]

peridot from, history of (Thoresen)Su11:121-122

Zaire, see Congo, Democratic Republic of the

Zambia

emerald mining at Kagem (GNI)Sp11:63-65

Zektzerite

gem (GNI)Sp11:61

Zimbabwe

diamonds from, naturally irradiated—(Crepin)Su11:105; hydrogen-rich (Breeding)Su11:129-130

Zircon

brownish red, from China (Chen)Sp11:36-41
from Ethiopia (GNI)F11:247-248
tenebrescent, from Australia (LN)W11:314-315

Zoisite, see Tanzanite

Zoning, see Color zoning; specific gem materials

AUTHOR INDEX

This index lists, in alphabetical order, the authors of all feature articles, Notes & New Techniques, and Rapid Communications that appeared in the four issues of Volume 47 of *Gems & Gemology*, together with the full title and inclusive page numbers of each article and the issue (in parentheses). Full citation is given under the first author only, with reference made from coauthors. Also included are presenters whose abstracts were published in the Summer 2011 (S11) issue, the proceedings of the Fifth International Gemological Symposium.

A

Abduriyim A.: Geographic origin determination of colored gemstones, 114-116 (Summer)

Abduriyim A., McClure S.F., Rossman G.R., Leelawatanasook T., Hughes R.W., Laurs B.M., Lu R., Isatelle F., Scarratt K., Dubinsky E.V., Douthit T.R., Emmett J.L.: Research on gem feldspar from the Shigatse region of Tibet, 167-180 (Summer)

Abduriyim A., see also Choi H.-M.

Adamo I., see Pezzotta F.

Ahn Y.-K., Seo J.-G., Park J.-W.: Spectral correlation of manganese and iron in tourmalines from Madagascar, 143-144 (Summer)

Ahn Y.-K., see also Kwon S.-R., Seo J.G.

Ai H., see Chen T.

Amorim H.S., see Schnellrath J.

Anthonis A., see Crepin N.

Atichat W., Chandayot P., Saejoo S., Leelawatanasook T., Sriprasert B., Pisutha-Armond V., Wathanakul P., Sutthirat C.: "Pigeon's blood" ruby and "royal blue" sapphire: Color standards for the gem trade, 157-158 (Summer)

Atichat W., see also Huong L.T.-T., Wathanakul P.

Ayalew D., see Rondeau B.

B

Balinskas S., see Magaña Q.

Barjon J., see Willems B.

Beattie R.A., Blackman K.N., Levonis H.:

Australian opal nomenclature and assessment, 116 (Summer)

Beavers B., Shepherd J.: Chinese freshwater cultured pearls with exotic metallic colors, 144 (Summer)

Benzel W., see Morton D.

Berger B., see Morton D.

Bidwell D., DelRe N., Widemann A., Epelboym M.: Natural non-nacreous pearls from the giant clam *Tridacna gigas*, 144-145 (Summer)

Blackman K.N., see Beattie R.A.

Blodgett T., Gilbertson A., Geurts R., Goedert B.: Length-to-width ratios among fancy shape diamonds, 129 (Summer)

Blodgett T., Shen A.: Application of discriminant analysis in gemology: Country-of-origin separation in colored

stones and distinguishing HPHT-treated diamonds, 145 (Summer)
Blodgett T., see also Geurts R.H.
Bodeur Y., see Rondeau B.
Breeding C.M.: Hydrogen-rich diamonds from Zimbabwe with natural radiation features, 129-130 (Summer)
de Brum T.M.M., see Juchem P.L., Schnellrath J.
Buckley S., see McManus C.

C

Carmona C., Cole J.E., Marks J.: "Too precious to wear": The role of the jewelry industry in coral conservation, 158 (Summer)
Caspi A.: Inclusion mapping in diamonds, 153 (Summer)
Caspi A., Kemer A.: Symmetry: From assessments to metrics, 153-154 (Summer)
Chandayot P., see Atichat W.
Chapman J.: Recent studies of colored diamonds from Argyle, 130 (Summer)
Chen H., see Zhang B., Zhang J.
Chen T., Ai H., Yang M., Zheng S., Liu Y.: Brownish red zircon from Muling, China, 36-41 (Spring)
Chen T., Yang M., Ai H.: Blue and pink sapphires from Muling, northeastern China, 136-137 (Summer)
Chodur N.L., see Juchem P.L.
Choi H.-M., Kim Y.-C., Kim S.-K., Abduriyim A.: Evidence of an interstitial 3H-related optical center at 540.7 nm in natural diamond, 131 (Summer)
Choi K.-M., see Lee B.-H.
Choudhary G.: Remarkable gems encountered at the Gem Testing Laboratory, Jaipur, India, 145-146 (Summer)
Choudhary G., Fernandes S.: Spectroscopic examination of commercially available quartz varieties: A gemological perspective, 146-147 (Summer)
Clanin J.C.: The fundamentals in mining for colored gemstones and mineral specimens, 107-108 (Summer)
Cole J.E., see Carmona C.
Coopersmith H.G.: The making of a diamond mine: Why everyone cannot have one, 108 (Summer)
de Corte K., Van Meerbeeck M.: IR and UV-Vis spectroscopy of gem emeralds—A tool to differentiate natural and synthetic stones, as well as geographic origin? 147 (Summer)
Crepin N., Anthonis A., Willems B.: A case study of naturally irradiated diamonds from Zimbabwe, 105 (Summer)

D

D'Haenens-Johansson U.F.S., Edmonds A.M., Green B., Newton M.E., Martineau P.M., Khan R.U.A.: Optical prop-

erties of silicon-related defects in CVD synthetic diamond, 131-132 (Summer)
Danisi R.M., see Pezzotta F.
DelRe N., see Bidwell D., Epelboym M.
Diella V., see Pezzotta F.
Dobrinets I., see Epelboym M.
Donaldson C.H., see Taylor R.P.
Douman M., see Kiefert L.
Douthit T.R., see Abduriyim A.
Dowe J., see McManus C.
Downs R.T., see Henderson R.R.
Drucker R.B.: Market trends in a changing global economy, 158-159 (Summer)
Dubinsky E., King J., Zucker B.: Gemstone color as nature's palette: Van Gogh's commentary on a 111 ct star sapphire and other gem-quality corundum, 159 (Summer)
Dubinsky E., see also Abduriyim A.

E

Eaton-Magaña S.C.: Observation of strain through photoluminescence peaks in diamonds, 132 (Summer)
Edmonds A.M., see D'Haenens-Johansson U.F.S.
Eickhorst M.: The impact of the choice of illumination in the wholesale buying, selling, and grading of gemstones, 123 (Summer)
Emmett J.L., see Abduriyim A.
Epelboym M., DelRe N., Widemann A., Zaitsev A., Dobrinets I.: Characterization of some natural and treated colorless and colored diamonds, 133 (Summer)
Epelboym M., see also Bidwell D.

F

Fallick A.E., see Giuliani G.
Feneyrol J., see Giuliani G.
Fernandes S., see Choudhary G.
Finch A.A., see Taylor R.P.
Fleck R., see Morton D.
Fritsch E., Massuyeau F., Rondeau B., Segura O., Hainschwang T.: Advancing the understanding of luminescence in gem materials, 123 (Summer)
Fritsch E., see also Karampelas S., Rondeau B.

G

Gasanov M., see Solodova Y.
Gatta G.D., see Pezzotta F.
Gauthier J.-P., see Karampelas S.
Geurts R.H., Reinitz I.M., Blodgett T., Gilbertson A.M.: GIA's symmetry grading boundaries for round brilliant cut diamonds, 286-295 (Winter)
Geurts R., see also Blodgett T.
Gilbertson A.M., see Blodgett T., Geurts R.H.
Giuliani G., Ohnenstetter D., Fallick A.E., Feneyrol J.: State of the art in the forma-

tion of high-value colored stones, 108-110 (Summer)
Goedert B., see Blodgett T., Shigley J.E.
Grambole D., see Nasdala L.
Green B., see D'Haenens-Johansson U.F.S.
Grizenko A.G., see Vins V.G.
Groover K., see Morton D.
Gumpesberger S.M.: Extreme conoscopy, 147 (Summer)

H

Häger T., see Huang L.T.-T.
Hainschwang T., see Fritsch E., Karampelas S.
Harlow G.E., Shi G.-H.: An LA-ICP-MS study of lavender jadeite from Myanmar, Guatemala, and Japan, 116-117 (Summer)
Harlow G.E., see also Nissinboim A.
Harrell J.A., see Thoresen L.
Harris J.W., see Nasdala L.
Henderson R.R., Downs R.T., La Sure J.: Determining the chemical composition of garnets using Raman spectroscopy, 148 (Summer)
Herzog F., see Krzemnicki M.S.
Hofmeister W., see Huang L.T.-T., Nasdala L.
Hoover D.B.: Determining garnet composition from magnetic susceptibility and other properties, 272-285 (Winter)
Hughes R.W., see Abduriyim A.
Huang L.T.-T., Hofmeister W., Häger T., Khoi N.N., Nhung N.T., Atichat W., Pisutha-Armond V.: Aquamarine from the Thuong Xuan District, Thanh Hoa Province, Vietnam, 42-48 (Spring)

I

Isatelle F., see Abduriyim A.
Ito M.: Circle and spot formation mechanisms and changes in luster, color, and roundness of cultured pearls by grafting methods in *Pinctada margaritifera*, 148 (Summer)
Iverson J.:
Great expectations, 259 (Winter)
New beginnings, 181 (Fall)

J

Janse B.: Mystery diamonds—From alluvial deposits, 110 (Summer)
Jia Q.: An analysis of the development and tax policy of China's gem industry, 159-160 (Summer)
Johnson M.: Mineral collectors—An overlooked gem market, 160 (Summer)
Johnson P.: Pink HPHT synthetic diamonds—A new coloration technique, 133 (Summer)
Juchem P.L., de Brum T.M.M., Chodur N.L., Liccardo A.: Gem materials in the south of Brazil, 137-138 (Summer)
Juchem P.L., see also Schnellrath J.

K

- Karampelas S., Fritsch E., Gauthier J.-P., Hainschwang T.: UV-Vis-NIR reflectance spectroscopy of natural-color saltwater cultured pearls from *Pinctada margaritifera*, 31-35 (Spring)
- Karampelas S., Fritsch E., Hainschwang T., Gauthier J.-P.: Spectral differentiation of natural-color saltwater cultured pearls from *Pinctada margaritifera* and *Pteria sterna*, 117 (Summer)
- Karampelas S., Fritsch E., Zorba T., Paraskevopoulos K.M.: Infrared spectroscopy of natural vs. synthetic amethyst: An update, 196-201 (Fall)
- Ke J., see Zhang B.
- Keller A., see Kimmel K.
- Kerner A., see Caspi A.
- Khan R.U.A., see D'Haenens-Johansson U.F.S.
- Khoi N.N., Sutthirath C., Tuan D.A., Nam N.V., Thuyet N.T.M., Nhung N.T.: Ruby and sapphire from the Tan Huong-Truc Lau Area, Yen Bai Province, northern Vietnam, 182-195 (Fall)
- Khoi N.N., see also Huong L.T.-T.
- Kiefert L., Douman M.: Ruby from Liberia, 138 (Summer)
- Kim K.Y., see Seo J.G.
- Kim S.-K., see Choi H.-M.
- Kim Y.-C., see Choi H.-M., Lee B.-H.
- Kimbrough D., see Morton D.
- Kimmel K., Keller A.: GIA Symposium 2011: Advancing the science and business of gems, 79 (Summer)
- King J., see Dubinsky E.
- Kistler R., see Morton D.
- Klettke J.A.: Systematic diamond descriptions for use in geology and exploration, 139 (Summer)
- Koivula J.L., see Shen A.
- Kozlov A.V., see Vasilyev E.
- Krzemnicki M.S., Herzog F., Zhou W.: A historic turquoise jewelry set containing fossilized dentine (odontolite) and glass, 296-301 (Winter)
- Krzemnicki M.S., see also Strack E.
- Kurbatov K., see Solodova Y.
- Kwon S.-R., Seo J.-G., Ahn Y.-K., Park J.-W.: Characterization of distinctive color zoning and various inclusions in low-grade diamonds, 134 (Summer)

L

- La Sure J., see Henderson R.R.
- Laurs B.M., see Abduriyim A.
- Lee B.-H., Choi K.-M., Kim Y.-C., Yon S.-J.: The observation of defects after the pre-treatment and simple heat treatment of ruby, 148-149 (Summer)
- Lee C.-T., see Morton D.
- Leelawatanasuk T., see Abduriyim A., Atichat W., Wathanakul P.

- Levonis H., see Beattie R.A.
- Lhuaamporn T., see Wathanakul P.
- Liccardo A., see Juchem P.L.
- Likes T., see McManus C., Yetter K.
- Limsuwan R., Sakimoto T.: Geology, exploration, mining, and processing of gems and gold from placer deposits on the Muhuwesi River, Tunduru, Tanzania, 110-111 (Summer)
- Limsuwan R., Sakimoto T.: Using a concrete mixer to sort gem-bearing gravels for artisanal and small-scale mining, 139 (Summer)
- Lithgow G., see McManus C.
- Liu Yan: Instrumental color measurement and grading of faceted gemstones, 154 (Summer)
- Liu Yungui, see Chen T.
- Lu R., Zhou C.-H., Sturman N.: Operational considerations of EDXRF, LA-ICP-MS, and photoluminescence techniques in the analysis of pearls, 149-150 (Summer)
- Lu R., see also Abduriyim A.
- Lu T., see Zhang B., Zhang J.
- Luke A.:
Everything old is new again: The appeal of the auction, estate, and vintage markets, 100-102 (Summer)
Jewelry design: From the masses to museums, 92-94 (Summer)
Playing a bigger game: Better business for a better world, 103-104 (Summer)
- Lule C.: Experiments on ancient gem treatment techniques, 150 (Summer)
- Lyckberg P.: Gem pockets in pegmatites—A worldwide study and comparison, 111-112 (Summer)

M

- Magaña Q., Balinskas S.: Automated real-time spectral analysis for gemstones, 154-155 (Summer)
- Marks J., see Carmona C.
- Martineau P.M., see D'Haenens-Johansson U.F.S.
- Massuyeau F., see Fritsch E.
- Matula L., see Niklewicz D.
- Mazzerro F., see Rondeau B.
- McClure S.F.: A gemological comparison of the two major Oregon sunstone deposits, 150-151 (Summer)
- McClure S.F., see also Abduriyim A., Renfro N.
- McManus C., Likes T., McMillan N., Yetter K., Dowe J., Wise M., Buckley S., Lithgow G., Stipes C., Torriano P.: Determining the provenance of gemstones using the Materialytics Sequencing System (M2S), 155-156 (Summer)
- McManus C., see also Yetter K.
- McMillan N., see McManus C., Yetter K.
- Miceli R.S.D., see Schnellrath J.
- Morton D., Sheppard B., Lee C.-T.,

- Kimbrough D., Berger B., Fleck R., Kistler R., Benzel W., Snee L., Groover K.: Petrogenesis of the Li-bearing Stewart pegmatite, Pala, California, 140 (Summer)
- Mosselmans F.J., see Taylor R.P.

N

- Nam N.V., see Khoi N.N.
- Nasdala L., Grambole D., Harris J.W., Schulze D.J., Hofmeister W.: Radio-colouration of diamond, 105-106 (Summer)
- Newton M.E.: Treated diamond identification, 106 (Summer)
- Newton M.E., see also D'Haenens-Johansson U.F.S.
- Nhung N.T., see Huong L.T.-T., Khoi N.N.
- Niklewicz D., Whetstone W., Matula L.: Hallmarking: A powerful benefit to the consumer, retailer, and international trade, 160-161 (Summer)
- Nissinboim A., Harlow G.E.: A study of ruby on painite from the Mogok Stone Tract, 140-141 (Summer)

O

- Ohnenstetter D., see Giuliani G.
- Ostrooumov M.: Gemstones from Mexico—A review, 141 (Summer)
- Ottaway T.L., see Shigley J.E.
- Overlin S.D.:
Digital age marketing: Are you still parrying like it's 1999?, 95-96 (Summer)
The future of gemstones and gemstones of the future, 97-99 (Summer)
A history of diamonds through philately: The Frank Friedman collection, 214-219 (Fall)
Navigating the current economy for business growth and success, 80-82 (Summer)
Shipwrecked! 126-128 (Summer)
Where is luxury in this brave new world? 89-91 (Summer)

P

- Paraskevopoulos K.M., see Karampelas S.
- Park J.-W., see Ahn Y.-K., Kwon S.-R., Seo J.G.
- Petrovsky V.A., see Vasilyev E.
- Pezzotta F., Adamo I., Diella V.: Demantoid and topazolite from Antetazambato, northern Madagascar: Review and new data, 2-14 (Spring)
- Pezzotta F., Adamo I., Diella V., Gatta G.D., Danisi R.M.: The Pederneira pegmatite, Minas Gerais, Brazil: Geology and gem tourmaline, 141-142 (Summer)
- Pisutha-Arnold V., see Atichat W., Huong L.T.-T., Wathanakul P.

R

- Reinitz I.M., see Geurts R.H.

Renfro N., McClure S.F.: Dyed purple hydrophane opal, 260-270 (Winter)
 Robertson S.: A case study in the perception of rarity—Ruby, 161 (Summer)
 Rondeau B., Fritsch E., Mazzero F., Ayalew D., Bodeur Y.: Amazing play-of-color opals from Wollo, Ethiopia—Toward a genetic model, 112 (Summer)
 Rondeau B., see also Fritsch E.
 Root C.K.: Abbreviated jewelry descriptions—A uniform standard, 161-162 (Summer)
 Rossman G.R.:
 Advanced gem characterization, 124-125 (Summer)
 The Chinese red feldspar controversy: Chronology of research through July 2009, 16-30 (Spring)
 Rossman G.R., see also Abduriyim A.

S

Saejoo S., see Atichat W.
 Sakimoto T., see Limsuwan R.
 Samosorov G., see Solodova Y.
 Scarratt K.: Pearl identification—A practitioner's perspective, 117-119 (Summer)
 Scarratt K., see also Abduriyim A.
 Schnellrath J., Amorim H.S., Juchem P.L., de Brum T.M.M., Miceli R.S.D.: Blue "opal" (or cristobalite?) from Rio Grande do Sul, Brazil, 142 (Summer)
 Schulze D.J., see Nasdala L.
 Sedova E., see Solodova Y.
 Segura O., see Fritsch E.
 Seo J.-G., Kim K.Y., Ahn Y.K., Park J.-W.: Changes in color and optical properties of various sapphires by electron-beam irradiation, 151 (Summer)
 Seo J.-G., see also Ahn Y.-K., Kwon S.-R.
 Serras-Herman H., Herman A.: Lectures—An inspirational way for artists to communicate, 162 (Summer)
 Shen A., Koivula J.L., Shigley J.E.: Identification of extraterrestrial peridot by trace elements, 208-213 (Fall)
 Shen A., see also Blodgett T.
 Shepherd J., see Beavers B.
 Sheppard B., see Morton D.
 Shi G.-H., see Harlow G.E.
 Shigley J.E., Goedert B., Ottaway T.L.: The GIA Gem Project—An online resource of information on gemstones, 151-152 (Summer)
 Shigley J.E., see also Shen A.
 Shor R.: Polished diamond supplies from secondary market sources, 163 (Summer)
 Smith C.P.: Natural-color tanzanite, 119-120 (Summer)
 Snee L., see Morton D.
 Solodova Y., Sedova E., Gasanov M., Samosorov G., Kurbatov K.: Mineralogical characteristics of diamonds from the Nurbin-skaya pipe, Yakutian diamond-bearing province, Russia, 134-135 (Summer)

Sriprasert B.: Spectroscopic characteristics of some gem tourmalines, 152 (Summer)
 Sriprasert B., see also Atichat W., Wathanakul P.
 Stachel T.: Diamonds and cratons—Does the relationship hold for the Canadian deposits? 112-114 (Summer)
 Steinbach M.P.: New artificially asteriated gemstones, 152-153 (Summer)
 Stipes C., see McManus C.
 Stone-Sundberg J.: Recent advances in synthetic sapphire growth, 156 (Summer)
 Strack E., Krzemnicki M.S.: Experimental treatments involving dye and heat for Chinese freshwater cultured pearls, and their detection with Raman spectroscopy, 120 (Summer)
 Sturman N., see Lu R.
 Sukharev A., see Vasilyev E.
 Sutthirat C.: Durability and safety testing of lead glass-treated ruby and beryllium-treated sapphire, and environmental impact assessments, 121 (Summer)
 Sutthirat C., see also Atichat W., Khoi N.N.

T

Tallaire A., see Willems B.
 Tashey T.E.: Recommendations for advancing the color science of gemology, 163 (Summer)
 Tawormmongkolkij M., see Wathanakul P.
 Taylor R.P., Finch A.A., Donaldson C.H., Mosselmans F.J.: Applications of fluorescence in gemology, 125 (Summer)
 Thoresen L., Harrell J.A.: Archaeo-gemology of peridot, 121-122 (Summer)
 Thuyet N.T.M., see Khoi N.N.
 Torrione P., see McManus C.
 Tuan D.A., see Khoi N.N.

V

Van Meerbeeck M., see de Corte K.
 Vasilyev E., Petrovsky V.A., Kozlov A.V., Sukharev A.: The nature of black coloration in gem-quality diamonds from Brazil, 135 (Summer)
 Vins V.G.: New ultra-deep diamond cleaning technology, 136 (Summer)
 Vins V.G., Yelissev A.P., Grizenko A.G.: Donor nitrogen aggregation in synthetic diamonds annealed in the graphite stability field, 135-136 (Summer)

W

Wang M., see Zhang J.
 Wang W.: A review of diamond color treatment and its identification, 107 (Summer)
 Wathanakul P., Wongkokua W., Lhuamporn T., Tawormmongkolkij M., Leelawatanasuk T., Atichat W., Pisutha-Armond V., Sriprasert B.:

Experiments on heating of blue sapphires with beryllium, 153 (Summer)
 Wathanakul P., see also Atichat W.
 Weldon R.: The Anahí ametrine mine: A model for gemstone sustainability, 163-164 (Summer)
 Whetstone W., see Niklewicz D.
 Widemann A., see Bidwell D., Epelboym M.
 Willems B., Tallaire A., Barjon J.: Exploring the origin and nature of luminescent regions in CVD synthetic diamond, 202-207 (Fall)
 Willems B., see also Crepin N.
 Wise M., see McManus C.
 Wongkokua W., see Wathanakul P.

Y

Yager T.R.: Recent trends in world colored gem production, 142-143 (Summer)
 Yang M., see Chen T.
 Yelissev A.P., see Vins V.G.
 Yetter K., McMillan N.J., McManus C., Likes T.: Provenance of rubies and sapphires: an application of laser-induced breakdown spectroscopy (LIBS) and advanced chemometrics for the gem industry, 157 (Summer)
 Yetter K., see also McManus C.
 Yon S.J., see Lee B.-H.

Z

Zaitsev A., see Epelboym M.
 Zhang B., Lu T., Chen H., Ke J.: Research and identification of natural and treated nephrite in China, 122 (Summer)
 Zhang J., Lu T., Wang M., Chen H.: The radioactive decay pattern of blue topaz treated by neutron irradiation, 302-307 (Winter)
 Zheng S., see Chen T.
 Zhou C.-H., see Lu R.
 Zhou W., see Krzemnicki M.S.
 Zorba T., see Karamelas S.
 Zucker B., see Dubinsky E.